Nondestructive evaluation of thermal barrier coatings

by Bo Tan, BSc, MSc

Thesis submitted to The University of Nottingham
for the degree of Doctor of Philosophy, May 2017



Abstract

Thermal barrier coatings at high temperature thermal cyclic oxidation generate stress concentration and result in coating failure, which can endanger the engine during operation. Regular nondestructive inspection of their quality condition has received increasing attention. This project is aimed to investigate the thermal cyclic oxidation behaviours of TBC system and evaluate thermal barrier coating during thermal cycling by optimised nondestructive evaluation techniques along with microstructure analysis using scanning electron microscopy.

The internal microstructure and exterior surface morphology of an unconventional TBC sample coated by ESAVD were investigated using two different laboratory X-ray CT scan systems. As a result, an image resolution of 0.6 μm is achieved by Xradia XRM-500 X-ray CT, five different layers were observed in the thermal barrier coating system including a few of cracks at the interface of YSZ layer and bond coat.

The thermal cyclic oxidation behaviour of conventional 7-8 wt.% YSZ air plasma sprayed TBC sample was evaluated using laser photoacoustic spectroscopy. The thickness of TGO layer of each sample after thermal cyclic oxidation was measured in a panorama BSE image using image analysis. A relationship was found between signal energy and TGO thickness, illustrating that signal energy decreases with the increasing TGO thickness. A physical model was studied to estimate the influence of crack inside TGO on signal attenuation, which indicated that the signal energy reduction is due to a combination of laser reflection at interfaces, laser attenuation by TGO layer and ultrasound reflection at interfaces. In addition, the position of the presence of crack inside of TGO alters the remainder of signal energy, where crack presented near the interface of TGO layer and bond coat attenuates more signal energy. Study on amplitude attenuation in a bond coat only sample has confirmed that ultrasound signal was generated in TGO layer which works as a constrained surface layer facilitate the laser ultrasonic generation at early oxidation stage. It is shown that the increasing thickness of TGO layer increased the attenuation of laser irradiation, and the increasing number of cracks in TGO layer increased the laser reflection at crack/TGO interfaces.

The analysis of asymmetric electrode geometry effect on YSZ material using the finite element simulation was demonstrated, subsequently the findings of which were

verified via electrochemical impedance spectroscopy using a set of YSZ ceramic bulk samples with asymmetric electrodes geometry. It is shown that asymmetric electrode geometry results in non-uniform current distribution in the simulated model. The direction of current diverges from the centre to the side by the radial electrical potential and then gradually return to the direction perpendicular to the surface. An equivalent electrode area is calculated which can be used to fix the influence of asymmetric electrode geometry in impedance spectroscopy measurement by replacing the area of applied conductive paint in the calculation. A linear relationship is revealed between the ratio of equivalent area to applied electrode area and the resistance of simulated model. The gradient of their plots is proportional to the thickness of the sample. Based on the relationship, a method is proposed to estimate the resistance of a sample with a known asymmetric electrode geometry via an inverse operation.

Acknowledgements

I wish to express my sincere gratitude to my supervisors, Prof. Steve Sharples for sharing his valuable knowledge, continuous support, guidance, and encouragement throughout my PhD study; Prof. Xianghui Hou for the motivation, his rigorous approach and attitude to science has given me, kind advice and comments on this thesis; and Prof. Matt Clark whose professional expertise provided me with valuable ideas and inspiration for the project.

I am also very grateful to Dr Wenqi Li's endless patience in teaching me over the years, starting from the basis of signal analysis and writing Matlab scripts; which guided me towards the right way of solving problems during the research.

I would also like to thank Dr Ming Li, Dr Rikesh Patel, Dr Peng Zhang and my colleagues at Wolfson building, for their valuable suggestions and discussions on my study.

I would like to thank Elisabeth Steer, Dr Nigel Neate, Rory Screaton and the staff and technicians at Wolfson Building and NMRC, for their guidance, training on the use of equipment and their kind help with sample preparation.

I would like to thank all my friends who supported me or influenced me along the way. I feel very lucky to have them by my side.

I would like to thank Dominika with all my heart, for all her love, support and encouragement.

Last but not least, I would like to thank my parents, for their unconditional support and encouragement through these years.

Contents

Abstract....1

Acknowledgements....3

List of Abbreviations....9

Chapter 1 Introduction....11

1.1 Gas turbine engines....11

1.1.1 Efficiency, temperature and advancements....12

1.1.2 Single crystal nickel-based superalloy....14

1.1.3 Thermal barrier coatings (TBCs)....17

1.2 NDT techniques for TBCs....19

1.3 Research aims and objectives....22

Chapter 2 Literature Review....25

2.1 Thermal barrier coating systems....25

2.1.1 Ceramic top coats....26

2.1.2 Bond coats....30

2.1.3 Thermally grown oxide....32
2.1.4 Failure mechanisms....33
2.2 X-ray CT....38
2.2.1 Introduction....38
2.2.2 Beer's Law....39
2.2.3 Linear attenuation coefficients....40
2.2.4 Previous researches....41
2. 3 Laser photoacoustic spectroscopy....44
2.3.1 Introduction....44
2.3.2 Mechanisms for laser generation of ultrasound....44
2.3.3 Previous researches....46
2.4 Impedance spectroscopy....48
2.4.1 Introduction....48
2.4.2 Fundamental principles....48
2.4.3 NDT for thermal barrier coatings using impedance spectroscopy....52
4.2.4 Calculation of resistance....55
2.5 Other nondestructive evaluation of TBCs....57
2.5.1 Infrared imaging....57
2.5.2 Pulse-echo thermal wave infrared imaging....59
2.5.3 Mid-infrared (MIR) reflectance....60
2.5.4 Luminescence spectroscopy....61
2.6 Comparison of the various NDT techniques for thermal barrier coatings....63
2.7 Summary....66

Chapter 3 Research Methodologies....68
3.1 Preparation of TBCs....70
3.1.1 Substrate preparation....70

3.1.2 High velocity oxygen fuel (HVOF) spray 72
3.1.3 Air plasma spray (APS) 74
3.2 Freestanding YSZ coating preparation 76
3.3 Preparation of ceramic bulk samples 77
3.4 High temperature cyclic oxidation 79
3.5 Microstructure characterisation 80
3.5.1 Sample preparation for SEM 80
3.5.2 Scanning electron microscopy (SEM) 80
3.5.3 Energy dispersive X-ray analysis (EDS) 81
3.5.4 X-ray diffraction (XRD) 81
3.6 SEM image analysis 82
3.7 Summary 84

Chapter 4 X-ray CT 85
4.1 X-ray CT measurement 86
4.1.1 Sample preparation 86
4.1.2 GE Phoenix nanotom 86
4.1.3 Xradia Versa XRM-500 87
4.2 Results 90
4.2.1 GE Phoenix nanotom 90
4.2.2 Xradia XRM-500 92
4.3 Discussion 94
4.4 Summary 95

Chapter 5 Laser Photoacoustic Spectroscopy 96
5.1 Laser photoacoustic spectroscopy measurement 97
5.1.1 Instrumentation 97

5.1.2 TBC sample sets 100
5.1.3 Signal detection 102
5.1.4 Data analysis 106
5.1.5 Laser attenuation in YSZ ceramic coating 114
5.1.6 Metallic bond coat testing using LPAS 115
5.2 LPAS results 116
5.2.1 Single crystal substrate TBC samples 116
5.2.2 Multigrain substrate TBC samples 122
5.2.3 Summary of LPAS results 127
5.3 Laser attenuation in YSZ ceramic coating 129
5.4 Amplitude attenuation in metallic bond coat 131
5.5 Oxidation behaviours of TBCs samples 132
5.6 Discussion 135
5.6.1 Substrate grain orientation of MG samples 135
5.6.2 Relation between signal energy and TGO thickness 137
5.6.3 Ultrasound attenuation by TGO layer 138
5.6.4 Cracks in the TGO layer 140
5.6.5 Physical model of laser attenuation in TGO 143
5.6.6 Oxidation of bond coat 150
5.6.7 Phase map analysis 154
5.6.8 Viability of the technique and applications 156
5.7 Summary 157

Chapter 6 Impedance Spectroscopy 159

6.1 Finite element simulation of the resistance of YSZ bulk with an asymmetric electrode geometry 161
6.1.1 Modelling approach 161

6.1.2 Results of finite element simulation 163
6.1.3 Calculation of resistance 167
6.1.4 Equivalent electrode area 169
6.1.5 Summary 172
6.2 Impedance spectroscopy measurement of the resistance of YSZ bulk with an asymmetric electrode geometry 173
6.2.1 Impedance spectroscopy measurement 173
6.2.2 Impedance spectroscopy results 175
6.2.3 Equivalent circuit fitting 179
6.2.4 Discussion 181
6.2.5 Summary 185

Chapter 7 Conclusions and Future Work 186
List of Achievements 190
Future Work 192
References 195
Appendix A 209
Appendix B 210
Appendix C 212
Appendix D 213
Appendix E 215

List of Abbreviations

8YSZ	8 wt.% Yttira stabilised zirconia
APS	Air plasma spray
BC	Bond coat
BSE	Backscattered electron
CMC	Ceramic matrix composite
CMT	Computed micro-tomography
CMSX-4	A typical second-generation single crystal alloy
CPE	Constant phase element
CT	Computed tomography
CTE	Coefficient of thermal expansion
CVD	Chemical vapour deposition
EB-PVD	Electron beam physical vapour deposition
EDS	Energy dispersive X-ray spectroscopy
ECD	Electrical current density
EIS	Electrochemical impedance spectroscopy
EPG	Electrical potential gradient
EPOT	Electrical potential
ESAVD	Electrostatic spray assisted vapour deposition
EVOL	Element volume
FCC	Face-centred cubic
FFT	Fast Fourier transform
FOD	Foreign object damage

HP	High pressure
HVOF	High velocity oxygen fuel
IP	Intermediate pressure
IR	Infrared camera
IS	Impedance spectroscopy
LAC	Linear attenuation coefficient
LP	Low pressure
LPPS	Low pressure plasma spray
M247	Mar-M-247
MCrAlX	(Nickel, Cobalt) - Chromium - Aluminium - (Zirconium, Hafnium, Silicon and Yttrium)
MG	Multigrain
MID	Mid-infrared
MIDS	Moisture induced delayed spallation
NDT	Nondestructive testing
NiCoCrAlY	Nickel-Cobalt-Chromium-Aluminium-Yttrium
PLS	Photoluminescence spectroscopy
PVA	Polyvinyl acetate
SAW	Surface acoustic wave
SEI	Secondary electron imaging
SEM	Scanning electron microscope
SRCL	Synchrotron radiation computed laminography
SX	Single crystal

TAFA	The Arcade Flyer Archive
TBC	Thermal barrier coating
TGO	Thermally grown oxide
TWI	Thermal wave image
VPS	Vacuum plasma spray
WEDM	Wire electrical discharge machining
XRD	X-ray diffraction
XRM	X-ray microscope
YSZ	Yttria stabilised zirconia

Chapter 1

Introduction

1.1 Gas turbine engines

'For every action, there is an equal and opposite reaction'. In 1686 Sir Isaac Newton presented Newton’s third law of motion, which later formed the fundamentals of modern aircraft propulsion theory. Based on the third law of motion, high-pressure exhaust gases produced from gas turbine engines provide a powerful thrust in opposite directions, which propel aircraft forward at high speed [1].

A turbofan is a type of gas turbine engine, in which thrust is mostly generated by a fan instead of the exhaust. It is mainly used for commercial aircraft flight at subsonic speed with high efficiency. A turbofan engine consists of four sections: fan, compressors, combustion and turbines. Figure 1.1 shows a cutaway of a typical turbofan engine [2]. Unlike rocket engines which carry an oxygen supply for its combustion, the gas turbine engine gets oxygen from the surrounding atmosphere. Most of the incoming air is flowing outside of the engine core to generate thrust for the aircraft, and the rest is taken into low-pressure compressors. Then the low-pressure air is compressed into a high-pressure compressor stage where the air is compressed about fifty times that of standard atmospheric pressure. In this process, the rotating blades convert mechanical energy into potential gaseous energy. Then the high-pressure air is delivered into the combustion chamber wherein the fuel is mixed with air which is controlled by fuel spray nozzles. When this high pressure mixture is ignited, it produces high temperature high pressure gases which expand to many times that of the original volume. These

combustion gases are channelled through three sets of turbines to turn three spool shafts. As the pressure and temperature fall, most of the energy stored within the gas is converted into mechanical energy which continuously supports the combustion process and turns the fan at the front of the engine, where generating thrust for the aircraft.

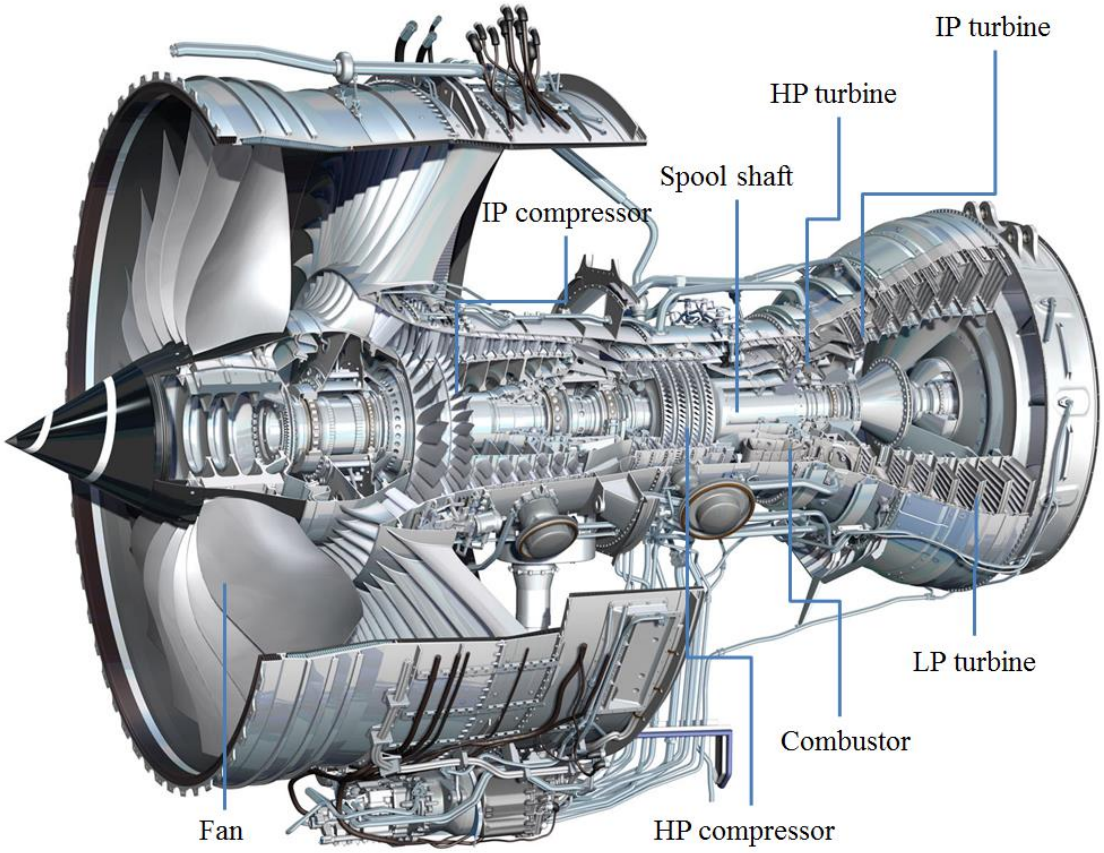


Figure 1.1 Cutaway view of turbofan engine (Trent 1000 Cutaway [2]) HP-High Pressure, IP-Intermediate Pressure, LP-Low Pressure.

1.1.1 Efficiency, temperature and advancements

The overall efficiency of the aircraft engine is directly related to fuel consumption and environmental impact. The propulsive efficiency as the main influence which depends on the bypass ratio of the engine, the aerodynamics of gas path components, the thrust to weight ratio, etc. Thermodynamic efficiency as the second influence can be increased using higher overall pressure ratios, higher combustor temperatures and

more efficient secondary systems, which involves innovation of compressor, combustor and turbine design, respectively [3, 4].

Increasing the inlet temperature is used as a direct approach to increase the efficiency of gas turbine engine. However, it is limited by the properties of materials, in terms of the maximum temperature that alloys can withstand at the first stage of a turbine. Typical alloy materials with the corresponding feasible gas operating temperature are shown in Figure 1.2. Nowadays, the commercial aircraft turbines temperature is above 1500 °C, and for military aircraft, temperatures can reach upwards of 1600 °C, both of which are well beyond the melting temperature of superalloys [5]. This has benefited from three advancements: increasing oxidation and creep resistance by using single crystal superalloys, increasing airflow by including channels underlying the turbine blades and applying thermal barrier coatings (TBCs) to the surface. The latter two allow a temperature drop of 100-300 °C between the gas and superalloy surface [6]. Ceramic matrix composites (CMCs) are developing materials for turbine engines, which are tough, lightweight and can withstand much higher temperature than metal alloys.

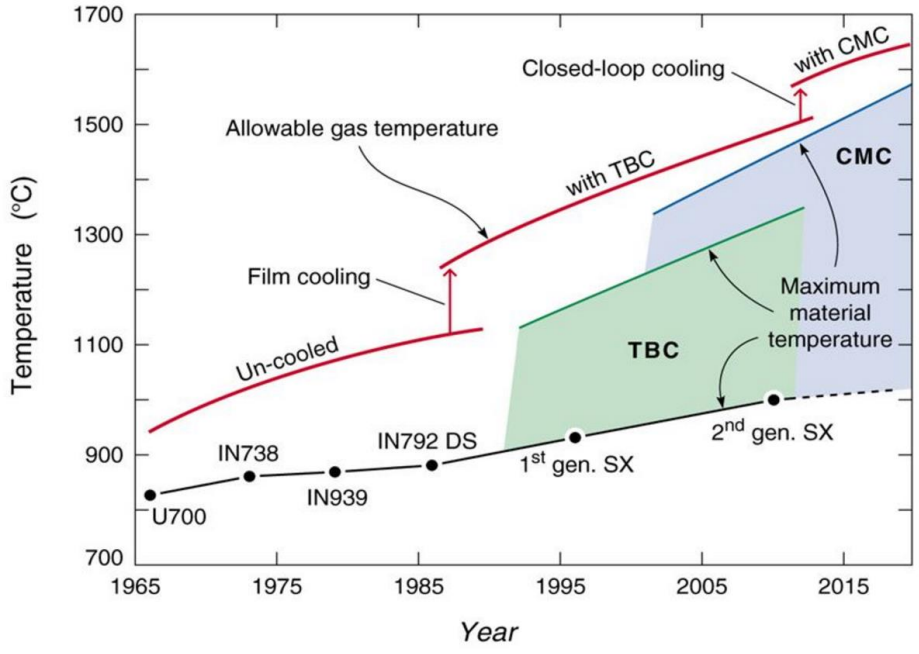


Figure 1.2 The development of materials for turbine blades with corresponding maximum temperatures [7]

1.1.2 Single crystal nickel-based superalloy

Superalloys combine several metallic elements which exhibit superior properties at extremely high temperature and load conditions, such as high mechanical strength, creep strength, phase stability, fatigue resistance and oxidation resistance [8]. Nickel-based superalloys are the most suitable candidates for use at high temperatures, which can maintain good mechanical properties even above 80% of their melting point in some applications [9]. The main strengthening methods sufficient enough to withstand the high temperature levels generated in aero-dynamic engines are a combination of solid-solution and precipitation hardening process in a γ matrix, often used to increase high temperature capability of metals.

The development of crystal structures in cast nickel-based superalloy turbine blades started by using the polycrystal structure followed by directionally solidified columnar-crystal to nowadays preferred single crystal superalloys. The metal temperature capability of turbine blades has significantly increased in the last five decades, as seen in Figure 1.3 [10]. When blades are operated in the first row of the turbine stage, superalloys not only require corrosion resistance to withstand the high temperatures but also strong creep strength due to the tensile stress caused by centrifugal forces. As shown in Figure 1.4, creep strength and thermal fatigue resistance are improved significantly in single crystal structures due to the absence of γ/γ' grain boundaries that increase the diffusion rate.

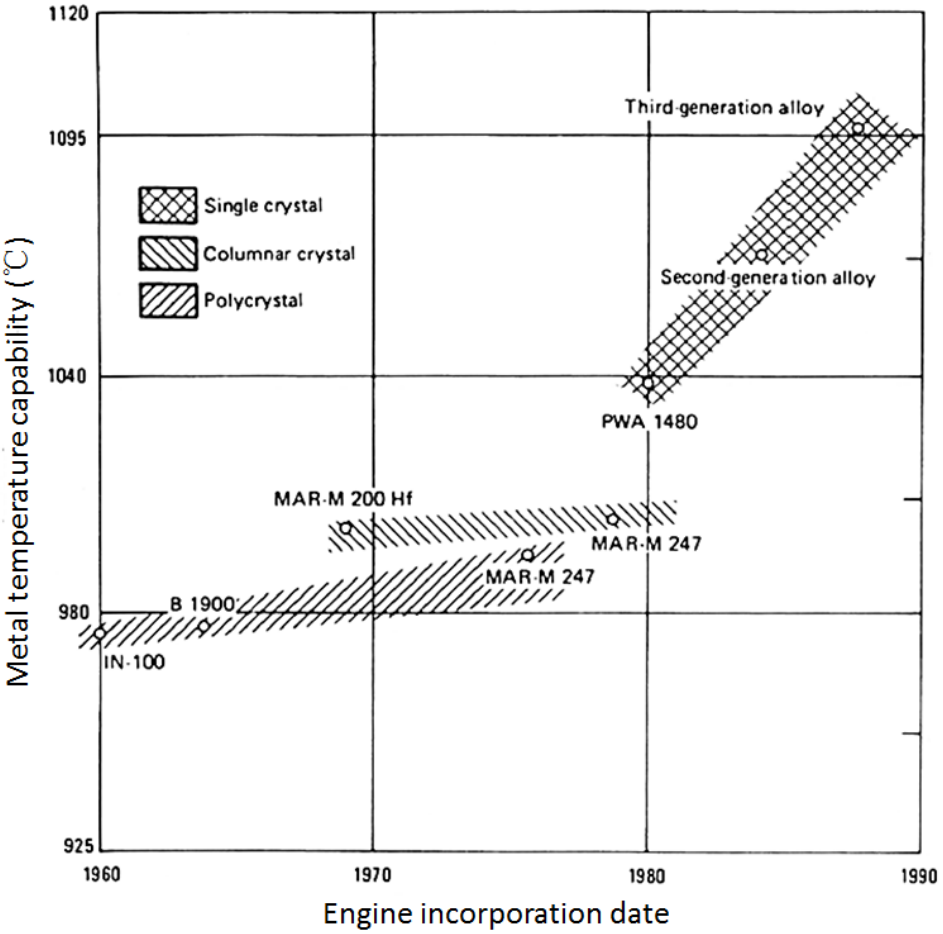


Figure 1.3 Progress in turbine blade metal temperature capability [10, 11]

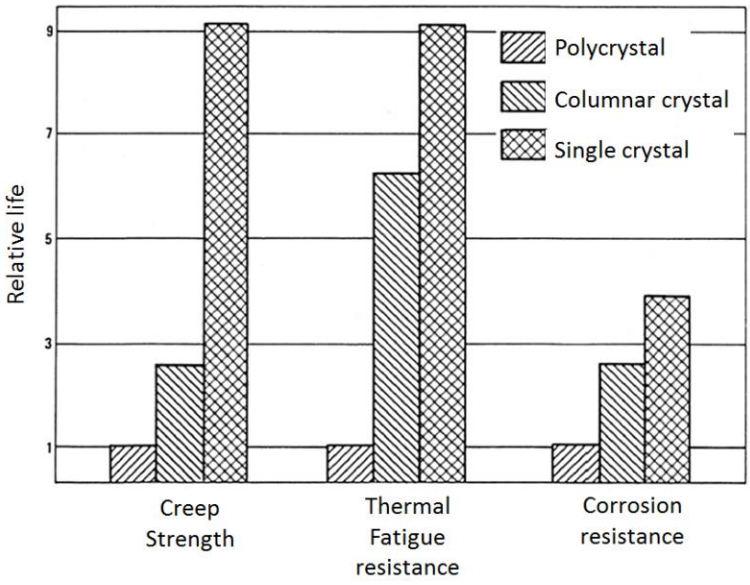


Figure 1.4 Comparative properties of polycrystal, directionally solidified columnar-crystal and single crystal superalloys [10, 11]

The typical single-crystal superalloy microstructure usually contains ordered γ'(Ni_3(Al,Ti)) precipitates of strenghteners coherently embedded within nickel-based solid solution γ matrix of FCC (Face-centred cubic) crystal structure [12], as shown in Figure 1.5. The resulting mechanical properties vary depending on volume fraction and its balance, atomic distribution and size, and the coherency between γ' precipitates and γ matrix. For example, creep strength is proven to be directly related to the function of volume fraction of solutioned and reprecipitated fine γ'. Additional components can be further added to the substrate to minimise individual causes of degradation, for example, boron or zirconium to improve creep resistance [13]. Single-crystal superalloys can avoid using these additives due to the absence of grain boundaries, and thus further increase the incipient melting temperature.

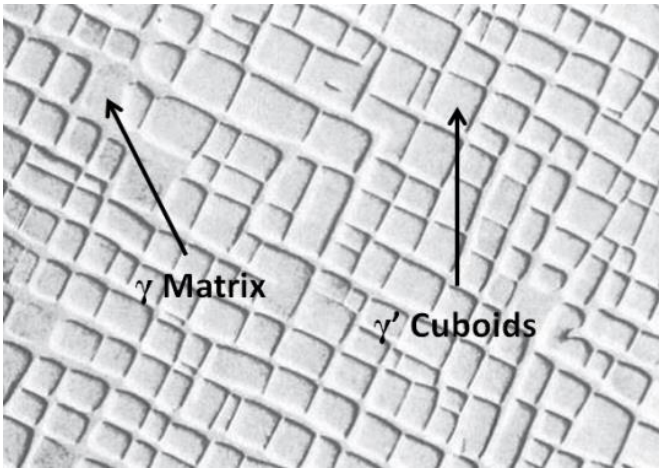


Figure 1.5 Micrograph of nickel based superalloy showing gamma prime precipitates (size 0.35 to 0.6 μm) [9]

Although the nickel-based single crystal superalloys have significantly improved turbine engine performance and durability, with the continuous increase in temperature to acquire higher efficiency of the engine, further high temperature corrosion protection is a priority. This is where non-metallic material coatings, such as yttria-stabilized zirconia (YSZ) thermal barrier coatings come into play as further protection for the superalloys.

1.1.3 Thermal barrier coatings (TBCs)

Thermal barrier coatings can provide extra heat insulation to engine components due to their low thermal conductivity, which increases engine operating temperatures and hence improves fuel efficiency and engine reliability [14]. Since the thermal barrier coating (TBC) is the main topic of this thesis, a more in-depth review of its structure, oxidation behaviour and failure mechanism will be presented in chapter 2.

Conventional thermal barrier coatings normally are a bilayer system: the top layer is a ceramic coating which provides thermal insulation for turbine blades, namely ceramic top coat; the bottom layer is a metallic coating which provides an adhesive bonding between the ceramic top coat and the superalloy substrate, namely bond coat [15]. An oxidised layer of bond coat is formed between the two layers at high temperature due to the oxygen penetrates through the ceramic top coat, namely thermal growth oxidised layer (TGO) which mainly consisting of alumina, as shown in Figure 1.6 [16, 17]. As thermal barrier coatings work under severe environmental conditions during long term thermal cyclic services, thermal expansion mismatch between each layer in the coating system generates internal residual stress which forms cracks at their interface and causes damage accumulation [18]. Consequently, the cracks lead to delamination while the TBC system is subjected to thermomechanical load during operation. A large scale spallation of the coating will occur when the delamination has exceeded a critical length, which eventually leads to coating failure and exposes the turbine blade components to extraordinarily high temperatures [19, 20]. This leads to rapid degradation of substrate material, and in consequence, potential engine failure during operation. Therefore, regular inspection of the quality of its condition is extremely important.

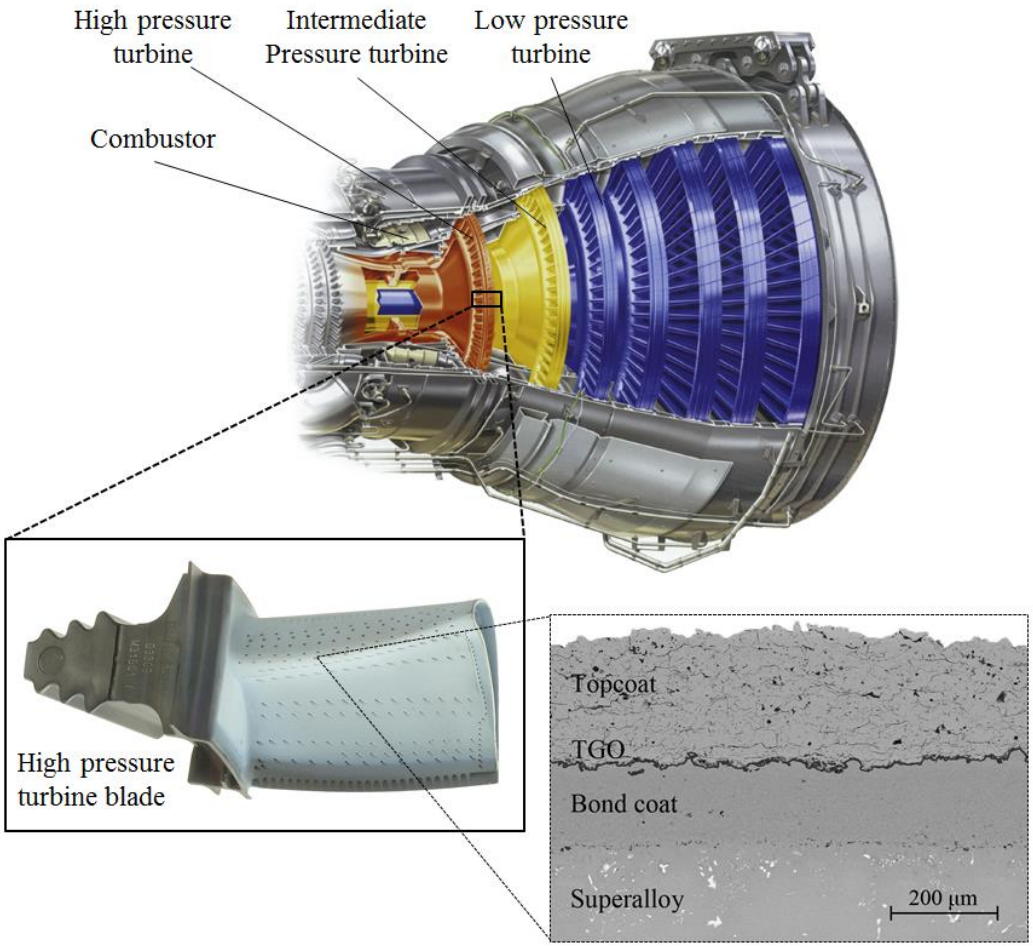


Figure 1.6 Thermal barrier coatings applied on gas turbine engine (Edited from [16, 17])

The degradation of thermal barrier coating degradation is usually characterised using classical metallographic techniques which require specimen preparation, including sectioning process, grinding and polishing, etc. Since ceramic coatings are very brittle, any external friction from a cut-off wheel or polishing disc will introduce artificial cracks or delamination in the microstructure. Artificial flaws will lead to confusion in any subsequent study and will hide the true cause of damage in the investigation. Therefore, it is important to develop nondestructive testing methods for the inspection of thermal barrier coatings.

1.2 NDT techniques for TBCs

Thermal barrier coatings have been successfully employed to increase gas turbine inlet temperature and improve the efficiency of turbine engines during service. But at the same time, TBC systems are subjected to extreme temperatures and complicated cyclic thermomechanical loading which can lead to failures of the coating. Since the operating temperature of turbines has exceeded the limitation of superally substrates, the TBC failures will expose the turbine blade components to a severe environment which can endanger the engine during operation. Consequently, regular health monitoring and life prediction of TBCs using nondestructive method have received increasing attention.

A number of researchers [21-25] have reviewed nondestructive measuring methods for the evaluation of thermal barrier coatings. Nondestructive testing techniques can be divided into two catergories dependent on whether they use an external stimulus to provoke material response which is subsequently observed and analysed, for example in ultrasonic testing [18, 26-28], or adopt a noncontact method of X-ray computed tomography [29-34], without significant interaction with measured material [24].

The choice of NDT techniques mainly depends on two things: the primary purpose of testing and the type of TBC, in particular, its microstructure which influences its optical and thermal properties [23]. For example, electron beam physical vapour deposition (EB-PVD) coated samples have better-defined columnar microstructure and are less prone to optical scattering compared to the porous and laminar microstructure of an air plasma sprayed (APS) coating. Therefore, the former is more suitable to be examined by laser-based optical NDT methods, such as laser ultrasound [35-41], photoluminescence spectroscopy [42-45] and developed laser photoacoustic spectroscopy, since the microstructure of the coating attenuated less incident laser light.

In laser ultrasound technique, both bulk wave and surface acoustic wave, also referred as Rayleigh wave, are generated spontaneously by a pulsed laser. The former propagates through the thickness of the coating which can be used to determine the elastic and acoustic properties of the coating and detection of cracks and delamination [38, 41]. The latter propagates along the coating surface with a penetration depth (amplitude) proportional to its wavelength, the elastic properties can be evaluated

using their group velocities in a dispersion curve [37, 46]. Compared to conventional ultrasonic technique, the advantage of laser ultrasonic technique are its noncontact character, capable of performing measurement on complex geometry, accurate time resolution due to the large bandwidth of the signal.

In the photoluminescence spectroscopy (PLS), laser penetrates the partially translucent ceramic top coat to the TGO layer, simulate the Cr^{3+} ions in the TGO layer which luminesce in two spectral lines, R_1 and R_2. The stress in the TGO layer leads to a spectral shift of the luminescence on these lines [24]. When the delamination occurred at the interface of top coat and bond coat, the residual stress is relieved in TGO which is detected from Cr^{3+} luminescence spectrum. Consequently, it has the potential to assess the damage buried beneath the YSZ top coat and estimate the remaining lifetime of thermal barrier coating in high temperature application.

Another type of optical methods involves measuring the change in thermal properties or heat distribution within a heat stimulated TBC, which includes thermal wave image (TWI) also called infrared image [47-49], mid-infrared reflectance [50-52], pulse-echo thermal wave infrared image [53, 54]. These type of methods is commonly used for detecting the delamination that has evolved in TBC systems.

Thermal wave imaging (TWI) essentially measures the temperature distribution across TBC samples to identify existing defects. The sample is exposed in front of a cyclic heat flow which establishes a temperatures gradient throughout the thickness of the sample, and the temperature distribution across the surface of the ceramic coating is monitored at the back by an infrared camera (IR). Microcracks and defects generated in the TBC samples after cyclic thermal exposure reduce heat transfer to the surface, which results in progressively cooler appearing areas [24].

Mid-infrared (MID) reflectance technique takes advantage of the fact that TBCs are translucent in the range 3 to 5 μm [24], delamination can be detected by measuring the reflectance of irradiated MID using an IR camera. The presence of a crack changes the refraction index lead to an increase in reflectance.

Pulse-echo thermal wave infrared imaging is a type of the thermal imaging method that exerts an external stimulus of heat to the TBC sample to subsequently monitor the temperature distribution across the sample by IR camera. Defects developed in TBC

system change thermal conductivity of the material in its immediate proximity which results in slower diffusion of heat [53]. Therefore, in contrast to the intact bonded interface in the thermal imaging, the areas with underlying defects present higher temperatures and take longer to cool down. This technique has been proven to identify various forms of damage generated at the ceramic-bond coat interface.

Other NDT methods also available to detect delamination and to measure thickness, such as eddy current [44-46] and impedance spectroscopy [47-62]. Eddy current is widely used for thickness measurement of ceramic top coat and bond coat. additionally, the delamination and degradation of the coating are evaluated by measuring the conductivity of bond coat.

Electrochemical impedance spectroscopy (EIS) is a well known technique for corrsion detection undernearth the coated surface [55]. The degradation of YSZ thermal barrier coatings can be evaluated by the impedance responses of an applied alternating current over a range of frequencies, where the variation of electrochemical parameters in the impedance spectra are related to oxide layer growth, composition change and presence of cracks or delamination in the microstructure of samples.

A more comprehensive review of nondestructive evaluation methods of thermal barrier coating will be given in Chapter 2, which will mainly focus on the three primary techniques applied for TBC system in this research, X-ray computed tomography, impedance spectroscopy and laser photoacoustic. The pros and cons will be discussed at the end of Chapter 2.

1.3 Research aims and objectives

In the previous section, a number of available NDT methods for evaluation of thermal barrier coating have been introduced. Each method has its own advantage and proper scope corresponding to different aspect measurement of the thermal barrier coating. Similarly, each method has limitation and drawback.

X-ray computed tomography (X-ray CT) visualise the interior structure of TBC system via 3D reconstruction which enables to observe internal crack and delamination and provides information such as coating density, pore size distribution, surface roughness. However, the resolution of X-ray image is influenced by a combination factor of sample size, the density of the material and the atomic number of the elements in the material, which could result in difficult to measure TBC system in high resolution due to the high density metallic substrate and the heavy elements in the YSZ. Therefore, in order to obtain a satisfied image in high resolution, a concession has to made on the sample size. Study on the influence of sample size on X-ray image resolution is essential.

Ultrasonic methods are capable for the characterisation of thermal barrier coating including the detection of delamination and measurement of coating thickness, porosity content and acoustic properties. However, there is energy loss of ultrasonic signal due to signal attenuation by the porous and microcracked microstructure of YSZ ceramic coating. Nevertheless, the interface of bond coat and substrate could not be detected by ultrasound due to the acoustic properties of these two layers are very close to each other. Moreover, ultrasonic generation/detection require use coupling medium between sample and transducer or operating fully immersed in the water, which could lead to contamination of sample or moisture induced delayed spallation (MIDS) [56]. A noncontact laser ultrasound technique detecting generated surface wave using interferometer has overcome this problem. However, it requires additional sample surface preparation by coating a reflection layer to increase the sensitivity of detection laser, which is hard to remove after testing. Therefore, a new NDT method for measuring TBC system is developed, referred to photoacoustic spectroscopy, which generates ultrasound at sub-layer to avoid signal attenuation by the surface YSZ layer and reduces the signal interference during the propagation through the porous laminated structure of YSZ.

Electrochemical impedance spectroscopy is widely used for evaluating the degradation of thermal barrier coating, particularly useful for ceramic materials. It is capable of measuring the TGO thickness [57-63], detecting microstructural and composition changes in the TGO [64, 65], and phase transformation in YSZ [66, 67]. However, previous researches [68, 69] on nondestructive testing of thermal barrier coatings using impedance spectroscopy have acknowledged the influence of asymmetric electrode geometry on impedance spectrum due to a smaller area of the applied electrode on YSZ surface. Consequently, inaccurate calculation of resistance was involved due to non-uniform current distribution through a specific electrode area of the sample. Therefore, analysis of asymmetric electrode geometry effect on YSZ material is essential and will be demonstrated using both finite element simulations and impedance spectroscopy measurements in the present work.

The primary aim of the present work is to investigate the thermal cyclic oxidation behaviours of TBC system and evaluate thermal barrier coating during thermal cycling by optimised nondestructive evaluation techniques along with microstructure analysis using scanning electron microscopy (SEM). In order to solve the previously stated problems, this project will foucus on three NDT methods for measuring TBC system which included X-ray CT, laser photoacoustic spectroscopy and impedance spectroscopy. The objectives of the present study are listed as followings:

- Manufacture TBC samples to study the thermal cyclic oxidation behaviour of TBC samples by SEM along with image analysis of the microstructure.
- Observe the internal microstructure and surface morphology of TBC using two currently available laboratory X-ray CT scanners along with 3D reconstruction technique to study the influence of sample size on X-ray image resolution.
- Design and assemble a laser photoacoustic spectroscopy to evaluate the cracks in the TGO layer of the TBC samples after thermal cyclic oxidation and investigate the mechanisms of the signal attenuation of the laser generated ultrasound in TGO layers.
- Analysis of asymmetric electrode geometry effect on YSZ material using both finite element simulations and impedance spectroscopy measurements.

This thesis consists of seven chapters, and it is organised as follows: The current chapter introduces the background of gas turbine engines and thermal barrier coatings along with the correlated NDT methods and explains the motivation, aim and objectives of the research. Chapter 2 presents a more comprehensive literature review of thermal barrier coating systems and the relevant nondestructive evaluation methods. Chapter 3 provides the details of experimental methodologies including sample preparations, thermal cyclic oxidation test and characterisation methods. Then, the observation of TBC microstructure using X-ray computed tomography is demonstrated in chapter 4. Chapter 5 presents the evaluation of thermal cyclic oxidation behaviours of TBC samples using the developed laser photoacoustic spectroscopy technique and investigates the mechanism behind of it. Chapter 6 analysis the asymmetric electrode geometry effect on YSZ material using both finite element simulations and impedance spectroscopy measurements. Chapter 7 summaries the work presented in this thesis and discusses potential improvements along with suggested future work.

Chapter 2

Literature Review

2.1 Thermal barrier coating systems

The first stage of turbine blade system is that behind the combustion chamber, which operates in one of the harshest environments of gas turbine engine. It is exposed to severe mechanical loads, corrosion and erosion environments, and most importantly the extremely high temperatures that already exceed the melting temperature of superalloys [70]. However, a higher operating temperature of gas turbine engine provides many more benefits, which forces the continuous development of more durable applied materials.

Over the past century, the manufacturing techniques of turbine blades were developed from cast materials to superalloys and then to single crystal casting technologies. Nevertheless, the temperature capability of nickel-based superalloys has approached an intrinsic limit. Any further improvement in their temperature capability has become increasingly difficult. An idea was thus put forward in the 1960s, which is to use thermal barrier coatings on the surface of a superalloy to protect it from environmental degradation.

Current state-of-the-art thermal barrier coatings are bilayer systems, which contain two layers of coating: yttria-stabilized zirconia (YSZ) as a top layer material which mainly provides insulation of high temperature for alloy component due to its low thermal conductivity and excellent corrosion resistance properties; and an inner bond coat,

usually made of diffusion aluminide or MCrAlY (M: Co, Ni or mixture of Co and Ni) which offers an interfacial bonding layer between the substrate and the top coat. Furthermore, due to the high temperature oxidation of the bond coat, a layer of thermally grown oxide (TGO) is formed between the bond coat and ceramic top coat. Once the TGO layer grows thicker than its critical thickness, it will lead to the failure of thermal barrier coating

This chapter will begin with the compositions and microstructure of a typical top coat, along with the coating processes. Next, the role of specific alloying constituents in bond coat and its two mainly used coating methods will be presented. Then their oxidation behaviour, TGO formation and failure mechanism will be presented in detail in the following section.

2.1.1 Ceramic top coats

The ceramic layer of TBCs is used to provide thermal insulation for turbine blades, which allows an increase in the inlet temperature without increasing the temperature of the alloy component. Zirconia has been chosen as a ceramic layer material for TBC due to a suite of desirable properties: low thermal conductivity, high thermal expansion coefficient, low density, high oxidation and thermal shock resistance and high melting point [6, 71]. Table 2.1 gives a summary of beneficial properties of zirconia.

Table 2.1 Summary of zirconia properties

Main property	Value (approximate)	Advantage
Thermal conductivitity	2.3 $W \cdot m^{-1} \cdot K^{-1}$	Scatter heat-conducting phonons by high concentration of point defects
Coefficient of thermal expansion (CTE)	11×10^{-6} $°C^{-1}$	Close to CTE value of alloy; Alleviate interfacial stresses arising from the thermal expansion mismatch
Elastic modulus	50 GPa	Further alleviate stresses by its microstructure feature: cracks and pores
Low density	6.4 $Mg \cdot m^{-3}$	Reduce the parasitic weight on turbine components
Hardness	14 Gpa	High resistance to erosion and paticle impact
High melting point	2700 °C	Suitable for high temperature application

Currently, yttria-stabilized zirconia (YSZ) is the most suitable material used for the top coat. The yttria-doping helps to stabilise zirconia at a desirable phase for high temperature applications. The concentration of yttria in the range of 6 to 8 wt.% has better performance on prolonging thermal cyclic life, which has been confirmed by previous research [72, 73]. Figure 2.1 shows the influence of YSZ composition on cyclic life time via laboratory cycling tests.

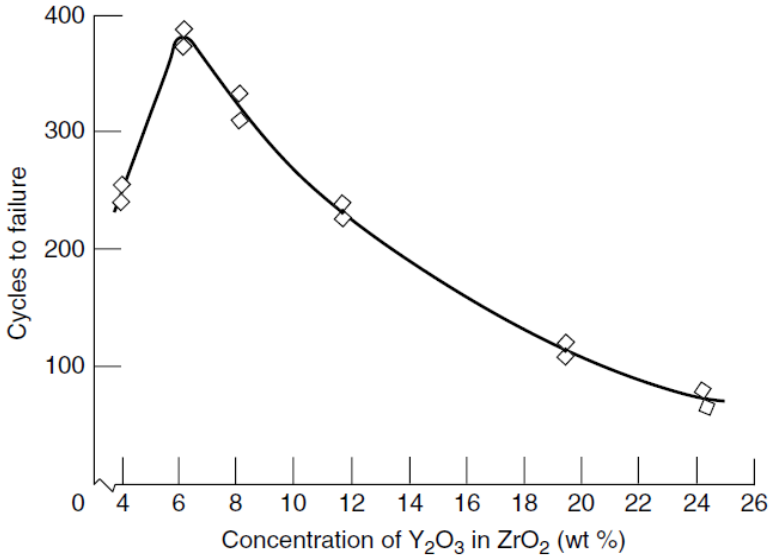


Figure 2.1 Optimum TBC composition shown by a laboratory cycling test [9].

Two most widely-used methods for TBC top coat deposition are air plasma spray (APS) [74] and electron beam physical vapour deposition (EB-PVD) [75, 76]. The TBC top coat produced by APS shows a laminar morphology which consists of flattened splats boundaries and volumetric pores parallel to the interface, which are highly effective in reducing the heat flow through the thickness of the coating, as shown in Figure 2.2(a). In contrast, the TBC top coat produced by EB-PVD has a columnar structure with elongated intercolumnar pores aligned perpendicular to the interface, as shown in Figure 2.2(b). These intercolumnar pores increase in size throughout the thickness of the coating which also increases the thermal conductivity of the coating. However, it increases the compliance of the coating which provides better strain tolerance than APS structure [70, 77].

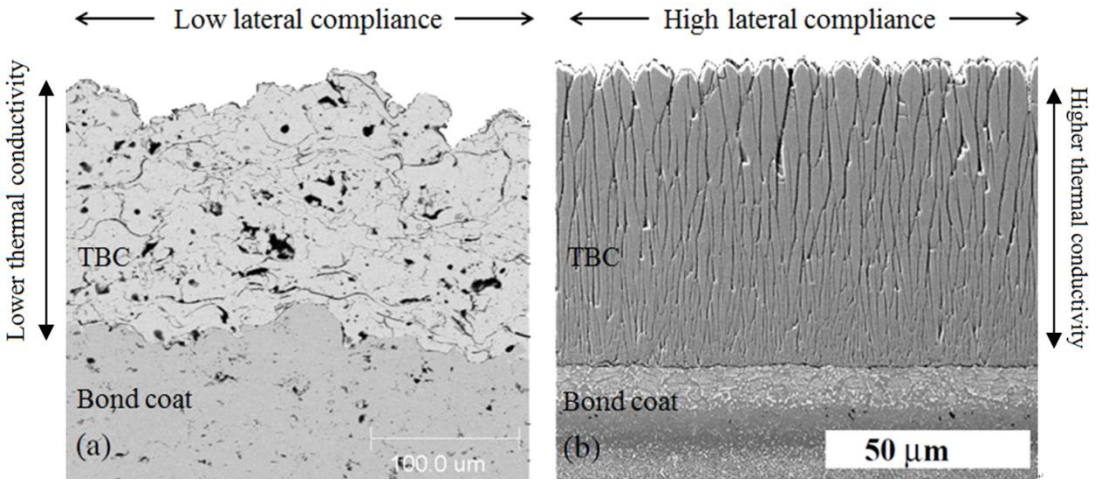


Figure 2.2 Microstructure of conventional 7 wt.% YSZ deposited by (a) APS; (b) EB-PVD [78]

In the plasma spraying process, the coating material in the form of powder is melted by a plasma jet and ejected within a frame. Then the accelerated molten particles impinged to the surface of the substrate, where they are rapidly solidified and form lamellae, continuously overlaying the particles on each other so that a lamellar structure is formed on the substrate. Interlaminar separations and vertical cracks are formed due to the thermal contraction during cooling [79]. Some un-melted particles during the deposition will form as large equiaxed grains in the microstructure, as shown in Figure 2.3. These separations and voids are efficient in lowering the thermal conductivity to a certain extent but also result in a rough surface finish, lower strain tolerance and erosion resistance [78]. Due to the relatively small CTE of YSZ compared with nickel superalloys substrate, significant strains are formed during thermal cycling which leads to the initiation of cracks at those separations or voids, which eventually results in the spallation of the coating.

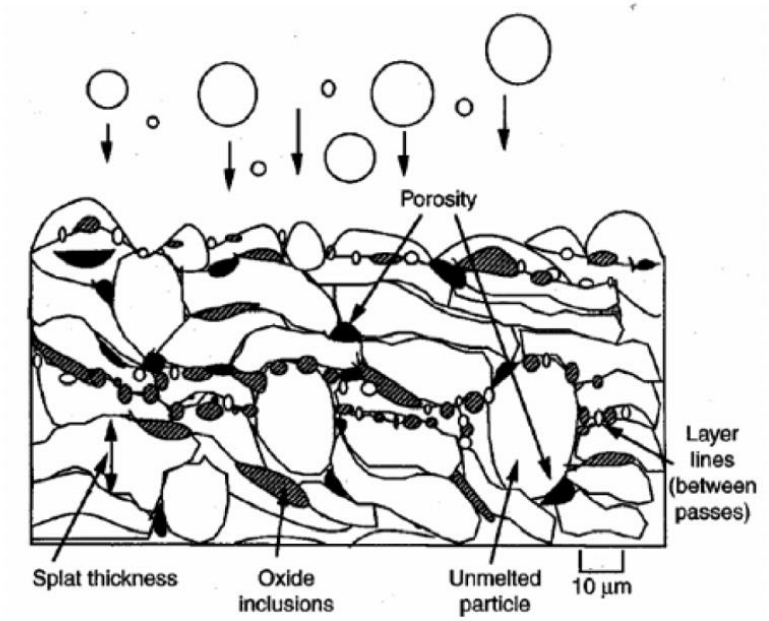


Figure 2.3 Schematic diagram of microstructure deposited by APS [80]

In the EB-PVD process, the coating material is melted and evaporated by multiple focused high-energy electron beams in a high vacuum chamber, while the substrate is preheated by some other electron beams inside the chamber. The material in a gaseous phase is then deposited on the substrate via condensation and forms a thin layer of coating with a columnar structure [81]. The ceramic coating produced by EB-PVD usually has a uniform microstructure and a smooth surface finish which provides better aerodynamics performance. Compared to APS, it has excellent strain tolerance, good erosion resistance and thus longer cyclic life than APS YSZ. Table 2.2 summarises the coating performances of EB-PVD and APS coating process

Table 2.2 Comparison of EB-PVD and APS coating performance on TBCs [81]

Properties	EB-PVD	Plasma sprayed
Thermal Conductivity (W/mK)	1.5	0.8
Surface roughness (μm)	1	10
Adhesive strength (MPa)	400	20-40
Young's modulus (Gpa)	90	200
Erosion Rate (Normalized to EB-PVD)	1	7
Microstructure	Columnar	Laminated

2.1.2 Bond coats

A bond coat is a layer of metallic coating between the ceramic top coat and the superalloy substrate, which protects the superalloy from the environmental degradation while provides an adhesive bonding between top coat and substrate. To meet two requirements bond coats should be provided with not only good oxidation resistance, corrosion resistance and high temperature stability but also strong cohesion with the metallic substrate, and the ability to relieve the thermal mismatch between the top coat and substrate [9]. Currently, two types of bond coats are mainly used, which are diffused aluminide coatings based on β-NiAl phase and overlay coatings based on MCrAlX system.

In diffused aluminide coatings, the β-NiAl phase is the predominant constituent due to its excellent oxidation resistance, high melting point and ability to form a protective alumina scale at high temperature. In the nickel-aluminium phase diagram, as shown in Figure 2.4, the β-NiAl phase exhibits the highest melting point among other phases when the atomic ratio of nickel to aluminium is around 1:1. The diffusion coating process including above pack process, pack process (including slurry) and chemical vapour deposition (CVD) [9].

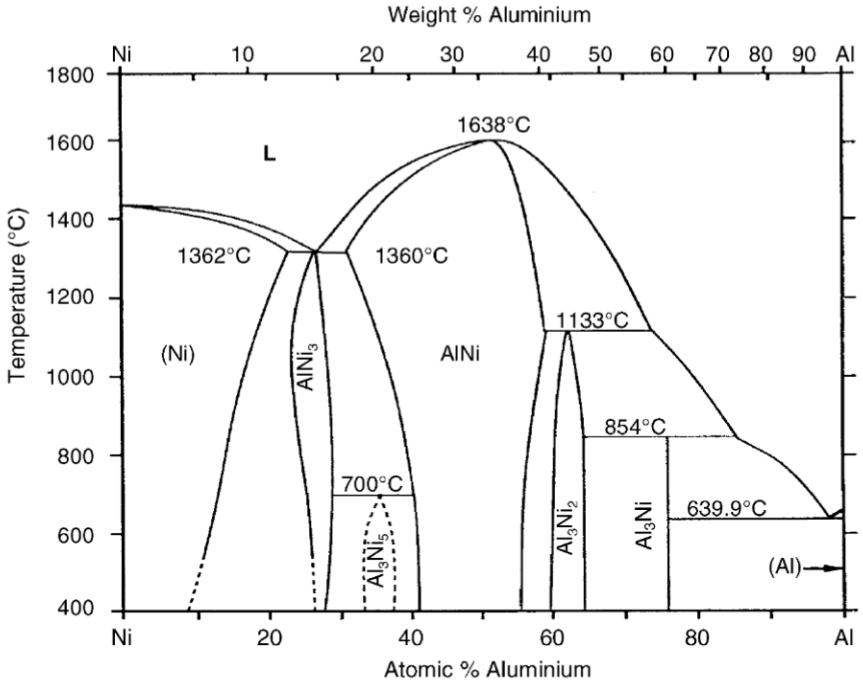


Figure 2.4 The Ni–Al phase diagram [82, 83]

For the MCrAlX system in an overlay bond coat, each element with a complex composition provides its own benefit. The element M stands for the base metallic element, where in high temperature application, cobalt, nickel or a mixture of them are commonly used due to their excellent high temperature corrosion resistance.

The function of aluminium is to improve the high temperature oxidation resistance by forming alumina and provides a reservoir of metal for replenishing oxide at a constant rate [84]. Chromium provides corrosion resistance at relatively low temperatures, increase aluminium activity and enhance its diffusivity rate [74]. The X refers to oxygen-reactive elements in the system, usually zirconium (Zr), hafnium (Hf), silicon (Si) and yttrium (Y). Yttrium is added to promote adhesive ability on thermal cycling [85]. The extra yttrium forms pegs that pin coating alloy and alumina film together [86]. In practice, MCrAlX coating usually contains 15-35 wt. % chromium, 4-8 wt. % aluminium and the concentration of yttrium is controlled between 0.5-1 wt.% [87-89].

Industrial available deposition methods for overlay bond coat included: Low Pressure Plasma Spray (LPPS), Electron Beam Physical Vapour Deposition (EB-PVD), Air Plasma Spray (APS), Vacuum Plasma Spray (VPS) and High Velocity Oxygen Fuel (HVOF) spray.

The surface finish of both types of bond coats is shown in Fig.2.2, which highly depends on the type of the chosen coating process. For a typical APS YSZ topcoat, a rough surface finish of MCrAlY overlay bond coat is required, in order to provide more anchoring point and thus enhance the adhesive bonding. For EB-PVD topcoat, the adhesion is enhanced by a strong chemical bonding. Therefore, the surface of bond coat is treated to flat and smooth finish to eliminate out-of-plane stress at the interface [78].

2.1.3 Thermally grown oxide

Thermally grown oxide (TGO) is known as an oxidation reaction product of bond coats during thermal exposure which is mainly formed of alumina at the interface between bond coat and ceramic top coat. A schematic diagram of the microstructure of TGO layer on an overlay NiCrAlY bond coat is shown in Figure 2.5 [90]. The grain scale of alumina changes throughout its thickness. The external layer of alumina is formed at the beginning of oxidation which contains fine and equiaxial grains in θ and γ phase [91]; α-alumina formed later close to bond coat side which is larger scale and elongated column grains. The formations of two types of grains are due to different diffusion methods of oxygen and Al ion. The formation of θ, γ-Al_2O_3 is due to aluminium ions diffuse outward from the bond coat and form transient alumina at the interface of the top coat and TGO, while the formation of α-Al_2O_3 is due to the oxygen diffuse inward through the ceramic top coat and TGO into the bond coat [92-94].

Although TGO is formed by the oxidised bond coat, it protects the bond coat from continuous oxidation and degradation due to its low oxygen diffusivity [95]. However, the growing thickness of TGO layer also generate considerable growth strain at the interface between top coat/TGO and TGO/bond coat [96] and also generates thermal expansion mismatch between ceramic coating and underlying bond coat during the cooling process. The critical thickness of TGO is usually around 7 μm, once the TGO grows beyond that, there is a higher chance of TBCs failure. TGO layer has a high impact on the durability of thermal barrier coating systems. Therefore, an accurate inspection is an indispensable work, and it is essential to develop new nondestructive evaluation methods which aimed at TGO layer.

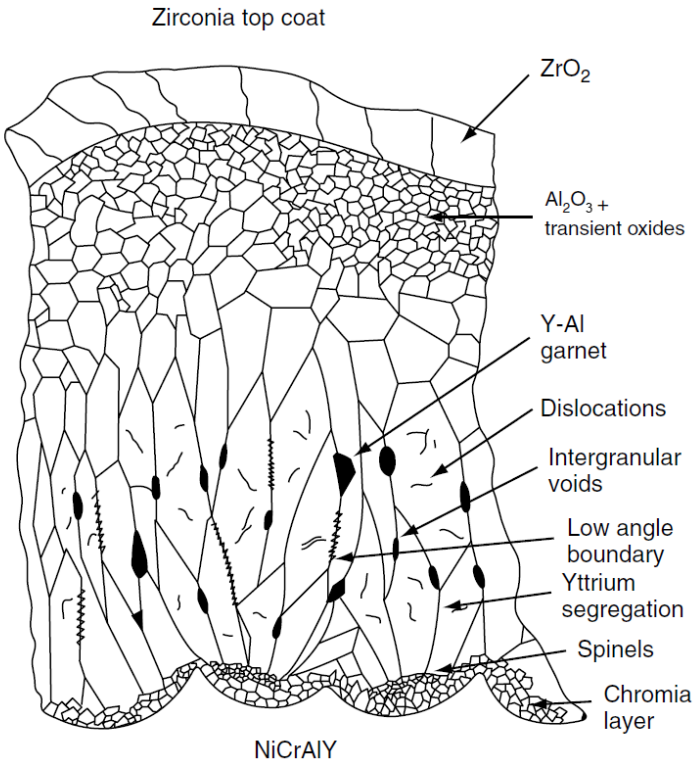


Figure 2.5 Schematic representation of the microstructure features present in TGO at Zr_2O – NiCrAlY interface [90]

2.1.4 Failure mechanisms

TBC failure involves a wide range of chemical and thermomechanical influences connected with the oxidation time, which results in a complicated failure mechanism. It is generally summarised in five major failure categories, as shown in Figure 2.6. The first two failure categories involve the formation of spinel at either interface of TGO/bond coat or between TBC and TGO due to Al depletion and Ni diffusion through TGO, respectively. It is surmised that the failure is due to the brittleness of spinel. However, this is not confirmed yet. The third and fourth categories are TGO imperfection failure and undulating interface which are related to thermomechanical properties of TGO layer. Both of them are considered as major influences that govern the TBC failure. The failure process involves crack nucleation, propagation and coalescence. The failure in the fifth category is caused by particle impact and foreign object damage (FOD). This can penetrate ceramic top coat and generate hot spots in the bond coat [97].

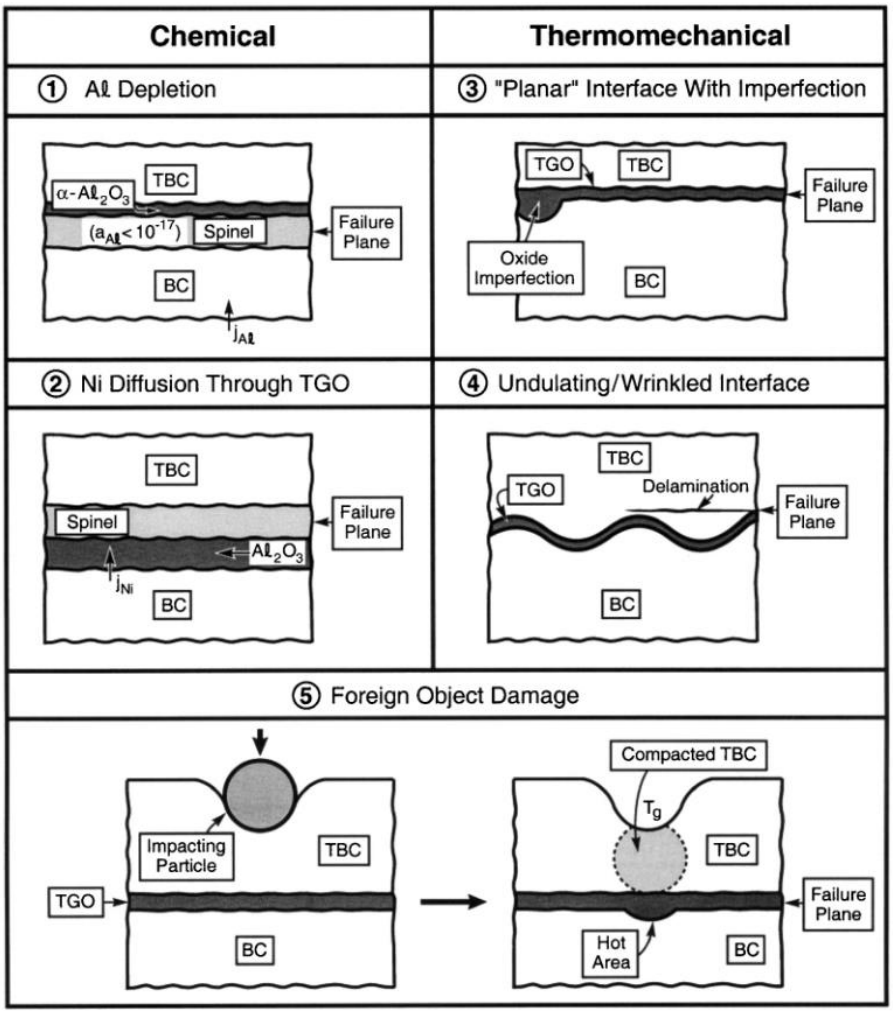


Figure 2.6 Summary of five major failure categories[97]

Aluminium depletion

During the thermal exposure in the air, the bond coat generates a dense protective oxidation film for superalloy substrate by supplying aluminum for the formation and growth of an alumina layer. The oxidation process lead to the content of aluminium decreases in the bond coat and the aluminium depletion takes place at the interface between TGO and bond coat [98]. The depletion of aluminum in the bond coat results in formation of other less desirable oxides, such as Ni- and Co-containing spinels, $Y_3Al_5O_{12}$, and Y_2O_3 [6, 99, 100], which create localised oxidation zones and increase the local oxygen diffusion rate. Moreover, the formed oxides with an increase in volume degrade the structural integrity of the TGO layer which may lead to localized cracking at the interface [97].

Undulating interface

Undulating interface is also known as rumpling of TGO which is considered as a prevailing failure mechanism in the thermal barrier coating system. One of the most common presumptions of the cause of rumpling is the misfit of thermal expansion coefficient between coating layers [101, 102]. During the cooling period of thermal cyclic oxidation, bond coat and adherent oxide experience plastic deformation, which lead to an in plane compressive stress due to the different thermalmechanical properties between the TGO and bond coat [103]. With increasing compressive stresses generated in the TGO during the thermal oxidation, cracks are initiated around the undulating interface and lead to delamination of at the interface. At the same time, the amplitude of rumpling growth with increased thermal cycles, when the rumpling reaches a critical level, as a consequence, the interface separation is occurred which is considered as TBC failure. Figure 2.7 illustrates the four different cracking mechanisms in air plasma sprayed thermal barrier coating.

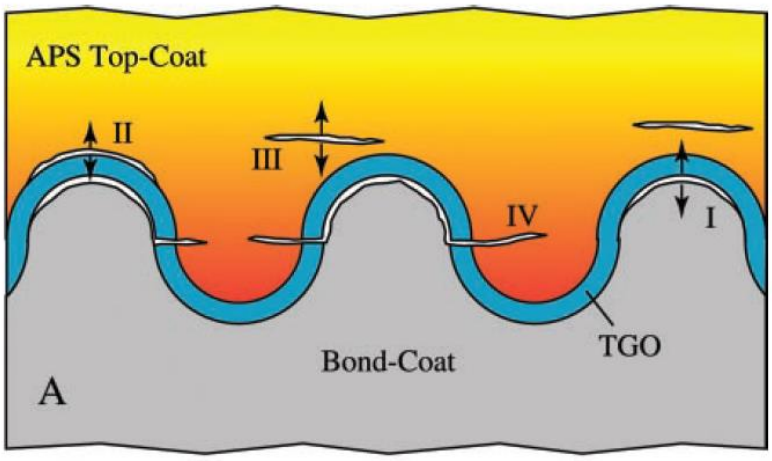


Figure 2.7 Schematic diagram illustrate four different cracking mechanisms in air plasma sprayed thermal barrier coating [6]

During the cooling period of thermal cyclic oxidation, the interfaces between top coat/TGO/bond coat is subjected two different residual stresses due to the misfit of thermal expansion coefficient. Since the bond coats have larger coefficient of thermal expansion than the top coats, which results in tensile stresses generated at the rumpling peaks of the BC/TGO interface and compressive stresses at the valleys. As the TGO

thickens, the tensile stress increases, leading to cracking at the BC/TGO interface, which corresponds to the cracking mechanism I in Figure 2.7.

Due to the different on coefficient of thermal expansion between ceramic top coats, bond coats and substrates, the ceramic top coats are always under compressive stresses at room temperature. However, these stresses are much lower compare to the residual stress in the TGO due to the porous and cracked microstructure of ceramic top coat and relatively lower thermal mismatch with bond coat. Due the rumpling of metal/ceramic interface, the out-of-plane tensile stresses cause fracture at the top coat/TGO interface and form cracks form in the vicinity of the undulation peaks, which corresponds to the cracking mechanism II and III in Figure 2.7.

As the TGO thickens with the thermal oxidation, the coefficient of thermal expansion of the combination of bond coat and TGO is reduced. When the thickness of TGO reach a certain point, the coefficient of thermal expansion is lower than both the ceramic top coat and the bond coat, which reverses the stresses at the valley and peak of rumpling from compressive to tensile or other way around. As a result, the reversal causes cracking at the middle part of the rumpling, which corresponds to the cracking mechanism IV in Figure 2.7. Failure of TBC system is occurred when small cracks coalesce into each other and form delaminiation at the interfaces.

Foreign object damage

Foreign object damage is considered to be a physical influence from the thermal barrier coating operation environment. This could happen by objected, such as sand, stone or bird, sucked into gas turbine engine during take-off. The impact by foreign object result in an indent damage on the top coat surface. The compression force from the impact causes plastic deformation of top coat and forms a densification zone underneath the impact site. Cracks are formed along the kink band from the densification zone to the TGO layer leading to delamination between top coat and TGO or bond coat, as shown in Figure 2.8.

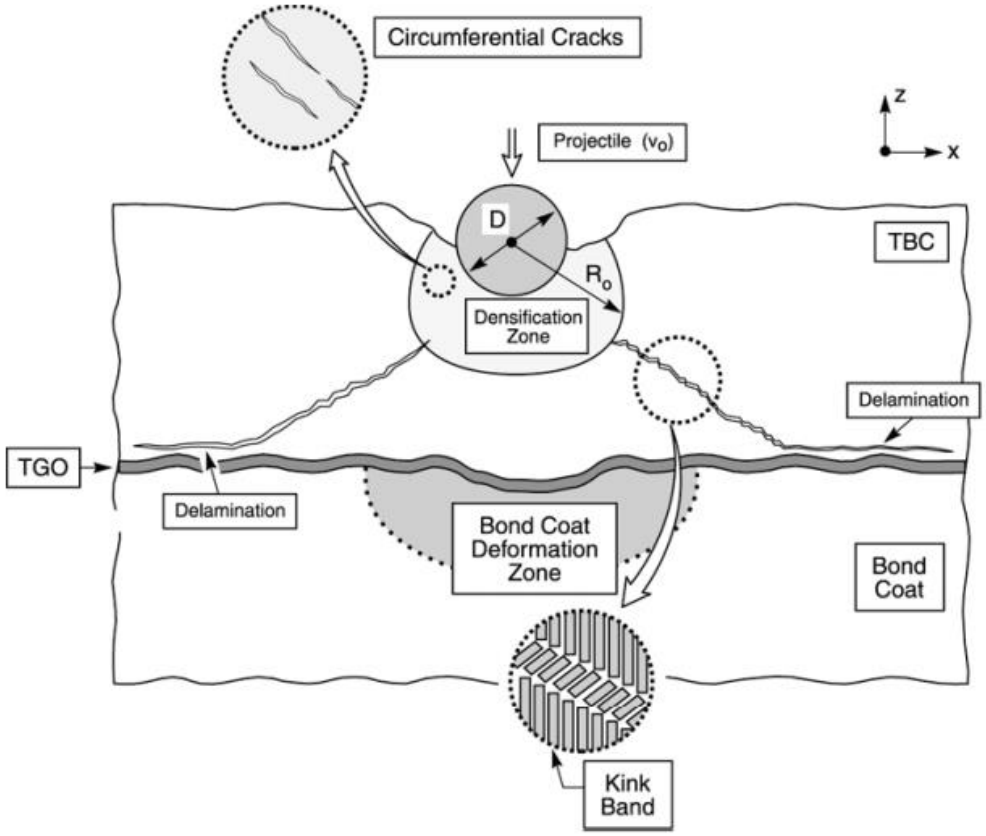


Figure 2.8 Schematic diagram of the damage by foreign object and the different impact zones[104]

In the current chapter, the thermal barrier coating system has reviewed in detail, including material selection for thermal barrier coating along with the compositions and microstructure of a typical top coat, two deposition process for YSZ ceramic top coat, comparison between diffusion aluminide coating and overlay coating, TGO formation along with oxidation behaviour of thermal barrier coating and its failure mechanism. Following three chapters will review the three main NDT methods studied this project, including X-ray computed tomography, laser photoacoustic spectroscopy, impedance spectroscopy.

2.2 X-ray CT

2.2.1 Introduction

According to Webster's Dictionary, the word tomography is derived from two Greek words: Tomos and Graphia. Tomos means slice, and Graphia means describing, so the tomography is imaging using slices [105].

X-ray computed tomography (CT) is a nondestructive three-dimensional characterisation technique for visualising interior features within solid objects such as ceramics, metal alloys and thin coatings such as thermal barrier coatings. An X-ray CT 3D image consists of layers of two-dimensional CT image which is called a slice that like a slice from a loaf of bread has thickness. CT slice is different to typically a digital image which is composed of pixels, whereas a CT slice is composed of voxels. Therefore, the complete volumetric representation of an object is reconstituted by stacking all of the CT slices, which is composed of various volume elements [106].

X-ray CT scanning is a significant nondestructive technique in the industry for component internal inspection which includes flaw detection, inner structure examination and failure analysis. It also has been widely used in many other areas such as medical inspection, geological investigation, security checks in the airport etc. Currently, X-ray computed tomography has been used to characterise thermal barrier coating microstructure and observation of its interfacial evolution during thermal cycling, which is essential for monitoring the build-up delamination which causes failure of the coating and assessing coating lifetime [34].

The principal advantage of CT technique is its 3D image analysis without any damage to the sample. Unlike conventional NDE methods of TBCs, such as optical microscopy and scanning electron microscopy, X-ray CT has no requirement for sample preparation, which therefore would not introduce any artificial cracks or cause any delamination of the ceramic coating. X-ray CT enables automatic reconstruction of the object using captured data, which is a time-saving and labour-saving method in creating a 3D model.

Every detection method has its limitations, so it is same with X-ray computed tomography. The basic limitation is sample size which must be small enough to be filled in detector system of the CT equipment. Also, the quality of the image is directly related to distance between X-ray source and detector, so that a smaller sample would provide better spatial resolution. Furthermore, smaller samples offer short travel distances and hence less attenuation of X-ray energy. The limitation not only on sample size but also the density of the material of the sample, in which denser material will cause more attenuating. These two parameters are directly related to the quality of resultant images which will be discussed in detail in the next section. Furthermore, to reconstruct 3D images requires that collect data is collected from a full 180 degrees rotation by the scanner (for small sample rotate sample stage 180 degrees is feasible). Since CT image does not accurately reflect the true structure that being detected, often is a limit to the accuracy of calculating density, dimensional, porosity from a CT image [107].

2.2.2 Beer’s Law

Basically, tomographic imaging is obtained by measuring the attenuation of a directing beam of X-ray through an object. And then reconstruct a 2D tomographic image from multiple orientations to form a final stereo 3D image. A fundamental principle of X-ray decrease is worth to be known, Beer's Law which describes intensity reduction influenced by X-ray energy, path length, and material linear attenuation coefficient [108].

The simplest expression of Beer's Law for a monochromatic X-ray beam passing through a homogeneous material is:

$$I = I_0 \exp[-\mu x] \tag{2.1}$$

where I_0 and I are the initial and final X-ray intensity, μ is the linear attenuation coefficient of the material, which has a unit of 1/length and x is the length of the X-ray path.

If X-ray passes through multiple materials, then the equation becomes to:

$$I = I_0 \exp[\sum_i (-\mu_i x_i)] \tag{2.2}$$

where μ_i is each additional attenuation coefficient of each individual material, x_i is the X-ray path for each material. This equation can be solved directly if the system using a monochromatic X-ray source, i.e. synchrotron or gamma-ray emitter.

If a polychromatic X-ray source is used in the system, then the effect of X-ray energy should be taken into account, in this situation the intensity decrease is calculated via the equation:

$$I = \int I_0(E) \exp\left[\sum_i (-\mu_i(E) x_i)\right] dE \tag{2.3}$$

However, for industrial CT attenuation coefficient is taken as an effective linear value, in another word, only one single value is calculated at each voxel. This effective linear attenuation coefficient is a function of both the X-ray spectrum and the properties of the scanned object. Therefore, Equation 2.2 is used for intensity decrease calculation for industrial CT [109].

2.2.3 Linear attenuation coefficients

There are three dominant attenuating processes according to applied X-ray energies, which can be put in order from low energy to higher energy as a photoelectric effect (50-100keV), Compton scatters (5-10MeV) and pair production (higher than 10MeV).

In general, industrial CT testing the photoelectric effect is the dominant attenuation mechanism which is proportional to atomic number Z of material. In the case that high energy X-ray is applied, then the Compton scatters have to take into account. As a different, Compton scattering is also proportional to the mass density of the material.

Therefore, more detail of material that has differences in composition can be distinguished using low energy X-rays, as a drawback less energy of X-ray is attenuated much more quickly, enhance limiting the thickness of high density sample. Conversely, in order to penetrate a thick and dense material, high energy X-ray is required.

2.2.4 Previous researches

X-ray computed tomography as a nondestructive three-dimensional characterisation technique is widely used for visualising the interior structure of the solid material and flaw detections. Additionally, it enables to provide other information for a component which includes coating density, pore size distribution, surface roughness. However only a few of published literature related to testing of thermal barrier coating due to the inherent high attenuating character of the coating composition.

Y.Zhao et al.[29] have conducted a four point bending test on APS conventional YSZ thermal barrier coatings to investigate the interfacial roughness after isothermal heat treatment at 1150°C. An X-ray micro CT has been used to observe the evolution of the TBC microstructure at the interface with increased thermal exposure times. Development of TGO layer has been revealed after exposure and been shown in 2D tomography image, as shown in Figure 2.9. They have pointed out that there is no significant change in the interfacial roughness after thermal exposure using the 3D reconstruction of the interface.

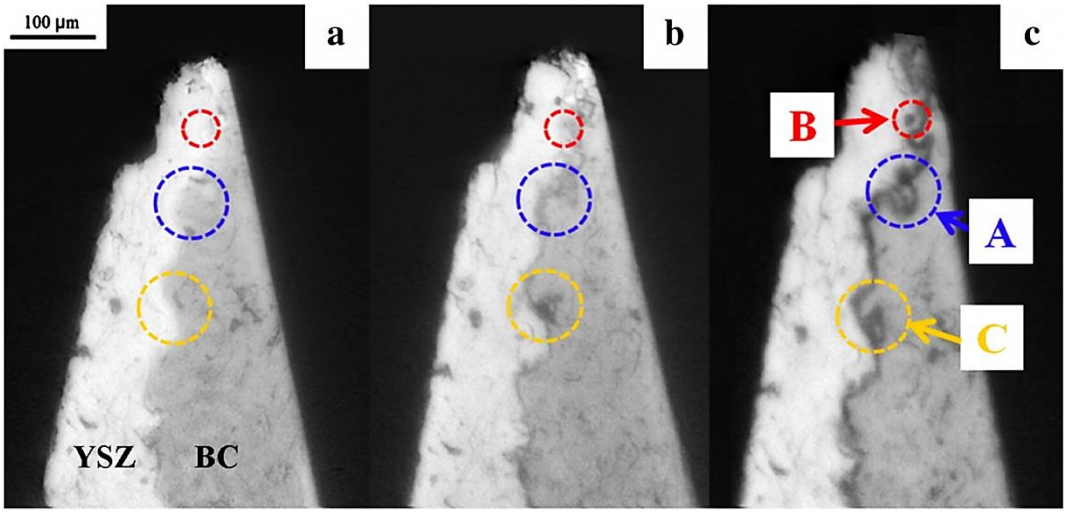


Figure 2.9 2D CT slices of TBC microstructure at interface after thermal exposure at 1150 °C for 0 (a), 20 (b), 120 h (c). [29]

A. Kulkarni et al.[110, 111] have investigated the microstructure and properties of EB-PVD coatings after isothermal heat treatment using X-ray micro CT. They have discovered the influence of exposure temperature and time duration on quantitative porosity variation with a thickness of EB-PVD thermal barrier coatings. Later A. Kulkarni et al.[112] have repeated experiment using APS thermal barrier coatings and have delineated the distributions of various void defects related to specific process controls.

Due to the limitation of a finite number of pixel number in X-ray CT detector the sample needs to be small enough to fit the field of view. In other words, the spatial resolution of X-ray CT is limited by sample size, and to achieve higher resolution sample preparation is required which would lead to artificial damage of sample. Otherwise, imaging artefacts will be induced while X-ray beam passes through a rotating sample with a large variation of the path. Synchrotron radiation computed laminography (SRCL) is developed to overcome this problem, which enables to detect a region of interest in a laterally extended sample in high resolution [113].

Another European group V. Maurel et al.[34] has first investigated the 3D microstructure of EB-PVD thermal barrier coating using synchrotron radiation computed laminography. The 3D microstructure of thermal barrier coating after 32 thermal cycles of one hour at a temperature of 1100°C was observed, as shown in

Figure 2.10. They have indicated that interfacial defects were related to the grain boundary network of the bond coat layer since defects intensive disperses at the triple junction points of grain boundary using an SRCL 3D image.

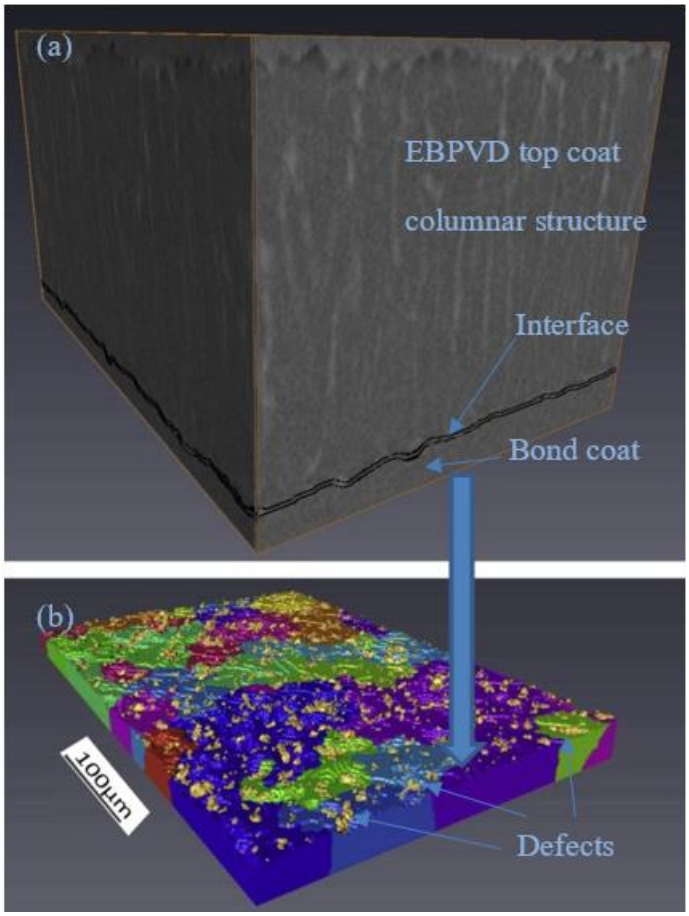


Figure 2.10 (a) 3D reconstruction of the interface and 3D ceramic column shape. (b) Bond coat layer and interfacial defects. Defects are highlighted in gold, bond coat grains are in colour.[34]

2. 3 Laser photoacoustic spectroscopy

2.3.1 Introduction

Nondestructive ultrasonic techniques such as pulse-echo or through-transmission methods are applications of the bulk wave, which have been widely used to determine elastic constants of a variety of materials. However, the conventional ultrasonic techniques lack an ability to measure the elastic properties of thin films such as thermal barrier coatings due to their inherent porosity and extensive microcracking.

2.3.2 Mechanisms for laser generation of ultrasound

Elastic wave generation in solids by pulsed laser irradiation was first demonstrated by White [114]. A comprehensive review of the generation mechanisms has been given by Hutchins [115], Scruby and Drain [116].

The fundamental mechanism of laser generation of ultrasound is the thermal expansion of material surface due to optic energy absorption from a laser beam. When a pulsed laser beam impinges on the surface of a material, part of the optical energy of the laser is converted to heat and absorbed by the material, which leads to a rapid localised temperature increasing. This results in an instantaneous local thermal expansion and/or laser ablation of a local region, which leads to the generation of ultrasound in the material [117]. Depending on the incident laser power the generation mechanism can be different, which the ultrasound is generated at either thermoelastic regime or ablative regime.

In the thermoelastic regime, the laser power is kept relatively low to avoid melting and ablation of the material surface. The thermal stress as a consequence of thermal expansion generates elastic waves, which is characterised by two orthogonal horizontal force dipoles parallel to the free surface [115, 118]. Furthermore, the amplitudes elastic waves increase linearly with increasing power density of laser [119]. Figure 2.11a schematically illustrates the thermoelastic generation of ultrasound by a pulsed laser source.

In the ablation regime, where the laser power is sufficiently high enough, the surface of the material is melted, ionised and plasma is formed. Simultaneously, some of the

material vaporises and ejects out of the surface, consequently results in a momentum transmit into the material, which generates a strong bulk wave normal to the surface [40], as shown in Fig.2.11b. However, as a consequence, it damages the surface of the material and typically not acceptable for nondestructive characterization of materials.

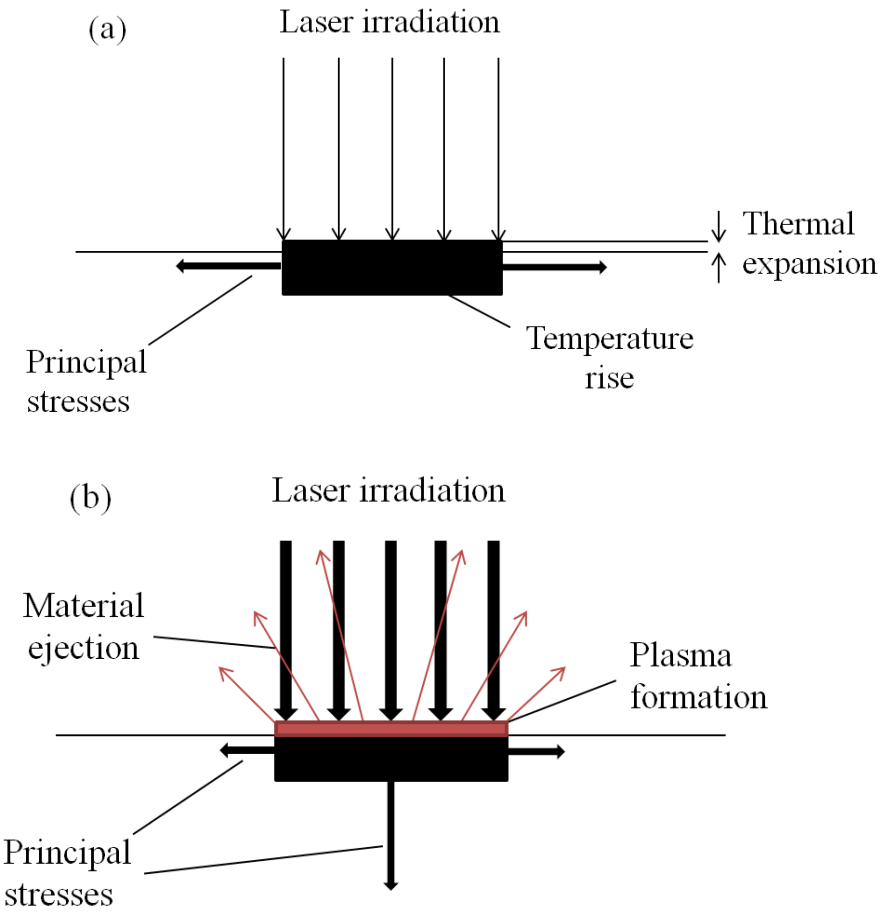


Figure 2.11 Schematic of laser generation of ultrasound in (a) thermoelastic regime and (b) ablative regime

To avoid surface damage of material a sacrificial layer is used for some applications, which is ablated by a laser beam to generate a strong bulk wave in the medium via momentum transfer reactive force. The sacrificial layer can be either coating such as paint and rust, a liquid such as oil and resin or transparent solid for instance glass. It is applied either unconstrained at the surface of the material, constrained between a medium or constrained upon surface [115, 120].

Furthermore, when a transparent coating is well bonded to the material surface, the elastic boundary condition is changed, unless bonded coating has exactly same elastic properties as material. The surface constraint will significantly modify the thermoelastic source, redistribute the ultrasonic energy in the directivity pattern and concentrate it into the perpendicular direction. As a result, the amplitude of the bulk wave is enhanced in the direction of the surface normal [116].

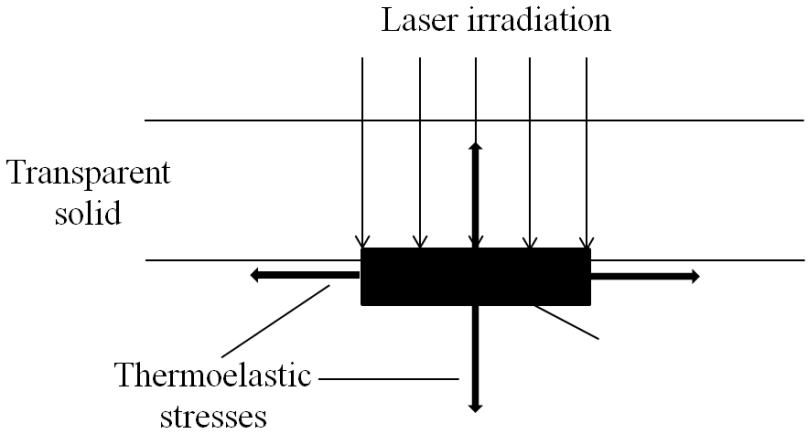


Figure 2.12 Schematic of laser generation of ultrasound in solid constrained layer

2.3.3 Previous researches

Aithal et al. [121] have developed photoacoustic characterisation method for detection of a subsurface defect in plasma sprayed coatings. In this method, a generation laser is chopped to low frequency, varied from 4 to 300 Hz, penetrates a transparent quartz window of a photoacoustic cell and heats the sample surface. A schematic diagram of photoacoustic experimental set up is shown in Figure 2.13. The heated sample surface generates a heat diffusion towards the surrounding gas while produces pressure fluctuations which are detected by an inserted microphone in the cell. The amplitude and phase of the acoustic signal depend on the temperature of the sample surface which is related to the heat diffusion within the sample. In the case of the presence of a defect, the thermal properties of the subsurface of the defect area are altered, which lowers the heat diffusion and shown as an increase in the amplitude of the detected acoustic signal.

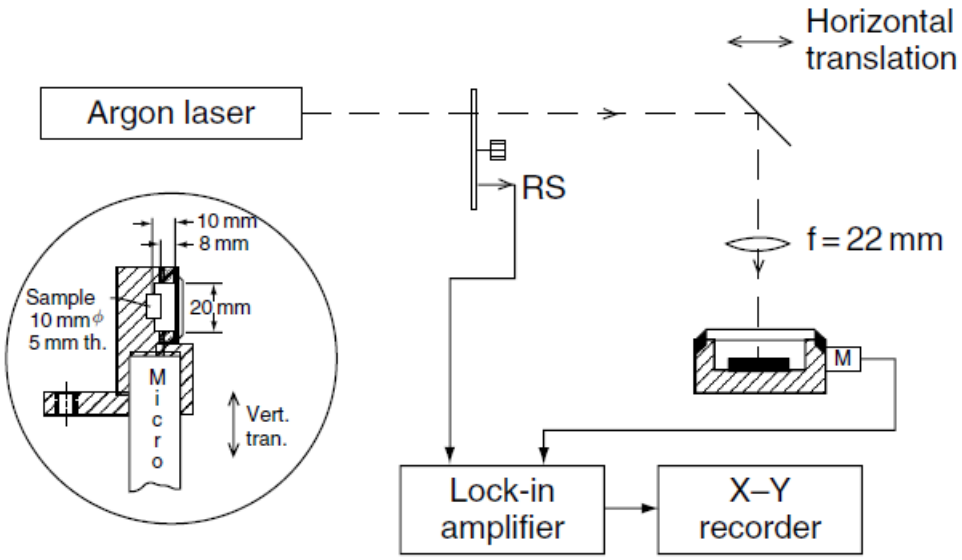


Figure 2.13 Schematic diagram of photoacoustic experimental set up, the inset shows the photoacoustic cell [24, 121]

2.4 Impedance spectroscopy

2.4.1 Introduction

Impedance spectroscopy (IS) is measuring an AC current response by an applied excitation potential with varying frequency, which is influenced by both resistance and capacitance associated with sample geometries. The degradation of YSZ thermal barrier coatings can be evaluated by the impedance responses of an applied alternating current over a range of frequencies, where the variation of electrochemical parameters in the impedance spectra are related to oxide layer growth, composition change and presence of cracks or delamination in the microstructure of samples. In this section, the fundamental principles of impedance spectroscopy will be reviewed along with correlated previous researches on thermal barrier coating. A resistance calculation based on sample geometry will be discussed, which is related to the analysis of the influence on asymmetric electrode geometry in impedance spectroscopy measurement in Chapter 6.

2.4.2 Fundamental principles

A basic review of impedance spectroscopy which related to thermal barrier coating testing is given in this section. A more comprehensive review has been given by Barsoukov and Macdonald [122], Lvovich [123] and Orazem and Tribollet [124].

Impedance is defined as the ratio between a sinusoidal potential and a response current. In a sinusoidal potential excitation, for a pure resistance there is no phase shift between the applied voltage and the measured current; for a pure capacitor, the current leads voltage by 90°. However, for most non-magnetic materials, the electrical behaviour is usually described by some combination of resistance and capacitor elements, which the phase difference is somewhere between 0 and 90°. Therefore, the impedance can be expressed in terms of a magnitude Z_0 and a phase shift:

$$Z = \frac{E_t}{I_t} = \frac{E_0 sin(\omega t)}{I_0 sin(\omega t + \phi)} = Z_0 \frac{sin(\omega t)}{sin(\omega t + \phi)} \quad (2.4)$$

Where, E_t is the potential at time t, E_0 is the amplitude of the signal, I_t is the response current signal, I_0 is the amplitude of the signal, and ω is the radial frequency, which is related to the applied AC frequency f as $\omega = 2\pi f$, ϕ is the phase shift.

Or using Euler relationship, it is possible to express the impedance as a complex function:

$$Z = \frac{E_0 e^{j\omega t}}{I_0 e^{j\omega t - j\emptyset}} = Z_0 \exp(j\phi) = Z_0(cos\phi + jsin\phi) \quad (2.5)$$

The modulus impedance $|Z|$ and phase angle ϕ, can be expressed as real part of the impedance Z' and imaginary part of the impedance Z'', and the relationships among these parameters are

$$|Z| = \sqrt{Z'^2 + Z''^2} \quad (2.6)$$

$$\phi = tan^{-1}\frac{Z''}{Z'} \quad (2.7)$$

In the IS measurement, two types of impedance diagrams are most frequently used, namely Nyquist plots and Bode plots. Figure 2.14 has shown the Nyquist plot and bode plot for a basic R|C circuit, resistor and capacitor connected in parallel. In the Nyquist plots, the real part Z' is plotted on the x-axis and imaginary part Z'' on the y-axis of the chart, and the impedance is represented by the formula:

$$Z(\omega) = Z + jZ'' \quad (2.8)$$

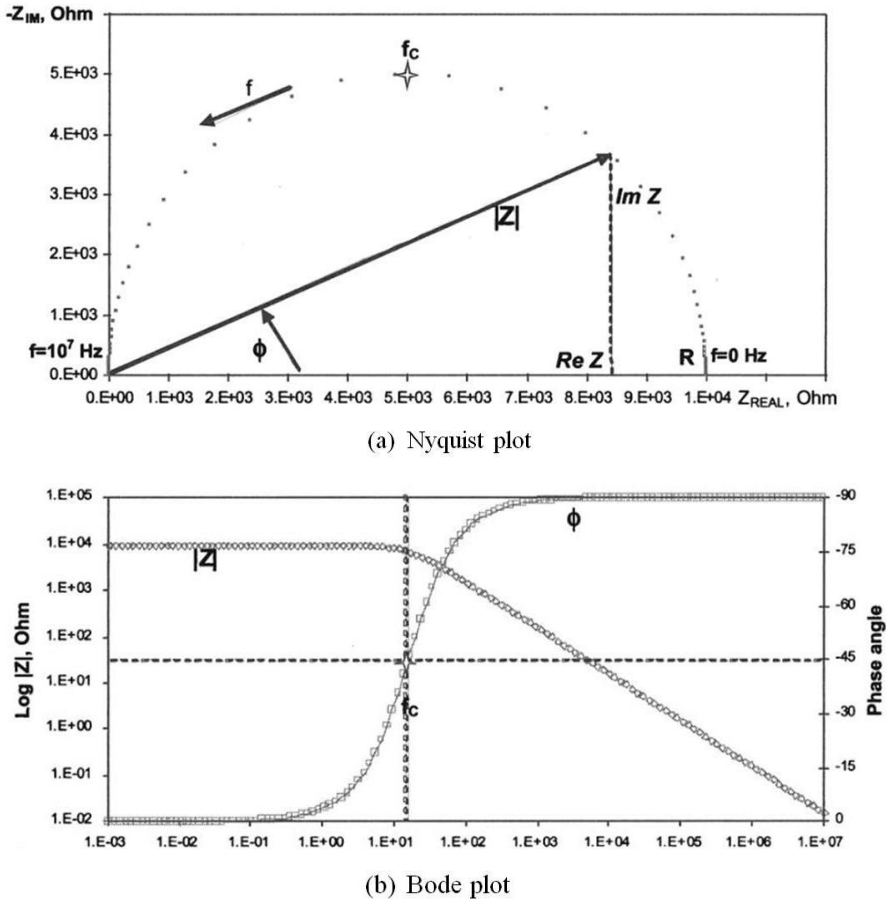


Figure 2.14 (a) Nyquist plot and (b) Bode plot for a basic R|C circuit [125]

In general, the Nyquist plot is used to determine the major parameters, such as resistance and capacitance corresponding to an electrochemical system. If there is only one semicircle in Nyquist plot, the resistance value, R, is determined directly from the intercept with the real Z axis. If the system is complicated, there may be a few semicircles present, and then spectra need to be fitted with an equivalent circuit model, which is representative of the microstructural features of the materials. In the Bode plots, the logarithm of impedance magnitude and the phase angle are both plotted as a function of the logarithm of frequency.

In this basic R|C circuit, the Nyquist plot is characterised by a semi-circle. The impedance equation for this circuit can be expressed as:

$$\frac{1}{Z} = \frac{1}{R} + j\omega C \tag{2.9}$$

$$Z(\omega) = \frac{R}{1+\omega^2 R^2 C^2} - \frac{j\omega R^2 C}{1+\omega^2 R^2 C^2} \tag{2.10}$$

where R and C can be defined as:

$$R = \frac{\rho\delta}{A} \tag{2.11}$$

$$C = \varepsilon_0 \varepsilon \frac{S}{\delta} \tag{2.12}$$

where j is imaginary number (j^2 = -1), ω (rad/sec) is angular velocity ($\omega = 2\pi f$), ρ (Ω·cm) is resistivity, ε and ε_0 = 8.9 × 10^{-12} F/m are relative dielectric constant and dielectric constant of vacuum, respectively, S (mm^2) and δ (mm) are the area of specimen exposed to electrode and thickness of specimen respectively. These parameters are taken as constant at a given temperature.

For some oxide system, constant phase element (CPE) is a more suitable to describe the electrical behaviour and modelled in the equivalent circuit. For example, thermal barrier coatings which have a rough or porous surface that may cause frequency dispersion due to heterogeneous current density distribution, using a CPE in a model in place of a capacitor can compensate for non-homogeneity in the system.

The impedance of a CPE, Z_{CPE}, is given by [59, 126-128]

$$Z_{CPE} = \frac{1}{A(j\omega)^n} \tag{2.13}$$

where A is a parameter independent of frequency, $j = \sqrt{-1}$, ω is angular frequency, and n is the exponential index which represents a dispersion of relaxation frequency. In most cases, n is between 0 and 1 and indicates the dispersion of electrode. When the exponential factor n= 0, the CPE functions as a pure resistor; when n= 1, the CPE acts an ideal capacitor and A, therefore, equals to the capacitance.

In the case of no ideal capacitive response, the value of A is used to calculate the effective capacitance of the system by [129-132]

$$C_{eff} = R^{(1-n)/n} A^{1/n} \tag{2.14}$$

where R is the resistance of element and can be obtained from the simulation.

2.4.3 NDT for thermal barrier coatings using impedance spectroscopy

In an impedance measurement of TBC system at 400 °C, normally there are three relaxation processes for the as-sprayed sample or sample at early oxidation stage and four for the oxidised sample, as shown in Bode plot of Figure 2.15. It has been confirmed that the highest frequency relaxation corresponds to YSZ grain at approximately 10^6 to 10^7 Hz, YSZ grain boundary between 10^3 to 10^5 Hz, TGO layer between 10 to 10^3 Hz respectively and the lowest frequency relaxation correspond to the electrode at around 10^{-2} Hz [59, 133, 134]. Song [135] has indicated that there is no impedance response from the TGO layer in the sample at early oxidation stage due to YSZ is much more conductive than the TGO and thus the current is conducted almost through the non-TGO areas. Nevertheless, the TGO relaxation process may overlap with YSZ grain boundary, as shown in the plot of 400 cycles, due to the mixed oxide is formed at TGO layer which leads to TGO less insulating than the pure alumina. Consequently, the disappearance of TGO relaxation frequency can be utilised as an indication of the degradation of thermal barrier coating.

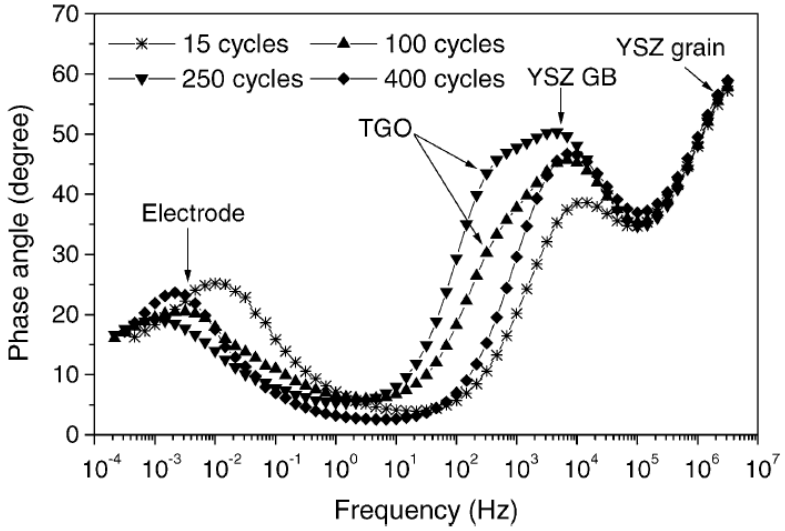


Figure 2.15 Phase angle as a function of frequency for the different thermally cycled specimens [135].

In Nyquist plot, two semicircles are normally presented in the as-sprayed sample, which corresponds to YSZ grain and grain boundary at high frequency (10^3-10^7 Hz).

In the presence of TGO layer, the third semicircle can be found at a lower frequency (10^2-10^3 Hz) [131], as shown in Figure 2.16.

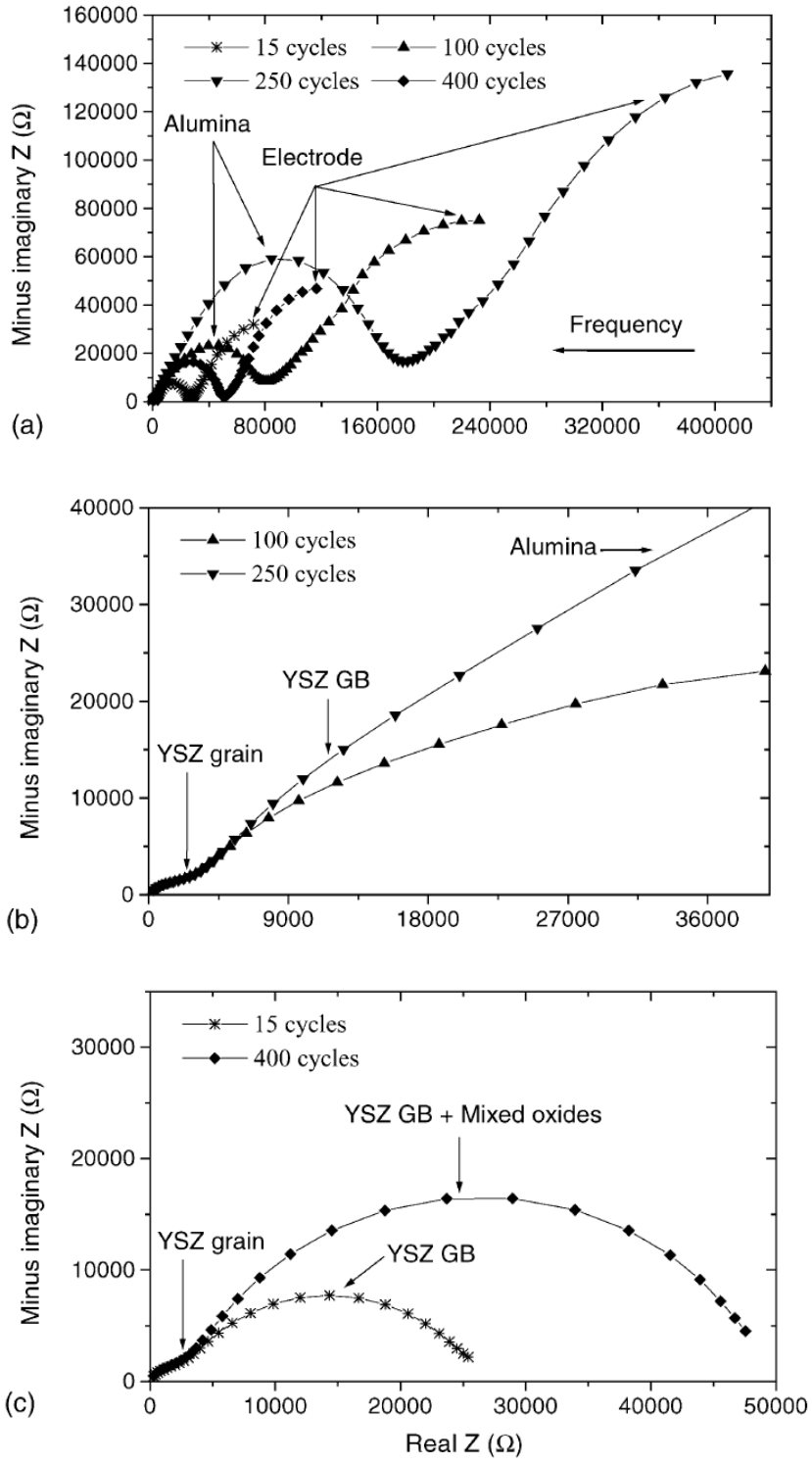


Figure 2.16 Nyquist impedance plots for different thermally cycled specimens. Panels (b) and (c) show the high frequency range in panel (a) [135]

To obtain the electrical properties of each layer of TBC system, the impedance spectrum is fitted with an equivalent circuit model using Zview impedace analysis software, which connects the microstructural features of thermal barrier coatings to their electrical properties.

Since the specific electrical resistances of YSZ layer is around five orders of magnitude lower than the alumina TGO layer. Also with increasing temperature, the resistivity of YSZ dropped down much faster than alumina. The thickness of alumina increases with increasing of oxidation time, as a result, the thickness of TGO layer in thermal oxidation can be evaluated via its resistance measured by impedance spectroscopy [60, 61, 136, 137], and this enables impedance spectroscopy to be a nondestructive testing tool for monitoring the TGO growth in thermal barrier coatings.

Ogawa et al. have reported that the impedance increased with an increase in the isothermal oxidation time of specimens due to the formation of the mixed oxide layer and alumina layer [57]. Further research by Wu et al. has noted that cracks in YSZ coating formed be thermal shock increase the impedance, which is due to the reduction of effective ionic-conduction in the cross-section area by cracking in thermal barrier coatings [138]. He also pointed out that the semicircle represent YSZ grain can only be observed at a testing frequency above 10^6 Hz and at a temperature above 327 °C as the conductivity of YSZ grain is dominated by temperature [125, 139]. Tanno et al. [69] investigated the influence of asymmetric electrode geometry on an impedance spectrum of APS TBCs that in the frequency below 10^5 Hz the asymmetric electrode geometry of TBC specimens induces the spread electrical conduction region outside electrode area. Hilpert and Tiffee [66] have revealed the microstructure changes in APS freestanding TBCs like densification, decreased microcrack density and phase transformation using impedance spectroscopy. Xiao's group has studied high temperature oxidation of thermal barrier coatings using impedance spectroscopy [58, 63, 64, 68, 135]. Their recent study has discovered the formation of the m phase increases the plastic deformation capability and decreases the electrical conductivity of TBCs [67].

4.2.4 Calculation of resistance

In the impedance spectroscopy measurement, non-conductive sample surface needs to be applied a layer of conductive coating as an electrode. For a smaller size of the sample, the conductive coating can be easily applied to both sides of the surface in the same size. The resistance between two areas can be calculated based on the equation of fundamental electrical properties of materials, following Pouillet's law which defined as:

$$R = \rho \frac{l}{A} \tag{2.15}$$

where R is the electrical resistance of a uniform specimen of the material, ρ is the electrical resistivity of the material, l is the length of specimen, A is the cross-sectional area of the specimen. The electrical conductivity of the material is defined as the inverse of resistivity:

$$\sigma = \frac{1}{\rho} \tag{2.16}$$

Therefore, resistance is proportional to material geometry with the inverse of the constant electrical conductivity at the same temperature.

$$R = \frac{l}{\sigma A} \tag{2.17}$$

However, in some cases that one side of the sample is conductive, and the other side of the sample surface is too wide to be covered with a conductive coating. If the area of both sides of a geometry is different, then the resistance of the geometry can be calculated via the integration along the thickness of a specimen. Considering a truncated cone geometry here, as shown in Figure 2.17, the r_x is defined as a radius of the cross-section with a distance of x to the bottom.

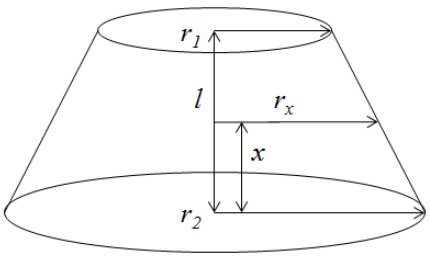


Figure 2.17 Truncated cone geometry

The variable r_x is derived by the ratio between the radiuses and thicknesses:

$$r_x = (r_1 - r_2)\frac{x}{l} + r_2 \tag{2.18}$$

Substitute r_x into Equation 2.15, gives

$$dR = \frac{\rho dx}{\pi r_x^2} = \frac{\rho dx}{\pi[\frac{(r_1 - r_2)}{l^2}x + r_2]^2} \tag{2.19}$$

$$R = \int_0^l \frac{\rho dx}{\pi\left[\frac{(r_1 - r_2)}{l^2}x + r_2\right]^2} \tag{2.20}$$

Simplify Equation 2.20 using an integration formula:

$$\int \frac{1}{(ax+b)^2} = -\frac{1}{a(ax+b)} \tag{2.21}$$

In the end, the resistance can be expressed by the following equation:

$$R = \frac{\rho l}{\pi r_1 r_2} \tag{2.22}$$

And in the case $r_1 = r_2$, then Equation 2.22 returns to Pouillet's law.

The truncated cone geometry is similar to the TBC samples measured in impedance spectroscopy, when both sides of the sample are circular and the area of the applied electrode on YSZ side is smaller than the substrate area. Unfortunately, the resistance between the electrode and substrate cannot be calculated using the Equation 2.22 due to the non-uniform electrical current density inside of the sample. The resistance in this case will be investigated via experimental measurement and finite element analysis as shown in Chapter 7.

2.5 Other nondestructive evaluation of TBCs

2.5.1 Infrared imaging

Infrared imaging is also known as thermal wave imaging (TWI) essentially measures the temperature distribution across TBC samples to identify existing defects. The sample is exposed to prior cyclic heat flow which establishes a temperatures gradient throughout the thickness of the sample, and the temperature distribution across the surface of the ceramic coating is monitored by an infrared camera, as shown in Figure 2.18. Microcracks and defects generated in the TBC samples after cyclic thermal exposure reduce heat transfer to the surface, which results in progressively cooler appearing areas [24].

Similarly, delamination can be detected by measuring the reflectivity of propagating thermal waves. The existence of defect between the TBC and substrate has higher thermal effusivity than its interface, thus higher thermal reflectivity under a stimulated heat, which creates a high contrast image of existing delamination [25], as illustrated in Figure 2.19.

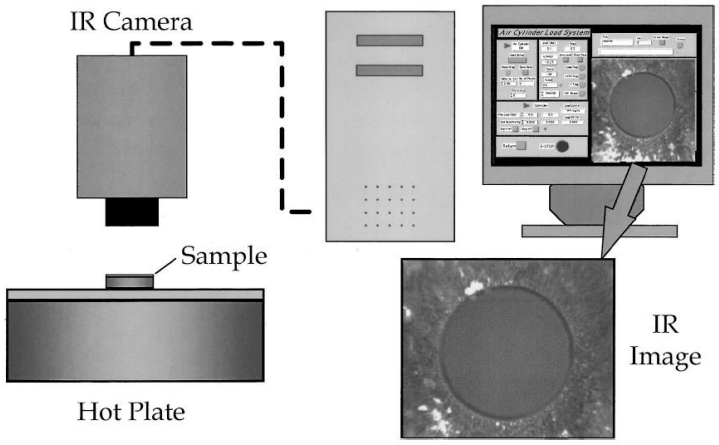


Figure 2.18 Infrared imaging of thermally excited thermal barrier coating [140]

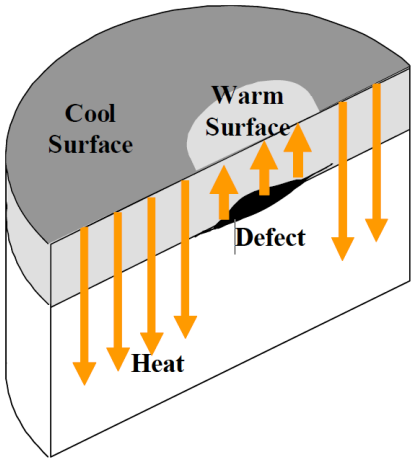


Figure 2.19 Schematic diagram of reflection of propagating thermal waves in thermal wave image. Heat diffuse from a heated sample surface through the specimen. In the presence of an interfacial defect, the thermal wave reflects back to the surface, which leads to a higher surface temperature above the defect area creates a high contrast image of existing delamination. [141]

2.5.2 Pulse-echo thermal wave infrared imaging

Pulse-echo thermal wave infrared imaging is a type of the thermal imaging methods in which a flash lamp (or a set of lamps) delivers an external stimulus of heat to the surface of TBC sample and subsequently monitor the temperature distribution and heat decay across the sample using an IR camera. A schematic diagram of the setup of pulse-echo thermal wave infrared imaging is shown in Figure 2.20. Defects developed in TBCs change the thermal conductivity of the material in its immediate proximity which results in a slower diffusion of heat by conduction and leads to a prolonged heat decay. Consequently, in contrast to the intact area within thermal imaging, the area with underlying defects present higher temperatures and take longer to cool down [53]. This technique has been proven to be able to detect various types of defects generated at the interface between YSZ ceramic top coat and bond coat [24].

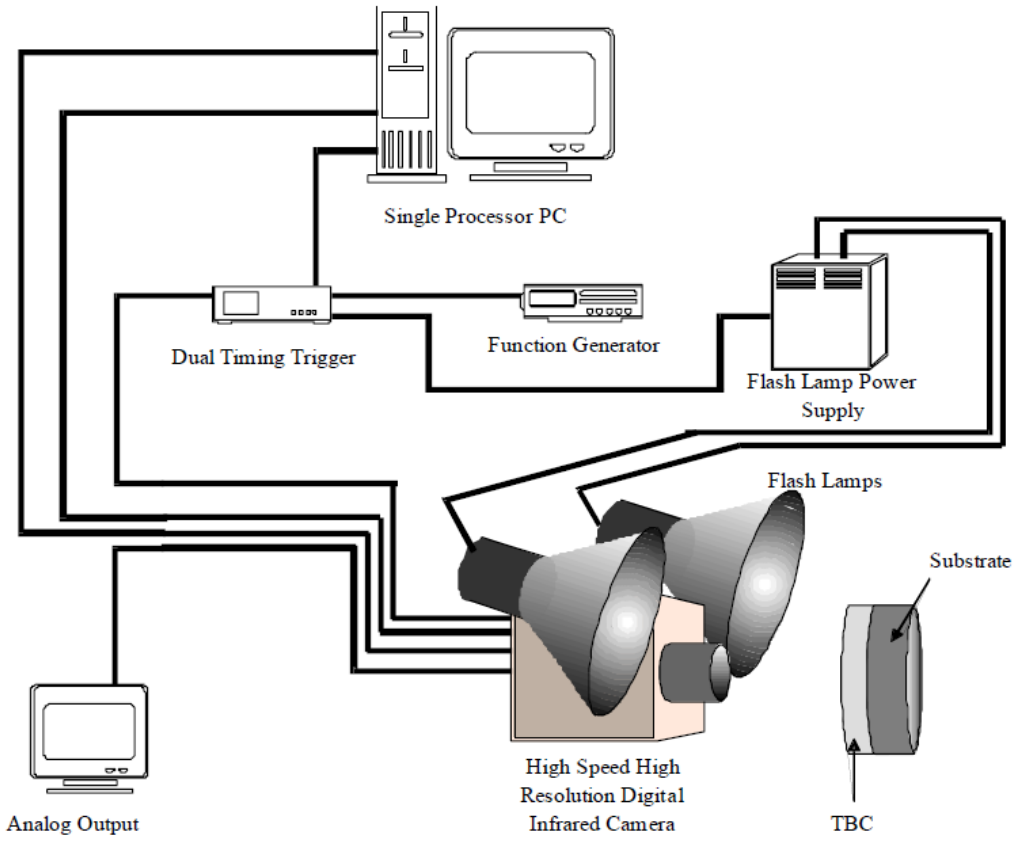


Figure 2.20 Schematic diagram of infrared thermal image setup for TBC measurement [23]

2.5.3 Mid-infrared (MIR) reflectance

Another approach to thermal imaging technology referred as mid-infrared (MIR) reflectance. This technique utilised the optical properties of YSZ which has greater transmittance at mid-infrared from 3 to 6 μm [142] , as shown in Figure 2.21. Therefore, it can be used for detecting highly scattering air plasma sprayed TBC system, while the laser-based techniques are difficult to be applied on due to the scattering and attenuation of YSZ layer. In the other word, MID wave can penetrate much deeper then visible light, therefore the cracks presented at the interface can be detected. During the testing, MID is generated by a SiC IR emitter and delivered to sample surface via an off-axis parabolic mirror, simultaneously, the reflectance of irradiated MID is measured using an IR camera. An increase in reflectance is attributed to the increase in damage level at the interface between YSZ layer and bond coat. A schematic diagram of mid-infrared reflectance image system is shown is Figure 2.22.

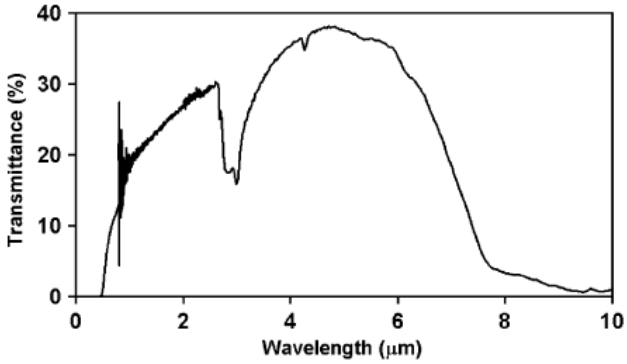


Figure 2.21 Transmittance spectrum of 170-mm-thick freestanding plasma sprayed 8YSZ coating [142]

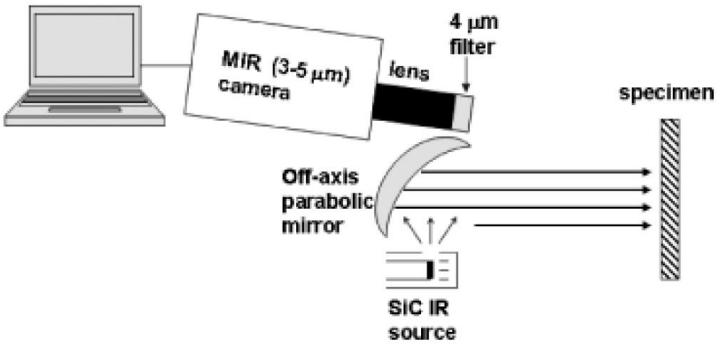


Figure 2.22 Mid-infrared reflectance imaging system [142]

2.5.4 Luminescence spectroscopy

Luminescence spectroscopy was pioneered by Clarke [143-148] and refined by Sohn, Gell, Jordan [42, 43, 149-152] which is applied to the nondestructive evaluation of thermal barrier coatings [141]. In the measurement of TBC system, laser penetrates the partially translucent ceramic top coat to the TGO layer, simulate the Cr^{3+} ions in the TGO layer which luminesce in two spectral lines, R_1 and R_2 which located at frequencies 14402 and 14432cm^{-1} for a stress-free α-Al_2O_3, respectively. The stress in the TGO layer leads to a spectral shift of the luminescence on these lines, as shown in Figure 2.23 [24]. In the case of delamination occurred at the interface of top coat and bond coat after thermal oxidation, the residual stress is relieved in TGO which is detected from Cr^{3+} luminescence spectrum. Therefore, it has the potential to assess the damage buried beneath the YSZ top coat and estimate the remaining lifetime of thermal barrier coating in high temperature application. Moreover, the luminescence spectroscopy has the ability to detect the phase transformation in TGO layer as other aluminium oxide phases such as θ-Al_2O_3 can be found on the corresponding lines, as shown in Figure 2.24. However, the luminescence spectroscopy faces limitations when testing TBC samples applied with APS coatings which contain laminar microcracks and pores that result in great attenuation of the incident laser. Further research on quantitative assessment of erosion of thermal barrier coating involved doping rare-earth ions such as Eu^{3+} and Dy^{3+} ions into standard YSZ material has been successfully studied and validated using both mechanical and optical devices [45].

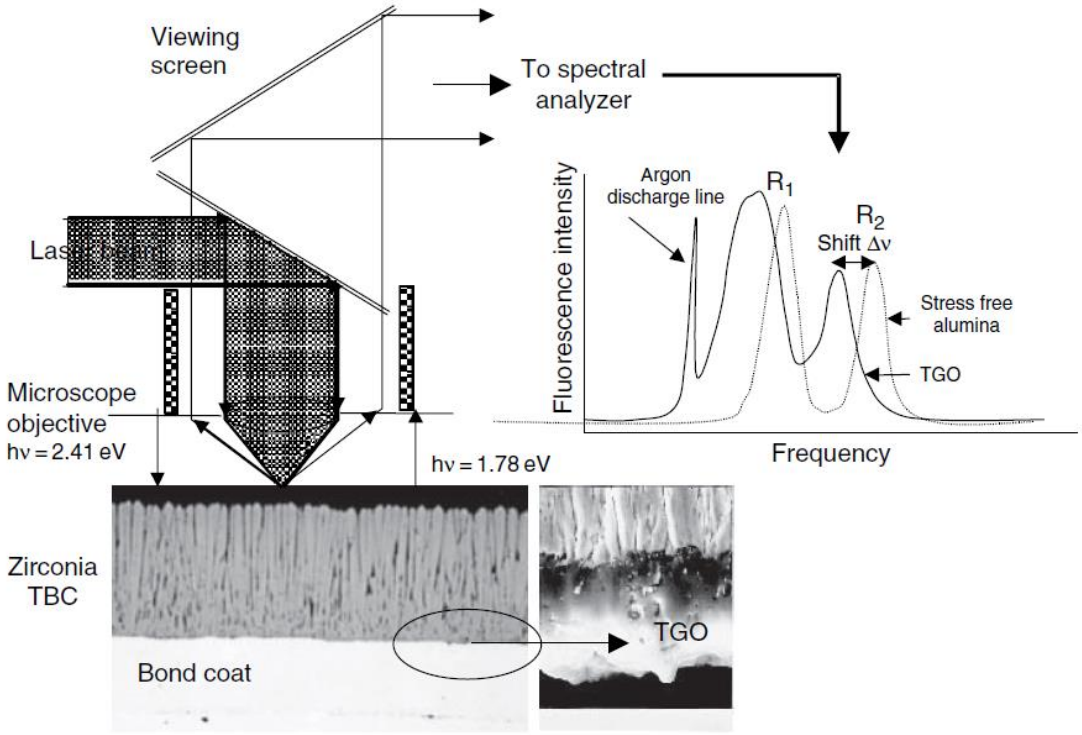


Figure 2.23 Schematic diagram of luminescence spectroscopy measurement for thermal barrier coating. The spectrum of Cr^{3+} ions on the right shows the typical R_1 and R_2 lines of α-Al_2O_3 without residual stress and the shifted spectra from TGO under compressive residual stress. [24, 44]

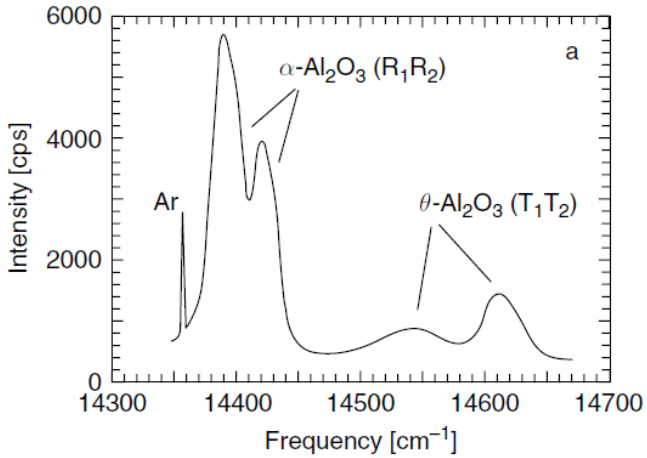


Figure 2.24 Fluorescence spectra from TGO containing both α-Al_2O_3 and θ-Al_2O_3 [24, 153]

2.6 Comparison of the various NDT techniques for thermal barrier coatings

Table 2.3 below compares the pros and cons of the various NDT techniques for thermal barrier coatings. All listed methods are capable to perform detection of cracks and delamination within TBC system via different techniques. In the opinion of the author, the optical methods, either thermal or laser-based techniques are the most promise for delamination detection. All of them are noncontact detection methods and further sample preparation is not required, except laser ultrasonic which require coating reflective layer to increase the sensitivity of detection laser. Thermal image methods utilised optical properties of YSZ which is translucent in the spectral between visible and near infrared. The stimulated thermal wave can penetrate through the thickness of sample reach the defects at the interface, compared to laser-based methods which have overcome the highly scattering air plasma sprayed YSZ layer. In a less attenuated microstructure of EB-PVD coated TBC sample, photoluminescence spectroscopy shows the good ability for assessing the damage buried beneath the YSZ top coat and estimate the remaining lifetime of thermal barrier coating in high temperature.

Table 2.3 Comparison of the various NDT techniques for thermal barrier coatings

NDT methods	Pros	Cons
Conventional ultrasonic techniques	1.No sample preparation required 2.Porosity measurement 3.Determine elastic properties	1.Difficult to measure the elastic properties of thin films or coatings 2.Liquid impingement into the opening surface pores 3.Signal highly attenuated by porous laminar YSZ layer (APS)
X-ray computed tomography	1.No sample preparation required 2.Visualise the interior structure of TBC system via 3D reconstruction 3.Determine coating density, pore size distribution, surface roughness.	1.Resolution is limited by sample size, density of material and atomic number of the element in the material 2.Resolution is limited by X-ray CT instrument
Laser ultrasound	1.Permits noncontact ultrasound generation and detection on complex geometry 2.Characterizing materials with depth dependent properties like coatings 3.High accuracy point to point measurement	1.Requires additional sample surface preparation by coating an irreversible reflection layer
Luminescence spectroscopy	1.No sample preparation required 2.Residual stress monitoring 3.Detect the phase transformation in TGO layer 4.Suitable for measurement on EBPVD coated TBCs	1.Laser highly attenuated by porous laminar YSZ layer (APS) 2.Accuracy limited on thickness of YSZ 3.Insufficient warning preceding failure
Laser photoacoustic spectroscopy	1.No sample preparation required 2.Generates ultrasound at sub-layer to avoid signal attenuation by the surface YSZ layer 3.Potentially noncontact measurement	1.Laser is highly scattered by YSZ layer 2.Evaluation rely on assessing area ratio of cracks
Thermal wave image	1.No sample preparation required 2.Visualise the defects in TBC system which appears cooler than bonded area 3.non-contact, non-invasive and whole-field technique 4. Testing large coating areas at a time	1.Low resolution in thermal image 2.Insufficient warning preceding failure

Table 2.3 Continuous

NDT methods	Pros	Cons
Mid-infrared (MID) reflectance	1.No sample preparation required 2.Take advantage that YSZ is translucent to mid-infrared leading to reflection from interface between ceramic and bond coat 3.Capable for monitoring delamination progression in TBC at early state	1.Low resolution in thermal image 2.restricted to thinner TBCs
Pulse-echo thermal wave infrared imaging	1.No sample preparation required 2.Visualise the defects in TBC system where the amplitude of thermal signal increased 3.Non-contact measurement	1.No sample preparation required 2.Visualise the defects in TBC system which appears cooler than intact area 3.non-contact, non-invasive and whole-field technique 4.Insufficient warning preceding failure
Eddy current	1.No sample preparation required 2.Thickness measurement	1.Only be used for electrically conducting materials
Impedance spectroscopy	1.Thickness measurement for each ceramic layer 2.Detect microstructural and composition change in TGO	1.Electrode is required on YSZ surface 2.Asymmetric electrode geometry lead to inaccurate calculation of electrical properties

2.7 Summary

In this chapter, a number of papers have been reviewed on thermal barrier coating system and correlated nondestructive evaluation methods. The first section has introduced the conventional bilayer thermal barrier coating system, namely, top coat and bond coat. The former provides thermal insulation for turbine blades and the later protects the superalloy from the environmental degradation while provides an adhesive bonding between the top coat and substrate. Yttria-stabilized zirconia is used as the material for top coat due to a suite of desirable thermal properties, which is normally deposited onto a substrate by either air plasma spray or electron beam physical vapour deposition. Two types of bond coats are mainly used in TBC system, which are diffused aluminide coatings based on β-NiAl phase and overlay coatings based on MCrAlX system. The former is produced by diffusion heat treatment, and the later is usually deposited by thermal spray technologies, such as APS and HVOF. During exposure to high temperatures, the oxidation of bond coat forms as an intermediate layer between the bond coat and the ceramic top coat, namely TGO layer which mainly contains α-Al_2O_3. The growth of TGO layer generates thermal expansion mismatch between ceramic coating and underlying bond coat during the cooling process, results in the formation of crack and spallation of coating and eventually lead to failure of TBC system. At the end of the first section, the failure mechanisms of TBC system are reviewed, including aluminium depletion, undulating interface along with the cracking mechanisms and damage induced by the foreign object.

Since the TBC failure will expose the turbine blade components to a severe environment which can endanger the engine during operation, regular health monitoring and life prediction of TBCs using nondestructive method are essential. Development of optimised NDT method has been receiving attention. In the subsequent sections of this chapter, a number of NDT methods for evaluating TBC system were reviewed. Three main NDT methods studied this project were covered in detail including the background and mechanism of the techniques and the previous researches applied to thermal barrier coating, which are X-ray computed tomography, laser photoacoustic spectroscopy and impedance spectroscopy. X-ray computed tomography can visualise the interior structure of TBC system using 3D reconstruction technology which enables to observe internal crack and delamination and provides information such as coating density, pore size distribution, surface roughness. The

laser photoacoustic spectroscopy utilised laser generated ultrasonic to detect the flaws in the TBC system. The mechanisms for laser generation of ultrasound was reviewed. Three regimes for laser generation of ultrasound were identified, which includes the thermalelastic regime, the plasma regime and the constrained surface source regime. Impedance spectroscopy can be used for evaluating the degradation of thermal barrier coating. It is capable of measuring the TGO thickness, detecting microstructural and composition changes in the TGO, and phase transformation in YSZ. Other available NDT methods were also reviewed, including thermal wave image, mid-infrared reflection and luminescence spectroscopy. At the end of the chapter, a comparison of the various NDT techniques for evaluating thermal barrier coating was concluded. As a result, the optical methods, either thermal or laser-based techniques are the most promise for delamination detection.

Chapter 3

Research Methodologies

In Chapter 2, the deposition process of TBCs and the related NDT methods have been reviewed. In this chapter details of sample preparation will be provided along with high temperature oxidation process and microstructure characterisation for all sample sets. The experimental scheme is presented in Figure 3.1.

The substrate preparation and deposition process of TBC samples will be introduced at first, followed by the preparation of freestanding YSZ coating samples and YSZ ceramic bulk samples. The setup and procedure of high temperature oxidation are given. Then the characterisation of TBC and the coating materials will be explained. At the end of the chapter, SEM (Scanning electron microscopy) image analysis for the thickness measurement of TGO layer along with other characterisation methods will be described in detail.

Since X-ray CT, laser photoacoustic spectroscopy and impedance spectroscopy are the three main NDT techniques discussed in this thesis, to maintain consistency of reading the thesis, the experimental part of each technique will be presented separately in Chapter 4, 5 and 6 respectively.

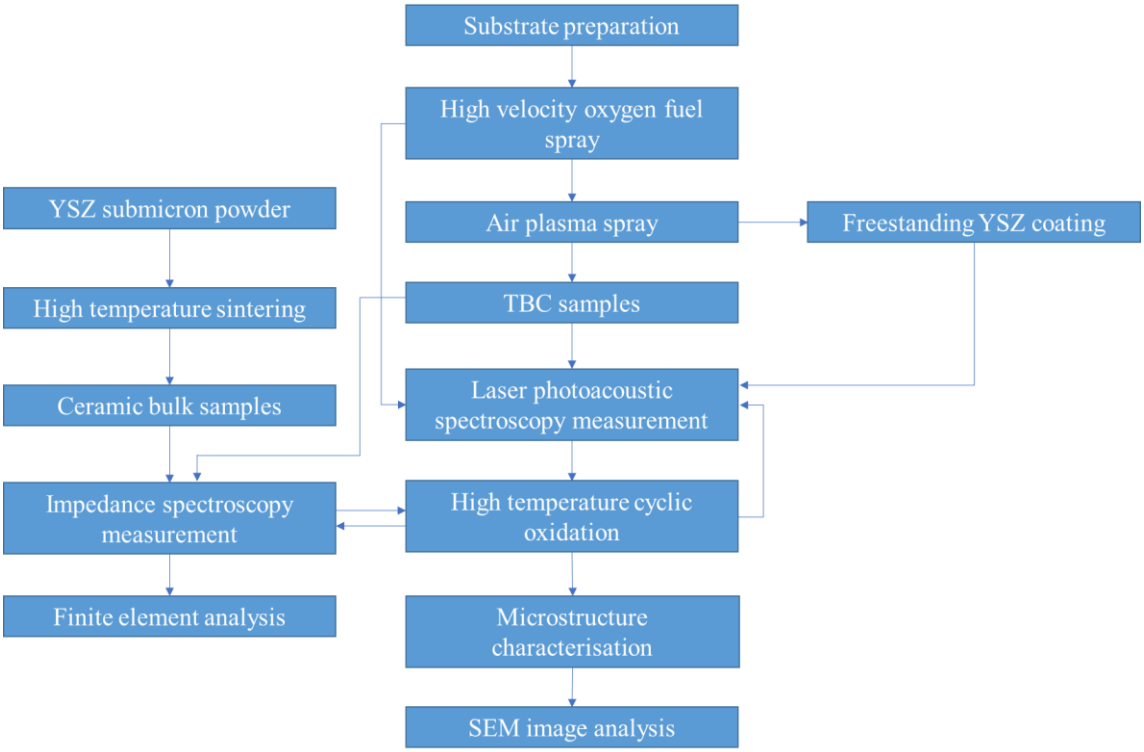


Figure 3.1 The process of experimental work

3.1 Preparation of TBCs

3.1.1 Substrate preparation

Two types of substrates were used in nondestructive evaluation experiments: single crystal superalloy CMSX-4 (A typical second-generation single crystal nickel-based superalloy, which was confirmed by an EDS elements analysis as shown in Appendix A) and nickel-based superalloy Mar-M-247 (M247, Advanced Alloy Services Ltd.). Both have similar chemical compositions which are summarised in Table 3.1. However, unlike single crystal superalloys with no grain boundaries, M247 contains either equiaxed grains or columnar grains depends on the cut during substrate preparation. A detailed explanation is given in Chapter 5.6.1. In the laser photoacoustic spectroscopy experiments, the polycrystalline structure of M247 causes an additional attenuation when an ultrasound wave is propagating through the material. Samples made from single crystal superalloy substrate simplifies the relationships, and this simplification removes the influence of these artefacts from the real signal response.

CMSX-4 substrates were cut into 5 mm thick round pellets from a solid circular rod with a diameter of 13.9 mm using ATM Brilliant 220 cutting machine with a BUEHLER AcuThin Abrasive Cut-off wheel. M247 substrates were cut from a cylinder ingot with a diameter of 135 mm using wire electrical discharge machining (WEDM). They were firstly cut into 5 mm thick circular disc and then machined into 20 mm diameter pellets according to a cutting layout, as shown in Figure 3.2.

After the WEDM, the corrosion surface of the M247 substrate was ground off. A surface treatment was carried out for both types of substrates using Guyson Formula 1400 sandblasting machine with F20 brown alumina (average size 1 mm). A surface of one side of each substrate was roughened to increase the bonding force in the subsequent HVOF spray. After sandblasting, substrates were successively cleaned with water and acetone in an ultrasonic bath and then dried by compressed air.

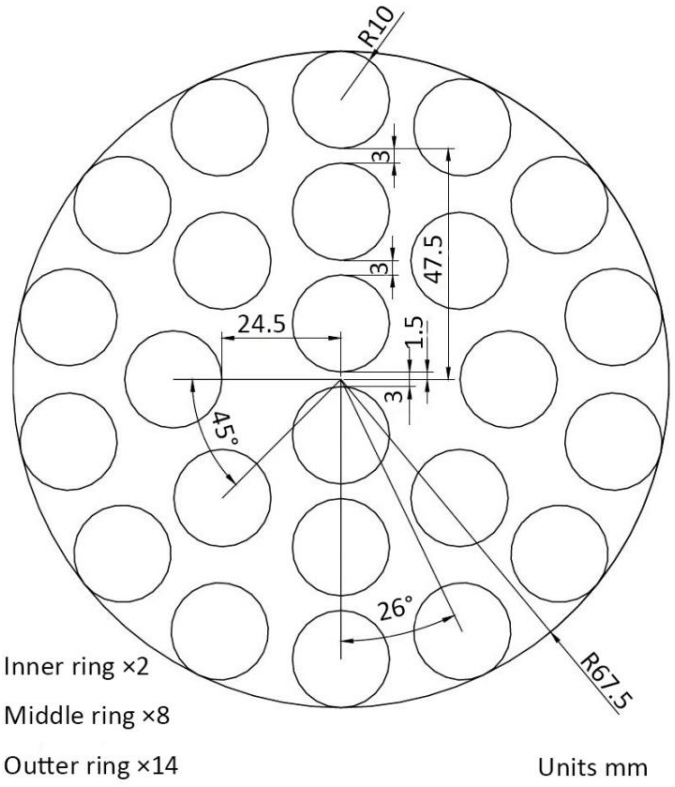


Figure 3.2 Cutting layout of the multigrain substrates from the cylinder ingot of M247 nickel-based superalloy.

Table 3.1 Chemical compositions of CMSX-4 and M247.

Element (wt. %)	C	Cr	Ni	Co	Mo	W	Ta	Al	Re	B	Zr	Ti	Hf
CMSX4	-	6.5	Bal.	9.6	0.6	6.4	6.5	5.6	3	-	-	1	0.1
Mar-M-247	0.16	8.2	Bal.	10	0.6	10	3	5.5	-	0.015	0.05	1	1.5

3.1.2 High velocity oxygen fuel (HVOF) spray

The bond coat was produced on the substrate by High Velocity Oxygen Fuel (HVOF) spray using NiCoCrAlY powder (Ni191-4, Praxair). The chemical composition of Ni191-4 is shown in Table 3.2. HVOF spraying process was carried out by a commercially available Metallisation HVOF system with a MetJet III spray gun, which is shown in Figure 3.3. The spray gun was installed onto a gun holder with movement manipulation controller, which was programmed to move vertically in a distance that based on the height of sample, as shown in Figure 3.4. The thickness of the sprayed coating is controlled by the number of passes, where one pass is defined as a complete cycle of spray gun moving up and down. The substrate samples were clamped into 12 sample holders on a carousel. The distance between sample and nozzle was adjusted to 356 mm.

Table 3.2 Chemical compositions of NiCoCrAlY powders Ni191-4.

Element (wt. %)	Al	C	Co	Cr	Ni	Total all other	Y
Ni191-4	12.6	0.02	20.51	17.8	Bal.	0.13	0.58

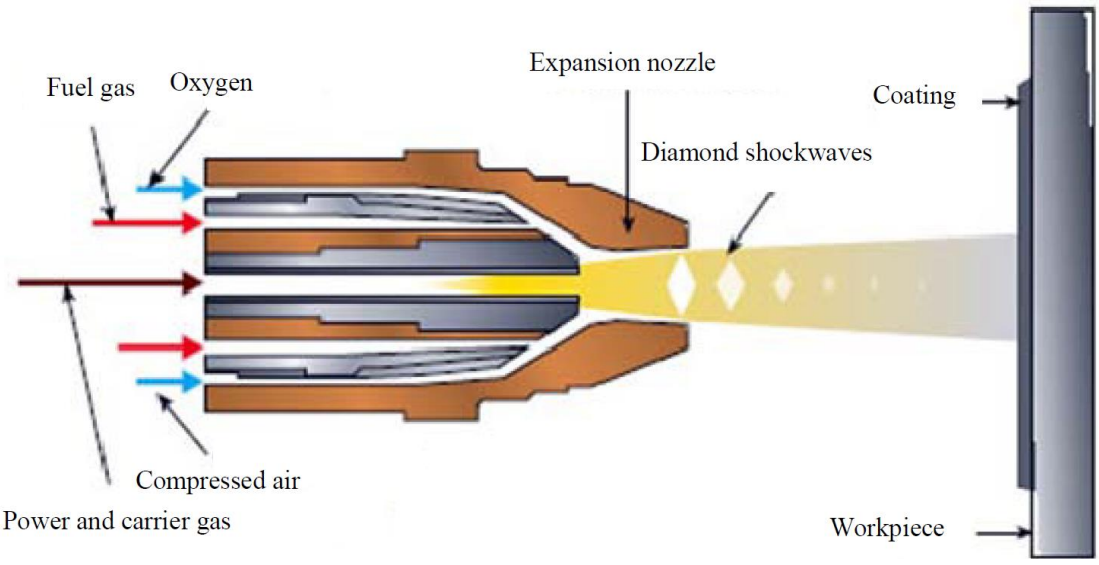


Figure 3.3 Schematic of HVOF thermal spraying by MetJet III gun. [154]

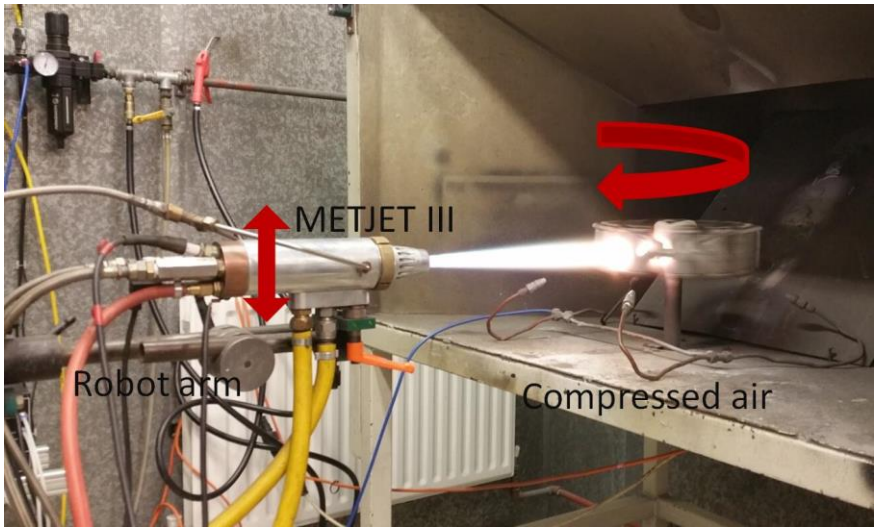


Figure 3.4 Photo of thermal spraying NiCoCrAlY bond coat using HVOF with a MetJet III gun.

During the spray process, the carousel rotated at a constant rotation speed of 73 rpm. Kerosene used as fuel was mixed with oxygen in the combustion chamber and ignited at the nozzle. Nitrogen was used as carrier gas for the sprayed power. The flow ratios of kerosene, oxygen and nitrogen were adjusted by a control unit during the spray process. Detailed HVOF spray parameters are shown in Table 3.3. Compressed air was used to cool the substrates during and after spraying process. After the HVOF spraying, the bond coat samples were heat treated in the vacuum furnace (TVH12/75/600, Elite) at 10-5 mbar 1100 °C for 2 hours. The heat treatment reduces the residual stress that built during the coating process and enhances the diffusion bonding.

Table 3.3 HVOF spray parameters for NiCoCrAlY powder Ni-191-4.

Spray parameter	Ni-191-4
Spray distance (mm)	356
Powder Feed rate (g/min)	186
Oxygen flow rate (L/min)	920
Kerosene flow rate (mL/min)	475
Carrier gas flow rate (L/min)	6
Number of passes	10

3.1.3 Air plasma spray (APS)

The ceramic topcoat was applied on the Ni191-4 bond coat by air plasma spray using 8 wt.% Y_2O_3-doped ZrO_2 ceramic powder (Al-1075, Praxair). The particle microstructure of Al-1075 observed by SEM is shown in Figure 3.5. APS was performed by a commercially available TAFA SG-100 plasma gun and 3710 plasma spray control console. The schematic of SG-100 plasma gun is shown in Figure 3.6. The plasma gun was installed on the same robot arm as in the HVOF spray process. The sample holder as shown in HVOF spray process was also used for APS process. The spray distance was reduced due to a shorter length of plasma flame, which is shown in Figure 3.7. Before the APS the samples were cleaned by compressed air. During the process, argon and hydrogen were used as the primary and secondary gas respectively. Argon was used as carrier gas. Detailed APS spray parameters are shown in Table 3.4.



Figure 3.5 Microstructure of 8 wt.% Y_2O_3-doped ZrO_2 particle. Particle size between 11 and 106 µm (Al-1075, Praxair).

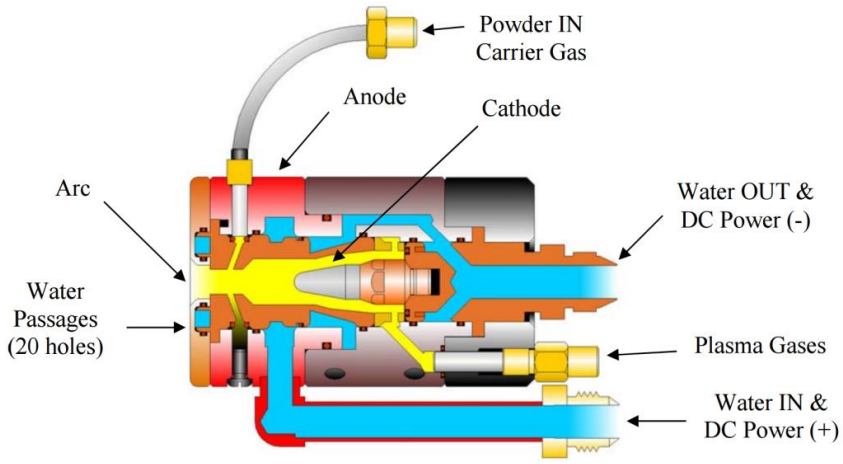


Figure 3.6 Schematic configuration of a TAFA SG-100 plasma gun. [155]

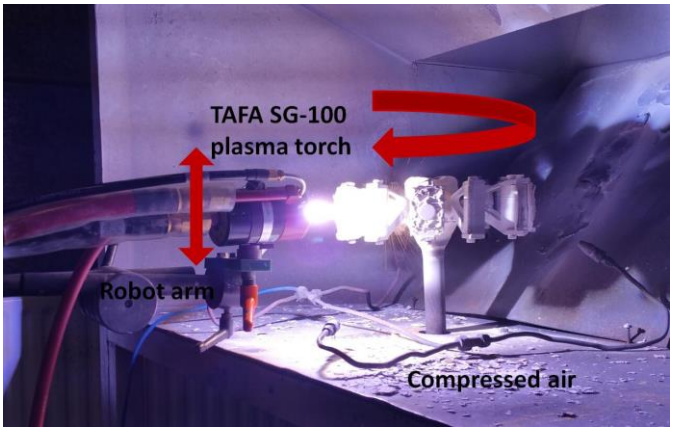


Figure 3.7 Photo of air plasma spraying YSZ top coat using TAFA SG-100 plasma gun.

Table 3.4 APS spray parameters for YSZ powder Al-1075.

Spray parameter	Al-1075
Spray distance (mm)	90
Powder feeder (rpm)	6
Main control current (A)	800
Main control voltage (V)	37.8
Primary gas Ar (psi)	39
Carrier gas Ar (psi)	40
Secondary gas H_2 (psi)	12
Number of passes	14

3.2 Freestanding YSZ coating preparation

Freestanding YSZ coating samples were used to investigate the optical attenuation and electrical properties in the ceramic top coat of thermal barrier coating. Same coating powder used to produce TBCs, 8 wt.% Y_2O_3-doped ZrO_2 ceramic powder (Al-1075, Praxair), was also used for freestanding coating. A bright drawn mild steel rod with a diameter of 20 mm was cut into 5 mm thick pellets used as substrates. Sand blasting was carried out to provide a rough surface for APS. After cleaning process, samples were divided into 5 groups and applied YSZ coating by same APS system with 8, 16, 32, 64 and 128 passes respectively. Then the coated samples were placed in 5M hydrochloric acid at 80 °C for 48 hours to detach the ceramic coatings from the substrates. The detached coatings were washed with acetone and then dried in an oven. A set of freestanding YSZ coating is shown in Figure 3.8.

The dimension of each freestanding coating was measured using a micrometer and weighed by a balance. The density of each sample was calculated by mass divided by volume. The parameters of freestanding coating samples are shown in Table 3.5.

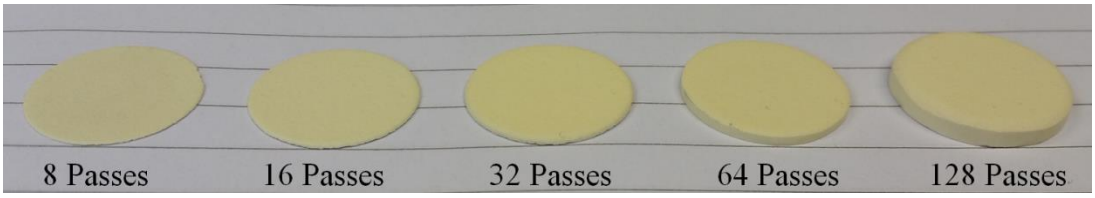


Figure 3.8 Detached APS YSZ coating as freestanding samples

Table 3.5 Parameters of freestanding coating samples

Sample	Number of passes	Avg. Thickness (μm) Error: ±1 μm	Weight (mg) Error: ±0.1 mg	Density (g/cm^3)
A	8	273	333.5	5.95
B	16	467	682.4	5.87
C	32	875	1373.3	5.798
D	64	1722	2794.6	5.818
E	128	3375	5536.9	5.763

3.3 Preparation of ceramic bulk samples

Ceramic bulk samples were used to investigate the effect of an electric field on asymmetric electrodes within an impedance spectroscopy (IS) test. Commercially available 8 wt.% Y_2O_3-doped ZrO_2 submicron powder (SIGMA-ALDRICH) was used to produce ceramic bulk samples. The microstructure of YSZ particle observed by SEM is shown in Figure 3.10(a). The YSZ powder was weighed and hand ground in an agate mortar. A few drops of diluted polyvinyl acetate (PVA) were added into the powder to increase adhesion between particles. The ground powder was loaded into a die with a diameter of 25 mm and pressed by a manual hydraulic press (Specac). The force was loaded between 1 to 2 tons (about 20 to 40MPa of pressure) dependent on the size of bulk. The pressure was held for one minute until there was no visible change in the indicator. Figure 3.9 shows the green pellets with a thickness of 0.52 mm. Then green pellet was calcined in a high temperature chamber furnace (Carbolite RHF 16/3). It was heated to 600 °C at a rate of 2 °C/min, held there for 2 hours, then heated to 1450 °C at a rate of 5 °C/min, held there for 6 hours and finally cooled to room temperature at a cooling rate of 5 °C/min.

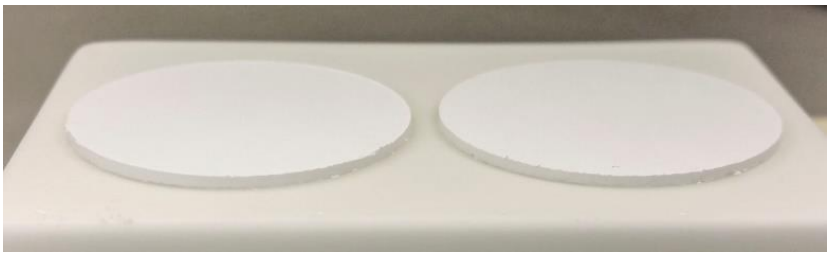


Figure 3.9 Green pellets with thickness of 0.52 mm, diameter of 25 mm

The density of each sample was measured using Archimedes' method. The theoretical density, 6.0476 g/cm^3, was calculated by X-ray diffraction (XRD). The relative density was calculated using measured density divided by theoretical density. The parameters of the ceramic bulk sample are shown in Table 3.6.

Table 3.6 Parameters of ceramic bulk samples

Sample	Avg. Thickness (mm) Error: ±1 μm	Avg. Diameter (mm) Error: ±1 μm	Weight (mg) Error: ±0.1 mg	Density (g/cm^3)	Relative density
A	0.493	19.505	858	6.034	99.8%
B	0.943	19.525	1823.3	5.954	98.5%
C	1.910	19.710	3450.9	5.949	98.4%
D	4.055	19.740	7367	5.979	98.9%

In order to observe the microstructure of YSZ bulk under SEM, the surface of ceramic was firstly polished and thermally etched at 90% calcination temperature for one hour. And then the surface was coated with a layer of platinum coating using a sputter coater (Manual, Agar scientific). Its surface morphology was observed by SEM, Secondary electron imaging (SEI) was taken and shown in Figure 3.10(b).

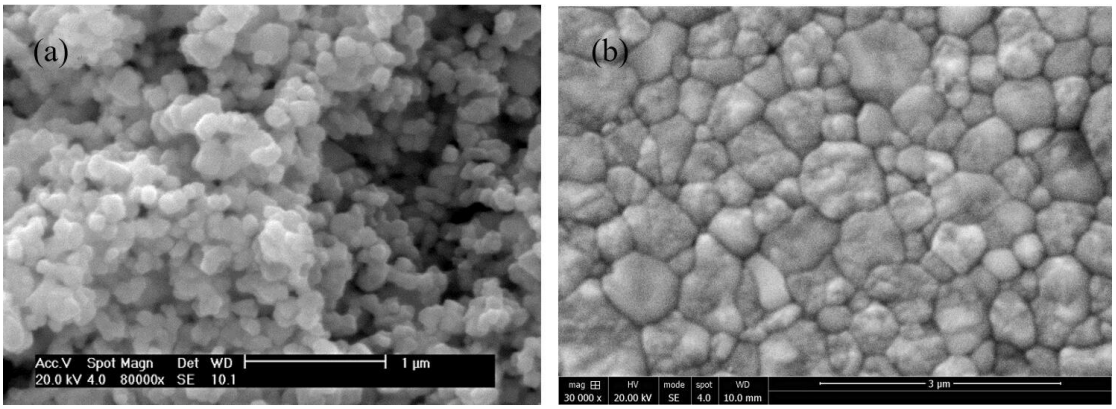


Figure 3.10 Secondary electron imaging of (a) particle microstructure of 8 wt.% Y_2O_3-doped ZrO_2 submicron powder (SIGMA-ALDRICH), (b) surface morphology of YSZ bulk sample after sintering.

3.4 High temperature cyclic oxidation

Thermal cyclic oxidation test was performed by a high temperature thermal cycling furnace (CM furnaces Inc. Rapid temp lab furnace 1608 BL) as shown in Figure 3.11(a). During the heating up process, samples were lifted by sample stage into the furnace chamber where the temperature increases rapidly. During the cooling down process, sample stage was taken out of furnace and samples were cooled by a fan, which is shown in Figure 3.11(b). In the present research, all thermal cycling procedures were programmed the same. During each thermal cycle, the furnace was heated up to 1150 °C in 10 minutes, held there for one hour and then followed by 20 minutes of fan cooling. The thermal cycling plan for each type of sample is given individually in later chapters. A list of thermally sprayed samples is shown in Appendix B, which has summarised the manufacturing information of each type of sample and which NDT technique it was used in.

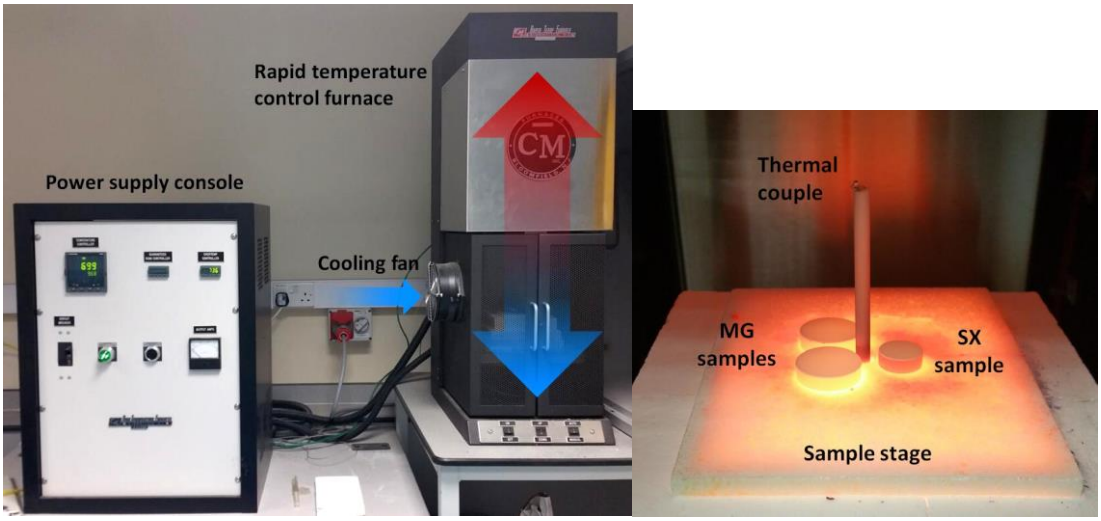


Figure 3.11 (a) Illustration of CM rapid temp lab thermal cycling furnace, (b) Samples during the cooling process.

3.5 Microstructure characterisation

3.5.1 Sample preparation for SEM

After high temperature cyclic oxidation, samples were sectioned using ATM Brillant 220 cutting machine with a BUEHLER AcuThin Abrasive Cut-off wheel for further microstructure characterisation. The feed speed was held at 0.005 mm/s to minimise the damage of the sample during cutting. Samples without ceramic coating were cut and then hot mounted in conductive epoxy resin. Samples with ceramic coating were mounted with low viscosity non-conductive resin both before and after cutting process to minimise the damage during cutting and the imposed stress in the hot mounting process.

All mounted samples were firstly ground using 240p, 400p, 800p, 1200p and 2500p grit grinding papers, and then polished using 6 μm and 1 μm diamond polishing paste wheel. At the final step, samples were polished by a synthetic cloth (MD-Chem, Struers) with 0.02 μm silica polishing suspension.

After polishing, samples were cleaned with methanol followed by an ultrasonic bath. Samples with ceramic coating were taped with a conductive tape on the surface of the non-conductive resin. The surface of the ceramic coating was coated with carbon using carbon coater (SEM turbo, Agar scientific) for better surface electrical conductivity.

3.5.2 Scanning electron microscopy (SEM)

Microstructure characterisation was conducted by three SEM systems: Phillips XL30 ESEM-FEG, FEI Quanta 600 MLA and FEI Quanta 650 ESEM. For each system, the accelerate voltage was set to 20 kV. The spot size of the electron beam was chosen such that the maximum resolution was obtained for an acceptable SNR level. The working distance was set around 10 mm. Both secondary electron (SE) image and backscattered electron (BSE) image were acquired for the different purpose of microstructure observation. The secondary electron image was used to reveal the detailed surface morphology including defects such as cracks, pores and impurities. The BSE image was used to observe the compositional distribution on the sample

surface as the intensity of the scattered electron beam is strongly related to the atomic number of the sample. A control software AZtec associated with Quanta 650 SEM was used to acquire high resolution panorama image along the cross section of samples, which has significantly increased the accuracy of oxidation image analysis.

3.5.3 Energy dispersive X-ray analysis (EDS)

Energy-dispersive X-ray spectroscopy (EDS, Oxford Instrument Silicon Drift Detector- X-Max^N) was conducted with associate AZtec software to analyse the qualitative and quantitative composition of TGO layer. The X-ray emitted from different elements by shooting electron beam onto the sample surface was examined by EDS detector. The accelerated voltage was set to 20 kV. The spot size of the electron beam was chosen such that the maximum resolution was obtained for an acceptable dead time of the system. Working distance was set to optimal distance, 10 mm, to maximise the X-ray counts. Point detection was conducted for a small area of the oxidized layer, while area scan was performed to give more accurate results. Furthermore, element mapping was conducted to observe the element distribution inside of coating.

3.5.4 X-ray diffraction (XRD)

Siemens D500 X-ray diffractometer (XRD) was used to investigate the phase transformation in the YSZ coating and to calculate theoretical density of ceramic bulk. The operating voltage and current were set at 40 kV and 25 mA respectively. Cu-Kα radiation was used as an X-ray source. For characterisation of YSZ powder, the scanning range of 2θ from 10° to 130° with a step size of 0.02° was applied.

3.6 SEM image analysis

Image analysis technique was utilised for measuring the thickness of TGO layer in TBC samples and counting the number of cracks formed in TGO layer. The principle of image processing is based on the scale of the brightness of the pixels in an image which varies between 0 and 255, where the higher the value, the brighter the pixel is. The brightness range of pixels within each layer of BSE image of TBCs was determined as follows: the ceramic YSZ layer has brightness range from 145 to 195; bond coat ranges from 110 to 160; TGO layer ranges from 18 to 45; cracks and pores have brightness below 20. It is worth noting that the brightness range of each layer in BSE image could slightly change between samples due to the variation in the intensity of the tungsten filament. However, the difference in brightness between layers remains the same for all samples.

The panorama BSE image of TGO layer was processed and analysed using Adobe Photoshop CC software for measuring the average thickness of TGO layer of TBC samples. The dark grey region of TGO layer was selected by the magic wand tool with a sampling size of 5 × 5 and the brightness tolerance at 20. Some oxides which were not connected with TGO layer were added in manually. The perimeter of TGO layer was measured in the number of pixels. Then the area of TGO was obtained by removing the cracks from the selected region, as shown in Figure 3.12(b). The length of one pixel was calculated using a ratio of the length of scale bar in the image to the number of pixels in scale bar. The actual scale of area and perimeter were calculated using the same ratio. Finally, the average thickness of TGO layer was calculated using the area of the TGO layer divided by half of its perimeter.

The thickness and the total length of cracks were measured using a similar method. The difference was that each layer in the TBCs except the cracks were replaced by white pixels before measurement, as shown in Figure 3.12(c). To calculate the total length of cracks, the processed image was converted to a matrix where the elements were replaced by the brightness of each pixel using MATLAB software (2016b). A program was written to count the number of columns that have an average value below 255, which equals the length of the cracks in pixels. Thickness was calculated by the total number of pixels of the crack area divided by the length of the cracks in pixels.

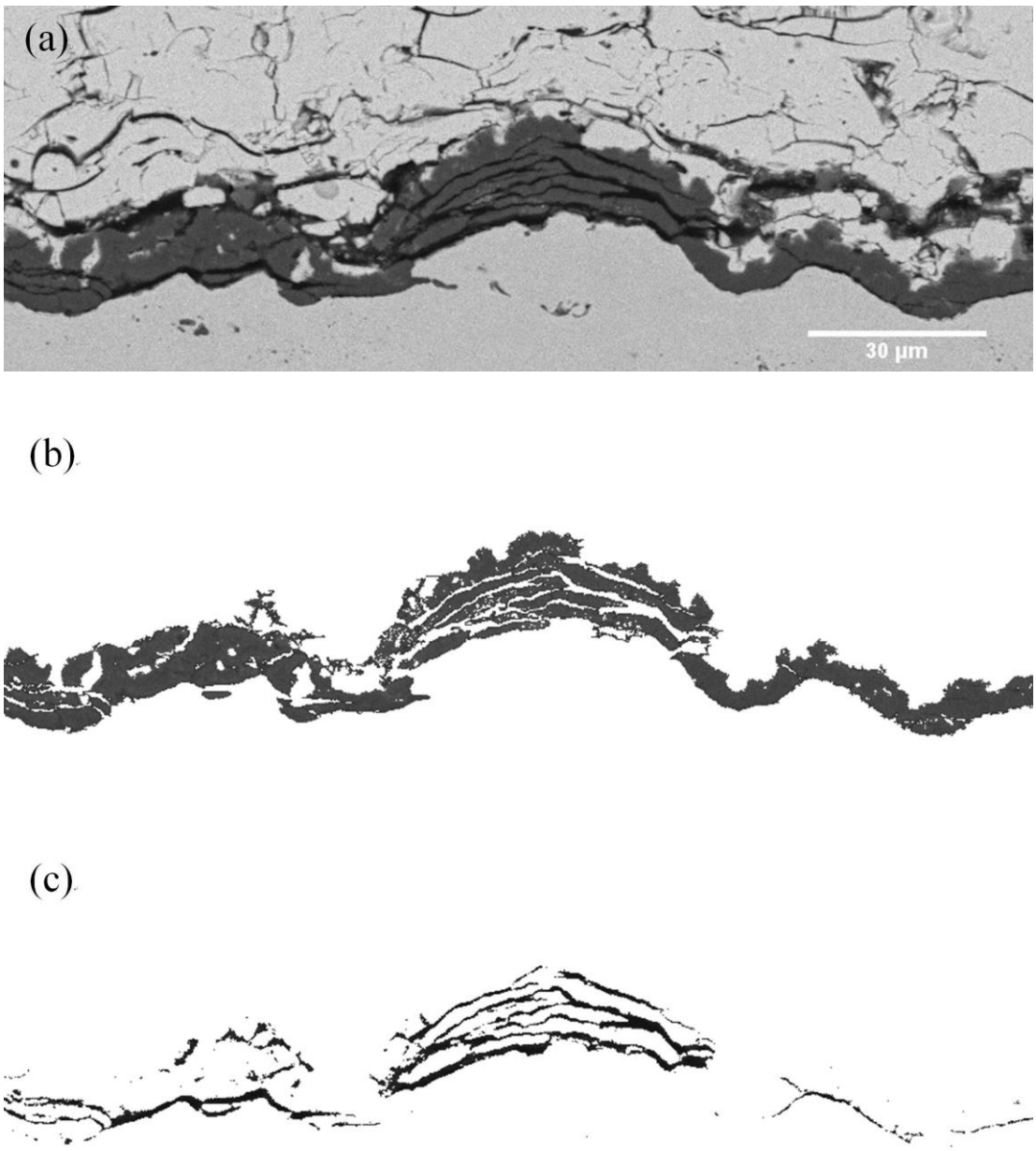


Figure 3.12 Illustrative diagrams of image analysis (a) BSE image of TGO layer after 80 thermal cycles at 1150 °C, (b) TGO layer selected by magic wand tool, (c) Cracks under the top surface of TGO layer.

3.7 Summary

This chapter has described the process of manufacturing thermal barrier coatings, along with two coating deposition techniques, high velocity oxygen fuel and air plasma spraying which were used to for bond coat and top coat deposition. Two types of TBC samples with either single crystal superalloy substrate or multigrain superalloy substrate were produced. The YSZ freestanding coating sample and ceramic bulk sample were manufactured for laser photoacoustic spectroscopy measurement and impedance spectroscopy measurement respectively, which will be presented in Chapter 5 and 6. The high temperature cyclic thermal oxidation test was carried out for TBC samples at 1150 °C. The microstructural characterization of all the TBC samples was conducted using scanning electron microscopy. The qualitative and quantitative composition of TGO layer was carried out using energy dispersive x-ray analysis. The analysis of phase transformation in the YSZ coating and the calculation of theoretical density of ceramic bulk were carried out using x-ray diffraction. The thickness of TGO layer and the size of the cracks within TGO layer were measured by image analysis.

In the following chapters, the three main NDT techniques applied on thermal barrier coating, X-ray CT, laser photoacoustic spectroscopy and impedance spectroscopy, will be discussed in detail.

Chapter 4

X-ray CT

This chapter demonstrates nondestructive evaluation of thermal barrier coatings using X-ray computed tomography (X-ray CT). The sample used for testing was an unconventional TBC sample which was manufactured by the previous researcher in the advanced material group using electrostatic spray assisted vapour deposition (ESAVD). The sample was cut into a small piece to complete X-ray CT measurement. Thermal oxidation test for observation of TGO growth has not been performed due to lack of samples. Basis X-ray CT study on thermal barrier coating was carried out using two available X-ray CT facilities at the University of Nottingham which are GE Phoenix nanotom and Xradia Versa XRM-500. Results from both machines will be presented and discussed in the following chapters.

4.1 X-ray CT measurement

4.1.1 Sample preparation

The dimension of the as-received sample is 25.2 mm × 14.1 mm × 2.5 mm. A primary test was performed with its original size by an X-ray computed tomography (GE nanotom). A blurry image was obtained in low resolution where each layer of thermal barrier coating was not able to distinguish due to the high attenuation caused by the size of the sample. For laboratory X-ray CT, in order to achieve higher resolution image, the TBC sample must cut into a smaller piece to accomplish X-ray CT experiments.

The sample was first mounted in a resin to reduce a certain extent of damage from the diamond saw. Then it was cut by a diamond saw at 3000 rpm and feed speed was held at 0.01 mm/s. Part of the substrate was also cut off to reduce the thickness of the sample, thus, reduce extra attenuation of X-ray by the substrate. As a result, the sample was cut into two different shapes with both thicknesses around 0.7 mm, as shown in Figure 4.1.

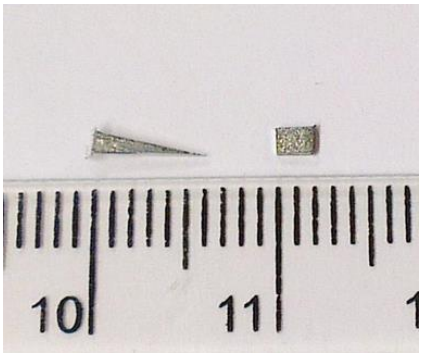


Figure 4.1 Two sectioned samples for X-ray CT

4.1.2 GE Phoenix nanotom

The X-ray CT measurement of the square sample was first conducted by GE Phoenix nanotom, as shown in Figure 4.2 (a). The sample was glued on top of a metal rod which was clamped by sample stage, as shown in Figure 4.2 (b)(c). The sample was fixed at 4 mm away from the X-ray source and 196 mm away from the detector. The beam

energy was set to 140 kV and 20 µA. Exposure time for each projection image was set to 500 milliseconds, and a total of 1440 images were taken to reconstruct a 3D image of the sample.

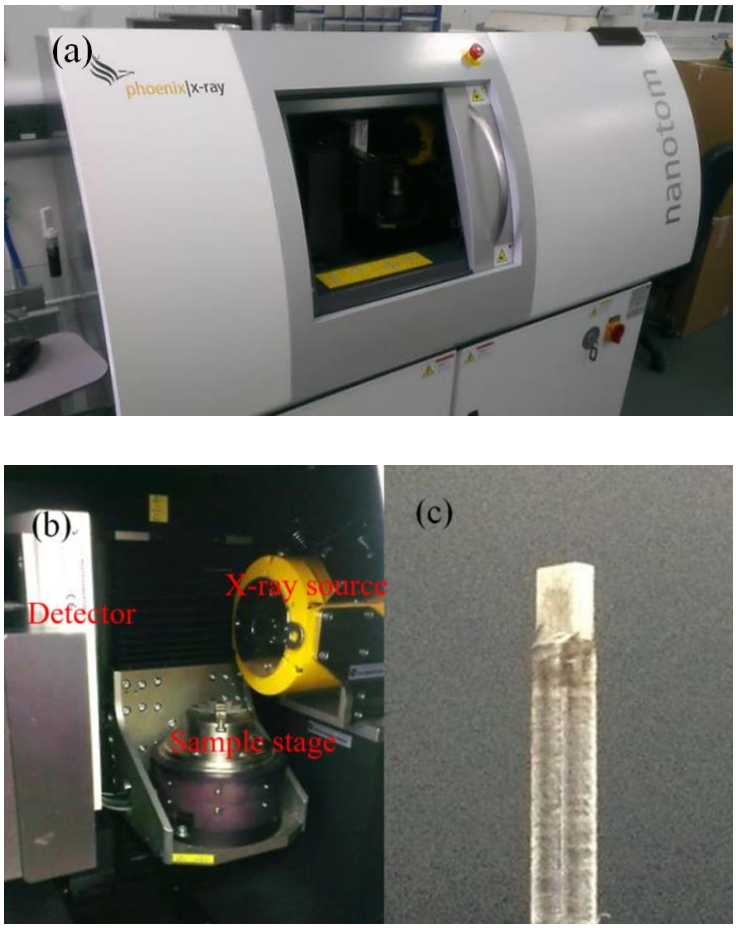


Figure 4.2 (a) GE Phoenix nanotom X-ray CT scanner (b) Internal configuration of GE nanotom (c) Square sample glued on top of sample holder

4.1.3 Xradia Versa XRM-500

Later on, both samples were measured using Xradia Versa XRM-500 X-ray CT. The internal structure is similar to GE nanotom but adds a live camera to monitor sample position during testing. The sample stage is driven by a rotational belt which enables provide ± 180 degrees rotation, as shown in Figure 4.3.

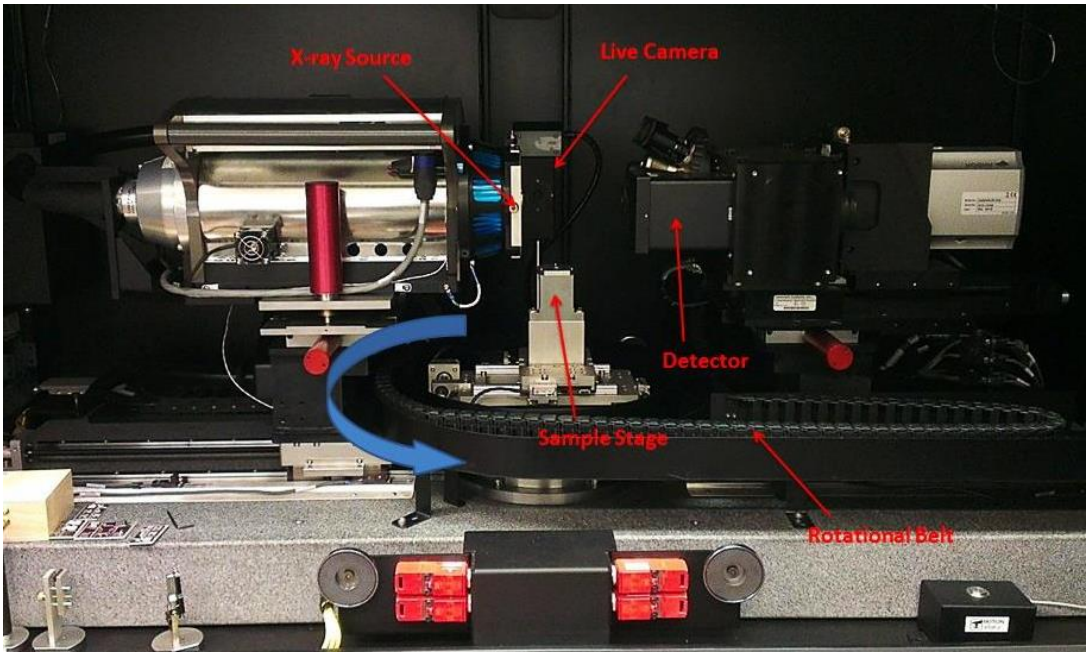


Figure 4.3 Internal setup of Xradia Versa XRM-500 X-ray CT Scanner

For the square sample, it was placed up to down and glued on the tip of the sample stage. However, the bottom part of the stage was too wide to move closer to X-ray source and detector, eventually, the distance between both of them was set as 12 mm. The beam energy was set to 140 kV and 71 μA, and 40× optical magnifications setting was used. Exposure time for each projection image was set to 180 seconds, and a total of 960 images were taken to reconstruct a 3D image of the sample.

The X-ray scanning results of the square sample with using the previous setting were still not good enough for TGO layer observation. A new sample stage with a thin metal rod was machined, which enables to move sample closer to both source and detector. This sample stage was applied in pointed spine sample measurement, as shown in Figure 4.4. The sample position was set as 8 mm to source and 10 mm to the detector. The beam energy was set to 60 kV and 84 μA. 20× optical magnifications are used. The exposure time for each projection image was set to 10 seconds, and a total of 1000 images was taken and used to reconstruct a 3D image of the sample.

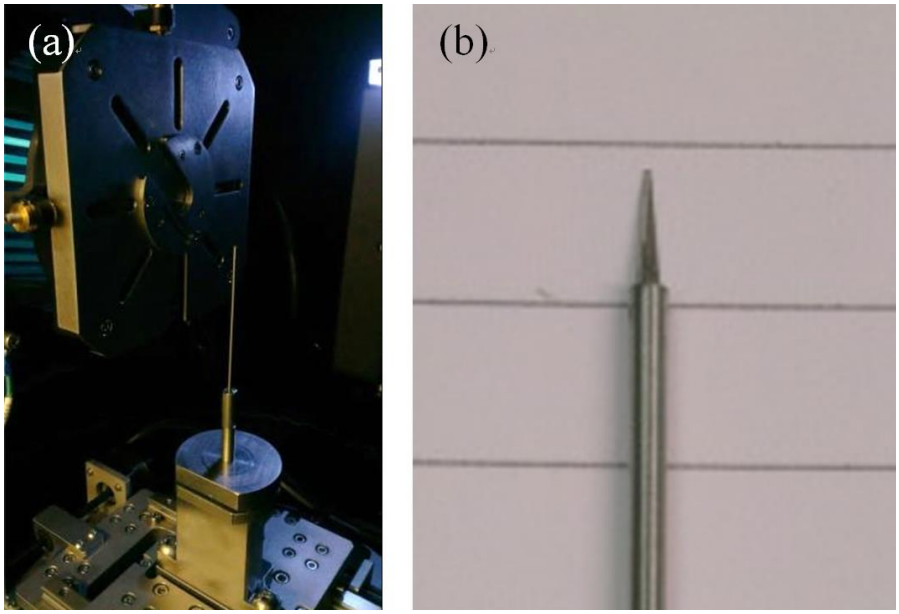


Figure 4.4 (a) New machined sample stage of XRM-500 X-ray CT Scanner (b) Pointed spine sample glued on thin metal rod stage

4.2 Results

4.2.1 GE Phoenix nanotom

Figure 4.5 shows one slice of the 2D image acquired by GE Phoenix nanotom which was exposed 500 milliseconds at 140 kV and 20 µA. The image quality is good enough to distinguish each layer and their interface. The thickness of each layer was measured, as shown in Figure 4.5. However, the TGO layer was not found in the image. Potential cracks were observed at the interface between YSZ layer and bond coat, which were mark with a red circle in the figure.

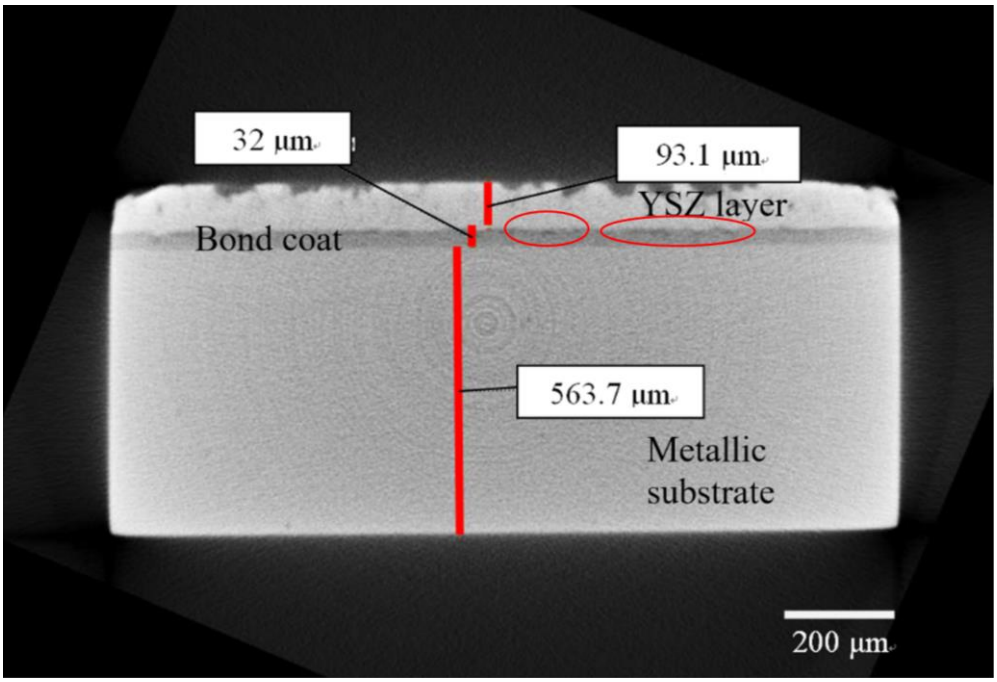


Figure 4.5 One slice of X-ray image of square sample taken by GE nanotom

From the top view of the sample, as shown in Figure 4.6, the columnar structure of ESAVD YSZ layer was observed. The exterior morphology of the square sample was restored and presented in the reconstructed 3D image, as shown in Figure 4.7.

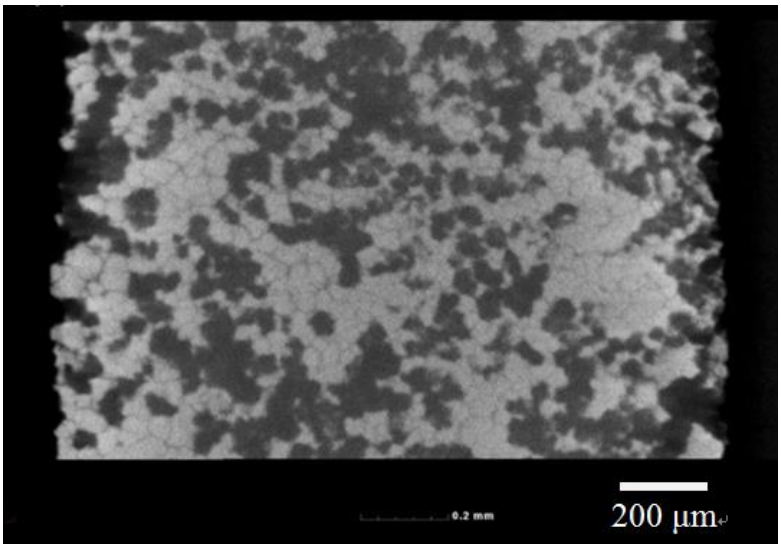


Figure 4.6 Columnar structure of ESAVD YSZ layer observed from the top of the square sample

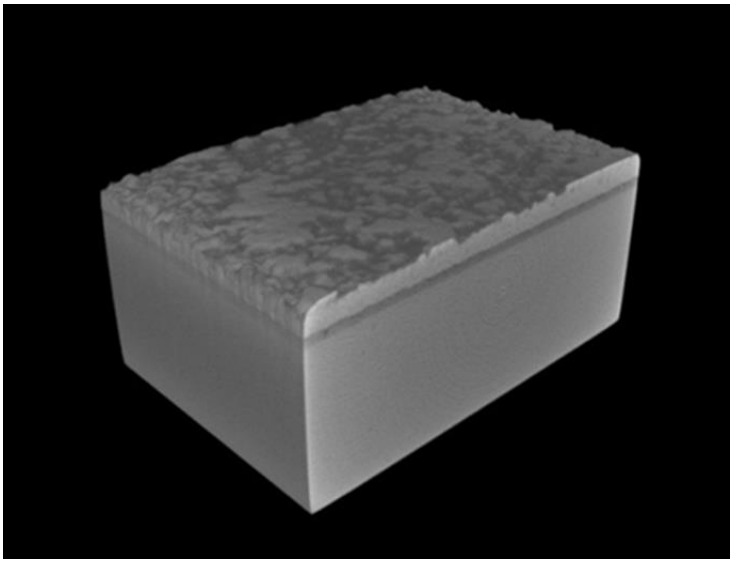


Figure 4.7 Reconstructed 3D image of square sample by GE nanotom

4.2.2 Xradia XRM-500

Figure 4.8 shows the reconstructed 3D images of the square sample taken by Xradia XRM-500. As a result, the image quality is quite similar to the image acquired previously from GE nanotom. A large amount of noise is present in the image, which is probably due to the long exposure time of the CT scan. In general, at 40× optical magnifications the image is not sharp enough to observe the TGO layer. Some potential cracks can be observed at the interface between the top coat and bond coat, however, in a blurry shade due to the noise from the scan.

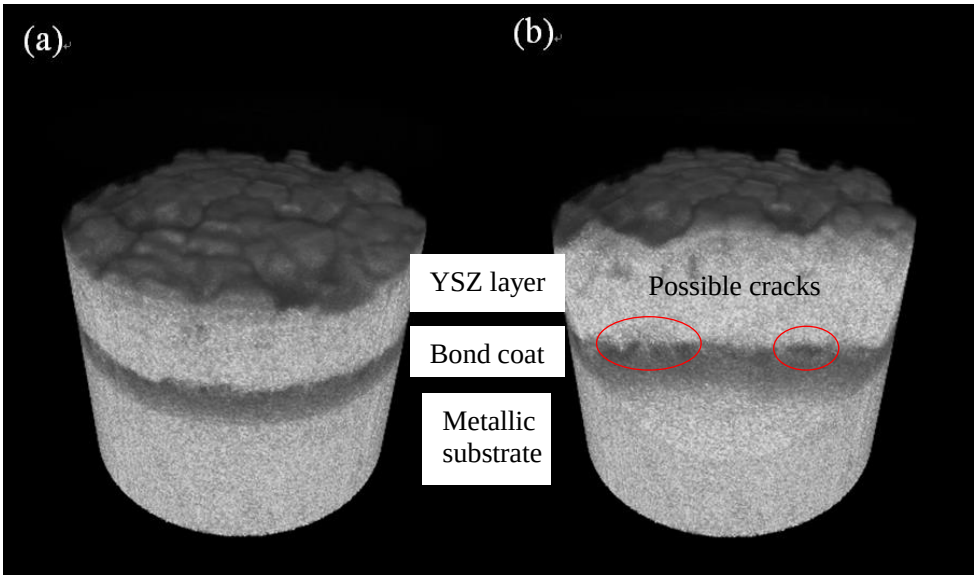


Figure 4.8 (a) Reconstructed cylinder 3D image from the square sample by Xradia XRM-500 (b) The possible cracks at the interface, dark area between YSZ layer and bond coat, are exposed in 45 degree cut view

Figure 4.9 shows the X-ray images of the pointed end of the spine sample taken by Xradia XRM-500. Compare to the results of the square sample, these images have shown much more details of the TBC sample in a different plane. In XY and XZ plane, cracks were clearly observed at the interface between the ceramic top coat and the bond coat, as shown in the marked red circles in Figure 4.9 (a) and (c). The grain boundaries of ESAVD coated YSZ layer were observed in YZ plane, where the columnar structure of the grains in the ceramic layer was clearly indicated. The surface morphology of the sample was presented in a 3D reconstructed image.

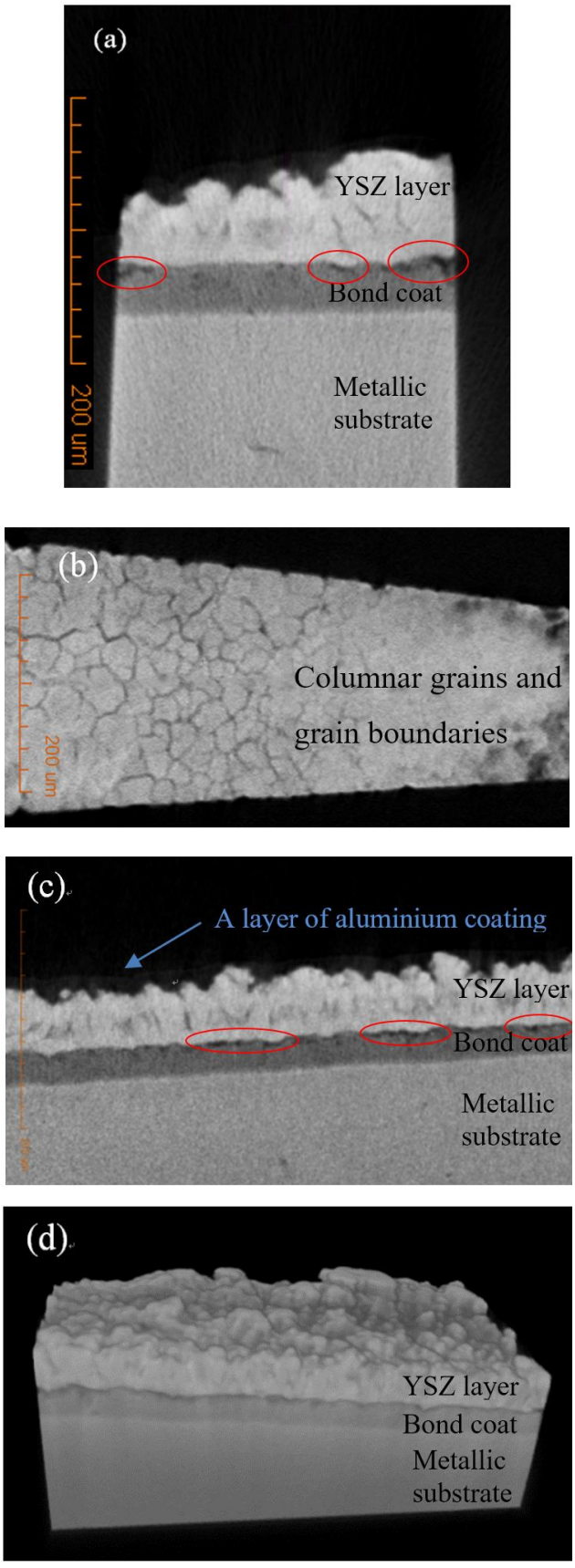


Figure 4.9 Sliced image acquired from (a) XY plane, (b) YZ plane and (c) XZ plane. (d) Reconstructed 3D image of pointed spine sample using Xradia XRM-500

The surface morphology of the ESAVD TBC sample was examined under SEM, which is shown in Figure 4.10 as a comparison to the reconstructive 3D image above. It is shown that the grain size on the surface was around 80 μm and the grain boundaries are similar to the sub-layer slice shown in Figure 4.9 (b).

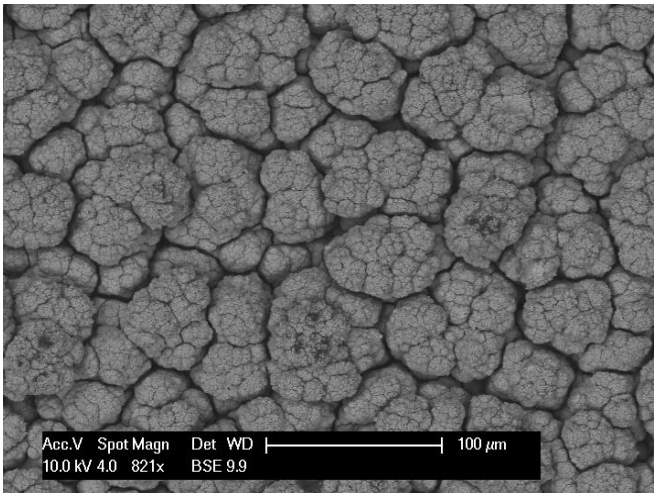


Figure 4.10 Back-scattered electrons image of the surface of ESAVD TBC sample

4.3 Discussion

As shown in Figure 4.9 (c), five layers were observed, material contains element with higher atomic number is shown brighter in the X-ray image: light grey at the bottom indicates metallic substrate, dark grey indicates bond coat, the thin black layers are cracks at the interface, bright layer is the YSZ coating, and a dark layer on top of the sample is aluminium coating (not very clear). As a result, resolution of 0.6 μm is achieved by Xradia XRM-500 X-ray CT under 20× optical magnifications and the image quality is much better than the previous measurement. It is competitive compared to the results from Y.Zhao et al.[29]

The X-ray CT study has revealed that the laboratory micro CT system can detect structure with high resolution only on a micrometre scale. The image resolution is directly related to the sample geometry and the configuration of X-ray CT, which can be improved by reduce the detected sample size and minimise the distance of sample to X-ray source and detector.

4.4 Summary

In conclusion, the internal microstructure and exterior surface morphology of an unconventional TBC sample coated by ESAVD were investigated using two different laboratory X-ray CT scan systems, namely GE Phoenix nanotom and Xradia XRM-500. As a result, an image resolution of 0.6 μm is achieved by Xradia XRM-500, five different layers were observed in the thermal barrier coating including a few of cracks at the interface of YSZ layer and bond coat. However, the samples for the X-ray CT testing are extremely small and required sample preparation, the best resolution of the image of thermal barrier coating was acquired at the pointed end of spine sample where the width is about 200 μm. Therefore, X-ray CT technique is not suitable for industrial in-situ detection for thermal barrier coating.

Chapter 5

Laser Photoacoustic Spectroscopy

A number of nondestructive testing methods for evaluating thermal barrier coating in the field of research have been reviewed in Chapter 2. Ultrasonic testing is one of the most commonly-used technique for flaw detection. However, ultrasonic generation and detection require use coupling medium between sample and transducer or operating fully immersed in the water, which could lead to contamination of sample or moisture induced delayed spallation (MIDS). Moreover, there is energy loss of ultrasonic signal due to signal attenuation by the porous and microcracked microstructure of YSZ ceramic coating. Laser photoacoustic spectroscopy technique (LPAS) has overcome problems by providing a noncontact laser ultrasound generation which generates ultrasound at sub-layer could avoid signal attenuation by the surface YSZ layer and reduces the signal interference during the propagation through the porous laminated structure of YSZ. However, it requires additional sample preparation by coating a reflection layer on the ceramic surface in order to increase the sensitivity of detection laser. The current chapter will demonstrate the nondestructive evaluation of thermal barrier coatings using laser photoacoustic spectroscopy. C-scan measurement will be carried out on two types of thermal barrier coating with either single crystal superalloy substrate or multigrain superalloy substrate at a different number of thermal oxidation cycles. Results will be shown in amplitude map, signal energy map, frequency map and phase map along with corresponded analysis technique. The microstructure of the oxidation of thermal barrier coating will be investigated via SEM. The thickness of TGO layer in each sample after thermal cyclic

oxidation will be measured via image analysis and related to the LPAS results. A physical model will be studied to estimate the influence of cracks inside TGO on signal attenuation. The viability of LPAS technique will be discussed along with some possible improvements and future plan of laser photoacoustic spectroscopy measurement will be given in the last chapter.

5.1 Laser photoacoustic spectroscopy measurement

5.1.1 Instrumentation

Laser photoacoustic spectroscopy (LPAS) measurement was carried out with a self-assembled system to facilitate the bespoke scanning process. The system consists of an ultrasound generation laser and a piezoelectric detection transducer, which are associated with certain optics, scanning stages, electronics and data acquisition equipment. The schematic diagram and photo of the key parts of the system are shown in Figure 5.1.

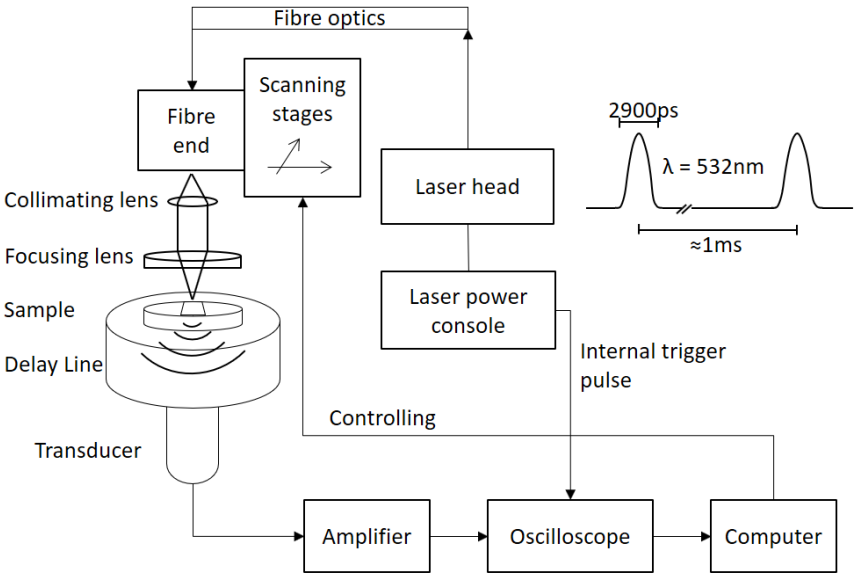


Figure 5.1 (a) Schematic diagram of LPAS System

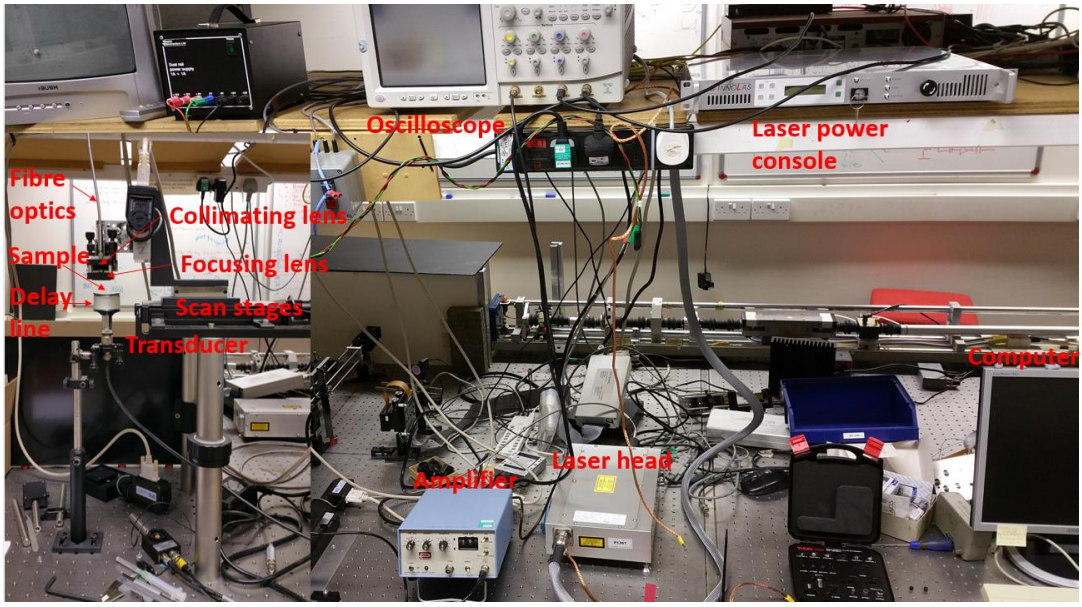


Figure 5.1 (b) Photo of the LPAS system setup

Excitation source

The laser used to generate the ultrasound is a Q-switched/diode-pumped/MOPA/ Nd:YAG laser with an interchangeable wavelength of 1064/532 nm. The Q-switch repetition rate is adjusted at 1 kHz for maximum laser output, which also determines the measurement speed limit. The laser pulse duration is approximately 2900 ps, which implies that the bandwidth of pulse output is around 340 MHz.

As mentioned previously, yttria-stabilized zirconia (YSZ) ceramic layer has a transmission range from around 320 nm to 7 μm, also the principle absorption band of Cr^{3+} ions in the TGO is in the range of 400 to 550 nm. During operation, the green laser with 532 nm wavelength was chosen to be used in order to obtain higher radiation absorption rate of TGO layer, thus, lead to the more efficient generation of ultrasound by laser. The oscillator current and amplifier current were set to 3.2 A and 2.8 A respectively. As a result, the total output power of the laser is around 256 mW, and the mean output power of the laser at fibre end is around 90 mW. The energy of each laser pulse is approximately 105 μJ. The surface temperature rise by single pulse is about 0.004 K which is predicted under the assumption that all laser energy of a single uniform pulse is fully absorbed by the surface material, the YSZ coating, and the laser pulse is extremely short, so that the conductivity from the radiated area to the bulk of sample can be neglected. The detail of the calculation is shown in Appendix C. In the

laser photoacoustic experiment, the rise of temperature of the sample caused by the laser would be even lower when taken the reflection of laser and heat flow into account, which means this detection method will not damage the surface of the sample, therefore it is an NDE method.

A primary test was conducted by pointing a laser beam at the surface of a piece of freestanding YSZ coating, which has shown that 532 nm green laser is able to pass through the top coat of thermal barrier coating, as shown in Figure 5.2a. However, most of laser light was reflected and scattered in all directions due to the rough surface of the top coat, as shown in Figure 5.2b. Further investigation on laser attenuation of YSZ ceramic coating will be presented in the following chapters.

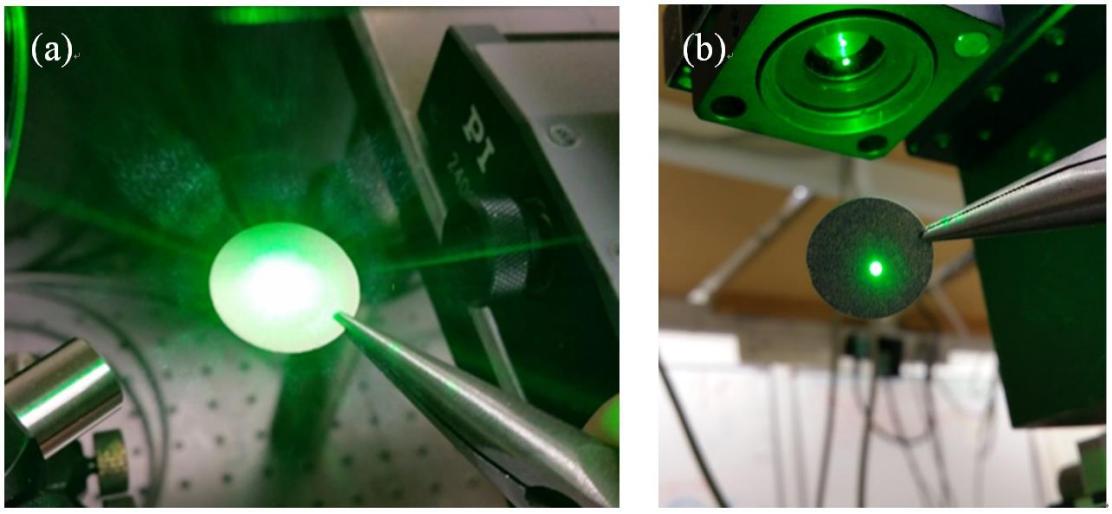


Figure 5.2 (a) Laser scattered on freestanding YSZ coating (b) Laser passing through YSZ layer, showing at the back of the coating.

Scanning stages

The laser coming out of the end of the fibre is convened and focused to a spot with a diameter around half a millimetre. The laser beam is adjusted to point perpendicularly to the surface of a sample by tilting stage which is mounted on XY stage. Scanning speed and step size are controlled by a program running on the Linux operating system. Non-single crystal samples with 20 mm diameter and single crystal samples with 14 mm diameter have different scanning parameters, as shown in Table 5.1.

Table 5.1 Scanning parameters of two types of samples with different substrates

Sample types	Diameter (mm)	Scan area (mm^2)	Step size (μm)	Data points (per sample)	Testing time (Hours)
Multigrain	20 mm	16 ×16	80	40401	8
Single crystal	14 mm	16 ×16	32	251001	27

5.1.2 TBC sample sets

There were three batches of the following samples tested by laser photoacoustic spectroscopy, single crystal substrate with 8 and 14 passes APS YSZ top coat samples (8-SX and 14-SX) and the multigrain substrate with 14 passes APS YSZ top coat samples (MG). Single crystal samples were tested to simplify the results, as ultrasound propagating through a multigrain material is affected by the microstructure, this simplification removes the influence of these artefacts. Parameter details of these samples were presented in Chapter 3.1.

After first LPAS scan, each sample was put into the thermal cycling furnace and thermally cycled from room temperature to 1150°C with a set number of times, as shown below in Table 5.2 and 5.3. An oxidised layer was formed on the surface of the substrate each time after high temperature thermal cycling. This rough and loosened layer would subsequently scatter and impede ultrasound waves during the LPAS test. Therefore, the surfaces of substrates were carefully ground and polished to a mirror gloss (surface roughness around 4μm) after thermal cycling. Subsequently, samples were water cleaned and dried in an oven at 60 °C for 5 hours before the next scan.

Table 5.2 The number of thermal oxidation cycles of SX sample

	Cycles	0	20	40	60	80
14-SX	A	●	●	●	●	○
	B	●	●	●	●	○
	C	●	●	●	●	○
	D	●				
	E	●	●			
	F	●		●		
	G	●			●	
	H	●				●
8-SX	I	●	●	●	○	
	J	●	●	●	●	
	K	●	●	●	○	
	L	●				
	M	●	●			
	N	●	●	●		
	O	●	●	●	●	
	P	●	●	●	●	
	Q	●	●	●	●	

In SX sample set, sample D to H and sample L, M, N were used as reference samples. The symbol ○ represents that sample was delaminated before the test, and the result has not been obtained. Sample O and P were tested once again to fill up the data set since sample I and K have failed earlier at 60 cycles.

Table 5.3 The number of thermal oxidation cycles of MG sample

	Cycles	0	5	10	20	40	80
MG	1	●	●	●	●	●	●
	2	●	●	●	●	●	●
	3	●	●	●	●	●	
	4	●	●	●	●	●	
	5	●	●	●	●		
	6	●	●	●	●		
	7	●	●	●			
	8	●	●	●			
	9	●	●				
	10	●	●				
	11	●					
	12	●					

It is worth noting that in MG samples 4, 6, 8, 10, 12 have a different type of grain orientation which has a direct influence on the results, and will be discussed in section 5.6.1.

5.1.3 Signal detection

Laser generated ultrasound waves propagate through the sample and a crystal delay line is then detected by a piezoelectric transducer. Ideally, the detection frequency of transducer should be high enough to correspond with the frequency of laser generated ultrasound which has broad bandwidth due to the 2.9 ns short laser pulse. However, only part of the signal was detected due to the limited bandwidth of piezoelectric transducer. As shown in a frequency map (Figure 5.10 in following section), the frequency of the maximum amplitude of most of the testing points in the scan was above 25 MHz when a 20 MHz transducer was used in detection, which means the frequency of peak amplitude of laser generated ultrasound has exceeded the response range of 20 MHz transducer and only part of the signal within the bandwidth of transducer was detected. Therefore, in order to increase the amplitude of the received signal, a transducer with higher frequency should be used. Nevertheless, the transducer with higher frequency tends to have a smaller element area. Considering the element area of 20 MHz transducer only has a diameter of 6 mm, which is too small for the detection of multigrain samples with a diameter of 20 mm, thus a 15 MHz transducer with element area diameter of 13 mm was applied for the measurements. A delay line was used to increase the contact area between sample and transducer. Although it has expanded the detection area of the sample the amplitudes around the edge of the sample are much lower than the centre signal due to extra attenuation of ultrasound. Ultrasonic couplant was applied between the sample, delay line and the transducer. In order to maintain sufficient amount of couplant for an overnight-long scan, two hollow rubber pads were fitted at both sides of the delay line with extra gel inside.

The energy distribution of the signal response of a complete scan within as-received TBC sample with single crystal substrate detected by 20 MHz transducer is shown in Figure 5.3 below. The energy distribution of the signal response is similar to a Gaussian distribution due to the signal attenuation differences among the test points where waves propagating longer distance from the edge of a sample lose more energy than those propagating shorter distance in the centre. This uneven signal distribution makes the detection of flaws inside of coating more difficult as a higher signal response at the centre could cover the actual low signal response due to the flaws, which means any delamination or crack cannot be observed visually in the energy distribution map or similarly in the amplitude map.

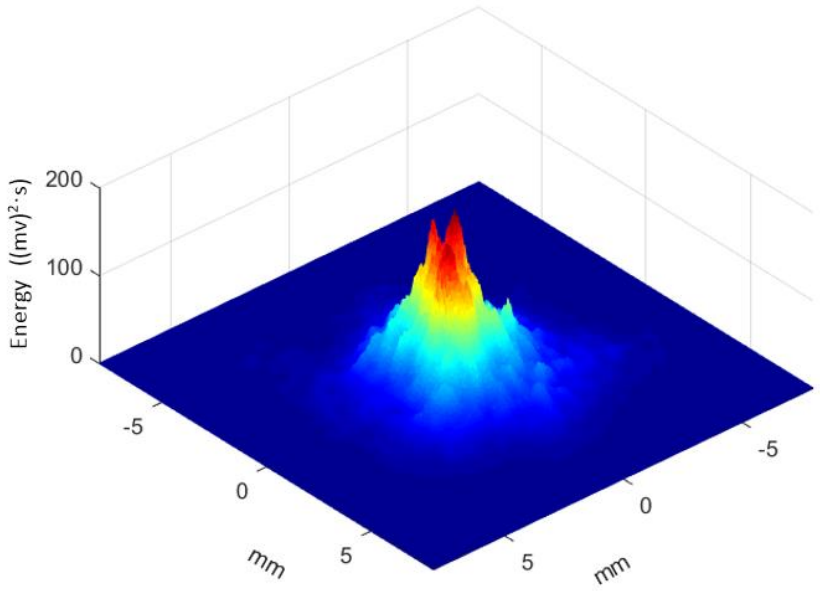


Figure 5.3 Energy distribution of the signal response of a complete scan within as-received TBC sample with single crystal substrate detected by 20 MHz transducer.

Furthermore, the difference in distance that the ultrasound wave propagates through leads to phase differences among the test points in a complete sample scan, as shown in Figure 5.4. The signal phases change periodically in a phase map at a relatively low frequency from the central of a sample to the edge. A random phase is shown in the map when the signal amplitude is lower than the noise level, which could due to the presence of flaws in the coating. In order to analysis the random phases caused by flaws the phase difference caused by sample geometry will be eliminated in a post signal analysis.

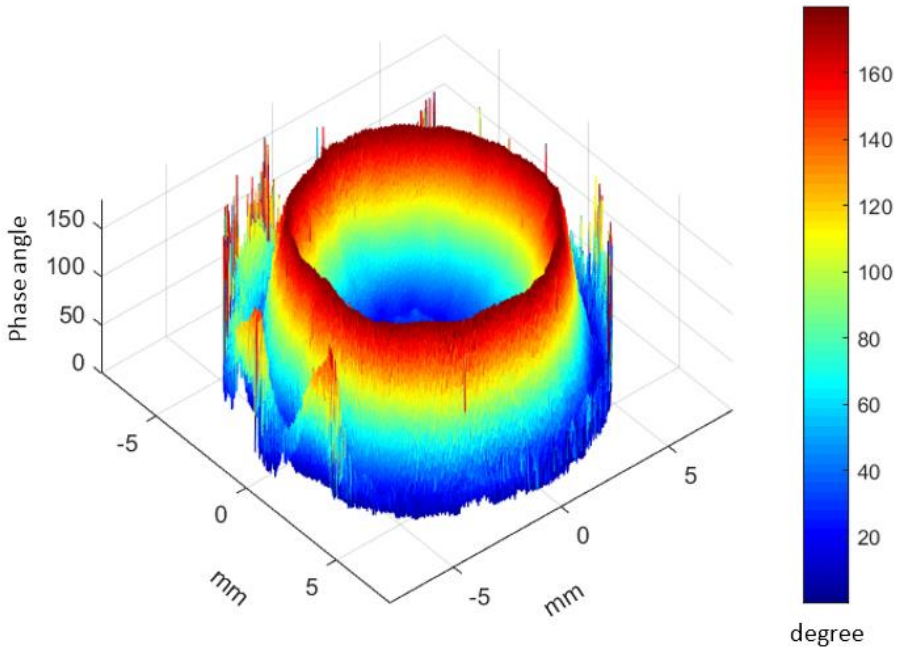


Figure 5.4 3D Phase map in the absolute value of a complete scan within as-received TBC sample with single crystal substrate

Data acquisition

The ultrasound bulk wave as an external stimulus vibrates the crystal element in the transducer which generates an electrical signal. The signal of each test point was amplified 100 times (40 dB) by an amplifier and captured using a digital oscilloscope. The first pulse of each ultrasound signal was captured with a sample rate of 400MHz and then averaged over a number of received signals (typically 256 for multigrain samples and 16 for single crystal samples) by the digital oscilloscope. Once the signal had been averaged, the entrire trace was sent to and recorded on a computer. Each measurement point (each trace) would take about half a second including the movement of the sample stage. Figure 5.5 shows a captured waveform of a single trace of a raw signal in time domain.

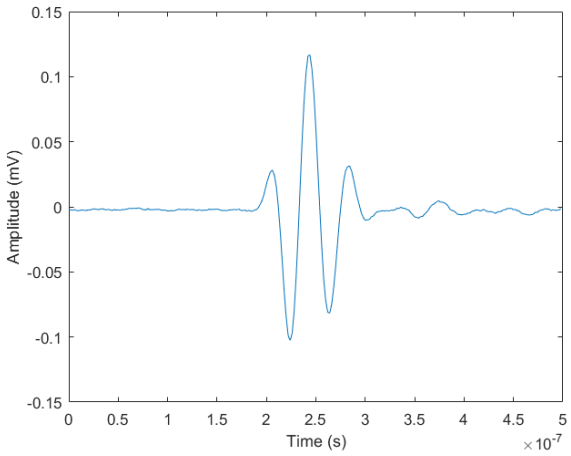


Figure 5.5 The first pulse of received ultrasound signal captured at the centre of an as-received TBC sample

5.1.4 Data analysis

Firstly, noise signal was captured while the laser beam has been blocked. The correct signal was therefore obtained using raw signal by subtracting the noise signal. In order to find out the amplitude of the signal at each frequency, the time domain signal, as shown in Figure 5.5, was converted to frequency domain by Fast Fourier Transform (FFT), and its absolute value was then obtained, which is shown below in Figure 5.6.

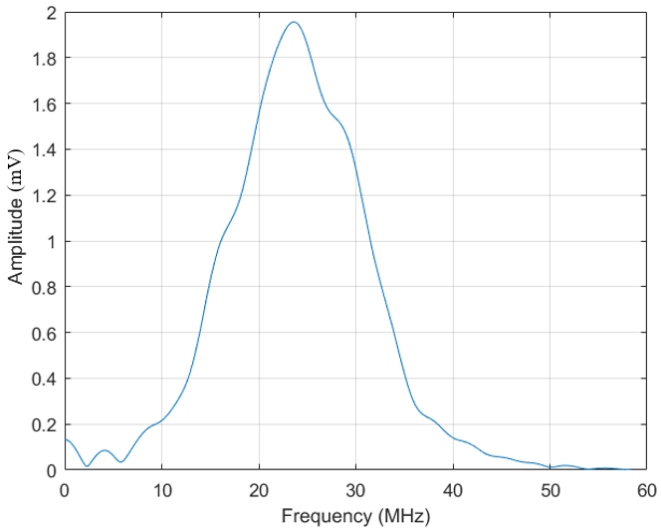


Figure 5.6 Signal after FFT in the frequency domain.

Amplitude map

The amplitude of the peak frequency value of each scanning spot was combined and reshaped to 501 × 501 points matrix. Then it was plotted onto an amplitude map which indicates the magnitude of ultrasound response across the entire sample. It is worth noting that some error points occur in the amplitude map, where the amplitude is much higher than adjacent values, which is possibly due to some unstable laser pulses or mistimed acquisition or both, as shown in Figure 5.7. The value difference between the error point and previous scanning point is normally greater than 0.1, the difference between non-error points, however, is less than 0.02. To reduce the calculation error, the error points were selected from the matrix of amplitude map and replaced by the value of the adjacent point at one row below using a MATLAB script. A more accurate estimate value can be obtained to replace an error point by averaging the surround

eight values of the error point, however, it is not necessary in this case. A noise filtered amplitude map as a comparison is shown in Figure 5.7.

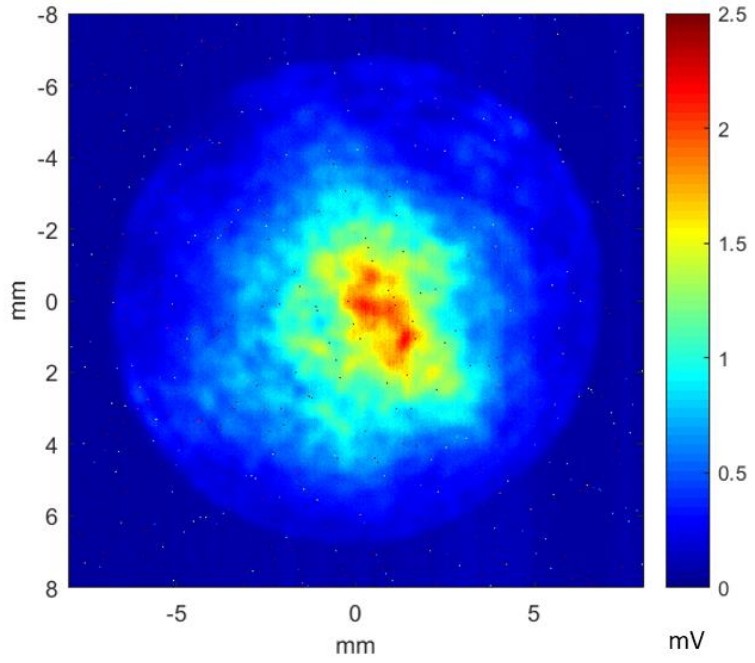


Figure 5.7 Laser error points in the maximum amplitude map of a complete scan within as-received SX TBC sample detected by 20 MHz transducer.

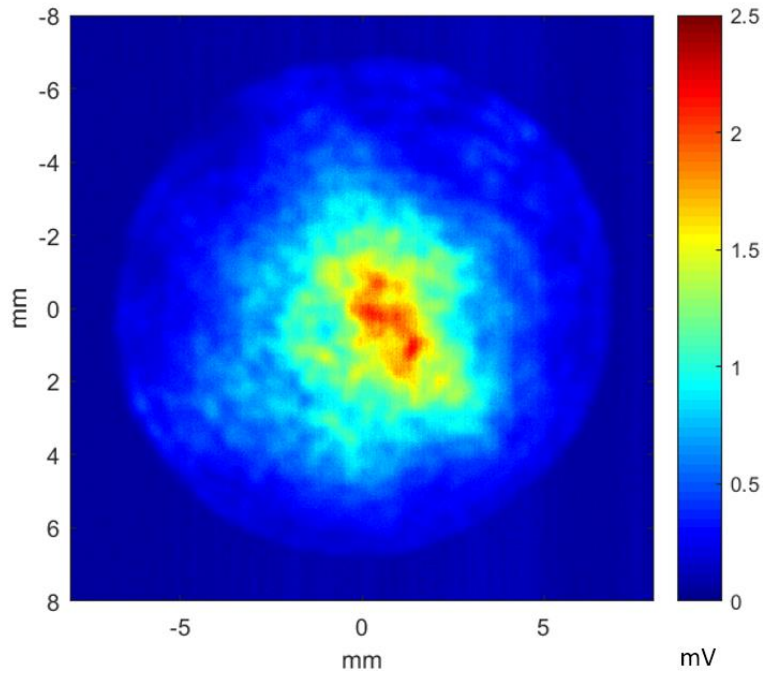


Figure 5.8 Noise filtered maximum amplitude map.

Amplitude map at 20 MHz was plotted using the same method as above, as shown in Figure 5.9. Sum of amplitudes at 20 MHz of each tested spot is regarded as one of the parameters to be compared between samples after different thermal cycles.

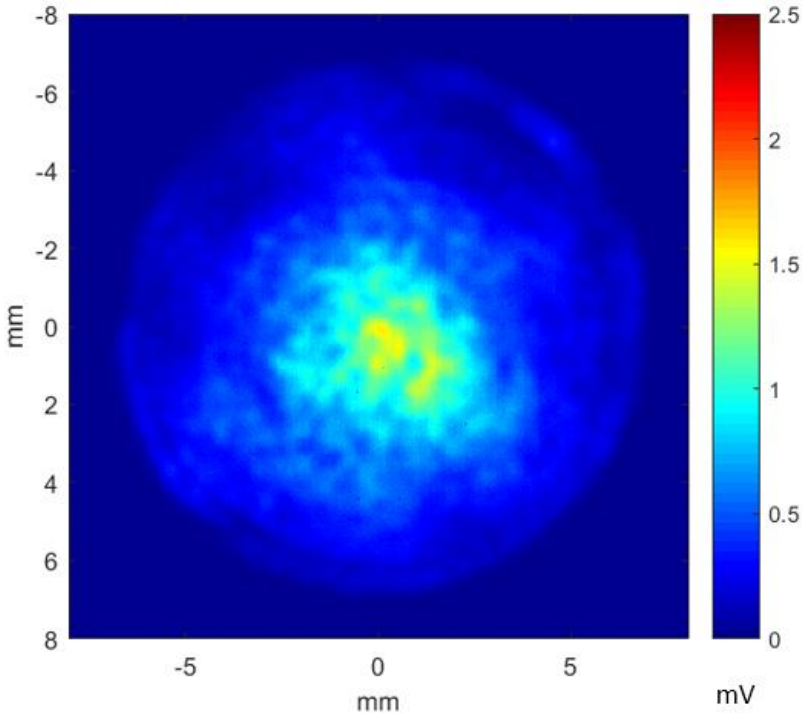


Figure 5.9 Amplitude map of 20 MHz of as-received SX TBC sample

Frequency map

In contrast, frequency map shows the frequency at the maximum amplitude of each spot. A scanned frequency map of a single crystal substrate sample is shown in Figure 5.10 below. The frequency changes were expected due to the defects present inside of the sample. Average frequency was calculated and compared among samples with different thermal cycles, which is shown in next sections.

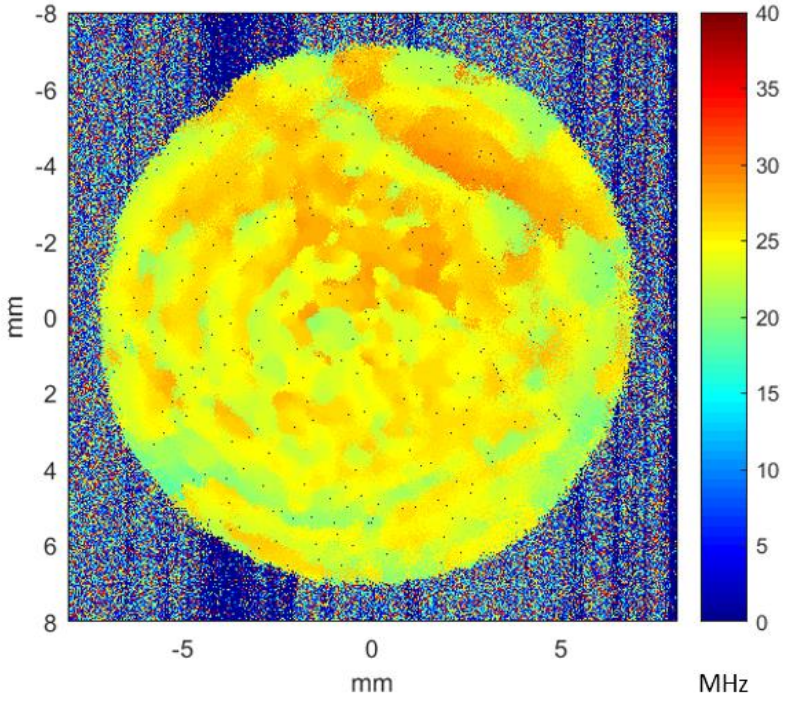


Figure 5.10 Frequency map of as- received SX TBC sample.

Energy map

Energy map is quite similar to amplitude maps, except it includes the magnitude of signal energy response across all frequencies. Signal energy of each scanning point was calculated following the Parseval's theorem by the sum up the squares of the amplitudes in all frequencies in the frequency domain. The total signal energy of a sample was calculated by summing up the energy of each spot. Signal energy map of as-sprayed SX sample was plotted by the same method as amplitude map, as shown in Figure 5.11.

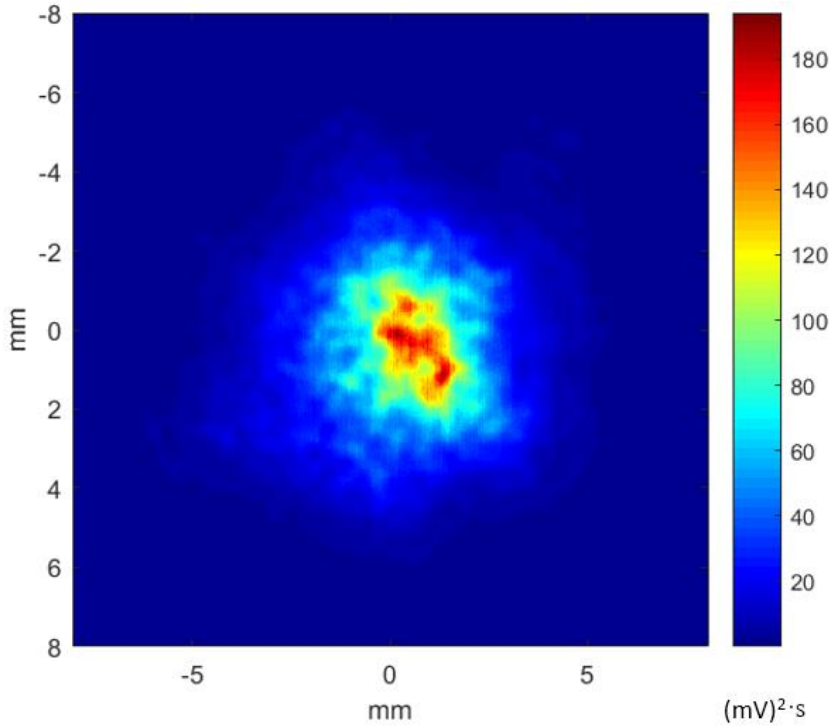


Figure 5.11 Signal energy map of as-received SX TBC sample.

Phase map

In order to plot a phase map at 20 MHz, the phase angle at each test point is determined and converted to an angle in degrees. The phase map shows the time difference of the signal received by the transducer, as shown in Figure 5.12. It normally has a large phase difference affected by the geometry of sample substrate and delay line, as mentioned previously. The area outside of the sample shows random phases as no ultrasound wave has been generated in that area. This can be used to indicate a potential damage of the sample after thermal cycling, which is shown in post data analysis.

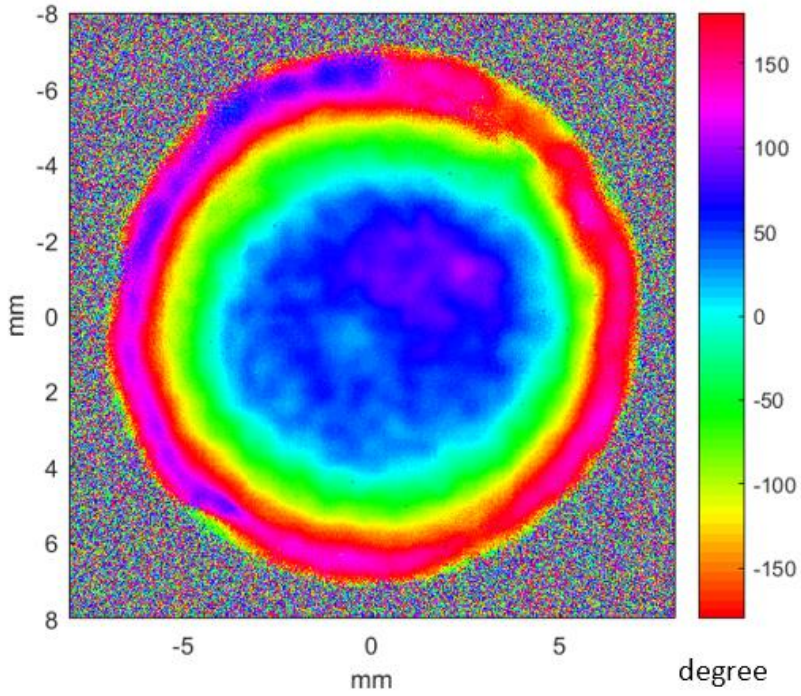


Figure 5.12 20 MHz phase map of as- received SX TBC sample.

As expected, after the thermal cycling, delamination occurred at the edge of the sample, which resulted in the occurrence of random phases around the edge. In order to quantify the area with random phases caused by delamination, the phases outside of the sample area are removed by a threshold. Considering the centre of scanning area is not right in the centre of the sample, therefore the centre of a sample was identified as the centre where the maximum energy received in the sample area out of the scanned square area using a MATLAB script. Then each row of absolute phase angles was

regarded as a signal with a maximum amplitude of 180 degrees, as shown in Figure 5.13a. Each signal was filtered by a Butterworth high-pass filter in MATLAB which eliminated the phase difference caused by geometries, as shown in Figure 5.13b. The MATLAB script for this part of analysis is shown in Appendix D.

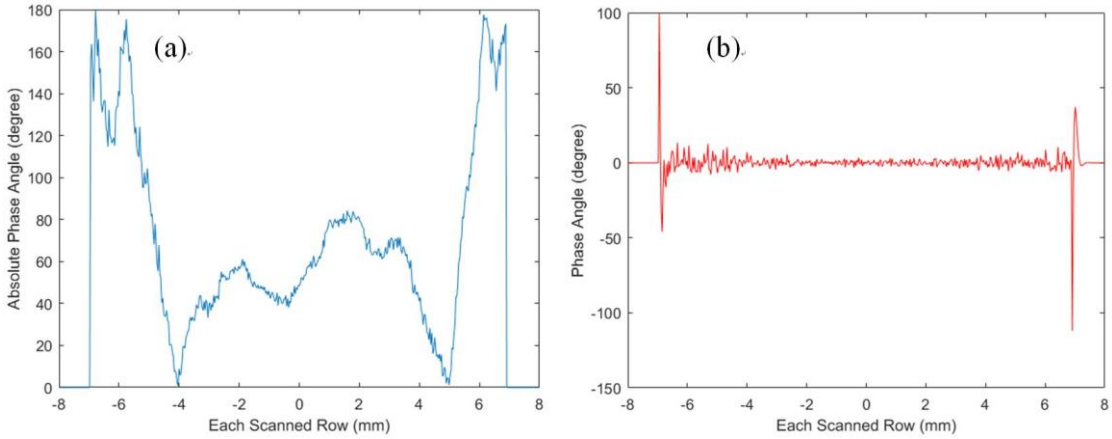


Figure 5.13 LPAS phase analysis (a) absolute phase angles in central row, (b) filtered phase angles by a high-pass filter.

A number of points that have a phase difference of adjacent points greater than 20 (10, 30) degrees were counted and marked as one of the random phase spots. This could be a result of either there has been no ultrasound generated or ultrasound wave could not propagate the sample at those points, which is then compared with samples after different thermal cycles and will be discussed in the following chapter. Below in Figure 5.14 are shown random phase spots in single crystal sample as-sprayed and sample after 60 cycles.

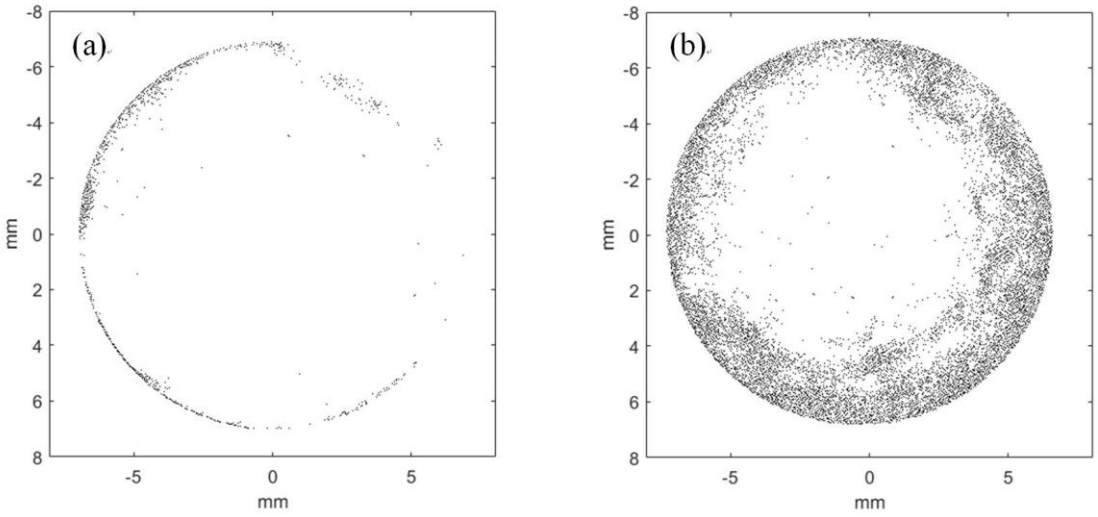


Figure 5.14 Random phase spots detected in TBC samples with signal crystal substrate, (a) as-sprayed sample and (b) sample after 60 thermal cycles.

There are two more variations on the method used to evaluate the phase condition. One is to calculate the standard deviation of the phase of each spot of the entire sample, which is analogous to high pass filtering. The higher the standard deviation value, the more random phases there are in the sample which also indicates the existence of more potential defects. The other method is to count the number of peaks in the waveform of each row of a phase map, as more peaks are expected in the sample after thermal cycles, due to the ramping of TGO layer.

5.1.5 Laser attenuation in YSZ ceramic coating

A primary test was conducted by pointing a laser beam at the surface of a piece of freestanding YSZ coating, which has shown that 532 nm green laser is able to pass through the top coat of thermal barrier coating. However, the most of laser light was reflected and scattered in all directions due to the rough surface of the top coat, and part of laser light was absorbed by the coating. Therefore, it was necessary to measure the laser attenuation using the different thicknesses of YSZ coating.

A set of freestanding YSZ ceramic coatings with various thicknesses was made for this test, see Table 3.5 for the details of sample information. The evaluation of laser attenuation in the YSZ ceramic coating was carried out by measuring the intensity of the laser at out-of-lens and behind of freestanding YSZ coating using a power meter. In order to evaluate the attenuation, the laser power Laser attenuations were calculated by Equation 5.1 as shown below.

$$\text{Attenuation}\ (-\text{dB}) = 10 \times \log_{10}\left(\frac{\text{Input intensity (W)}}{\text{Output intensity (W)}}\right) \tag{5.1}$$

Furthermore, the freestanding YSZ coating samples were also tested using the same LPAS system to eliminate the possibility that ultrasound was generated at the top coat layer.

It is worth noting that the sintering effect of the YSZ ceramic, caused by high temperature thermal oxidation, has reduced the porosity of the coating. Moreover, the size of the cracks inside of YSZ coating has grown due to the high temperature cycling. Both factors affect the laser attenuation of YSZ coating. Therefore, two sets of freestanding coating samples were made by detaching the top coat from two as-received TBC samples and two after 80 cycles, see Table B.3 of Appendix B. The laser attenuation in these samples were measured and compared, the result is shown in section 5.3.

5.1.6 Metallic bond coat testing using LPAS

In order to find out whether ultrasound was generated at the bond coat layer, a sample with bond coat only (sample A in the Table B.2 of Appendix B) was tested by the LPAS system. A square of 1.28 × 1.28 mm^2 of the centre of the sample was scanned with a step size of 64 μm after being exposed to thermal cyclic oxidation at 2, 5, 10, 20, 40 and 80 cycles respectively. The result of this experiment is shown in section 5.4. Furthermore, a set of reference samples was used for observating the surface mophology of TGO layer at different thermal oxidation cycles. The SEM images of the TGO surface will be discussed in later section 5.6.6.

5.2 LPAS results

The results of SX samples and MG samples taken by laser photoacoustic spectroscopy scan are presented in this chapter. Evaluation methods from a different aspect of the received signal are compared.

5.2.1 Single crystal substrate TBC samples

Amplitude map

Figure 5.15 shows the amplitude map at 20 MHz of sample J at 0, 20, 40 and 60 cycles respectively, acquired using LPAS scanning system. The scanning image size is 8 × 8 mm; the scanning step size (the pixel size) is 32 × 32 μm in each figure. The colour bar presents the amplitude from 0 to 2.

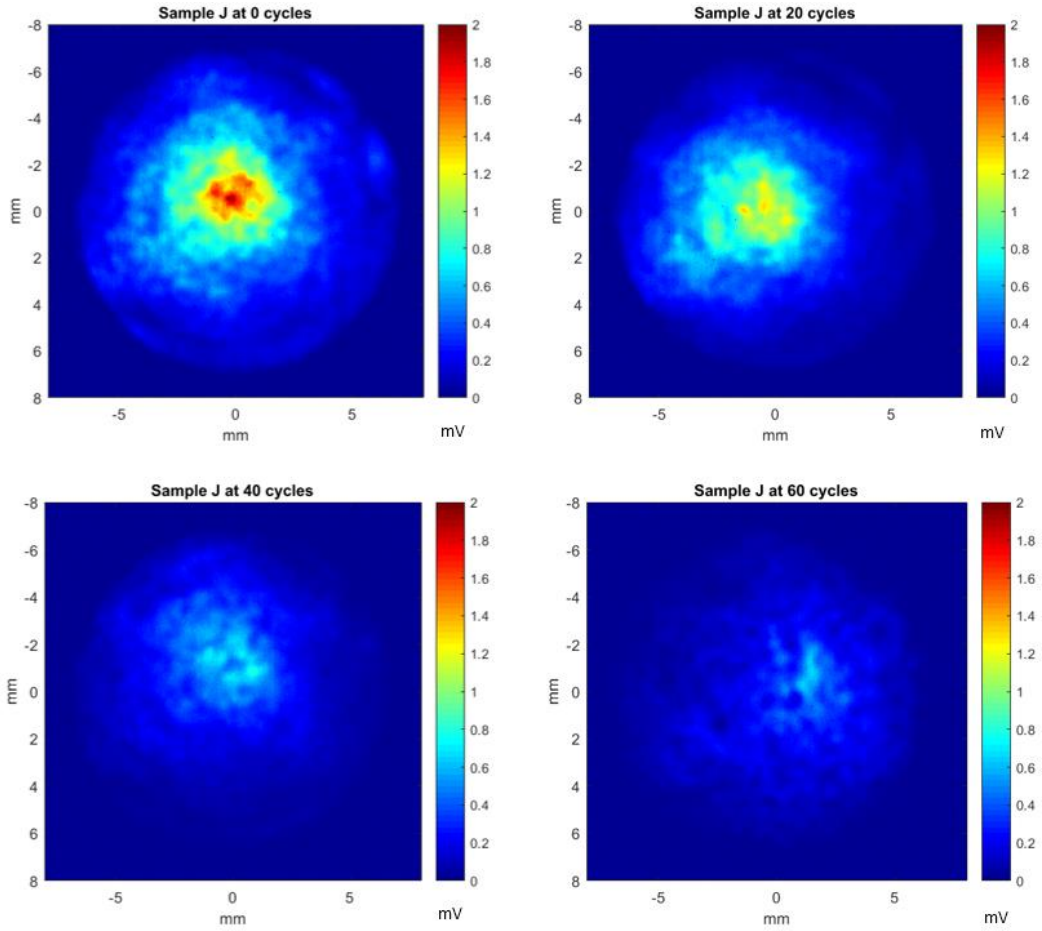


Figure 5.15 20 MHz amplitude maps of sample J at 0, 20, 40 and 60 thermal cycles

It is shown that the amplitude at each spot decreases with the increase in the number of thermal cycles. The uneven speckle in the map is caused by the variable thickness of the ceramic coating. The original evaluation purpose is ideally to find delamination or cracks inside the coatings directly from examining the amplitude map. Due to the laser spot size and the scattering of the laser beam by ceramic layer, it is not possible to accurately indicate the defects in the TGO layer. However, it can be evaluated by assessing the relation between amplitude, among other relevant factors, and thickness of TGO layer along with its defects. Therefore, the total amplitude at 20 MHz and total maximum amplitude of each sample at different thermal oxidation cycles are compared and plotted in Figure 5.16 and Figure 5.17 respectively.

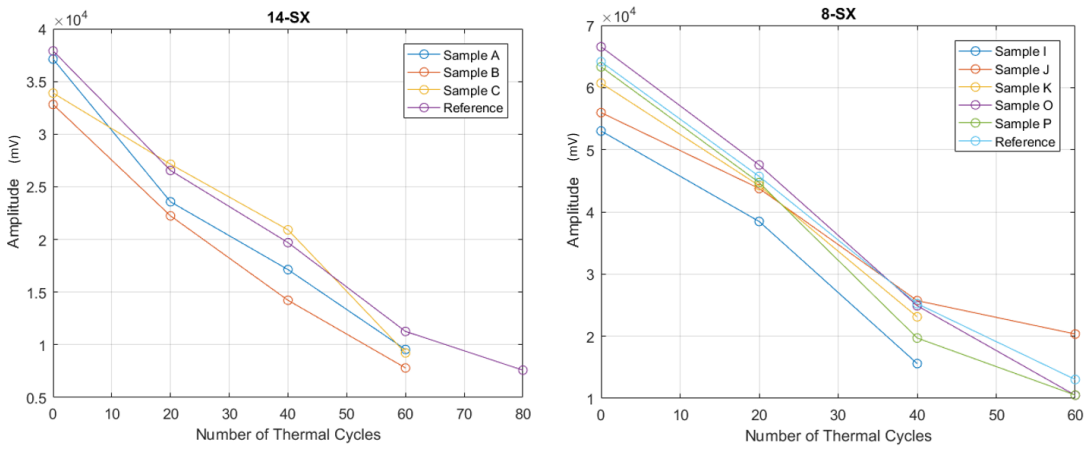


Figure 5.16 Total amplitudes at 20 MHz of SX samples in thermal cyclic oxidation.

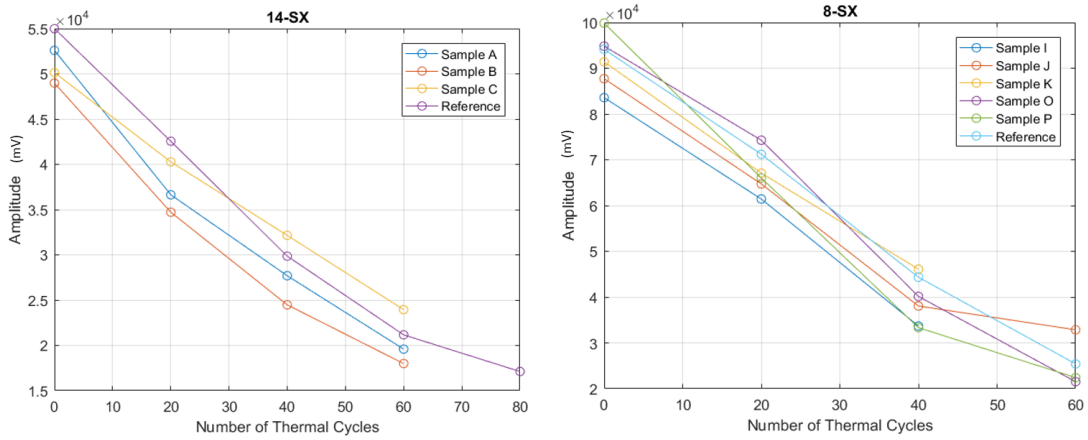


Figure 5.17 Total maximum amplitudes of SX samples in thermal cyclic oxidation.

It is shown that the maximum amplitude plot and amplitude at 20 MHz plot have different magnitude but the same tendency, which decreases with increasing the number of thermal cycles. Due to the extra attenuation by the thicker YSZ top coat, 14-SX samples show lower amplitudes at every thermal cycle than 8-SX samples.

Mean frequency

Figure 5.18 shows the mean frequencies of each sample at a different number of thermal oxidation cycles. Different to previous expectations, there is no obvious indication that higher frequency appears after more thermal oxidation cycles as the data points are distributed randomly.

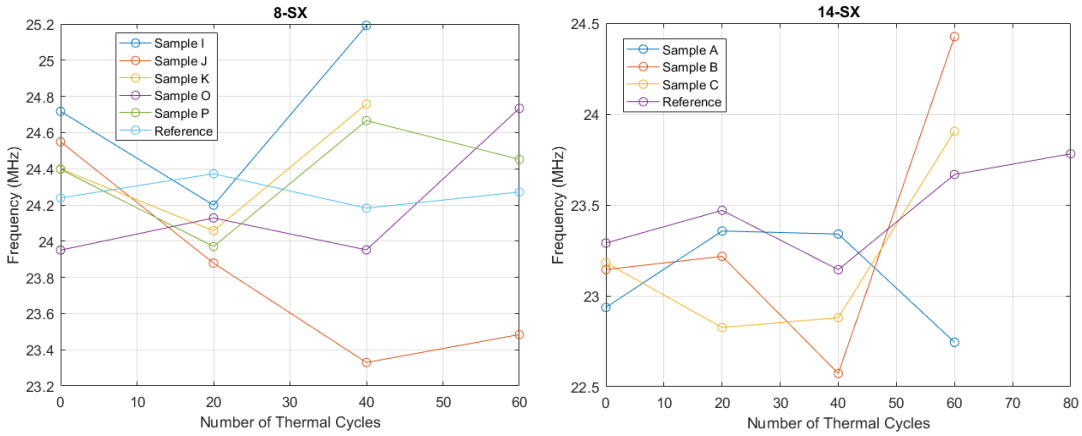


Figure 5.18 Mean frequencies of ultrasound passing through SX samples.

Signal energy

Figure 5.19 shows the received total signal energy of ultrasound that has passed through each sample at a different number of thermal oxidation cycles. The plot of 14-SX samples shows a parabolic tendency which could relate to parabolic oxidation behaviour of thermal barrier coatings, as shown in Figure 5.20.

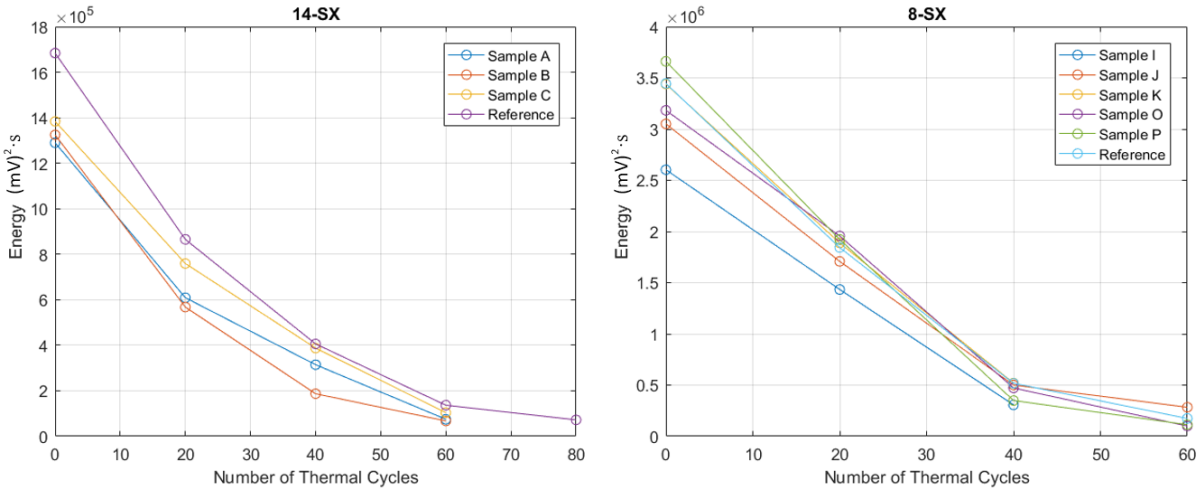


Figure 5.19 Total signal energy received of SX samples in thermal cyclic oxidation.

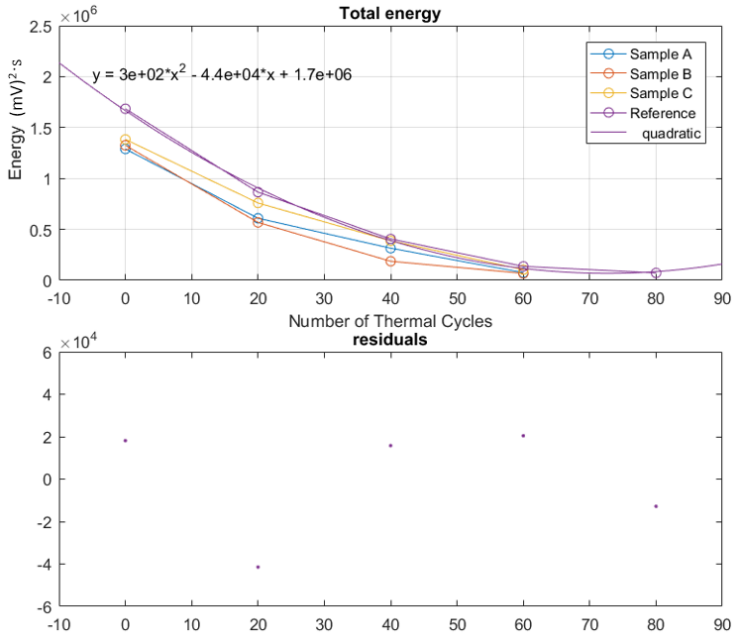


Figure 5.20 Parabolic tendency of total signal energy received of 14-SX samples in thermal cyclic oxidation.

Phase map analysis

Figure 5.21 shows the percentage of points that have phase angle difference greater than 10, 20 and 30 degrees respectively at different cycles of thermal cyclic oxidation. As expected, it has shown that the percentage increases as more random phases occurred at the edge of the sample after thermal cyclic oxidation. However, there is no obvious tendency change is shown in the plots despite the increase of threshold from 10 degrees to 30 degrees.

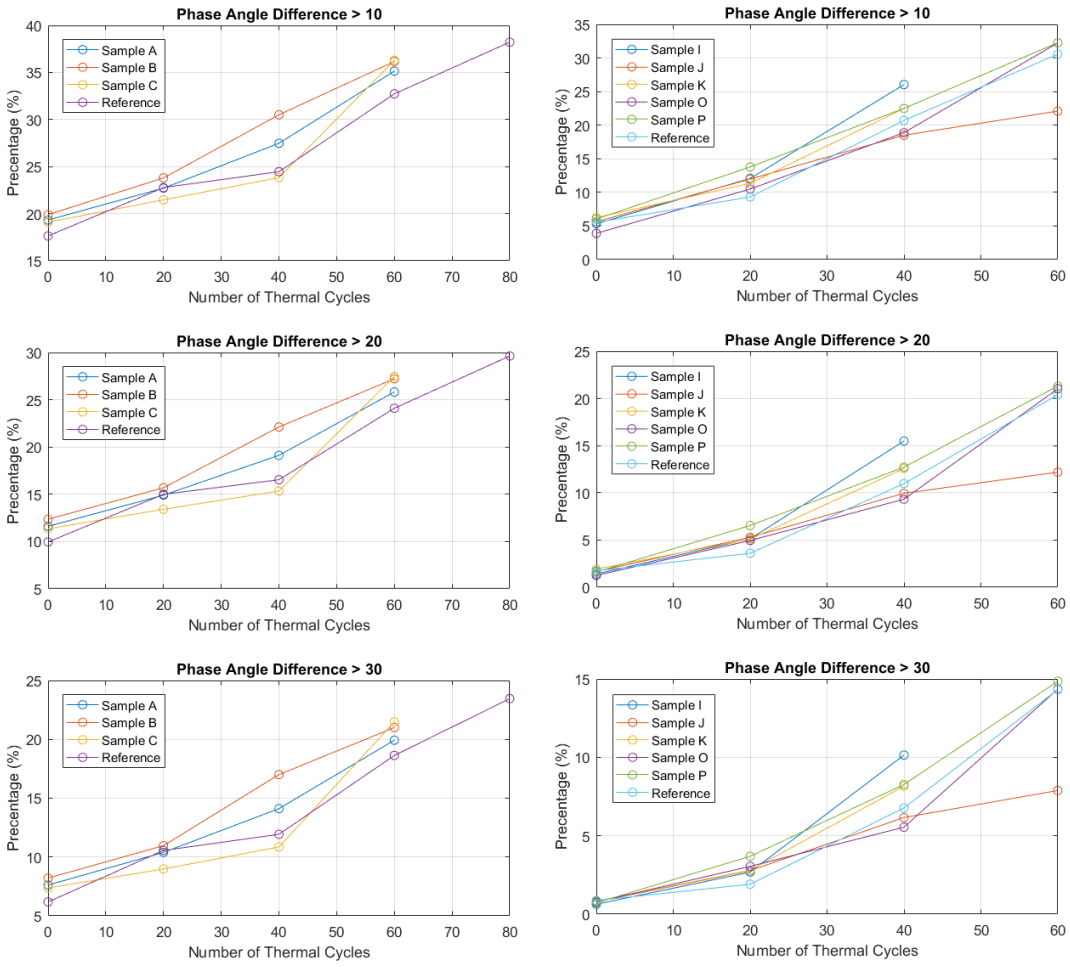


Figure 5.21 Percentage of phase angle difference in the phase map of SX samples in thermal cyclic oxidation.

The standard deviation of phase angles of each sample at different cycles of thermal cyclic oxidation is plotted in Figure 5.22, which shows great consistency with phase angle difference plots.

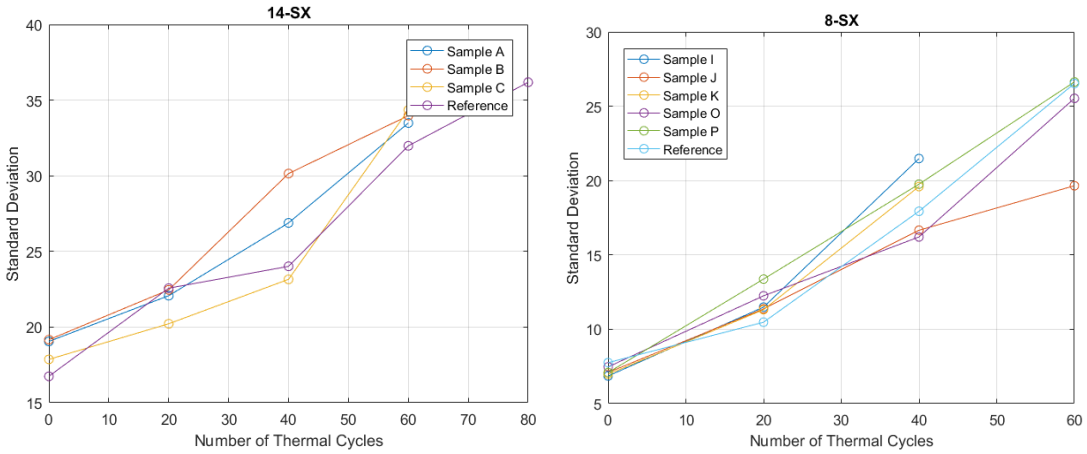


Figure 5.22 Standard deviation of phase angle in the phase map of SX samples in thermal cyclic oxidation.

The number of peaks in phase map of SX samples at different thermal oxidation cycles is plotted in Figure 5.23. It is shown that there is no obvious tendency between the number of peaks and the number of thermal cycles.

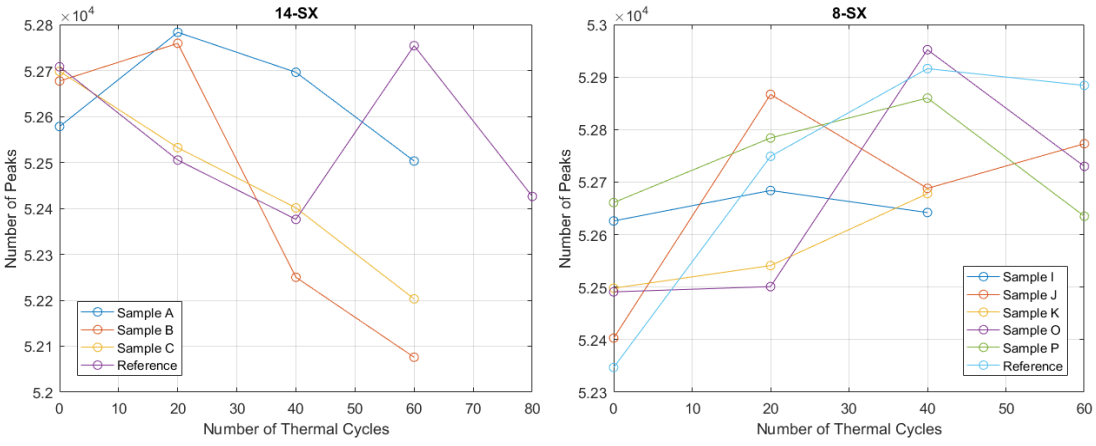


Figure 5.23 Number of peaks in the phase map of SX samples in thermal cyclic oxidation.

5.2.2 Multigrain substrate TBC samples

The LPAS results of MG TBC sample 1 to 12 at 0, 5, 10, 20, 40 and 80 thermal cycles presented respectively in this section, are acquired using LPAS system with a 15 MHz transducer. The scanning image size is 8 × 8 mm; the scanning step size (the pixel size) is 80 × 80 μm.

Figure 5.24 shows 15 MHz amplitude maps of sample 1 from as-received to 80 thermal cycles. Similar to single crystal substrate sample, it is shown that the amplitude of each spot decreases with the increase in the number of thermal cycles. Different to SX samples each MG sample shows a unique pattern in the amplitude map due to different grain orientation in the substrate. The total amplitudes at 15 MHz of each MG sample at different thermal oxidation cycles are compared and plotted in Figure 5.25.

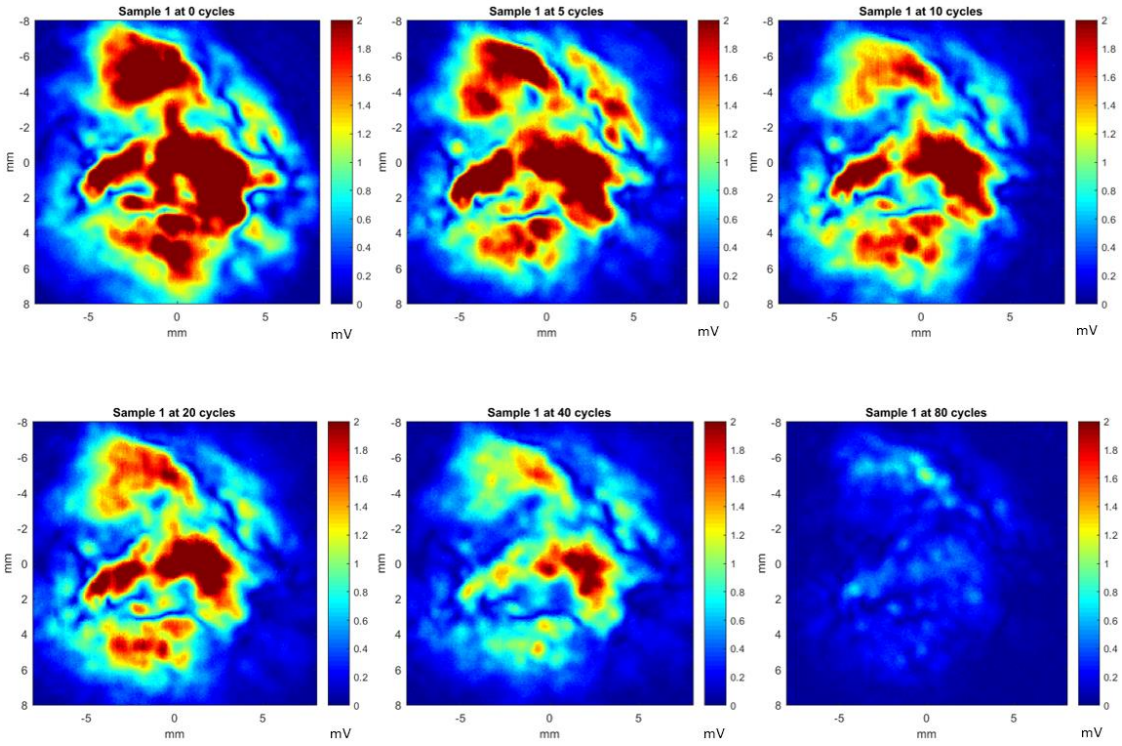


Figure 5.24 Amplitude maps at 15 MHz of sample 1 at 0, 5, 10, 20, 40 and 80 thermal cycles

Amplitude map analysis

Total amplitudes at 15 MHz of each MG sample at different thermal oxidation cycles are compared and plotted in Figure 5.25 below. It is shown that the total amplitude decreases with the increasing number of thermal cycles, which might be due to either the increased thickness of TGO layer or presence of delamination inside the coating. It is worth noting that amplitude plot has shown data segregation between samples with two types of grain, where sample 1, 2, 3, 5, 7, 9, 11 show higher total amplitude than the rest of the samples at same thermal oxidation condition, which will be discussed in detail later in section 5.6.1.

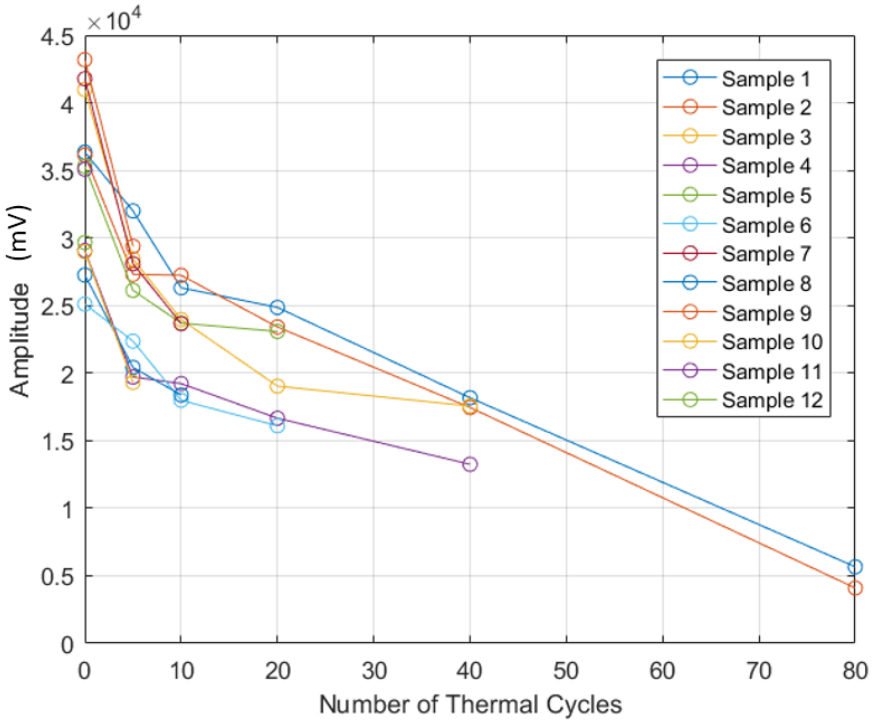


Figure 5.25 Total amplitudes of MG samples at 15 MHz in thermal cyclic oxidation.

Signal energy

Total signal energy received during the scans of MG samples at different thermal oxidation cycles are compared and plotted in Figure 5.26 below. It is shown that signal energy decreases with increasing oxidation time. Similar to the amplitude plot, the signal energy plot has shown data segregation between samples with two types of grain.

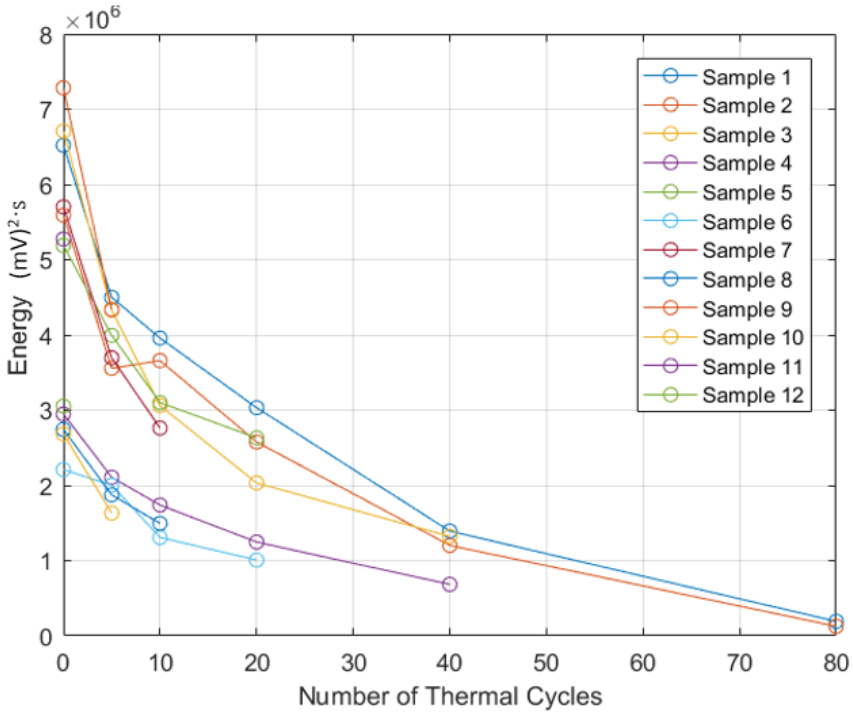


Figure 5.26 Total energy received during the scan of MG samples in thermal cyclic oxidation.

Phase map analysis

Figure 5.27 shows the percentage of points that have phase angle difference greater than 20 degrees in the phase map of each sample at different cycles of thermal cyclic oxidation. It is shown that the percentage varies mainly between 2% and 6% without a clear relevance of thermal oxidation of TBC samples. However, sample 1 and 2 after 80 thermal cycles clearly show an increase in the percentage of points that have phase angle difference greater than 20 degrees in the phase map, which can be considered as an indication when MG TBC sample is about to failure.

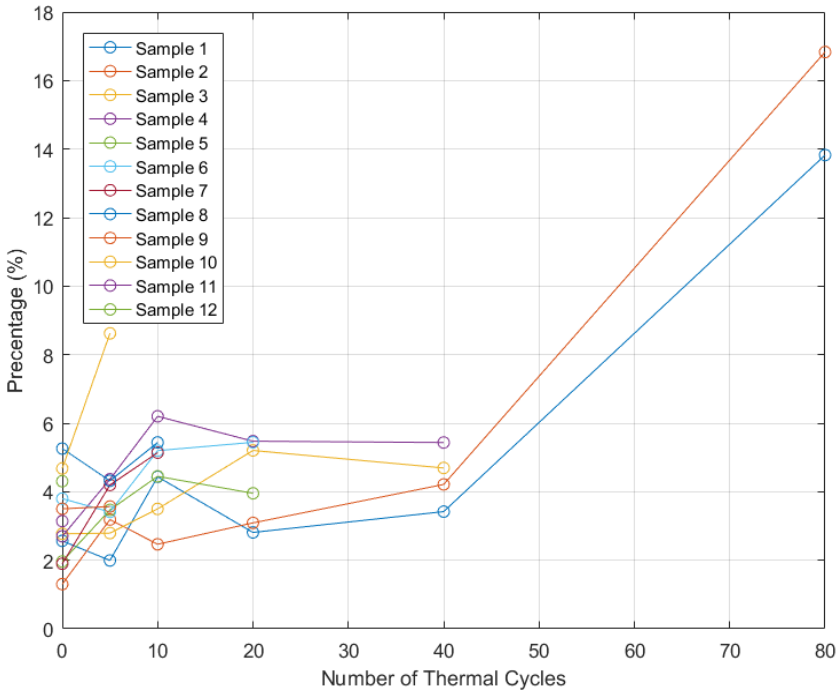


Figure 5.27 Percentages of phase angle difference in the phase map of MG samples in thermal cyclic oxidation.

The standard deviations of phase angles in the phase map of all MG samples at different cycles of thermal cyclic oxidation are shown in Figure 5.28.

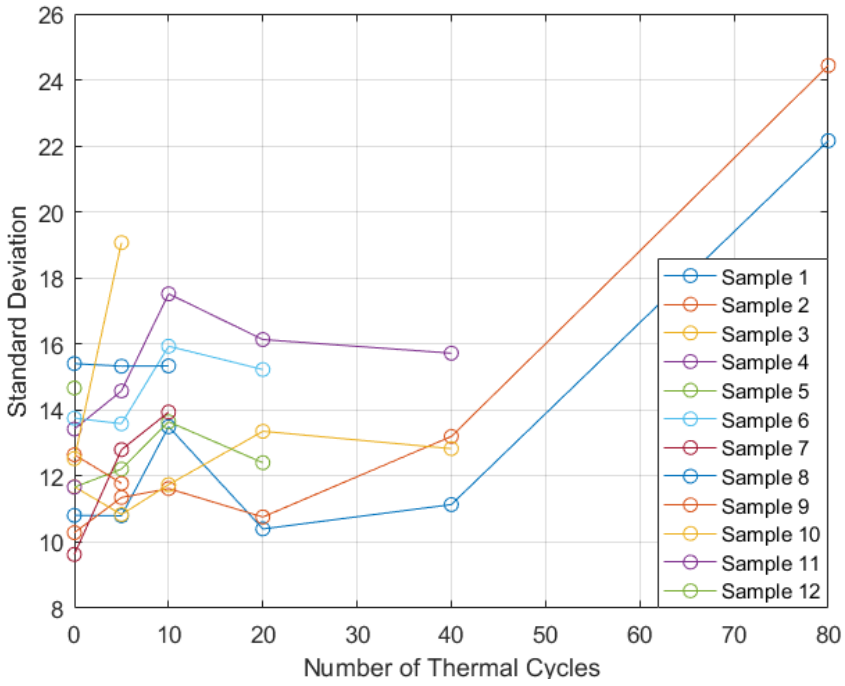


Figure 5.28 Standard deviation of phase angle in the phase map of MG samples in thermal cyclic oxidation.

It is shown that the standard deviation of phase angle at a lower number of thermal cycles has inaccurate data which is not in accord with oxidation behaviour in cyclic thermal oxidation. It is due to the scanning step size of MG samples as it is 2.5 times larger than SX samples, which reduces the scanning resolution. Also, the number of scanned spots has decreased which subsequently reduced the accuracy of the data analysis.

In contrast, reducing the number of points in each scan has increased the percentage of peaks that were caused by random phase angles in the phase map. Different to the results of SX samples, it is shown that the number of peaks increased with increasing number of thermal cycles. The number of peaks in the phase map of all MG samples at different cycles of thermal cyclic oxidation is shown in Figure 5.29.

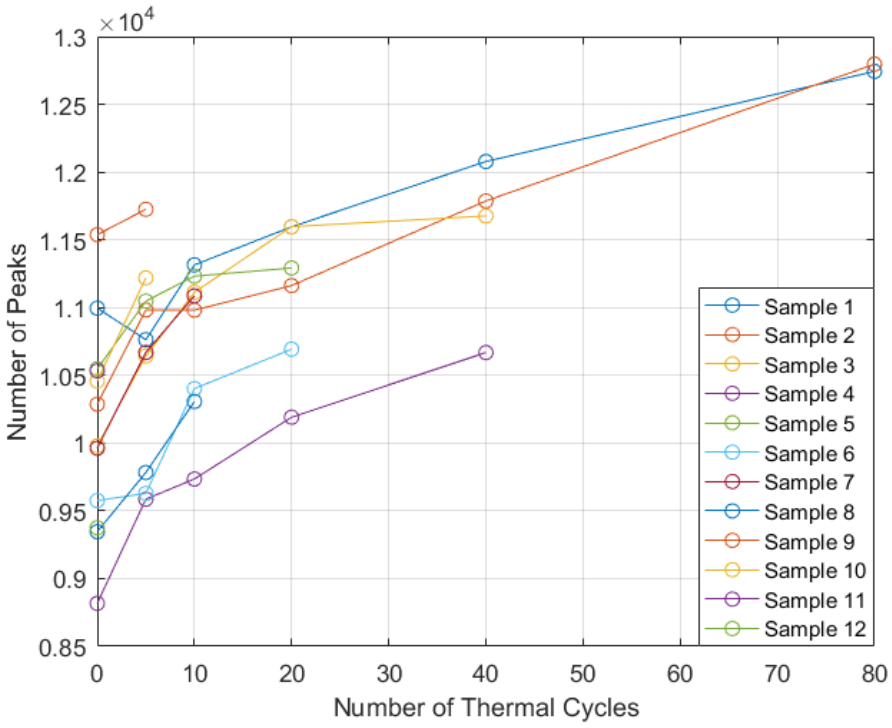


Figure 5.29 Number of peaks in the phase map of MG samples in thermal cyclic oxidation.

5.2.3 Summary of LPAS results

LPAS results of SX samples and MG samples were presented in this chapter. Examples of amplitude maps of each type of sample from as-received condition to different stage of thermal oxidation were shown. A relationship was found between the amplitude levels and the number of thermal cycles, illustrating that the amplitude decreases with an increasing number of thermal cycles, which is clearly shown in both examples. A difference between the amplitude maps was found between SX samples and MG sample, the former shows a Gaussian distribution in the amplitude map due to the signal attenuation differences among the test points, while the latter shows a unique pattern in the amplitude map due to different grain orientation in the substrate. In addition, the rough surface and uneven thickness of YSZ layer of TBC sample also lead to uneven signal distribution. In conclusion, the uneven signal distribution causes the original evaluation purpose to detect flaws inside of coating as visually

unachievable. Therefore, the thermal oxidation of TBC samples was evaluated by comparing the total value of their amplitude maps. As a result, it is shown that the total amplitude decreases with the increasing number of thermal cycles, which might be due to either the increased thickness of TGO layer or presence of delamination inside the coating. Data segregation between samples with two types of multigrain samples was noted, where sample 1, 2, 3, 5, 7, 9, 11 show higher total amplitude than the rest of samples at same thermal oxidation condition.

Further analysis on signal energy map revealed that energy of received signal decreases with an increase in oxidation time as a parabolic function in energy-thermal oxidation plot which could relate to parabolic oxidation behaviour of thermal barrier coatings.

The mean frequencies of each sample at a different number of thermal oxidation cycles were plotted. Different to previous expectations, there is no obvious indication that higher frequency appears after more thermal oxidation cycles as the data points are distributed randomly.

In the phase map analysis, there are two differentiated results between SX samples and MG samples due to the scanning resolution. The phase difference percentage and phase standard deviation of SX samples with higher scanning resolution (smaller scanning step size) both increase with increasing oxidation time. While the same analyses were not working for MG sample at lower thermal oxidation stage and can only be utilised as an indication when MG TBC sample is about to fail. On the other hand, the number of peaks in the phase map analysis of MG samples has shown a relationship that the number of peaks increases with increasing of thermal oxidation time, while this method for SX samples is invalid.

In Chapter 5.6, LPAS results will be further analysed with other relevant factors and thickness of TGO layer along with its defects.

5.3 Laser attenuation in YSZ ceramic coating

The evaluation of laser attenuation in YSZ ceramic coatings was carried out by measuring the intensity of the laser before and after penetrating freestanding coatings, see Chapter 5.1.3. A set of freestanding air plasma sprayed YSZ ceramic coatings with various thicknesses was made for this test, see Table 3.5 for the details of sample information. Figure 5.30 shows the laser attenuation in the freestanding YSZ coatings with the number of passes of 8, 16, 32, 64 and 128.

The freestanding samples have also been tested by the same LPAS system. It is shown that there was no ultrasound signal received during the scan, which proved that the ultrasound signal received at the substrate of TBC sample is not generated in YSZ layer.

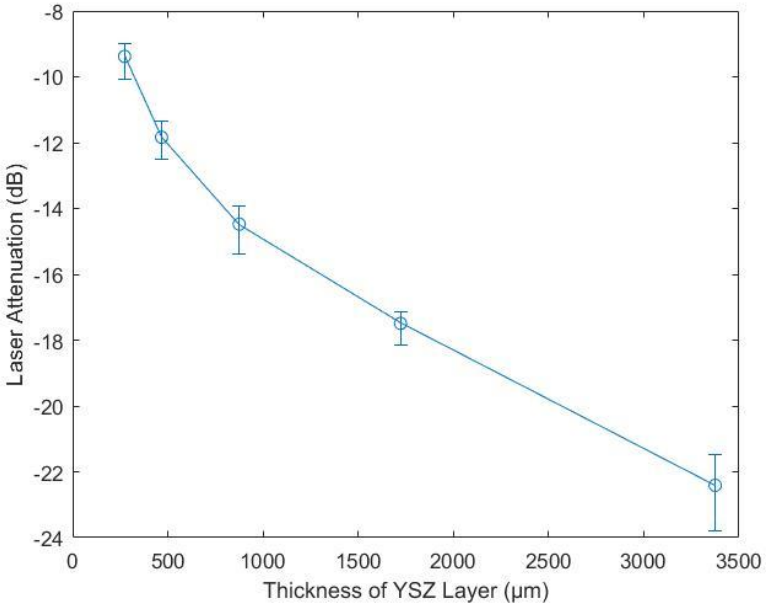


Figure 5.30 Laser attenuation in YSZ ceramic layer with various thicknesses

The laser attenuation of as-sprayed samples and samples after 80 thermal cycles is compared, as shown in Figure 5.31. Upon observation of the microstructure of the coatings using SEM, it is shown that the laser attenuation of YSZ coating after 80 thermal cycles have increased around 3.6% due to the growing size of cracks and the

increasing number of the cracks which formed inside of YSZ layer during the thermal cycling.

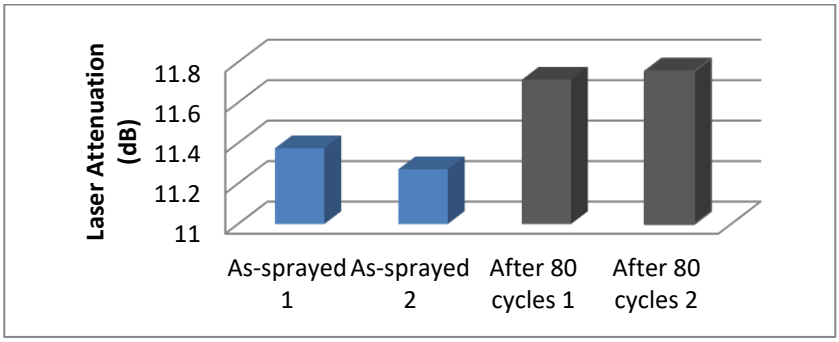


Figure 5.31 The laser attenuation in as-sprayed samples and samples after 80 thermal cycles

5.4 Amplitude attenuation in metallic bond coat

The experimental result of the amplitude attenuation in the metallic bond coat is shown in this section. The total amplitudes of the ultrasound signal at 20 MHz of a bond coat only sample after 2, 5, 10, 20, 40 and 80 thermal cycles are shown in Figure 5.32.

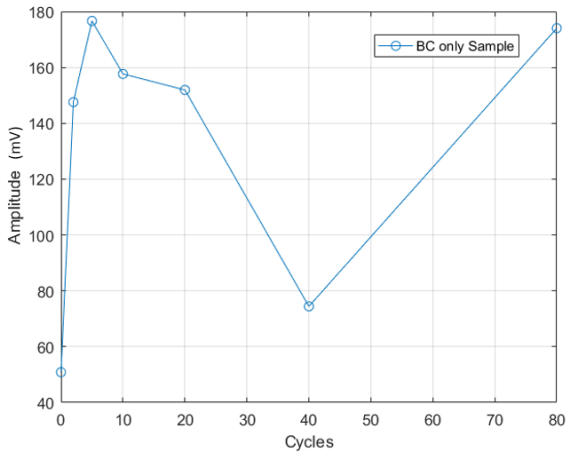


Figure 5.32 Total amplitudes of ultrasound signal at 20 MHz of bond coat only sample in thermal cyclic oxidation.

It is shown that the total amplitude of ultrasound signal has increased dramatically after the first two thermal cycles, while TGO layer was formed due to high temperature oxidation. This indicates that the formation of TGO layer has contributed to the ultrasound generation. However, it is shown that the amplitude starts decreasing after five thermal cycles, which is due to the increase in ultrasound attenuation caused by an increasing thickness of TGO layer. At 80 cycles, the amplitude has increased again which is probably due to the spallation of TGO layer. The surface morphology of TGO layer at different thermal oxidation cycles was observed under SEM, which will be discussed in the following section 5.6.6.

5.5 Oxidation behaviours of TBCs samples

As mentioned in the previous result section, both signal amplitude and signal energy decrease with the increasing number of thermal cycles, which might be due to either the increased thickness of TGO layer or presence of delamination inside the coating. In order to explain the findings in laser photoacoustic spectroscopy measurements and correlate the LPAS results with the cyclic oxidation behaviour of TBC samples, all TBC samples after scheduled laser photoacoustic spectroscopy measurements (See Table 5.2 for SX samples and Table 5.3 for MG samples) were observed and measured using SEM.

For demonstration purpose, the microstructures of fabricated multigrain TBC samples after various thermal oxidation cycles at 1150 °C are shown in Figure 5.33. The thickness of TGO layer is increasing with an increased oxidation time which is observed. Globular pores, interlamellar pores and pull-out pores inside of YSZ ceramic layer are indicated in Figure 5.33a. Pull-out pores were formed during the sample preparations which should not be taken into account in porosity measurement of YSZ layer. Spinel was found at the interface between the ceramic layer and TGO layer crossing the TBC samples. The β phase and γ phase in NiCoCrAlY bond coat are indicated in Figure 5.33b. The compositions of β phase and γ phase in NiCoCrAlY bond coat tested by EDX are shown in Table 5.4. Initial cracks are observed in TGO pegs. Isolated TGO particles are found in bond coat, as shown in Figure 5.33c. Cracks and spallation at bond coat side of TGO are observed after 20 thermal cycles. Larger cracks are also found in the YSZ ceramic layer after 80 thermal cycles.

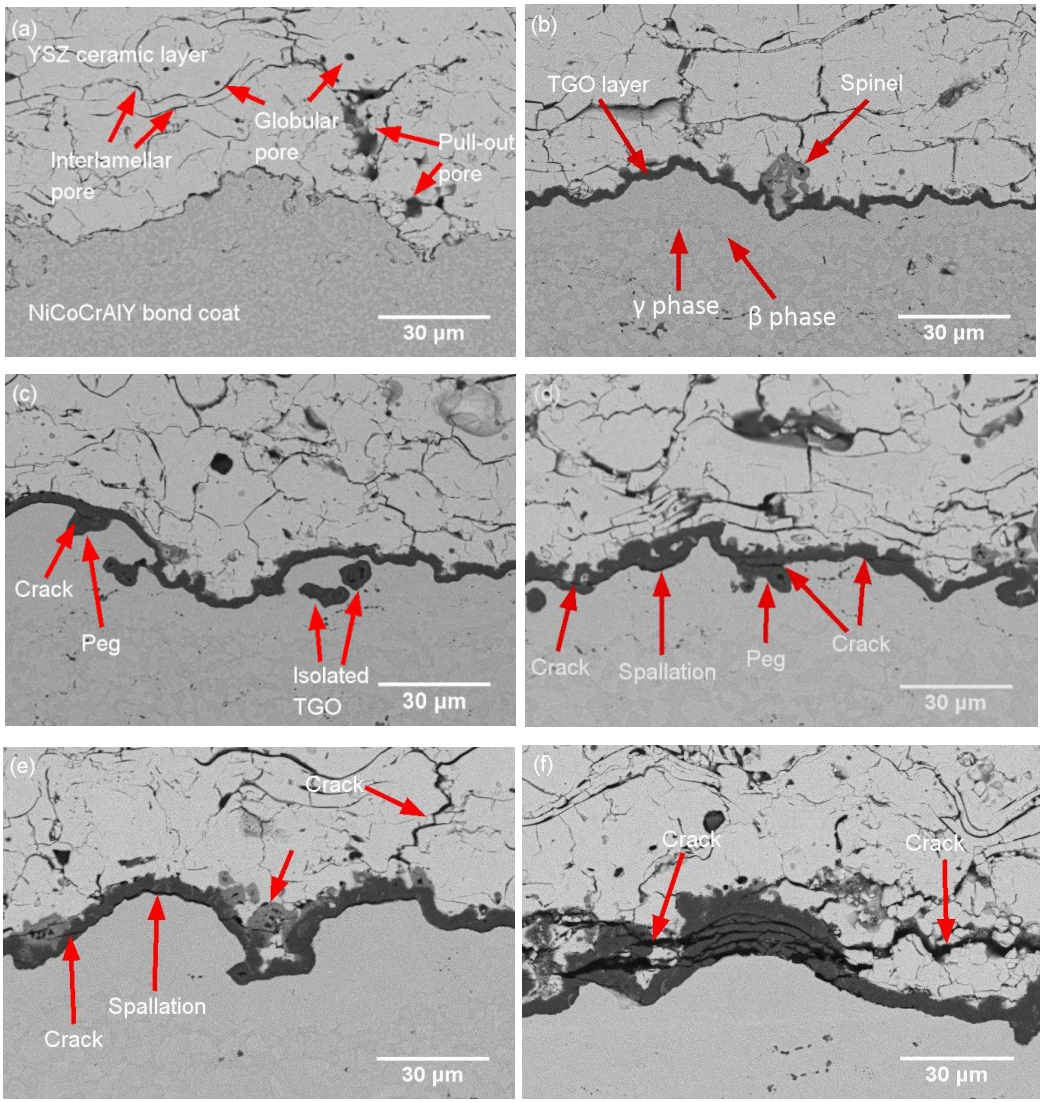


Figure 5.33 Microstructure evolutions of air plasma sprayed YSZ coating with NiCoCrAlY bond coat in thermal cyclic oxidation. (a) As-sprayed, (b) 5 cycles, (c) 10 cycles, (d) 20 cycles, (e) 40 cycles, (f) 80 cycles.

Table 5.4 EDX result of β phase and γ phase in NiCoCrAlY bond coat

Element (wt.%)	Al	Cr	Co	Ni
β Phase	17.99	7.43	12.12	62.36
γ Phase	6.81	17.94	20.81	50.44

The thickness of the TGO layer in the BSE image was measured by image analysis (described in chapter 3.5.5). The results of SX and MG samples were summarised and plotted against the number of thermal cycles, as shown in Figure 5.34. In single crystal substrate samples, 8-SX samples have faster TGO growth rate than 14-SX sample due to its thinner YSZ coating. As a result, 8-SX samples have higher TGO thickness than 14-SX samples at each cycle. On the contrary, MG samples have a steady consistency of the TGO thickness and clearly show parabolic oxidation behaviour.

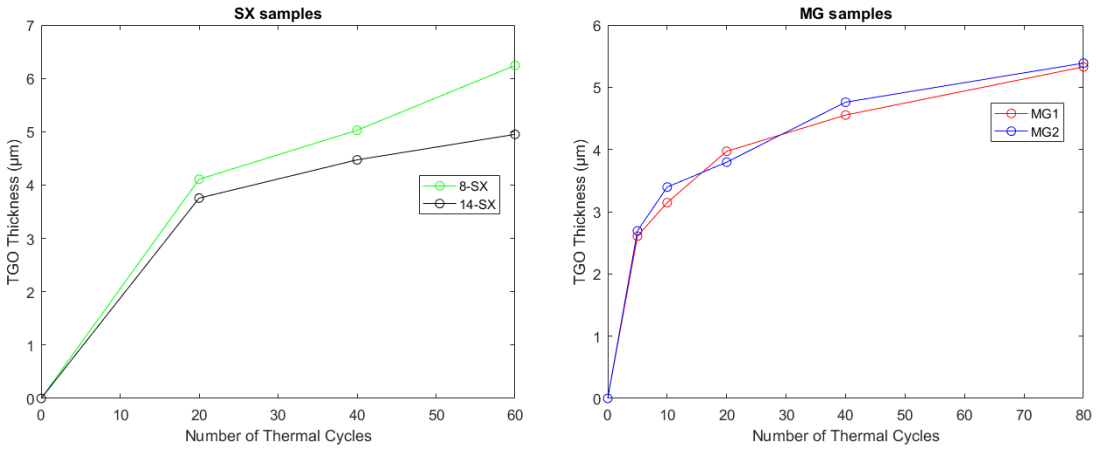


Figure 5.34 The thickness of TGO layer within SX samples and MG samples as a function of thermal exposure cycles

5.6 Discussion

5.6.1 Substrate grain orientation of MG samples

According to the results of MG2 samples, sample 3, 5, 7, 9 and 11 showed lower amplitudes and received less signal energy than the rest of the samples at the same number of thermal cycles. This is due to the different grain orientation of substrate of samples. The samples that have equiaxed grains in the substrate responded with higher amplitude and received more energy, such as sample 1 shown in Figure 5.22. An example of the sample which has columnar grains, for instance, sample 4, is shown in Figure 5.35.

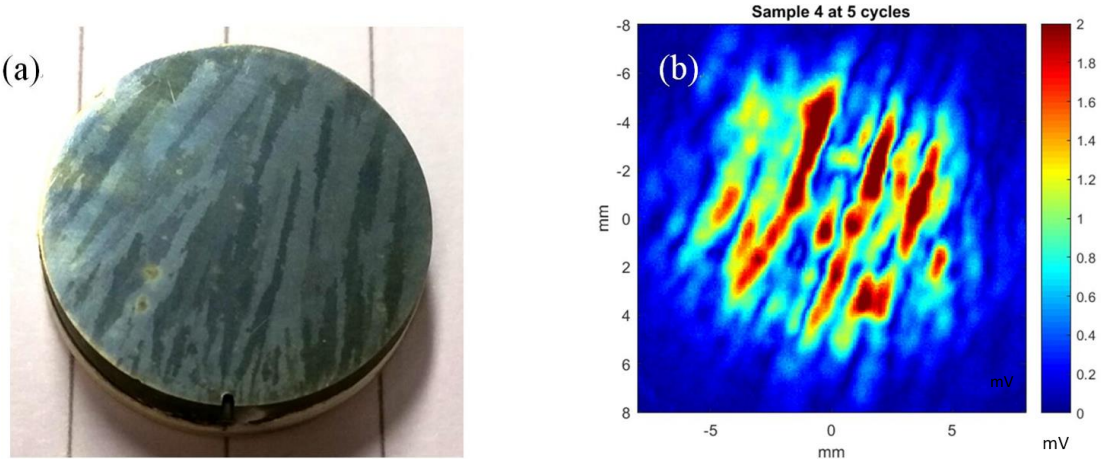


Figure 5.35 (a) Columnar grains are shown at the bottom of sample 4 after polishing oxidised layer. (b) The amplitude map of sample 4 after five thermal oxidation cycles.

As described previously in the sample preparation section, the Nickel superalloy substrates were cut from a cylinder ingot. Due to the temperature gradient during its solidification, there are three types of grains with different orientations which were crystallised inside of ingot. The temperature of melted metal dropped dramatically on the inner surface of the mould which formed small grains in the quench zone. The metal was then cooled from outside to the centre of the mould which led to a columnar crystallisation. At the centre of mould, the temperature gradient began to flatten, the solid phase thermal diffusivity was relatively lower, which resulted in the formation

of equiaxed grains. Figure 5.36 illustrates the crystallisations inside of Nickel superalloy ingot. Therefore, substrate material that has been cut from central of ingot has equiaxed grains whereas if cut from the outer layer it has columnar grains. The substrate that contains columnar grains inside also has more grain boundaries, which attenuate more energy of ultrasound wave during the test. As a result, sample 3, 5, 7, 9 and 11 had lower amplitudes and received less energy than rest of the samples at the same number of thermal cycles.

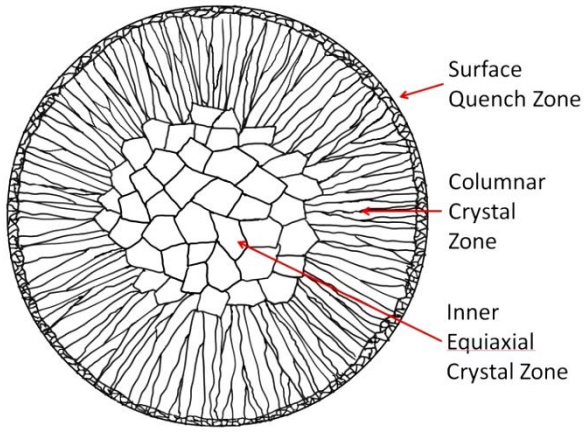


Figure 5.36 Schematic cross-section of three types of crystallisations in nickel superalloy ingot

5.6.2 Relation between signal energy and TGO thickness

Figure 5.37 shows the average of the signal energy of SX samples and MG samples plotted against the corresponding TGO thicknesses. Error bars show the variation of measured energy values in the sample sets. It is shown that signal energy decreases with increasing TGO thickness. Also, a linear relationship between signal energy and TGO thickness is found in MG samples.

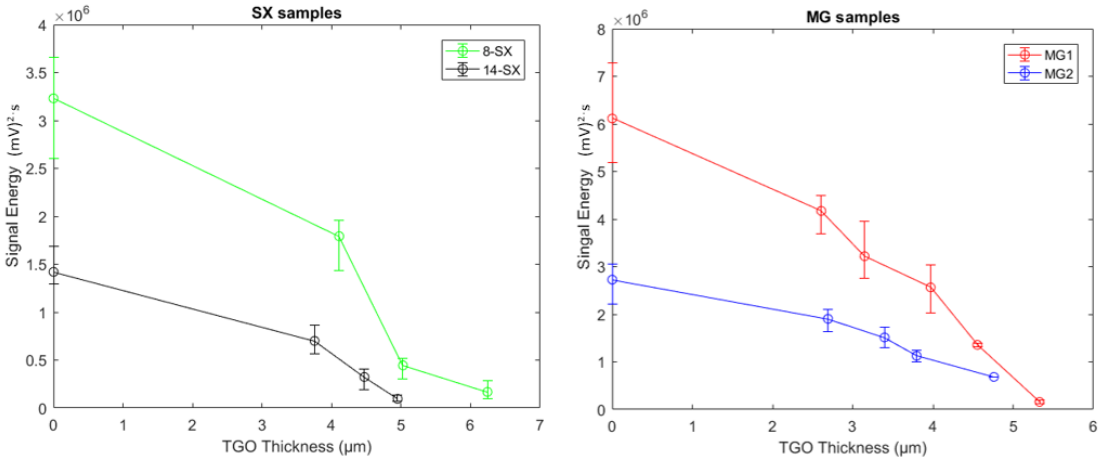


Figure 5.37 Plots of average signal energies of SX samples and MG samples at corresponding TGO thicknesses

5.6.3 Ultrasound attenuation by TGO layer

Since the magnitude of total signal energy is directly related to TGO thickness, a primary hypothesis is proposed that the laser energy was fully absorbed in the surface of the TGO layer, which generates ultrasound bulk waves. The bulk wave is then attenuated by the TGO layer while propagating to the bottom of the substrates. As a result, the signal energy decreased with increasing TGO thickness. The ultrasound attenuations are calculated and compared with measured energy attenuations.

The attenuation of the total signal energy between before and after thermal oxidation of each sample is calculated by Equation 5.2. An estimated energy of ultrasound signal after propagating through TGO layer is calculated by the Beer-Lambert law, as shown in Equation 5.3, where the ultrasound attenuation coefficient of α-alumina, α, is around 1.6 dB/cm between 15 to 20 MHz [156], d is the thickness of TGO layer. And then the ultrasound attenuation is calculated using Equation 5.2. The results of measured signal attenuation and estimated ultrasound attenuation are shown in Table 5.5.

$$\text{Signal Attenuation } (-\text{dB}) = 10 \times \log_{10}\left(\frac{\text{Energy}_{before\ oxidation}}{\text{Energy}_{after\ oxidation}}\right) \tag{5.2}$$

$$E_{estimated} = E_0 e^{-\alpha(f)\cdot d} \tag{5.3}$$

Table 5.5 Calculated attenuations of LPAS measurement and TGO thickness

Samples	Total signal energy	Energy attenuation (-dB)	TGO thickness (μm)	Estimated ultrasound attenuation (-dB)
8-SX	3.23E+06	-	-	-
	1.79E+06	2.56	4.109	0.003
	4.45E+05	8.61	5.027	0.003
	1.68E+05	12.84	6.242	0.004
14-SX	1.42E+06	-	-	-
	7.00E+05	3.07	3.755	0.003
	3.24E+05	6.42	4.472	0.003
	9.57E+04	11.71	4.950	0.003
MG1	6.11E+06	-	-	-
	4.17E+06	1.66	2.607	0.002
	3.22E+06	2.78	3.146	0.002
	2.57E+06	3.77	3.971	0.003
	1.36E+06	6.54	4.553	0.003
	1.59E+05	15.85	5.327	0.004
MG2	2.73E+06	-	-	-
	1.90E+06	1.56	2.691	0.002
	1.51E+06	2.56	3.396	0.002
	1.13E+06	3.84	3.796	0.003
	6.84E+05	6.01	4.760	0.003

According to the results, the estimated ultrasound attenuations caused by TGO layer are around three orders of magnitude lower than measured signal attenuations from LPAS measurement. Therefore, the ultrasound attenuation in TGO layer is not the major cause of the signal energy reduction of the ultrasound in LPAS measurement.

5.6.4 Cracks in the TGO layer

In further research on the BSE image of TGO cross section, cracks are easily observed at TGO layer after 40 thermal cycles. Nevertheless, a small number of fine cracks that have emerged at TGO layer were also found in samples at early oxidation stages. All cracks can be classified into three types: crack at the interface of the ceramic layer and TGO layer, crack inside of TGO layer and crack at the interface of TGO layer and bond coat, as shown in Figure 5.38.

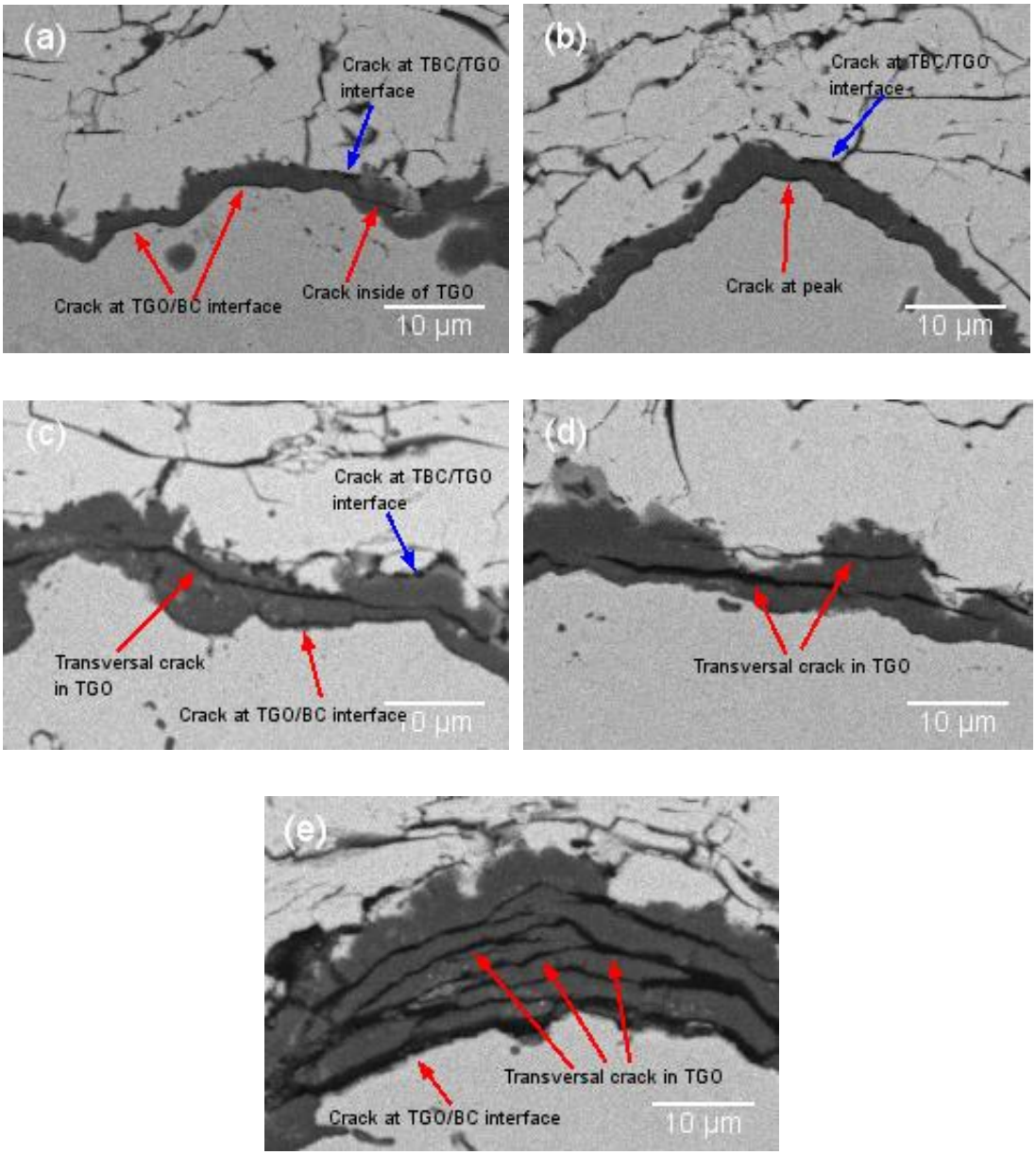


Figure 5.38 Microstructures of TGO layer of MG sample after thermal cyclic oxidation at 1150 °C of (a) 5 cycles, (b) 10 cycles, (c) 20 cycles, (d) 40 cycles and (e) 80 cycles.

As mentioned in chapter 2.2.3, the acoustic waves are reflected at boundaries where two materials have different acoustic impedances on each side of the boundary. Therefore, part of the ultrasounic longitudinal wave which is generated at the top surface of TGO layer is reflected by the cracks inside of the TGO layer. The reflection coefficient is calculated by Equation 5.4.

$$R = \left(\frac{Z_2 - Z_1}{Z_2 - Z_1}\right)^2 \tag{5.4}$$

where Z is the acoustic impedance of material, which is defined as the product of density and the acoustic velocity of the material. The acoustic impedance of alumina is found as 1.002×10^3 g/cm^2·sec [27]. The acoustic impedance of air at 20 °C is calculated by the product of the density of air and the speed of sound, which is 41.3 g/cm^2·sec. The reflection coefficient between alumina and air has been calculated almost equal to 1, which means ultrasound is fully reflected by the interface of TGO/crack. Thus, ultrasound cannot propagate via TGO layer where there is crack underneath its surface.

In order to quantify the influence of cracks on total signal energy, the image analysis on BSE image was conducted to estimate sample bonding condition via measuring crack ratio in TGO layer (the method is presented in chapter 3.5.5). The sample bonding condition is defined as a ratio of the area without any crack underneath TGO to total sample area, which is simply calculated by one minus crack ratio. The signal reduction ratios are calculated as a ratio of measured signal energy between after oxidation and before oxidation. Results are plotted against thickness of TGO, as shown in Figure 5.39.

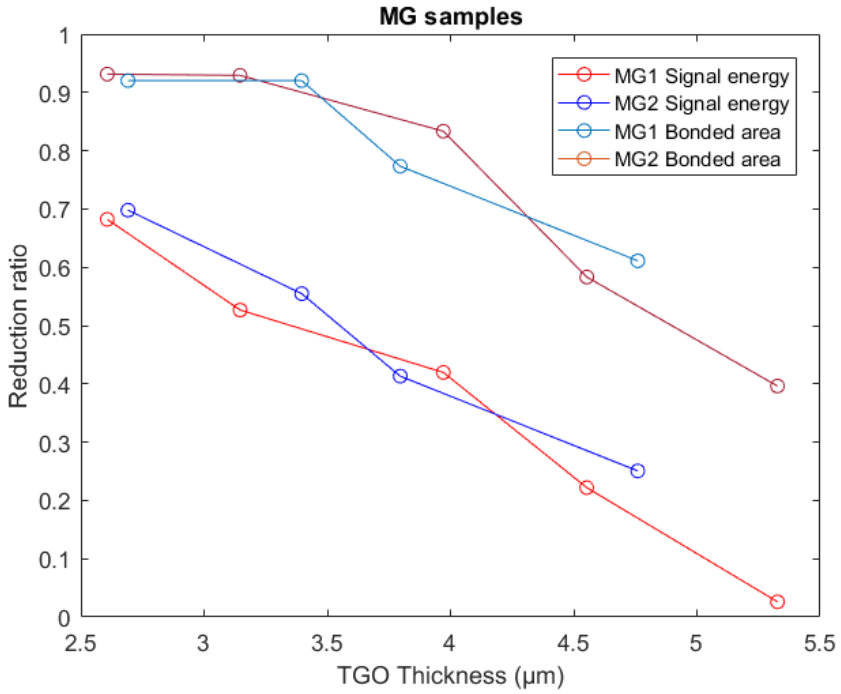


Figure 5.39 Comparison between LPAS measured signal reduction ratio and image analysed sample bonded ratio

Results show a similarly attenuated tendency with approximately 40% differences between LPAS measured signal energy ratio and corresponding sample bonding condition. This has proved that cracks underneath the interface between TGO and ceramic topcoat have the main influence on the signal attenuation. Furthermore, the differences between two values are representing other influencing factors: laser reflection at the interface between TGO layer and cracks, laser absorption of TGO layer and transmission of the remainder laser.

5.6.5 Physical model of laser attenuation in TGO

Considering there is no crack inside of TGO layer, after the laser passes through YSZ ceramic top coat and irradiates on TGO layer, the energy provided by the laser is partially reflected off their interface, partially absorbed by the TGO and partially transmitted to the bond coat. The amount of the energy reflected, absorbed by the TGO layer and transmitted to the bond coat depends on the optical properties of both the TGO and the bond coat. At the wavelength of the laser used, 532 nm, the TGO layer is semi-transparent. The extinction coefficient of α-alumina, the main component in TGO, is found 0.02 [157], and the skin depth is calculated as 2.12 μm [158]. Therefore, the optical transmittance is strongly dependent on the TGO thickness, which varies between 0.081 and 0.292 for tested samples.

In practice, laser energy is also partially reflected by cracks appeared in TGO layer. A simple model is purposed to estimate the influence of crack inside TGO on laser attenuation, which is under a few assumptions and constraints:

(1) The intensity of laser is too low for ablation TGO;
(2) All interfaces are smooth, and no laser scattered at interface;
(3) TGO is homogeneous and isotropic;
(4) Neglecting effect of thermal diffusion in TGO;

Figure 5.40 shows a schematic diagram of the physical model to demonstrate the laser attenuation in TGO layer with crack inside.

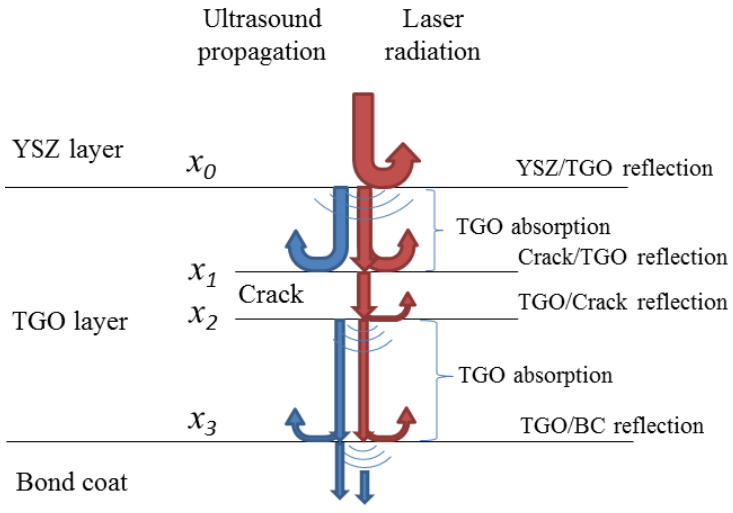


Figure 5.40 Schematic diagram of laser attenuation in TGO layer with crack inside

As demonstrated in Figure 5.40, the laser after passing through YSZ layer is partially reflected at YSZ/TGO interface. Then part of the laser is absorbed in TGO layer which generates ultrasound, and the other part of laser passes through the crack where it has been reflected twice at the interface of TGO and crack. The ultrasound that has been generated in TGO layer is fully reflected by crack. Then the remaining laser passes through the rest of TGO where the laser is absorbed again. The generated ultrasound at lower TGO propagates through the rest of TGO layer into bond coat after an acoustic reflection at the interface. Finally, the laser is absorbed by bond coat after one more reflection at the interface of TGO and bond coat, while the remaining laser energy transfer into heat; ultrasound is generated and propagated through towards the substrate.

It is worth noting that, in practice, the laser which passing through TGO layer would be scattered by its grain boundaries and defect inside. Therefore, to simplify the calculations, the influence of interference due to TGO layer thickness should not be involved in when calculating the reflectance of laser light.

Hence, the laser reflectance at each interface is calculated by the following Fresnel equation:

$$\mathrm{R}_{YSZ/TGO} = \left|\frac{n_{YSZ}-n_{TGO}}{n_{YSZ}+n_{TGO}}\right|^2 \tag{5.5}$$

$$\mathrm{R}_{TGO/crack} = \left|\frac{n_{TGO}-n_{air}}{n_{TGO}+n_{air}}\right|^2 \tag{5.6}$$

$$\mathrm{R}_{crack/YSZ} = \left|\frac{n_{air}-n_{YSZ}}{n_{air}+n_{YSZ}}\right|^2 \tag{5.7}$$

$$\mathrm{R}_{\frac{TGO}{BC}} = \left|\frac{n_{TGO}-n_{nickel}}{n_{TGO}+n_{nickel}}\right|^2 \tag{5.8}$$

where n_{YSZ} is refractive index of YSZ which is 2.2 at 532 nm wavelength [159, 160]. n_{TGO} is refractive index of α-alumina which is 1.729 at 532 nm wavelength [157]. n_{air} is refractive index of air which is 1. The refractive index of nickel, n_{nickel}, is used as refractive index of bond coat to complete the model, which is 1.738 [161].

The laser absorption by TGO upper layer is calculated following Beer's law:

$$I_1 = I_0 \mathrm{e}^{-\alpha_{TGO}(x_1 - x_0)} \tag{5.9}$$

where I_0 and I_1 are intensities of laser before and after TGO layer. $x_1 - x_0$ is the distance in TGO upper layer that laser has passed through. α_{TGO} is the absorption coefficient of TGO layer, which is derived by extinction coefficient of α-alumina:

$$\alpha_{TGO} = \frac{4\pi f k_{\alpha-alumina}}{c} \tag{5.10}$$

where f is the frequency of laser, $k_{\alpha-alumina}$ is extinction coefficient of α-alumina, found as 0.02 at 532 nm wavelength, c is speed of light.

The reflection coefficient and the transmission coefficient of intensity reduction induced by ultrasonic longitudinal waves propagating between TGO layer and bond coat are given by the relations:

$$\mathrm{R}_{\frac{TGO}{BC}} = \left|\frac{Z_{TGO} - Z_{BC}}{Z_{TGO} + Z_{BC}}\right|^2 \tag{5.11}$$

$$\mathrm{T}_{\frac{TGO}{BC}} = \frac{4 Z_{TGO} Z_{BC}}{(Z_{TGO} + Z_{BC})^2} \tag{5.12}$$

where the acoustic impedance of alumina, Z_{TGO}, is found as 1.002×10^3 g/cm^2·sec, the acoustic impedance of NiCoCrAlY bond coating, Z_{BC}, is found as 4.257×10^3 g/cm^2·sec [27].

Under the assumptions, the laser power after passing TGO layer with one crack inside is derived by combining all equations, derived as:

$$\mathrm{I}_{laser\ out} = \left(1 - \mathrm{R}_{\frac{YSZ}{TGO}}\right) \mathrm{e}^{-\alpha_{TGO}(x_1 - x_0)} \left(1 - \mathrm{R}_{\frac{TGO}{crack}}\right)^2 \mathrm{e}^{-\alpha_{TGO}(x_3 - x_2)} \left(1 - \mathrm{R}_{\frac{TGO}{BC}}\right) \tag{5.13}$$

Substitute each reflectance into Equation 5.13 gives:

$$\mathrm{I}_{laser\ out} = \left[\frac{2^8\, n_{YSZ}\, n_{TGO}^4\, n_{nickel}}{(n_{YSZ} + n_{TGO})^2 (n_{TGO} + 1)^4 (n_{TGO} + n_{nickel})^2}\right] \mathrm{e}^{-\alpha_{TGO}\mathrm{d}} \tag{5.14}$$

where d represents the total thickness of TGO layer.

If there are two or more cracks inside TGO layer, the output power of the laser is derived as:

$$I_{2cracks} = \left[\frac{32n_{TGO}^{6}}{(n_{TGO}+1)^{8}}\right]\left[\frac{16\, n_{YSZ}\ n_{nickel}}{(n_{YSZ}+n_{TGO})^{2}(n_{TGO}+n_{nickel})^{2}}\right] e^{-\alpha_{TGO}d} \quad (5.15)$$

$$I_{Ncracks} = \left[\frac{16Nn_{TGO}^{2N+2}}{(n_{TGO}+1)^{4N}}\right]\left[\frac{16\, n_{YSZ}\ n_{nickel}}{(n_{YSZ}+n_{TGO})^{2}(n_{TGO}+n_{nickel})^{2}}\right] e^{-\alpha_{TGO}d} \quad (5.16)$$

where N is the number of cracks.

The intensity of ultrasound waves that generated at the lower part of TGO layer is calculated as:

$$I_{u} = \left[\frac{4Z_{TGO}Z_{BC}}{(Z_{TGO}+Z_{BC})^{2}}\right] e^{-\alpha_{TGO}(x_3-x_2)} \quad (5.17)$$

Therefore, the total power output at bond coat surface when there is one crack inside of TGO layer is:

$$I_{output} = \left[\frac{2^{8}\, n_{YSZ}\, n_{TGO}^{4}\, n_{nickel}}{(n_{YSZ}+n_{TGO})^{2}(n_{TGO}+1)^{4}(n_{TGO}+n_{nickel})^{2}}\right] e^{-\alpha_{TGO}d} + \left[\frac{4Z_{TGO}Z_{BC}}{(Z_{TGO}+Z_{BC})^{2}}\right] e^{-\alpha_{TGO}(x_3-x_2)} \quad (5.18)$$

For there are N cracks inside of TGO layer:

$$I_{N_output} = \left[\frac{16Nn_{TGO}^{2N+2}}{(n_{TGO}+1)^{4N}}\right]\left[\frac{16\, n_{YSZ}\ n_{nickel}}{(n_{YSZ}+n_{TGO})^{2}(n_{TGO}+n_{nickel})^{2}}\right] e^{-\alpha_{TGO}d} + \left[\frac{4Z_{TGO}Z_{BC}}{(Z_{TGO}+Z_{BC})^{2}}\right] e^{-\alpha_{TGO}(x_{2N+1}-x_{2N})} \quad (5.19)$$

The Equation 5.18 for one crack model shows that the output of laser varies depending on the position of appeared crack. Equation 5.20 and 5.21 is derived to determine the output of laser for at least one crack appearing on top or bottom surface of TGO, which is when spallation occurs at two TGO interface in the samples.

$$I_{N_top} = \left[\frac{16Nn_{TGO}^{2N}}{(n_{TGO}+1)^{4N-2}}\right]\left[\frac{4\, n_{YSZ}\ n_{nickel}}{(n_{YSZ}+1)^{2}(n_{TGO}+n_{nickel})^{2}}\right] e^{-\alpha_{TGO}d}$$

$$+\left[\frac{4Z_{TGO}Z_{BC}}{(Z_{TGO}+Z_{BC})^2}\right]e^{-\alpha_{TGO}(x_{2N+1}-x_{2N})} \quad (5.20)$$

$$I_{N_bottom} = \left[\frac{16Nn_{TGO}^{2N}}{(n_{TGO}+1)^{4N-2}}\right]\left[\frac{4\,n_{YSZ}\;n_{nickel}}{(n_{YSZ}+n_{TGO})^2(1+n_{nickel})^2}\right] e^{-\alpha_{TGO}d} \quad (5.21)$$

The simulated value is used to analyse the influence of crack position in TGO layer on laser attenuation by calculating the output power after TGO layer using Equation 5.19, 5.20 and 5.21. The laser power after passing through YSZ ceramic layer is set to 1, the total thickness of TGO layer is set to 5 μm and N equal to 1. Results are shown in Table 5.6.

Table 5.6 Simulated results for laser output influence on the crack position

Layer	Thickness (μm)	Refraction index	Absorption coefficient (μm^{-1})	Total power	Transmittance	Energy absorbed	Interface	Reflectance
Crack inside of TGO								
YSZ	-	2.200	-	1.000	-	-		
							YSZ/TGO	0.014
TGO	2.5	1.729	0.472	0.986	0.307	0.683		
							TGO/Crack	0.071
Crack	0.1	1.000	-	0.281	-	-		
							Crack/TGO	0.071
TGO	2.5	1.729	0.472	0.261	0.307	0.181		
							TGO/Bond coat	0.000
Bond coat	-	1.738	-	0.080	-	-	Remainder	0.192
Crack at YSZ/TGO interface								
YSZ	-	2.200	-	1.000	-	-		
							YSZ/Crack	0.141
Crack	0.1	1.000	-	0.859	-	-		
							Crack/TGO	0.071
TGO	5.0	1.729	0.472	0.798	0.094	0.723		
							TGO/Bond coat	0.000
Bond coat	-	1.738		0.075	-	-	Remainder	0.522
Crack at TGO/Bond coat interface								
YSZ	-	2.200	-	1.000	-	-		
							YSZ/TGO	0.014
TGO	5.0	1.729	0.472	0.986	0.094	0.893		
							TGO/Crack	0.071
Crack	0.1	1.000	-	0.086	-	-		
							Crack/Bond coat	0.073
Bond coat	-	1.738	-	0.080	-	-	Remainder	0.080
No crack in TGO layer								
YSZ	-	2.200	-	1.000	-	-		
							YSZ/TGO	0.014
TGO	5.0	1.729	0.472	0.986	0.094	0.893		
							TGO/Bond coat	0.000
Bond coat	-	1.738	-	0.093	-	-	Remainder	0.645

It is shown that the laser outputs have reduced to around 8% of original power; the values are not much different among the three positions of cracks and when the crack is absent; the reduction in laser power is mainly caused by the absorption of TGO layer. However, the remainder power shows the significant difference when a crack appeared near the top surface or at the bottom, which is mainly due to the signal loss of ultrasound at the bottom of the crack. It can explain the relationship between signal energy ratio and bonded area ratio in previously presented Figure 5.39, where the tendency of data points is related to the appearance of cracks, and the difference of measured value is due to the laser attenuation.

Furthermore, analysis of the depth of cracks in TGO layer is conducted between top and bottom of TGO layer. The fitted result shows remainder power decreases exponentially with increasing of crack depth in TGO layer, as shown in Figure 5.41.

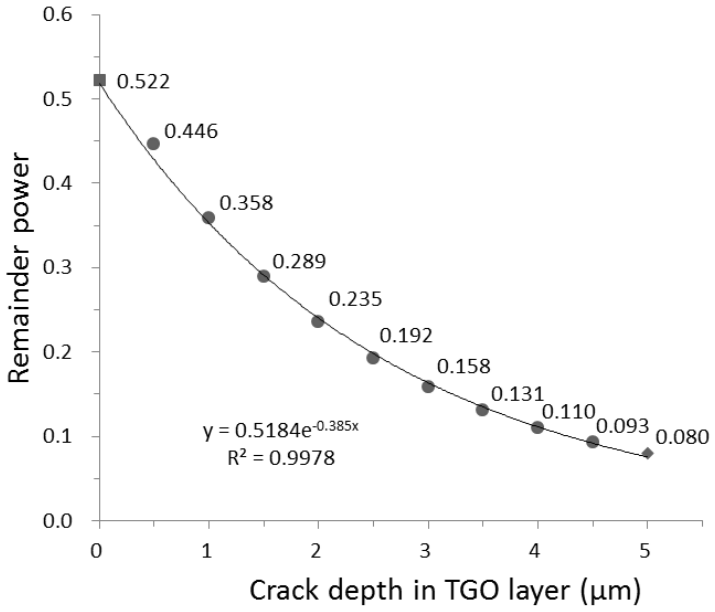


Figure 5.41 Remainder power decreases exponentially with crack depth

Current analysis method using crack ratio has only considered the energy loss of ultrasound signal due to the area where cracks occur beneath the TGO layer. In practice, the position and the number of cracks in TGO layer are much more complicated than the simple model. An idea came up to refine the calculation by taking into account the reduction of laser attenuation by TGO layer where no crack appeared, then adding the remaining laser energy after passing through TGO layer and the energy of ultrasound generated under the crack. This method involved similar image processing and a more complicated calculation in MATLAB. In other words, the thickness of cracks and TGO layer were measured in each pixel column, and then the remainder energy in each column was calculated using a corresponding equation chosen from the simple physical mode. The image analysis and calculation method will be given in detail in the future plan of the last chapter.

5.6.6 Oxidation of bond coat

Previously, the LPAS result of bond coat only samples have shown a dramatic increase in amplitude between as-sprayed sample and sample after thermal cyclic oxidation. After further investigation by observing the surface morphology under SEM, possible influence factors were discovered here.

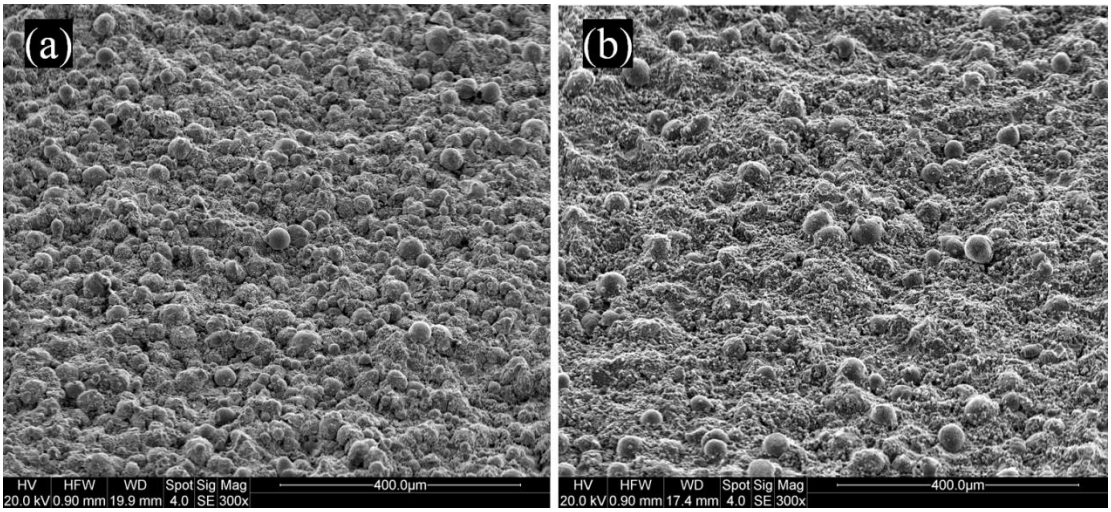


Figure 5.42 Surface morphologies of (a) as-sprayed and (b) after two thermal cycles NiCoCrAlY bond coat. SE image: stage 45° tilted, scale bar: 400 µm, 300X magnifications

Figure 5.42 shows the surface morphologies of as-sprayed and after two thermal cycles bond coat at lower magnifications. It is shown that the surface of the as-sprayed sample is ‘looser’ than sample after oxidation as un-melted metallic powders by HVOF spray were mostly exposed outside and partially buried in the surface. Essentially, it has less contact area than samples after oxidation; in other words, it could act as a light barrier rather than transferring mechanical wave. After oxidation, a layer of alumina is formed on the surface which fills up the gaps below powders, and covers the surface with a rough film, as shown in Figure 5.43 (b) and (c). This rough layer of alumina could reduce the reflectivity of the surface, thus increasing its absorption. Furthermore, this film could change the elastic boundary condition of the surface due to the difference in coefficient of thermal expansion, of which NiCoCrAlY is about twice larger than alumina. The constrained surface generates dipolar stress when there are thermal

stresses parallel to surface. The effect can enhance the amplitude significantly, which has been experimentally proved by many researchers, details were described previously in chapter 2.3.3.

Figure 5.43 shows SE images taken at 45° which focused on un-melted powder to help observe the TGO layer, which provides more representative three-dimensional view rather than an oxidised surface.

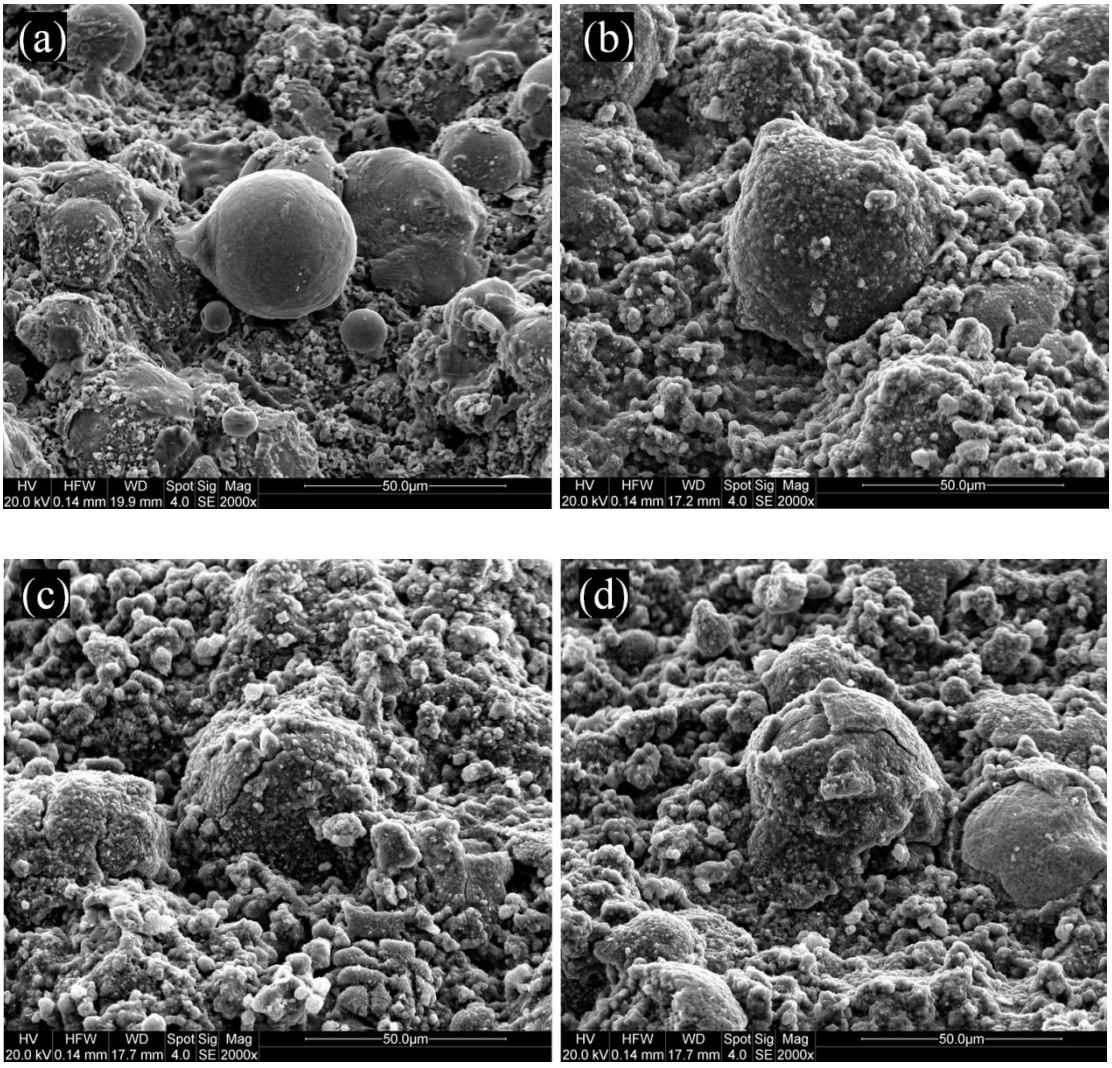


Figure 5.43 Surface morphologies of un-melted NiCoCrAlY powder (a) as-sprayed and after (b) 2 thermal cycles, (c) 10 thermal cycles, (d) 20 thermal cycles, respectively. SE images were taken at 2000X magnifications, stage 45° tilted, by Quanta 600 MLA, scale bar 50 μm. An EDS element mapping of the un-melted NiCoCrAlY particle after thermal oxidation is shown in Appendix E.

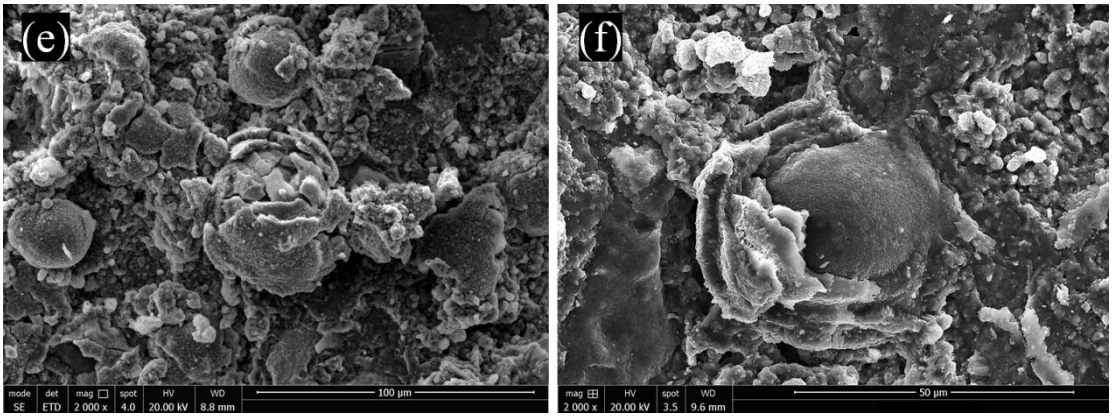


Figure 5.43 Surface morphologies of un-melted NiCoCrAlY powder after (e) 40 thermal cycles and (f) 80 thermal cycles. SE images were taken at 2000X magnifications, stage 0° tilted, by Quanta 650 ESEM, scale bars in (e) and (f) are 100 µm and 50 µm.

The images above not only show the surface oxidation of NiCoCrAlY bond coat with an increase in TGO volume but also illustrate the crack formation at the surface with increasing number of thermal cycles. After ten thermal cycles, some fine cracks were able to identify on the surface. After 20 thermal cycles, partial separation of TGO layer is observed, more separations occurred after 40 thermal cycles. The increasing thickness of TGO layer increased the attenuation of laser irradiation and the increasing number of cracks in TGO layer increased the laser reflection at crack/TGO interfaces. Consequently, in LPAS measurement the amplitude decreases with increase in thermal oxidation time. Eventually, spallation of TGO layer occurred, which has explained that the amplitude of the bond coat sample has increased again after 80 cycles, as shown in Figure 5.32.

Furthermore, the observation of surface morphology of bond coat has revealed the grain structure of alumina at spallation layer, as shown in Figure 5.44. The grain scale of alumina changes throughout its thickness. The external layer of alumina contains fine and equiaxial grains, and alumina close to bond coat side are larger scale and elongated column grains. The previous theoretical modelling assumed that TGO layer is homogeneous and isotropic to simplify the calculation. In practice, the laser would be scattered by the presented grain boundaries and lose part of its energy. Since scattering is related to the sample grain size, shape of grains and the porosity, further

research on the scattering of the laser beam passing through alumina is suggested, which could potentially provide more information of TGO conditions and improve the accuracy of testing.

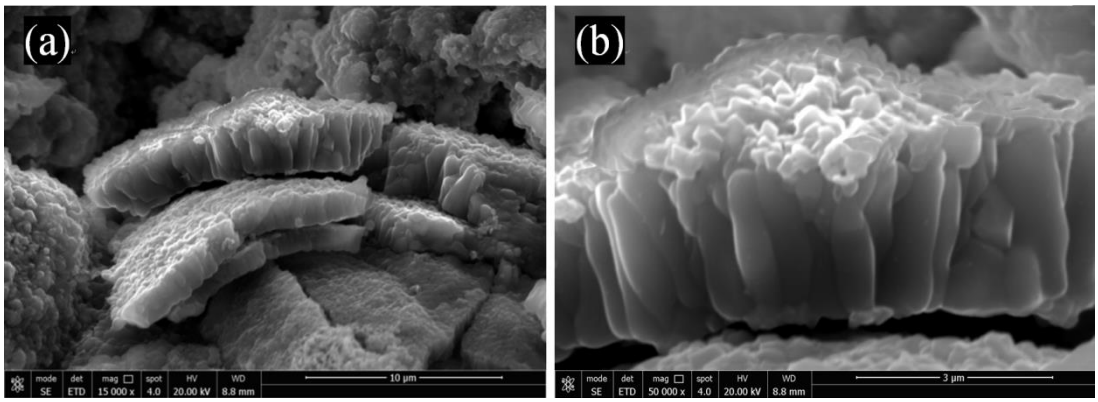


Figure 5.44 Spallation TGO layer on the oxidised bond coat. SE images were taken at 15000X magnifications, stage 45° tilted, by Quanta 650 ESEM, scale bars in (a) and (b) are 10 μm and 3 μm.

5.6.7 Phase map analysis

In the previous chapter 5.1.3, Figure 5.14 has shown a comparison of two sets of random phase spots extracted from phase map of as-sprayed sample and sample after 60 cycles, which has indicated the signal loss at the edge of the sample after thermal cycling. The cause of the random phase appearing is due to a negative signal-to-noise ratio at the edge of the sample, where amplitude has reduced below the noise as no ultrasound was received by the transducer.

There are two influence factors causing the lower amplitude at the edge of the sample. The transducer, as an intrinsic factor, produces and receives a Gaussian distribution of amplitude along a radial dimension, as shown in Figure 5.3, which directly lead to lower amplitudes at the edge. The cracks and delamination, as an external factor, form at the edge and grow towards the centre of the sample, which is due to a larger thermal expansion mismatch at the edge of the sample. Figure 5.45 shows the microstructure at the edge of MG as-sprayed sample and samples after thermal cyclic oxidation of 5, 10, 20, 40 and 80. It is shown that cracks have gradually increased in a ceramic layer with the increasing of thermal oxidation cycles. As a result, most of the laser were scattered by the cracks inside of top coat at the edge, and less energy was transferred to the transducer. Therefore, the random phases appeared at the edge of the sample due to a combination of the two influence factors. Furthermore, delamination of the sample after 80 thermal cycles is identified, as shown in Figure 5.45 (f), which reflects the sharp increase in the percentage of phase angle difference and standard deviation at 80 cycles, shown in Figure 5.27 and 5.28 respectively. As explained previously, this method is highly dependent on the total number of scanning points. With more data points acquired in the scan the standard deviation and the percentage will be more accurate as a result. Further improvement of this method can be achieved by measuring the displacement of the substrate surface using a laser interferometer, which could eliminate the influence that introduced by the transducer.

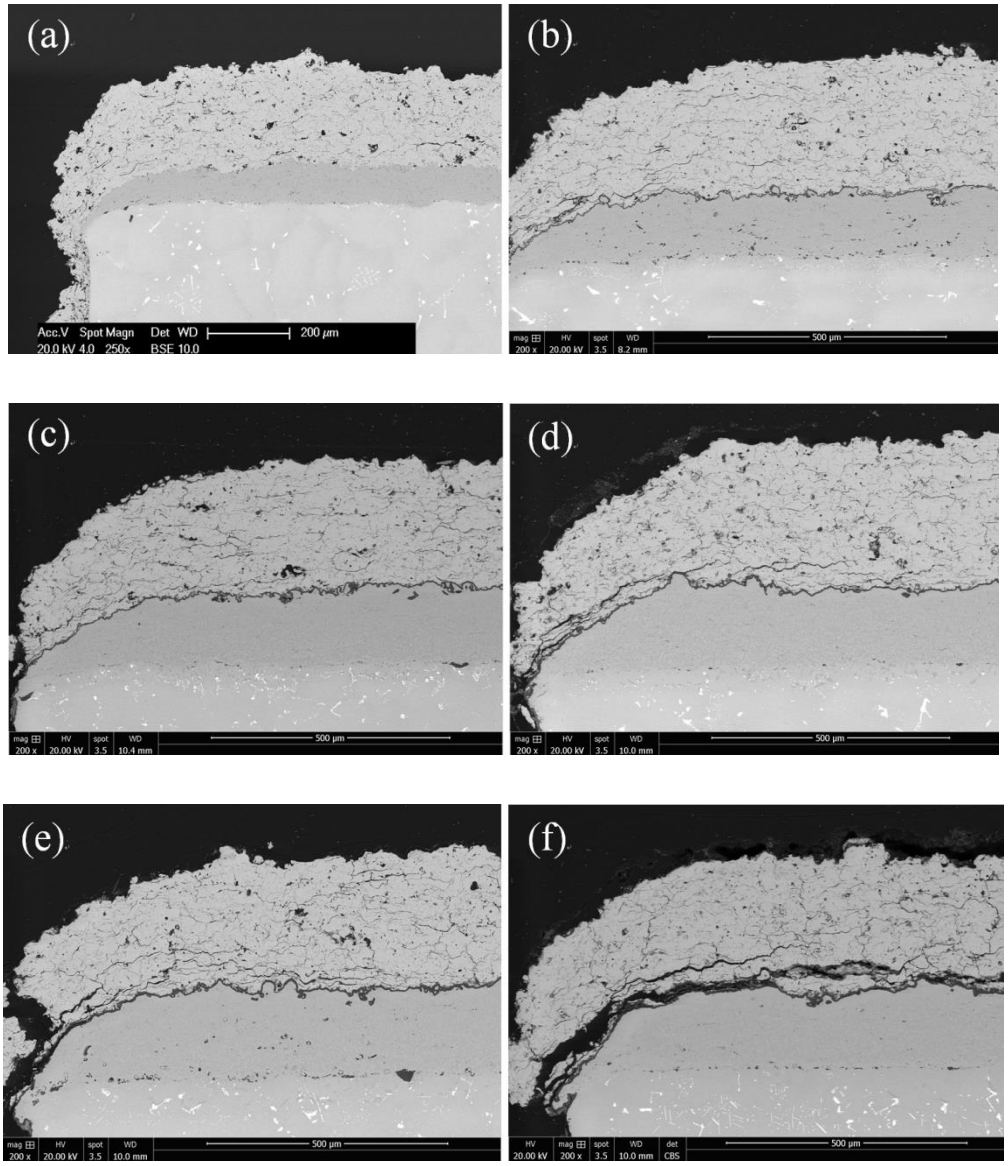


Figure 5.45 Formation of cracks and delamination at edge of MG sample at (a) as-sprayed, after (b) 5 cycles, (c) 10 cycles, (d) 20 cycles, (e) 40 cycles and (f) 80cycles

5.6.8 Viability of the technique and applications

Compare to the conventional pitch-catch ultrasound technique, the LPAS technique has two advantages: noncontact with sample surface and sub-layer ultrasound generation. Noncontact laser generated ultrasound does not require a liquid couplant which could cause contamination on the sample surface in some case. It can accommodate in many circumstances what a transducer could not achieve, for instance complicate sample geometry that transducer cannot attach or in a high temperature environment, or an inspection environment involved radioactive or corrosive. Since laser has the ability to penetrate certain materials which in some cases are highly attenuate for high frequency ultrasound. Therefore, by generates ultrasound at sub-layer, it could avoid signal attenuation by the surface material and reduces the signal interference during the propagation through the surface material. These advantages are reflected in the measurement of the thermal barrier coating, the noncontact laser ultrasound generation avoids the contamination of YSZ layer by absorbing the silicon couplant. Air plasma sprayed YSZ layer has a porous laminated structure and highly attenuate ultrasound, where LPAS technique overcomes this problem by generating ultrasound at TGO layer directly after the laser penetrated YSZ layer.

Currently, this laser photoacoustic spectroscopy system uses a laser to generate ultrasound but detect the response signal by a transducer. The detection using transducer caused an uneven signal distribution in the energy and amplitude map lead to the visual inspection of flaws inside of coating more difficult. Therefore, an overall evaluation of thermal barrier coating was carried out by monitoring the total value of signal energy and analysing the change of phase angle of each scan. In order to improve this limitation and enable to detect the flaws in the coating, a noncontact detection will be used in the future by measuring the surface displacement using an interferometer. In addition, a generation laser with more power is required to generated ultrasound with higher signal energy. After modification of detection system, the laser photoacoustic spectroscopy technique could be used for purposes such as coating quality control, flaw examination in sub-layer. It is also possible used for coating thickness measurement where the amplitude of generated ultrasound varies with the thickness of the surface layer due to the laser attenuation.

5.7 Summary

This chapter has demonstrated the nondestructive evaluation of thermal barrier coatings using laser photoacoustic spectroscopy. The LPAS system has been successfully designed and assembled. Thermal barrier coating sample with two different types of substrate, namely single crystal superalloy substrate and multigrain superalloy substrate, at different thermal cyclic oxidation condition were measured. C-scan was carried out across each sample and result was shown in amplitude map, signal energy map, frequency map and phase map along with corresponded analysis technique.

A relationship was found between the amplitude levels and the number of thermal cycles, illustrating that the amplitude decreases with an increasing number of thermal cycles, which is due to the increased thickness of TGO layer and presence of delamination inside the coating. Analysis on signal energy map revealed that energy of received signal decreases with an increase in oxidation time as a parabolic function in energy-thermal oxidation plot which is related to parabolic oxidation behaviour of thermal barrier coatings. Both amplitude plot and signal energy plot have shown a data segregation between multigrain TBC samples due to the ultrasound attenuation of two types of crystal grains in the substrate. The thickness of TGO layer of each sample after thermal cyclic oxidation was measured in a panorama BSE image using image analysis. A relationship was found between signal energy and TGO thickness, illustrating that signal energy decreases with the increasing TGO thickness. A physical model was studied to estimate the influence of crack inside TGO on signal attenuation, which indicated that the signal energy reduction is due to a combination of laser reflection at interfaces, laser attenuation by TGO layer and ultrasound reflection at interfaces. In addition, the position of the presence of crack inside of TGO alters the remainder of signal energy, where crack presented near the interface of TGO layer and bond coat attenuates more signal energy. A more comprehensive image analysis was suggested to accommodate more complicated signal attenuation calculation.

Furthermore, the study of laser attenuation in YSZ ceramic coating indicated that the ultrasound signal is not generated in YSZ layer. It is also shown that thermal cyclic oxidation could increase the laser attenuation by growing the size of cracks and the increasing number of the cracks which formed inside of YSZ layer. Further study on

amplitude attenuation in a bond coat only sample has confirmed that ultrasound signal was generated in TGO layer which works as a constrained surface layer facilitate the laser ultrasonic generation at early oxidation stage. Subsequently, the amplitude decreases with the increasing thermal cycles. It is shown that the increasing thickness of TGO layer increased the attenuation of laser irradiation and the increasing number of cracks in TGO layer increased the laser reflection at crack/TGO interfaces. The observation of surface morphology of the oxidation of bond coat has well explained the amplitude change in the LPAS measurement.

Phase map analysis was carried out and used to indicate the signal loss at the edge of the sample after thermal cycling. The microstructure at the edge of MG as-sprayed sample and samples after thermal cyclic oxidation of 5, 10, 20, 40 and 80 indicated that cracks gradually increase in a ceramic layer with the increasing of thermal oxidation cycles, which leads to the lower amplitudes at the edge. Evaluation of thermal barrier coating using phase map analysis is highly dependents on the scanning resolution. The phase difference percentage and phase standard deviation of SX samples with higher scanning resolution both increase with increasing oxidation time. While the same analyses were not working for MG sample at lower thermal oxidation stage and can only be utilised as an indication when MG TBC sample is about to fail. On the other hand, the number of peaks in the phase map analysis of MG samples has shown a relationship that the number of peaks increases with increasing of thermal oxidation time, while this method for SX samples is invalid.

Further improvement of this method can be achieved by measuring the displacement of the substrate surface using a laser interferometer, which could eliminate the influence that introduced by the transducer. Some possible improvements and future plan of laser photoacoustic spectroscopy measurement will be given in the last chapter.

Chapter 6

Impedance Spectroscopy

Impedance spectroscopy (IS) is measuring an AC current response by an applied excitation potential over a range of frequencies, which is influenced by both resistance and capacitance associated with sample electrical properties and geometries. For impedance of TBC system, YSZ is an oxygen ion conductor at high temperature, while TGO acts as an oxide semiconductor, which contributes to distinguishing a frequency response from an impedance spectrum due to their difference in electrical properties. The literature review in Chapter 2 has introduced nondestructive testing of thermal barrier coating using impedance spectroscopy in the field of research, including thickness measurement, measuring of porosity of sintered YSZ materials, composition changes of TGO layer during thermal oxidation, and detection of cracks and delamination within TBCs. In the impedance measurement a conductive paint (normally platinum paste, silver paste or coated with carbon) is applied on both sides of the sample with the same amount of area act as two contact electrodes. In the case of IS testing of thermal barrier coating coated on a metallic substrate which is conductive and acts as a counter electrode. On the other side of the sample, the YSZ ceramic layer is applied with conductive paint. To avoid the effects of surface leakage current, the electrode is normally applied away from the edge of the sample, which leads to a smaller electrode on one side of the sample. Moreover, the surface area of the testing sample in some case could be relatively large that fully covered by conductive paint is impractical which resulting in asymmetric electrode geometry.

Previous researches on nondestructive testing of thermal barrier coatings using impedance spectroscopy have acknowledged the influence of asymmetric electrode geometry on impedance spectrum. In other words, inaccurate calculation of resistance was involved due to non-uniform current distribution through a specific electrode area of the sample.

In this chapter, analysis of asymmetric electrode geometry effect on YSZ material will be demonstrated using both finite element simulations and impedance spectroscopy measurements. The resistances of the simulated model with various scale factors of geometry are calculated, which are compared with the measured resistances of YSZ bulk samples from impedance spectroscopy measurement. A good agreement is found on the tendency between simulated and measured resistances with the corresponded scale factors of geometry. An estimated equivalent area of the electrodes of the simulated models can be derived from the simulated resistance. By replaces the area of applied conductive paint with this value in the calculation of impedance spectroscopy, the influence of asymmetric electrode geometry is fixed, thus, a more accurate resistance measurement will be achieved. Furthermore, a linear relationship is revealed between the ratio of equivalent area to applied electrode area and the resistance of the sample. Moreover, the gradient of their plots is proportional to the thickness of the sample. As a result, an estimated resistance can be calculated without simulation process by using the discovered relationship among them.

6.1 Finite element simulation of the resistance of YSZ bulk with an asymmetric electrode geometry

6.1.1 Modelling approach

The simulation approach is based on the fundamental electrical properties of materials, where all materials follow Pouillet's law.

$$R = \rho \frac{l}{A} \tag{6.1}$$

where R is the electrical resistance of a uniform specimen of the material, ρ is the electrical resistivity of the material, l is the length of specimen, A is the cross-sectional area of the specimen.

As described in chapter 2.4.4, the material in a slightly more complicated truncated cone geometry, where the area of top and bottom are asymmetric, the resistance can be calculated via the integration of specimen along the thickness by Equation 6.2 and 6.3.

$$R = \int_0^l \frac{\rho dx}{\pi\left[\frac{(r_1 - r_2)}{l^2}x + r_2\right]^2} \tag{6.2}$$

$$R = \frac{\rho l}{\pi r_1 r_2} \tag{6.3}$$

This geometry is similar to a sample with cylinder shape which has asymmetric electrodes at two ends. However, it has been proved by a simulation model and calculation that this formula is incapable of calculating the resistance between two electrodes due to the non-uniform electrical current density in the sample. Figure 6.1 illustrates the direction and the magnitude (shown as the length of the arrow) of current flows in an asymmetric electrode geometry using the simulation model, where the part of the current from the centre of top electrode flows diversely towards the edge, and then gradually returns to the direction perpendicular to the surface throughout the thickness of geometry. As a result, the resistance of tested geometry is neither the resistance of inner cylinder under top electrode nor the truncated cone geometry; instead, it varies between these two values, which depends on the area of electrodes on both sides and the thickness of the geometry.

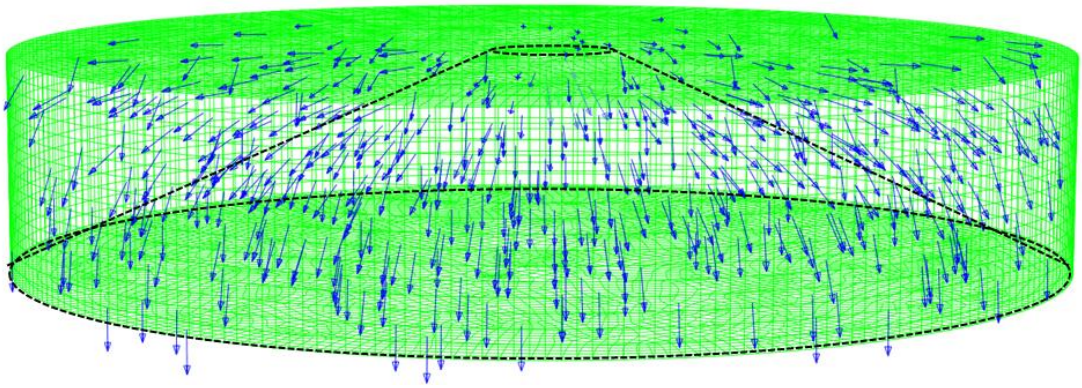


Figure 6.1 Direction and magnitude (the length of the arrow) of current flows in an asymmetric electrode geometry

In order to investigate the influence of asymmetric electrode geometry on the resistance, several three-dimensional finite element models with different geometry were developed for the electrical simulation analyses using Abaqus/CAE (6.14). Yttria-stabilized zirconia (YSZ) was used as the material for modelling, the electrical conductivity of 1.164×10^{-4} S • m^{-1} and dielectric constant of 29.682 were utilised in the simulation, which was obtained from the previous study.

The finite element models were designed as a round pellet geometry with 20 mm in diameter and thicknesses of 0.5 mm, 1 mm, 2 mm and 4 mm respectively. A circular area with diameters of 2 mm, 4 mm, 8 mm and 16 mm was sketched on one side of the model act as the electrode with a variable area in the simulation. The other side of the surface acted as a counter electrode which has a fixed area. Therefore, there were totally 16 variable scale factors in the simulation, which is defined as an area divided by the thickness of the sample. In the modelling, the element size is set to be 0.25 mm, corresponding to approximately 6200 elements in each layer which are sufficiently high as results tend to converge after this setting. A finer element size can be used to increase the accuracy of modelling with at the expense of a longer running time.

To simulate the electric current flows through the models, coupled thermal-electric procedure type was used in the Abaqus. An electrical potential was applied between two surfaces as a boundary condition, where the variable area on one side of the model was subjected to 1 volt, and the other side with a fixed area was set to zero. The output

of simulation provides electrical potential (EPOT), electrical potential gradient vector and magnitude (EPG), electrical current density distribution (ECD) and element volume (EVOL).

6.1.2 Results of finite element simulation

The simulated results of two models with distinct geometries are demonstrated in this section. One model is 4 mm thick with 2 mm diameter of the simulated electrode on the top, which has the smallest scale factor in the model set, as shown in Figure 6.2. In contrast, the other one has 0.5 mm in thickness with 16 mm diameter of the simulated electrode on the top, which is less affected by the asymmetric electrode geometry, as shown in Figure 6.3.

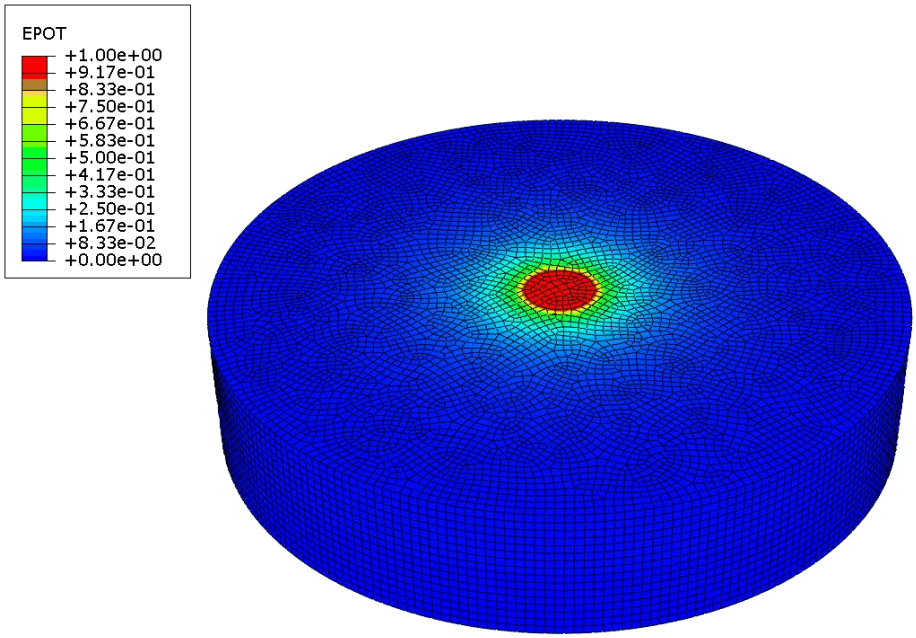


Figure 6.2 Electrical potential distribution on the surface of the finite element model with 4 mm in thickness and 2 mm in diameter of simulated electrode on the top

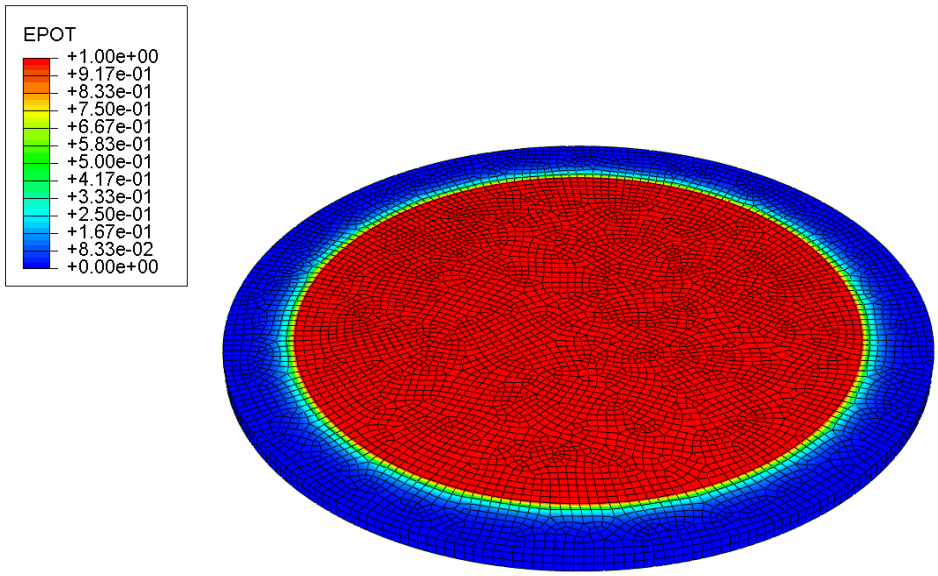


Figure 6.3 Electrical potential distribution on the surface of the finite element model with 0.5 mm in thickness and 16 mm in diameter of simulated electrode on the top

Figure 6.4 illustrated the electrical potential distribution of 4 mm model in a cut view. It is shown that the electrical potential decreases while radiating from the centre to surrounding elements. The electrical current density distribution of the model is shown in Figure 6.5, where the magnitude and direction of electrical current in each element is represented by the arrows. It is shown that the current density is higher in the elements beneath the electrode than surrounding area, which then decreases through the thickness while spreading out to uniform current at the bottom. The direction of current diverges from the centre to the side by the radial electrical potential and then gradually return to the direction perpendicular to the surface.

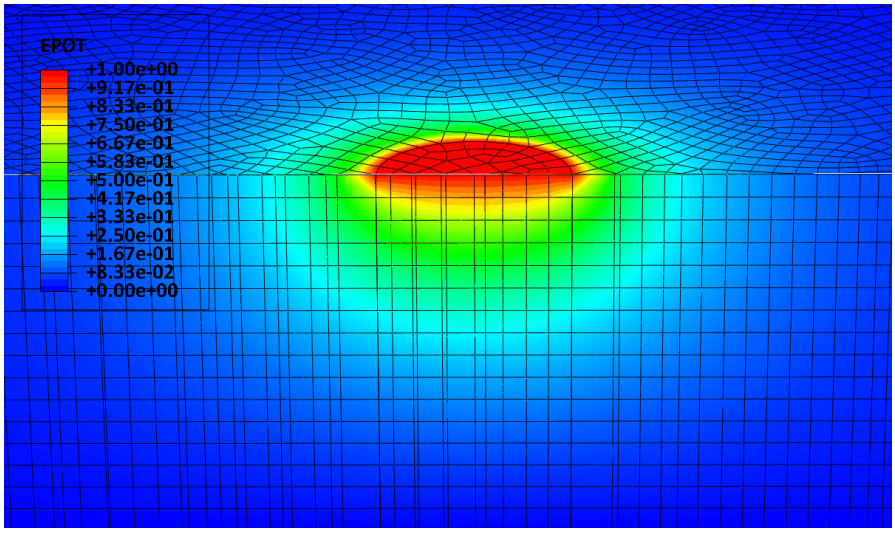


Figure 6.4 Cut view of electrical potential distribution in 4 mm model

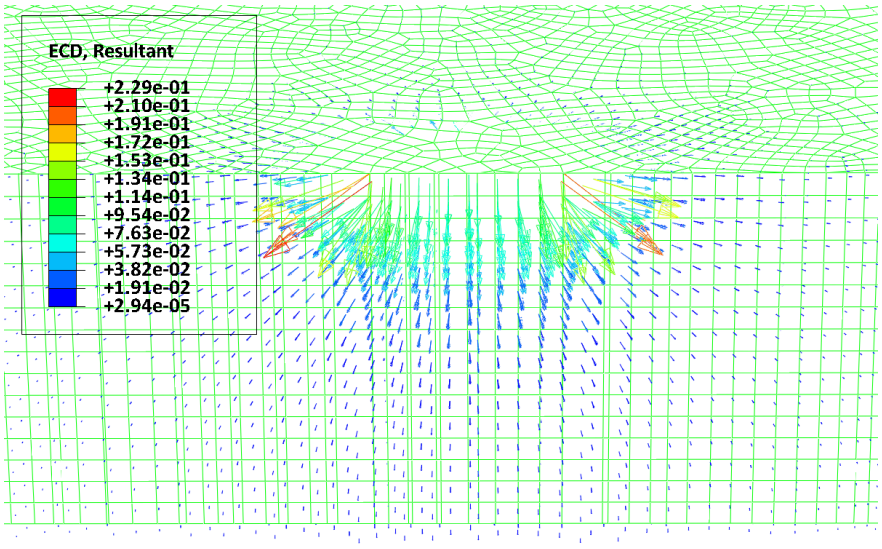


Figure 6.5 Cut view of electrical current density distribution in 4 mm model

Compared to the 4 mm model, the electrical potential distribution in the 0.5 mm model is more uniform, as shown in Figure 6.6, which leads the current flow perpendicular to the bottom. The cut view of electrical current density distribution in the thin model is shown in Figure 6.7. It is shown that only a part of the current generated at the edge of electrode area diverges to the corner of the sample. As a result, the mode is less affected by asymmetric electrode geometry as the current generated in this model

mainly flows in the elements under the electrode area. Therefore, the resistance calculated using the electrode area on the top is relatively accurate compare to the 4 mm model.

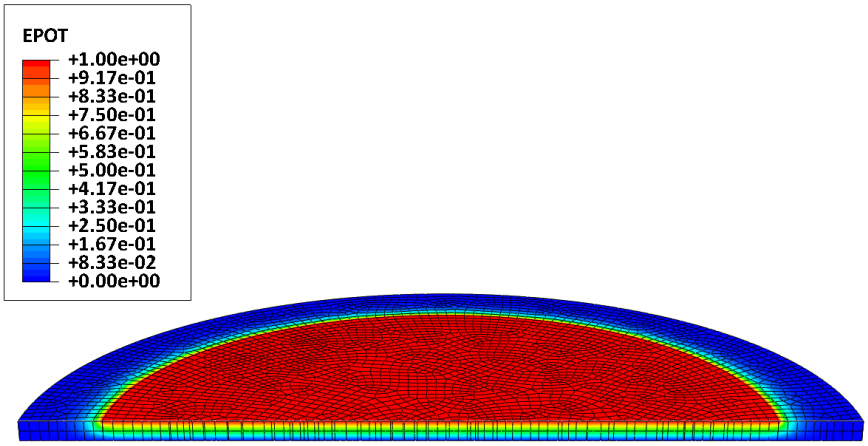


Figure 6.6 Cut view of electrical potential distribution in 0.5 mm model

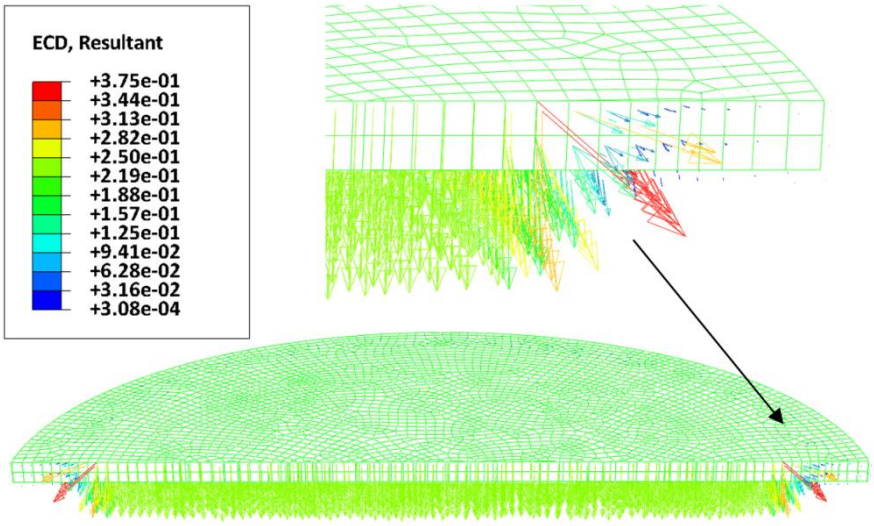


Figure 6.7 Cut view of electrical current density distribution in 0.5 mm model

6.1.3 Calculation of resistance

The resistance was calculated to quantify the influence of asymmetric electrode geometry in the simulation. Firstly, the normal component of electrical current density in the model was selected, as shown in Figure 6.8. Since the magnitude of total current in each layer of the model is same, therefore the total magnitude of the current cross in the model is then calculated by multiply the electrical current density of each element in one of the layers of the model by its corresponded element area. The area of each element was calculated by dividing the volume of each element by the thickness of one layer of the model. The resistance of the model was calculated by dividing the magnitude of electrical potential difference by the magnitude of current in cross-section.

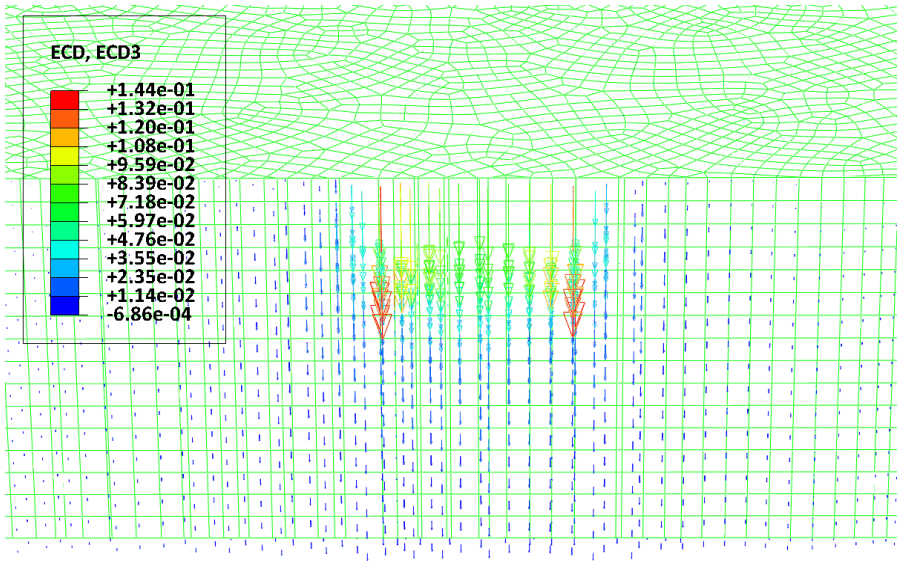


Figure 6.8 Magnitude of electrical current density in perpendicular direction to the surface in thick model

The calculated resistance results were plotted against the reciprocal of the scale factor of the model, as shown in Figure 6.9. The resistance results were fitted with a quadratic polynomial function, which has shown good agreement as the coefficient of determination, R squared, is close to 1. Therefore, the resistance of a sample with same thickness but different electrode area can be estimated by the fitted quadratic polynomial function. The red sloping trend line is representing the resistivity of YSZ,

which is a constant independent of the geometry of the material. However, it is shown that all calculated resistances were plotted on the right side of the slope and offset of it in different levels, which means all calculated resistance from the simulation are lower than the resistance calculated by its electrode area. Moreover, it is shown that the resistances of the model with a larger scale factor are close to the resistivity slope, which means the thin model with larger electrode area is less affected by asymmetric electrical field. Furthermore, it is worth noting that there are several models have different values of resistance with the same scale factors. It is shown that under same scale factor, the geometry with larger volume has smaller resistance.

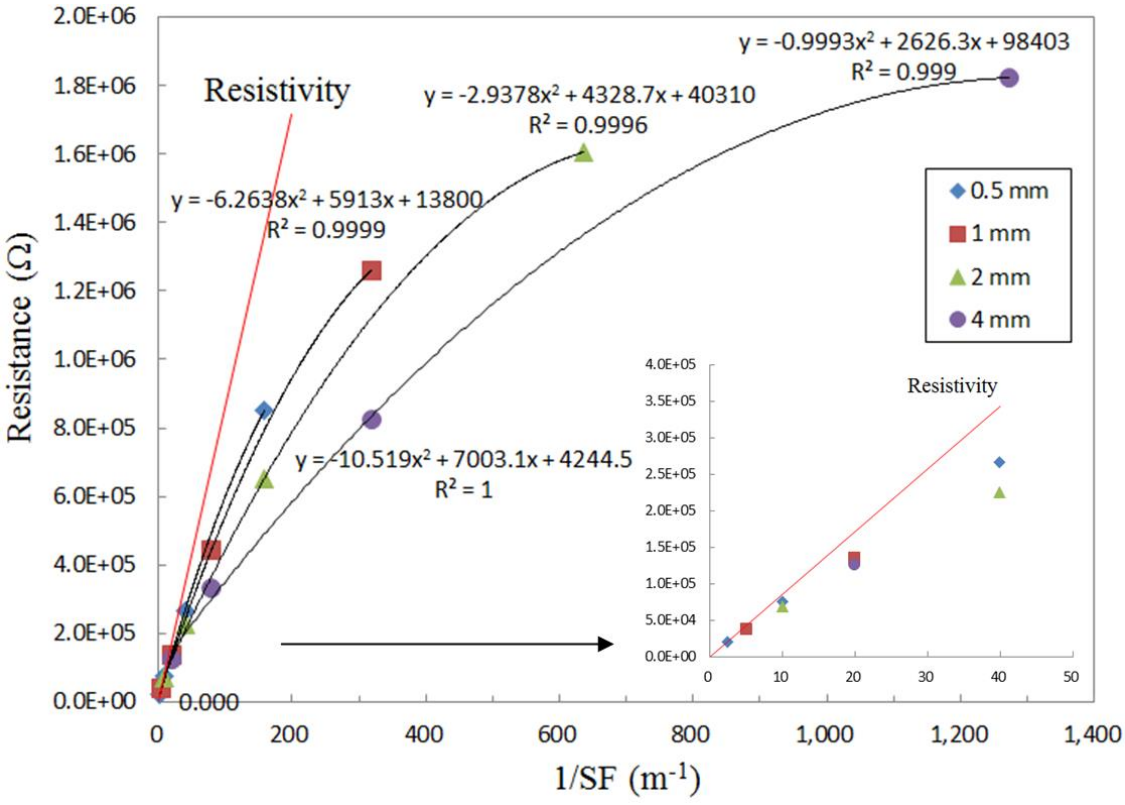


Figure 6.9 Calculated resistances of simulated model plotted against the reciprocal of the scale factor fitted with quadratic polynomial function

6.1.4 Equivalent electrode area

Considering the geometry of measured resistance is a cylinder, and since the thickness of the geometry is known, an estimated equivalent electrode area of the measured resistance can be calculated by Equation 6.4.

$$A_{equivalent} = \frac{l}{\sigma R_{measured}} \tag{6.4}$$

This estimated value can be used to correct the resistance measurement in an impedance spectroscopy experiment by replacing the area of applied conductive paint in the calculation, which will fix the influence of asymmetric electrode geometry on resistance calculation, thus, provide a more accurate resistance measurement of the tested material.

In order to find a relationship between the resistance and applied electrode area further calculation was carried out. An area ratio was calculated by divided the equivalent area by applied electrode area. The area ratio of each geometry is plotted with the calculated resistance respectively, as shown in Figure 6.10.

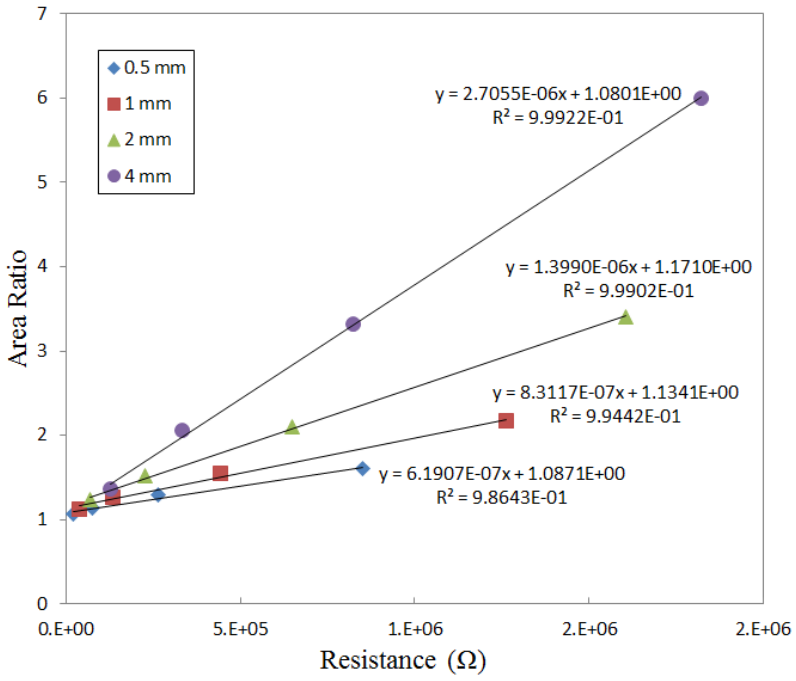


Figure 6.10 Area ratios of the effective area to applied electrode area plotted with each corresponding calculated resistance from the simulation. Models with the same thickness are fitted with a linear tendency line.

As a result, it is shown that the area ratio increases linearly with corresponding calculated resistance. The gradient of fitted tendency line increases with increasing the thickness of geometry, which is plotted in Figure 6.11. The coefficient of determination of fitted slope close to 1, thus, the linear model is a good fit for the data. The R square value also indicates the geometry with larger thickness has better agreement with the linear relationship.

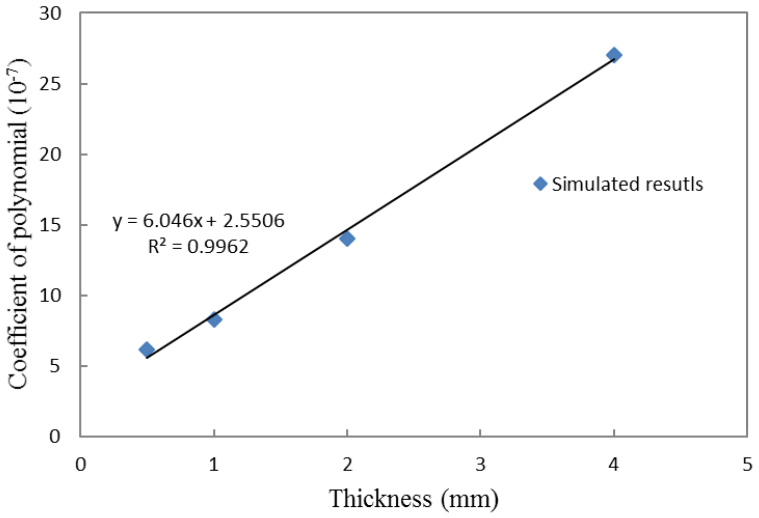


Figure 6.11 Gradient of fitted tendency line from area ratio-resistance plotted with each corresponding thickness of the geometry

As shown in Figure 6.11, a linear relationship between the gradient and corresponding thickness was found. The values were fitted with a linear tendency line where the R squared close to 1. As a result, an estimated resistance of a sample with a known asymmetric electrode geometry can be calculated via an inverse operation using the relationship found in Figure 6.10 and Figure 6.11. For example, the gradient of fitted tendency line of a certain thickness of the sample can be obtained from Figure 6.11.

The relationship between the area ratio and estimated resistance can be express as

$$Area\ ratio = \frac{A_{equivalent}}{A_{electrode}} = kR_{estimated} + \mathrm{c} \tag{6.5}$$

where k is the gradient of fitted tendency line, intercept c is a number close to 1. Then substitute the equivalent area from Equation 6.4, gives

$$\frac{l}{\sigma R_{measured} A_{electrode}} = kR_{estimated} + \mathrm{c} \tag{6.6}$$

Since the area of applied electrodes and geometry of measured specimen are known, also the electrical conductivity of the material is a constant, thus, an estimated resistance is calculated via equation 6.6. This method can be applied to estimate the resistance due to the change of thickness of the specimen based on previous simulated results. However, in the case of the sample has symmetric electrode geometry where two electrodes are applied with the same size, the area ratio equals 1, the estimated resistance should be equal to the measured resistance, while, an inaccurate value of estimated resistance would be obtained from Equation 6.5 which equals (1-c)/k. Therefore, the estimated resistance by this method is inaccurate when the area ratio close to 1. Furthermore, the uncertainty of the value of intercept c in Equation 6.6 could lead to an inaccurate estimation. Further study on analysis the variation of this value is necessary.

6.1.5 Summary

This chapter has demonstrated the analysis of asymmetric electrode geometry effect on YSZ material using the finite element simulation. It is shown that asymmetric electrode geometry results in non-uniform current distribution in the simulated model where the current density is higher in the elements beneath the electrode than surrounding area, which then decreases through the thickness while spreading out to uniform current at the bottom. The direction of current diverges from the centre to the side by the radial electrical potential and then gradually return to the direction perpendicular to the surface. To investigate the influence of electrode size on the resistance of a sample, simulated models with 16 different scale factors within four sample geometries were calculated. It is shown that the resistances of the model with a smaller scale factor, a model with larger thickness and smaller electrode area, is more affected by asymmetric electrode geometry effect. An equivalent electrode area is calculated which can be used to fix the influence of asymmetric electrode geometry in impedance spectroscopy measurement by replacing the area of applied conductive paint in the calculation. Furthermore, a linear relationship is revealed between the ratio of equivalent area to applied electrode area and the resistance of simulated model. Moreover, the gradient of their plots is proportional to the thickness of the sample. Based on the relationship, a method is proposed to estimate the resistance of a sample with a known asymmetric electrode geometry via an inverse operation. Further study is suggested on analysis of the variation of the value of intercept c in the equation of resistance estimation.

6.2 Impedance spectroscopy measurement of the resistance of YSZ bulk with an asymmetric electrode geometry

To verify the previous findings in finite element simulation, a set of YSZ ceramic bulk samples with asymmetric electrodes geometry were measured using electrochemical impedance spectroscopy (EIS). The impedance spectroscopy measurement process along with self-assembled instruments are introduced at the beginning of this chapter. The impedance spectrums of 4 mm sample with various electrode area over the temperature range 250 °C to 350 °C are presented as an example to demonstrate the relaionship among sample resistance, measurement temperature and applied eletrode area. Equivalent electrical circuits for modelling YSZ bulk sample is given along with the data verification using the Arrhenius plot. A comparison between fitted resistance from impedance spectroscopy measurement and calculated resistance from finite element simulation is shown. The feasibility and potential application of this simulation method will be discussed at the end of the chapter.

6.2.1 Impedance spectroscopy measurement

The process of fabrication of ceramic bulk samples has been described in chapter 3.3. The previous measurement has shown that relative densities of all the samples were above 98% which has ensured the influence of porosity on impedance measurement was negligible. A layer of platinum paste was applied to both sides of the samples as two electrodes, where one side was fully covered act as counter electrode, and the other side was applied to a round area with diameters around 2.3 mm, 4.4 mm, 7.5 mm, 12 mm and 16.5 mm, which increased gradually between EIS tests. The platinum paste was cured in an oven at 200 °C for 30 minutes followed by 900 °C for one hour, and the temperature gradient was 10 °C/min during the heating and cooling. Figure 6.12 shows both sides of 4 mm sample with 2.3 mm electrode on the front side. To ensure the accuracy of the calculation, the area of electrodes with diameters of 2.3 mm and 4.4 mm was measured by an optical microscope. The rest of the samples were scanned by a photo scanner in a high resolution, where the area of the electrodes was measured in the number of pixels then converted to really scale.

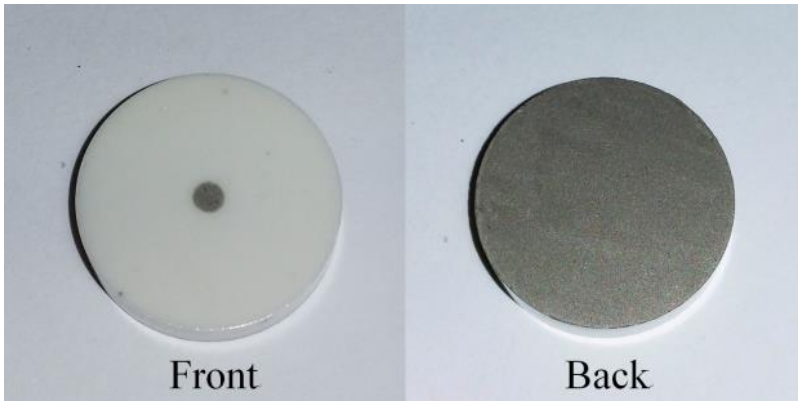


Figure 6.12 Example of YSZ ceramic bulk sample with coated electrodes: 4 mm sample with electrode diameter of 2.3 mm on the front side.

The sample with coated electrodes was connected in a self-made ceramic sample jig, as shown in Figure 6.13 (a). A spring was installed at the end of the jig which can hold the sample without letting it touches the internal wall. The platinum wires connected sample were covered by alumina tube which was shielded in two sections of steel tube. The sample jig with the loaded sample was then placed in a wound furnace (Carbolite MTF 12/38/400) where the temperature was controlled to ±1 °C over the temperature range 250 °C to 350 °C by an extra thermal couple placed in the jig. The self-assembled impedance spectroscopy instrument is shown in Figure 6.13 (b). Impedance spectroscopy measurement was performed at 25 °C intervals using an impedance analyser (Solartron analytical ModuLab xm) at frequencies ranging from 0.1 Hz to 1 MHz.

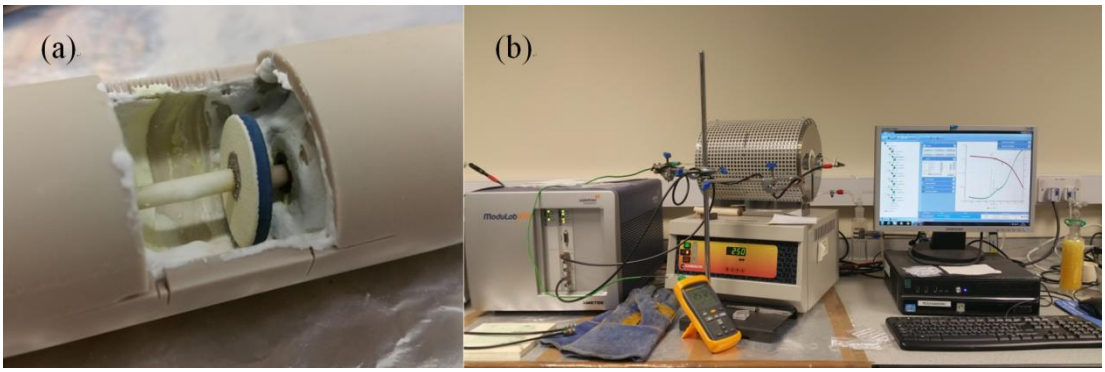


Figure 6.13 (a) Self-made ceramic sample jig for impedance spectroscopy measuring (b) Self-assembled impedance spectroscopy instrument

6.2.2 Impedance spectroscopy results

The complete IS data were acquired from 24 different geometries of four samples, each geometry was measured at five temperature points, which was sufficient to ensure the accuracy of the measurement and achieve the purpose of the experiment. The IS results of 4 mm YSZ bulk sample are shown here as an example to to demonstrate the relationship among sample resistance, measurement temperature and applied eletrode area. Figure 6.14 illustrates a Nyquist plot of the 4 mm sample with electrode diameter of 2.3 mm over the temperature range 250 °C to 350 °C. Two semicircles presented in the plot corresponding to the YSZ grain at a higher frequency and YSZ grain boundary at a lower frequency. The spike at the end of spectrum corresponds to the electrode reaction. It is shown that the semicircles reduced with increasing measurement temperature due to the decreasing resistivity of YSZ material.

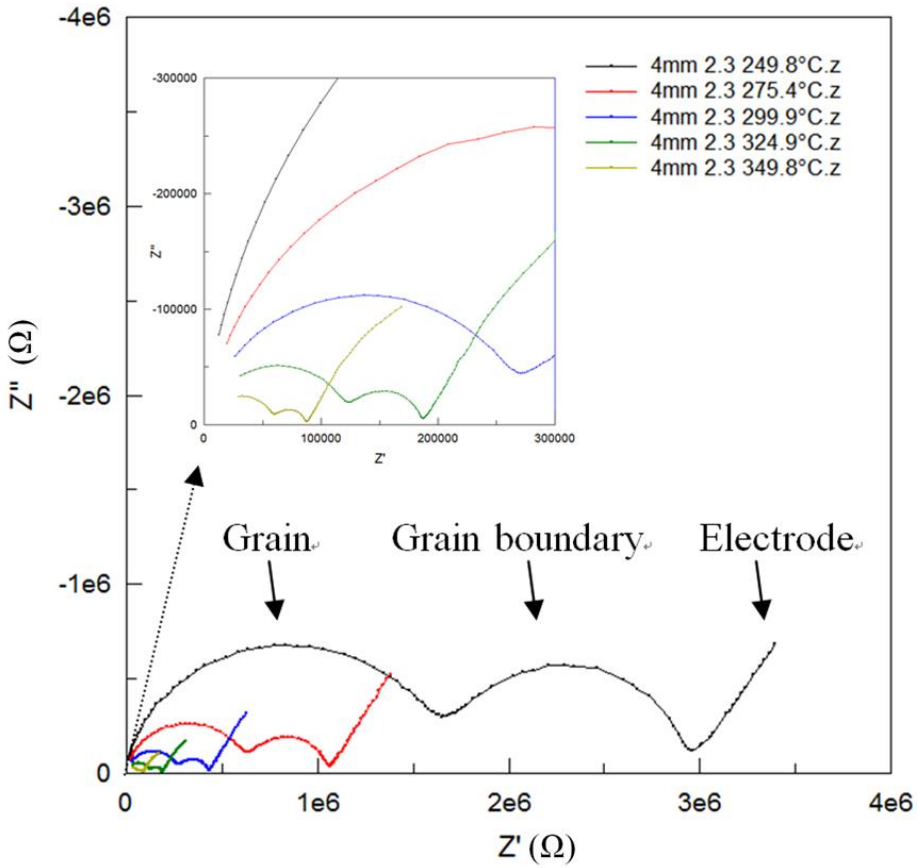


Figure 6.14 Nyquist plot of 4 mm YSZ bulk sample with electrode diameter of 2.3 mm over the temperature range 250 °C to 350 °C

Figure 6.15 illustrated the Bode plot of 4 mm YSZ bulk sample with electrode diameter of 2.3 mm over the temperature range 250 °C to 350 °C. It is shown that the magnitude of the impedance of YSZ bulk sample also decreases with increasing measurement temperature, while the phase angle of the spectrum shifts towards a higher frequency. The peaks in the Bode plot refer to the maximum phase angle, the frequency of the maximum phase angle shift to the higher frequency indicating that the electrochemical reaction is accelerated.

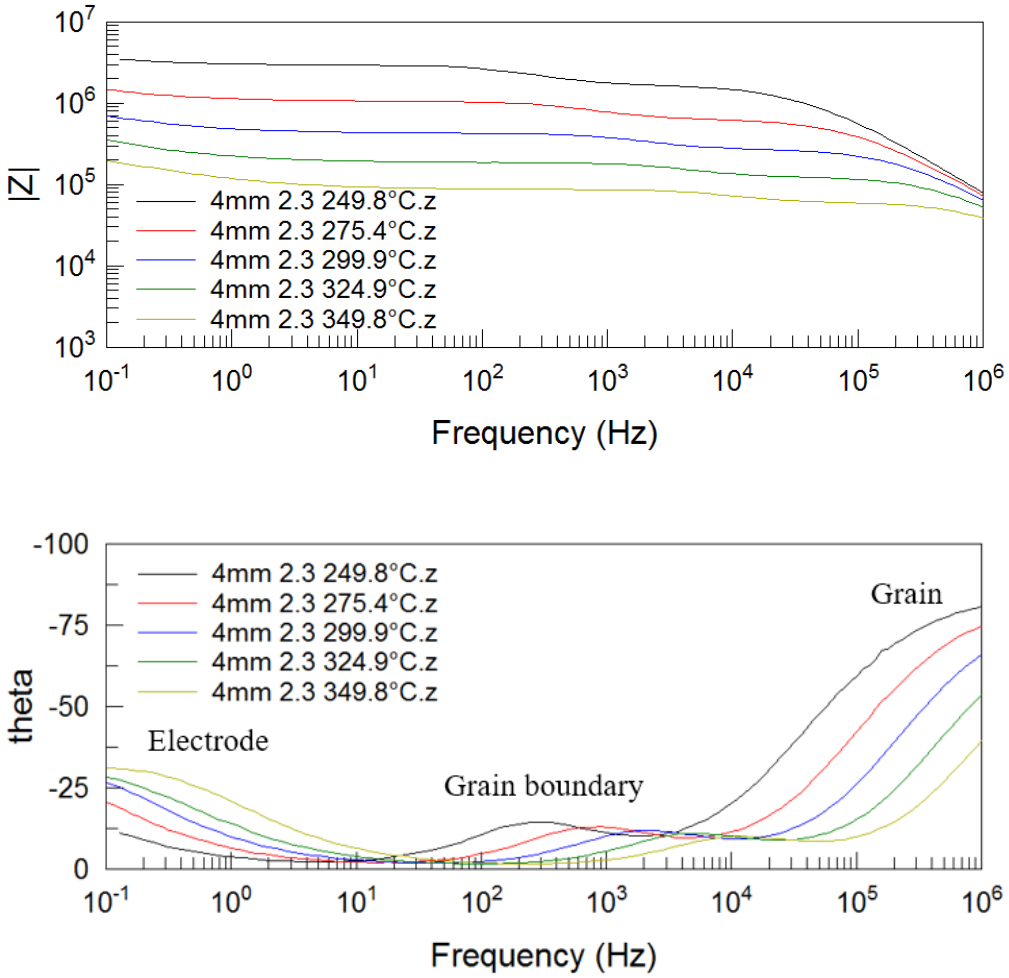


Figure 6.15 Bode plot of 4 mm YSZ bulk sample with electrode diameter of 2.3 mm over the temperature range 250 °C to 350 °C

Figure 6.16 illustrated the Nyquist plot of 4 mm YSZ bulk sample with electrode diameter vary from 2.3 mm to 19.6 mm (Symmetric electrode) at 250 °C. Similar to the spectrum in Figure 6.14, the arc corresponding to the YSZ grain and YSZ grain boundary reduced with increasing the area of the electrode. The change of the resistance of the sample is due to the change in sample electrode geometry while the resistivity of YSZ remained same as all measurements were taken at the same temperature.

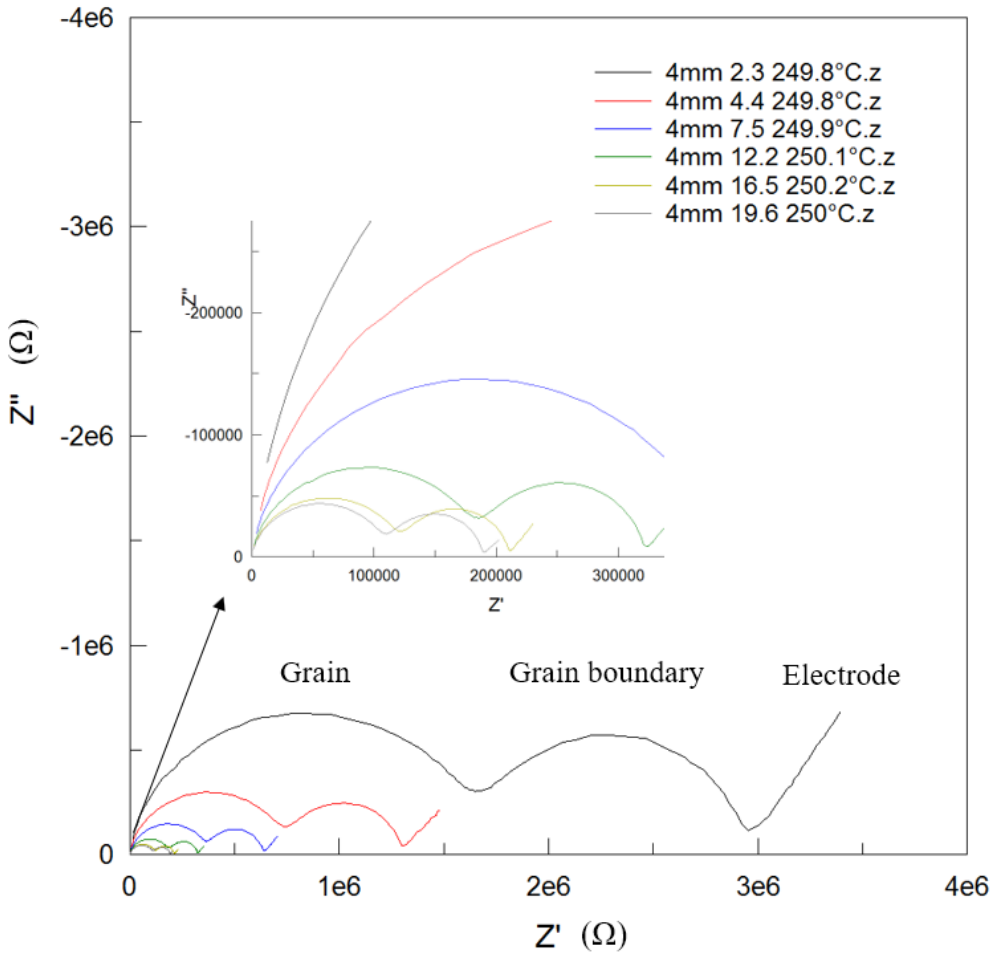


Figure 6.16 Nyquist plot of 4 mm YSZ bulk sample with electrode diameter varies from 2.3 mm to 19.6 mm (Symmetric electrode) at 250 °C

Figure 6.17 illustrated the Bode plot of 4 mm YSZ bulk sample with electrode diameter vary from 2.3 mm to 19.6 mm (Symmetric electrode) at 250 °C. It is shown that the magnitude of the impedance of YSZ bulk sample decreases with increasing measurement temperature, while the maximum phase angle remained at the same frequency. Therefore, the electrochemical reaction rate remained same as all measurements were taken at the same temperature.

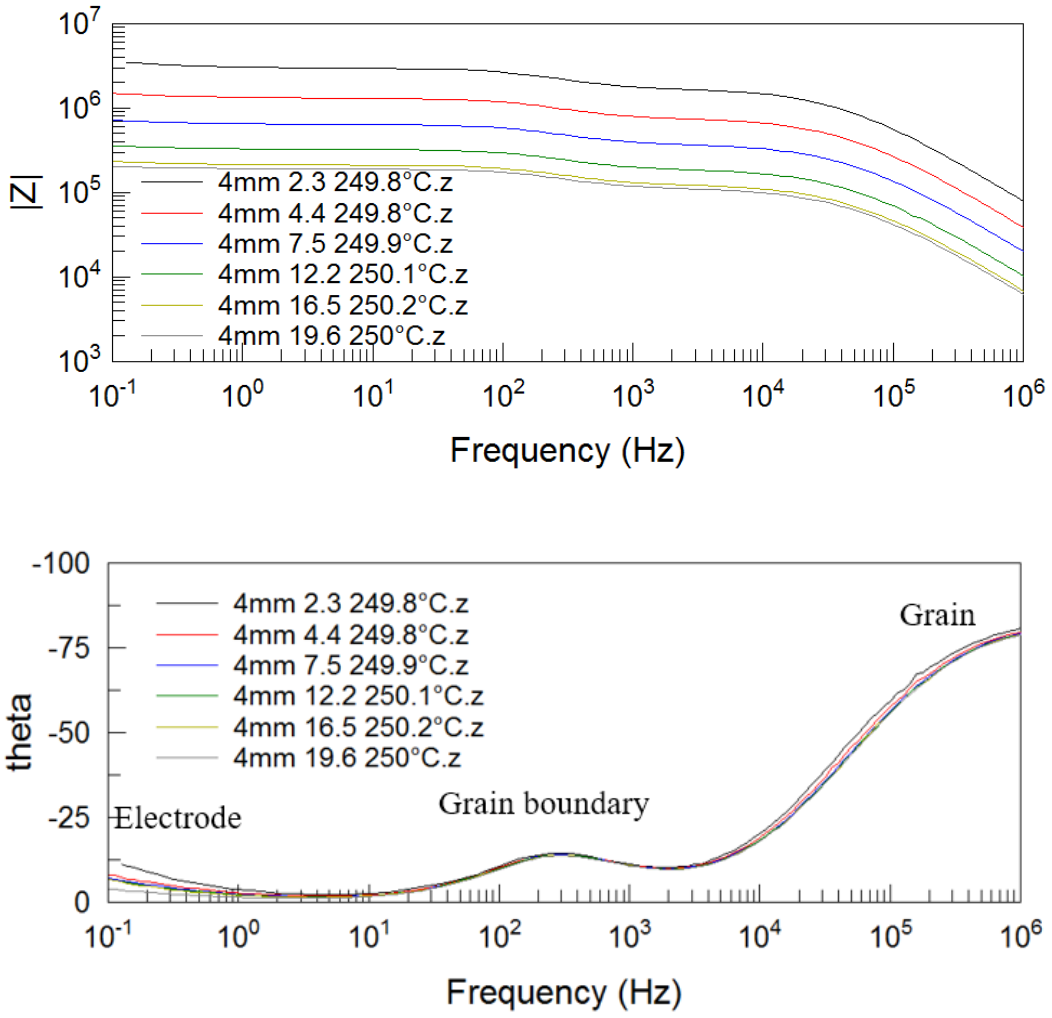


Figure 6.17 Bode plot of 4 mm YSZ bulk sample with electrode diameter varies from 2.3 mm to 19.6 mm (Symmetric electrode) at 250 °C

6.2.3 Equivalent circuit fitting

After the IS measurement, the spectrum was fitted with equivalent electrical circuits using Zview fitting software (Scribner Associates, Inc.). The equivalent circuit used for fitting impedance of YSZ ceramic sample is presented in Figure 6.18. In the model, two sets of the parallel connected resistor, capacitor and CPE component were used to simulate the resistance and capacitance of grain and grain boundary respectively. A finite length Warburg element was added to the equivalent circuit to fit the electrode response.

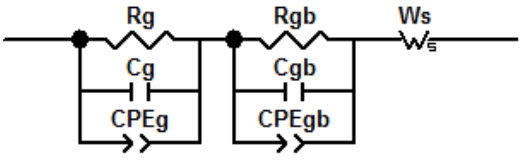


Figure 6.18 Equivalent electrical circuits for modelling YSZ bulk sample.

The conductivity of each tested sample at temperature range 250 °C to 350 °C was calculated using the fitted value of resistance. The conductivity is then verify using Arrhenius plot, where the tendency of the plot is a straight line if the electrochemical reaction has a rate constant that obeys the Arrhenius equation [162], as shown in Equation 6.7.

$$lnk = \frac{-E_a}{RT} + lnA \tag{6.7}$$

where k is the rate constant of chemical reactions on the temperature T in absolute temperature, E_a is activation energy, A is the pre-exponential factor and R is the universal gas constant.

Therefore, Arrhenius plot of all sample geometries was plotted by the natural logarithm of conductivity against 1000/T, where T is the temperature in Kelvin, as shown in Figure 6.19. All equivalent circuit fitted data shown are valid as the R squared of the fitted trend line is close to 1.

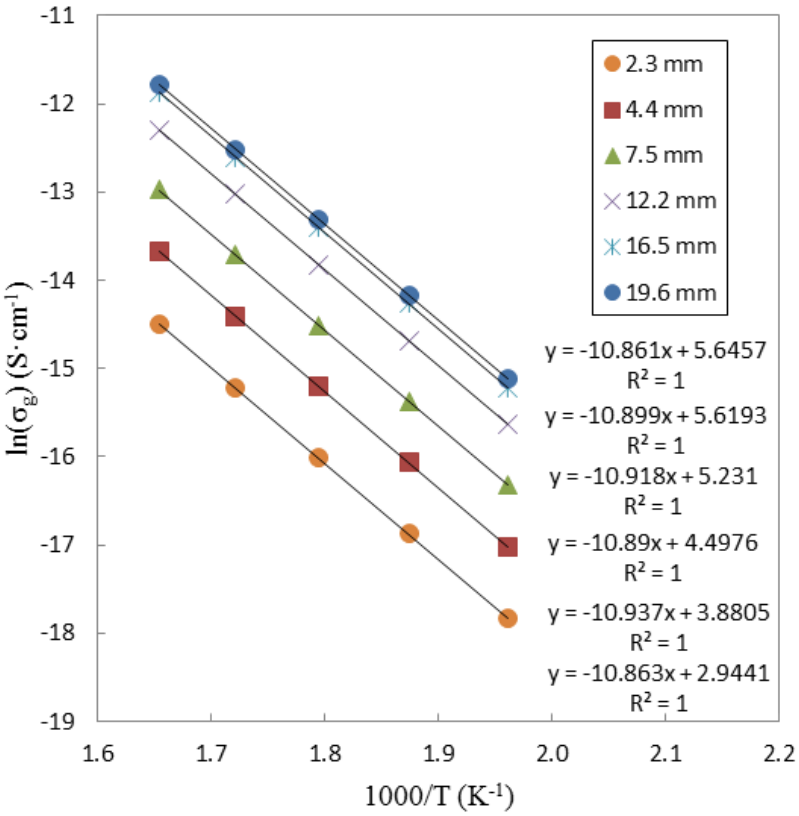


Figure 6.19 Natural logarithm of conductivity in Arrhenius plot of 4 mm sample with various diameter of electrode

6.2.4 Discussion

Same analysis process used for the finite element simulation results was also conducted for analysing results measured by impedance spectroscopy. As a demonstration the resistances at 250 °C were plotted against the reciprocal of the scale factor of the model, as shown in Figure 6.20. For comparison purpose, a finite element model is simulated using the same geometry and same electrode area of the sample with a thickness of 4.055 mm, which has the smallest scale factor in the sample set. The calculated resistance from the simulation with various asymmetric electrode geometry was plotted in the Figure 6.20. All results of resistance were fitted with a quadratic polynomial function, which has shown good agreement as the R squared is close to 1. It is shown that the IS measured resistances and the finite element simulated resistances have good agreement on their tendency with the corresponded scale factor. However, there is a difference of resistances between simulation and experiment in 4 mm sample which varies in a range from 3.6% to 11.2%.

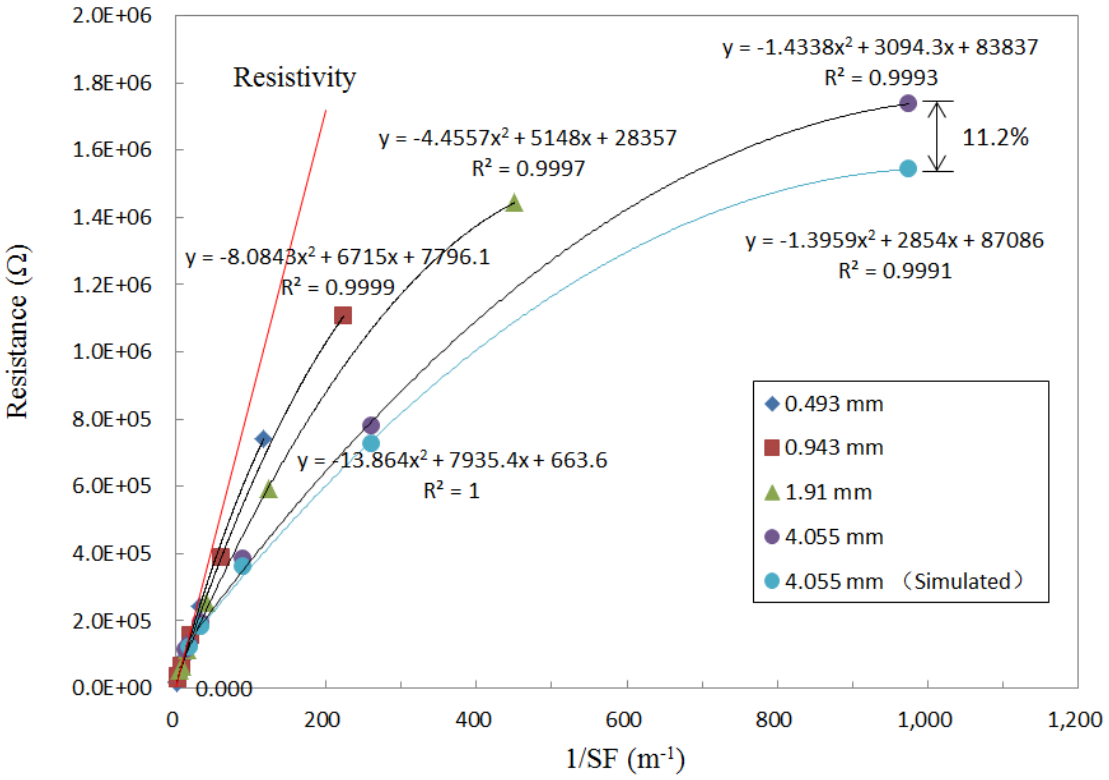


Figure 6.20 Calculated resistances of simulated model plotted against the reciprocal of the scale factor fitted with quadratic polynomial function IS measured resistances of corresponded scale factors at 250 °C

Same as previous method of analysis of simulation results, the resistance of a sample with a known asymmetric electrode geometry can be estimated using IS measured resistance via an inverse operation. The estimated equivalent electrode areas of the measured resistances were calculated using Equation 6.4. The area ratio was then calculated by divided the equivalent area by applied electrode area. The area ratio of each geometry is plotted with the calculated resistance respectively. However, the first data point that has relatively smaller area ratio is identified as an outlier. Therefore, the increment area ratios excluding first data point were plotted against resistances, as shown in Figure 6.21. The coefficient of determination of fitted slope is close to 1, thus, the linear model is a good fit for the data.

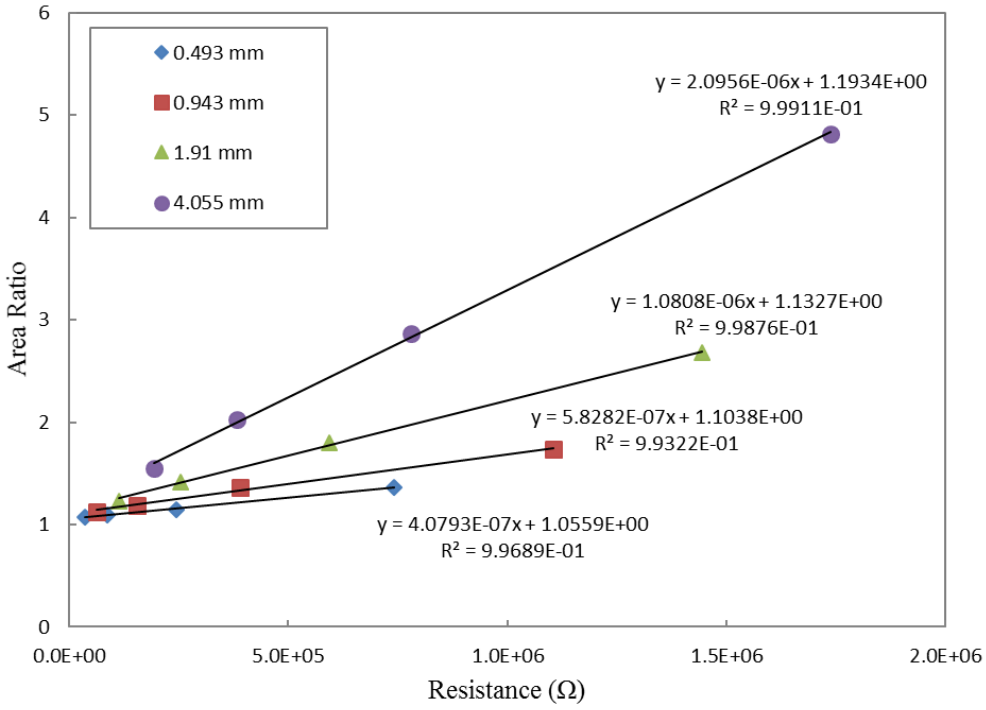


Figure 6.21 Area ratios of the effective area to applied electrode area plotted against each corresponding fitted resistance from impedance spectroscopy measurement at 250 °C. Models with the same thickness is fitted with a linear tendency line.

The gradient of fitted tendency line from area ratio-resistance is plotted with each corresponding thickness of the geometry, as shown in Figure 6.22. It is shown that experiment results have better agreement with the fitted trend line than simulated results.

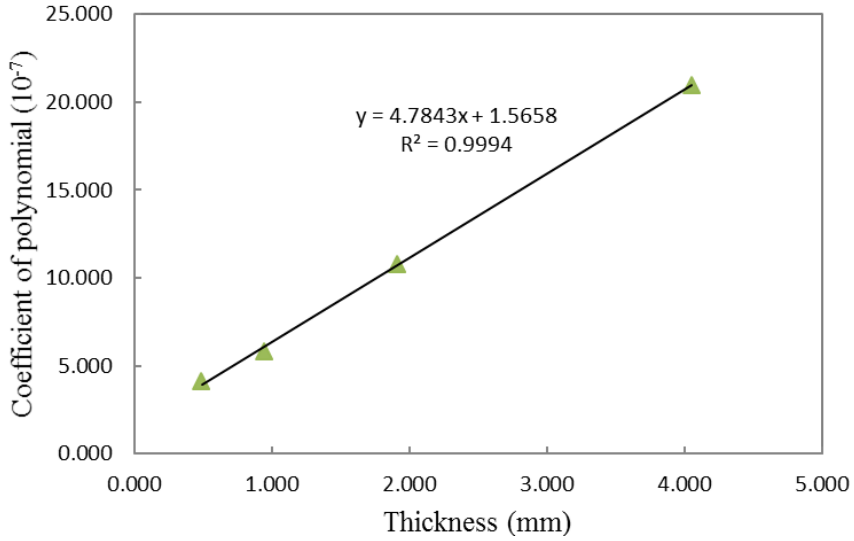


Figure 6.22 Gradient of fitted tendency line from area ratio-resistance plotted with each corresponding thickness of the geometry

As shown in Figure 6.20, the error between the simulated resistance and measured resistance of the sample with the smallest scale factor is 11.2%, where the area of the electrode on the top of the sample is only 4.16 mm^2. However, impedance measurement of a thick sample using an extremely small electrode is not common in practice. It is also shown that the error reduced to 3.6% when the top electrode area increased to two-thirds of the bottom electrode area. As mentioned previously, the asymmetric electrode geometry occurs in impedance spectroscopy measurement mainly in order to avoid the effects of surface leakage current. In this case, the finite element simulation method for measuring the resistance of the sample is fairly accurate, especially for measuring thin coating material. The simulated resistance can be used to calculate an equivalent electrode area to improve the accuracy of impedance spectroscopy measurement. Furthermore, the resistance of the sample with various electrode area at the same thickness can be estimated directly using a fitted quadratic polynomial function.

One potential application, which is also the source of the idea of this research, is to measure the resistance of thermal barrier coating on a turbine blade via a simulated impedance spectroscopy measurement. In practice, to perform an evaluation of thermal barrier coating on turbine blade using impedance spectroscopy, a tested area is coated with carbon act as one electrode, the exposed metallic substrate at the base of the blade is act as a counter electrode. In this case, the current density distribution in the thermal barrier coating is unknown due to the asymmetric electrode geometry and the curved surface of the turbine blade, however, this can be observed in the finite element simulation. Furthermore, by applying the calculated equivalent electrode area in impedance spectroscopy measurement, more accurate electrical properties of the thermal barrier coating will be obtained as a result. Currently study has only focused on YSZ bulk sample, while the influence of asymmetric electrode geometry on thermal barrier coating system still lack understanding. Therefore, further study will first focus on analysis the asymmetric electrode geometry on air plasma spayed freestanding YSZ coating and then move on to thermal barrier coating in thermal oxidation, where TGO layer will be investigated.

6.2.5 Summary

In this chapter, the previous findings in finite element simulation were verified via electrochemical impedance spectroscopy using a set of YSZ ceramic bulk samples with asymmetric electrodes geometry. The impedance spectroscopy measurement process was demonstrated at the beginning of this chapter. The impedance spectrums of 4 mm sample with various electrode area over the temperature range 250 °C to 350 °C were presented as an example to demonstrate the relaionship among sample resistance, measurement temperature and applied eletrode area. Two semicircles were found in Nyquist plot corresponding to the YSZ grain at a higher frequency and YSZ grain boundary at a lower frequency. The spike at the end of spectrum corresponds to the electrode reaction. It is shown that the semicircles reduced with increasing measurement temperature due to the decreasing resistivity of YSZ material. The phase angle of the spectrum in the Bode plot shifts towards higher frequency was noted, indicating that the electrochemical reaction is accelerated due to the increase of measurement temperature. Equivalent electrical circuits for modelling YSZ bulk sample was shown along with the data verification using the Arrhenius plot. All equivalent circuit fitted data shown are valid as the R squared of the fitted trend line is close to 1. The fitted resistance from impedance spectroscopy measurement and the calculated resistance from finite element simulation were compared, good agreement on their tendency with the corresponded scale factor was shown. The difference of resistances between simulation and experiment in 4 mm sample varies in a range from 3.6% to 11.2%. The feasibility and potential application of this simulation method were discussed at the end of the chapter. Further study on the influence of the asymmetric electrode geometry on thermal barrier coating system was suggested.

Chapter 7

Conclusions and Future Work

The work presented in this thesis has studied the oxidation behaviours of thermal barrier coatings in high temperature cyclic oxidation using three different non-destructive evaluation techniques along with microstructure analysis, including X-ray computed tomography, laser photoacoustic spectroscopy and impedance spectroscopy.

In Chapter 4, the internal microstructure and exterior surface morphology of an unconventional TBC sample coated by ESAVD were investigated using two different laboratory X-ray CT scan systems. As a result, an image resolution of 0.6 μm is achieved by Xradia XRM-500 X-ray CT, five different layers were observed in the thermal barrier coating system including a few of cracks at the interface of YSZ layer and bond coat. However, the samples for the X-ray CT testing are required to be made extremely small to reduce the X-ray attenuation by sample, the best resolution of the image of the thermal barrier coating was acquired at the pointed end of spine sample where the width is about 200 μm. In conclusion, X-ray CT technique is not suitable for industrial in-situ detection for thermal barrier coating.

In Chapter 5, the thermal cyclic oxidation behaviour of conventional 7-8 wt.% YSZ air plasma sprayed TBC sample was evaluated using laser photoacoustic spectroscopy. Thermal barrier coating sample with two different types of substrate, namely single crystal superalloy substrate and multigrain superalloy substrate, at different thermal cyclic oxidation condition were measured. C-scan was carried out across each sample

and result was shown in amplitude map, signal energy map, frequency map and phase map along with corresponded analysis technique.

A relationship was found between the amplitude levels and the number of thermal cycles, indicated that the amplitude decreases with an increasing number of thermal cycles, which is due to the increased thickness of TGO layer and presence of delamination inside the coating. Analysis on signal energy map revealed that energy of received signal decreases with an increase in oxidation time as a parabolic function in energy-thermal oxidation plot which is related to parabolic oxidation behaviour of thermal barrier coatings. Both amplitude plot and signal energy plot have shown a data segregation between multigrain TBC samples due to the ultrasound attenuation of two types of crystal grains in the substrate. The thickness of TGO layer of each sample after thermal cyclic oxidation was measured in a panorama BSE image using image analysis. A relationship was found between signal energy and TGO thickness, illustrating that signal energy decreases with the increasing TGO thickness. A physical model was studied to estimate the influence of crack inside TGO on signal attenuation, which indicated that the signal energy reduction is due to a combination of laser reflection at interfaces, laser attenuation by TGO layer and ultrasound reflection at interfaces. In addition, the position of the presence of crack inside of TGO alters the remainder of signal energy, where crack presented near the interface of TGO layer and bond coat attenuates more signal energy. A more comprehensive image analysis was suggested to accommodate more complicated signal attenuation calculation.

Moreover, the study of laser attenuation in YSZ ceramic coating indicated that the ultrasound signal is not generated in YSZ layer. It is also shown that thermal cyclic oxidation could increase the laser attenuation by growing the size of cracks and the increasing number of the cracks which formed inside of YSZ layer. Further study on amplitude attenuation in a bond coat only sample has confirmed that ultrasound signal was generated in TGO layer which works as a constrained surface layer facilitate the laser ultrasonic generation at early oxidation stage. Subsequently, the amplitude decreases with the increasing thermal cycles. It is shown that the increasing thickness of TGO layer increased the attenuation of laser irradiation, and the increasing number of cracks in TGO layer increased the laser reflection at crack/TGO interfaces. The

observation of surface morphology of the oxidation of bond coat has well explained the amplitude change in the LPAS measurement.

Phase map analysis was carried out and used to indicate the signal loss at the edge of the sample after thermal cycling. The microstructure at the edge of MG as-sprayed sample and samples after thermal cyclic oxidation of 5, 10, 20, 40 and 80 has shown that cracks gradually increase in a ceramic layer with the increasing of thermal oxidation cycles, which leads to the lower amplitudes at the edge. Evaluation of thermal barrier coating using phase map analysis is highly dependents on the scanning resolution. The phase difference percentage and phase standard deviation of SX samples with higher scanning resolution both increase with increasing oxidation time. While the same analyses were not working for MG sample at lower thermal oxidation stage and can only be utilised as an indication when MG TBC sample is about to fail. On the other hand, the number of peaks in the phase map analysis of MG samples has shown a relationship that the number of peaks increases with increasing of thermal oxidation time, while this method for SX samples is invalid.

Further improvement of this method can be achieved by measuring the displacement of the substrate surface using a laser interferometer, which could eliminate the influence that introduced by the transducer. Some possible improvements and future plan of laser photoacoustic spectroscopy measurement will be given at end of the chapter.

Chapter 6 has first demonstrated the analysis of asymmetric electrode geometry effect on YSZ material using the finite element simulation, subsequently the findings of which were verified via electrochemical impedance spectroscopy using a set of YSZ ceramic bulk samples with asymmetric electrodes geometry. It is shown that asymmetric electrode geometry results in non-uniform current distribution in the simulated model where the current density is higher in the elements beneath the electrode than surrounding area, which then decreases through the thickness while spreading out to uniform current at the bottom. The direction of current diverges from the centre to the side by the radial electrical potential and then gradually return to the direction perpendicular to the surface.

To investigate the influence of electrode size on the resistance of a sample, simulated models with 16 different scale factors within four sample geometries were calculated. It is shown that the resistances of the model with a smaller scale factor, a model with larger thickness and smaller electrode area, is more affected by asymmetric electrode geometry effect. An equivalent electrode area is calculated which can be used to fix the influence of asymmetric electrode geometry in impedance spectroscopy measurement by replacing the area of applied conductive paint in the calculation. Furthermore, a linear relationship is revealed between the ratio of equivalent area to applied electrode area and the resistance of simulated model. Moreover, the gradient of their plots is proportional to the thickness of the sample. Based on the relationship, a method is proposed to estimate the resistance of a sample with a known asymmetric electrode geometry via an inverse operation. Further study is suggested on analysis of the variation of the value of intercept c in the equation of resistance estimation.

In the impedance spectroscopy measurement, two semicircles were found in Nyquist plot corresponding to the YSZ grain at a higher frequency and YSZ grain boundary at a lower frequency. The spike at the end of spectrum corresponds to the electrode reaction. It is shown that the semicircles reduced with increasing measurement temperature due to the decreasing resistivity of YSZ material. The phase angle of the spectrum in the Bode plot shifts towards higher frequency was noted, indicating that the electrochemical reaction is accelerated due to the increase of measurement temperature. Equivalent electrical circuits for modelling YSZ bulk sample was shown along with the data verification using the Arrhenius plot. All equivalent circuit fitted data shown are valid as the R squared of the fitted trend line is close to 1. The fitted resistance from impedance spectroscopy measurement and the calculated resistance from finite element simulation were compared, good agreement on their tendency with the corresponded scale factor was shown. The difference of resistances between simulation and experiment in 4 mm sample varies in a range from 3.6% to 11.2%. The feasibility and potential application of this simulation method were discussed at the end of the chapter. Further study on the influence of the asymmetric electrode geometry on thermal barrier coating system was suggested.

List of Achievements

- Fabricated thermal barrier coating sample for this study including substrate preparation, HVOF sprayed NiCoCrAlY bond coat, air plasma sprayed YSZ top coat and performed 1150 °C high temperature cyclic oxidation for TBC samples.

- Reported microstructure evolutions of air plasma sprayed YSZ coating with NiCoCrAlY bond coat in thermal cyclic oxidation.

- Established a high accurate SEM image analysis method enabling measures both the TGO layer and cracks in a panorama BSE image using Photoshop software.

- Observed the internal microstructure of thermal barrier coating coated by ESAVD within an image with a resolution of 0.6 μm using X-ray computed tomography, while the exterior morphology of the TBC sample was observed using 3D reconstruction.

- Realised nondestructive evaluation of thermal barrier coating in thermal cyclic oxidation using a self-assembled laser photoacoustic spectroscopy. This technique has overcome the short of conventional ultrasound technique by providing a noncontact laser ultrasound generation which generates ultrasound at sub-layer could avoid signal attenuation by the surface YSZ layer and reduces the signal interference during the propagation through the porous laminated structure of YSZ.

- Illustrated and analysed the relationship between the number of thermal cycles and the signal amplitude, signal energy and phase angle from LPAS measurement, respectively.

- Purposed a physical model to study the influence of crack inside TGO on signal attenuation, which indicated that the signal energy reduction is due to a combination of laser reflection at interfaces, laser attenuation by TGO layer and ultrasound reflection at interfaces. Indicated the position of the presence of crack inside of TGO alters the remainder of signal energy in LPAS measurement.

- Discovered that ultrasound signal was generated in TGO layer by investigating on amplitude attenuation in freestanding YSZ ceramic coating and bond coat only sample. Explained the amplitude change in the LPAS measurement by observing the surface morphology of the oxidation of bond coat under SEM. Indicated that TGO layer which works as a constrained surface layer facilitate the laser ultrasonic generation at early oxidation stage.

- Revealed the electrical current density distribution in YSZ bulk with an asymmetric electrode geometry using finite element simulation.

- Established a method to calculate the resistance of a finite element model and estimate the resistance of the sample with various electrode area at the same thickness. (the thickness of estimated sample has to be the same, high accurate) An equivalent electrode area is calculated from the simulated resistance, which can improve the accuracy of impedance spectroscopy measurement by replacing the area of the applied electrode.

- Revealed a relationship among thickness, applied electrode area and sample resistance. Based on the relationship, a method is proposed to estimate the resistance of a sample with a various thickness in an asymmetric electrode geometry via an inverse operation. (thickness of estimated sample can be any value, not accurate when area ratio close to 1)

Future Work

The c-scan images and other results from LPAS measurement in chapter 5 illustrate the feasibility of this technique for evaluation of thermal barrier coating. However, there are still some improvements to be done in the method such as carry out a more accurate crack measurement in TGO layer, eliminate the non-uniform signal response in c-scan and perform a noncontact detection. In chapter 6, a finite element simulation method was established for measuring the resistance between a pair of asymmetric electrodes. Nevertheless, there is still much research to be done in order to apply this method to nondestructive evaluation for thermal barrier coating on the turbine blade.

Crack measurement via an optimised image analysis

In practice, the position and the number of cracks in TGO layer are much more complicated than the simple physical model shown previously. However, it can be solved by image analysis using Photoshop and a MATLAB script. A pre-process is carried out in Photoshop which is similar to previous crack image analysis, except it selects TGO layer without removing the cracks at the top. Then the brightness of cracks is set to 0, TGO layer is set to 129 and everything else is set to 255, as shown in Figure 7.1.

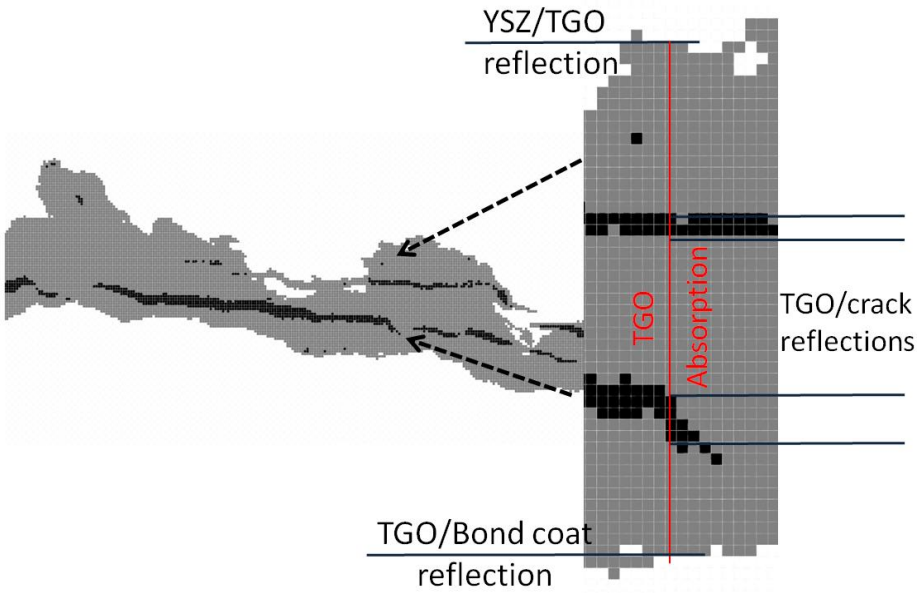


Figure 7.1 Pre-process for image analysis by Photoshop

After the pre-processing, the image is loaded in MATLAB as a matrix consisting of elements of the value of 0, 129 and 255. Each column of the matrix is analysed in a loop of a Matlab script to identify the number of element sets, which is noted as N + 3. The total number of elements which are 129 is counted, defined as the thickness of TGO layer, d. In order to identify the bonding condition at two ends, the first and the last element of value which is not 255 is found. If only the first element is 0, means crack is presented at the interface of YSZ and TGO, Equation 5.20 is applied; if only the last element is 0, means crack is presented at the interface of TGO and bond coat, then Equation 5.21 is applied; if none of them is 0, Equation 5.19 is applied and N = 0; and if they both are 0 the following Equation 7.1 is applied. By calculating the average value of the total remainder power of each column a more accurate evaluation of microstructure of TGO layer can be obtained.

$$I_{N_both} = \left[\frac{16Nn_{TGO}^2}{(n_{TGO}+1)^{4N}}\right]\left[\frac{4\,n_{YSZ}\,n_{nickel}}{(n_{YSZ}+1)^2(1+n_{nickel})^2}\right] e^{-\alpha_{TGO}d} \quad (7.1)$$

Comparing with previous image analysis of crack ratio which has only considered the ultrasound lost by the area where cracks beneath the TGO layer, this method is more comprehensive. It has taken account of the reduction of laser attenuation by TGO layer where there no crack appeared, added the remaining laser energy after passing through TGO layer and the intensity of ultrasound generated under the crack.

Subtraction of transducer response

Due to the signal attenuation differences among the test points caused by the geometry of the sample and delay line, the amplitude and the energy of a signal response are shown with a non-uniform distribution in a c-scan. There are two potential solutions to eliminate the influence that introduced by the transducer. One is to subtract the signal response of metallic substrate from the signal response of TBC sample, which requires matching the centre of c-scan images from two signal responses. The other solution is by using noncontact signal detection.

Noncontact signal detection

Noncontact signal detection can be achieved by measuring the displacement of the substrate surface using a laser interferometer. This method not only eliminates the influence of the transducer response, but also enables the measurement more

accurately. Since the laser interferometer is considerably less sensitive than the piezoelectric transducer, a generation laser with higher output power is recommended in the future measurement.

Future work on impedance spectroscopy

For impedance spectroscopy, further study on analysis the variation of the value of intercept c in the equation of resistance estimation is suggested, which can be carried out by complete the sample geometry in the simulation. Impedance spectroscopy currently is unable applied on nondestructive testing of the thermal barrier coating on the turbine blade component due to lack of understanding of asymmetric electrode geometry. Therefore, further study will first focus on analysis the asymmetric electrode geometry on air plasma spayed freestanding YSZ coating, and then move on to thermal barrier coating in thermal oxidation, where TGO layer will be investigated. Eventually, the research will focus on TBC system with the asymmetric electrode geometry caused by a turbine blade.

References

1. Hu, H., W. Shyy, and T.I.P. Shih, *Lift, Thrust, and Flight.* Encyclopedia of Aerospace Engineering, 2010.
2. Clark, S.F., *787 Propulsion System, AERO*. 2012.
3. Haselbach, F., *Hot end technology for advanced, low emission large civil aircraft engines*, in *28th international congress of the aeronautical sciences*. 2012, Rolls-Royce plc.
4. Mach, K.D., *Improving Turbine Component Efficiency.* Journal of Engineering for Power, 1980. 102(2): p. 434-436.
5. Beele, W., G. Marijnissen, and A. van Lieshout, *The evolution of thermal barrier coatings — status and upcoming solutions for today's key issues.* Surface and Coatings Technology, 1999. 120–121(0): p. 61-67.
6. Padture, N.P., M. Gell, and E.H. Jordan, *Thermal barrier coatings for gas-turbine engine applications.* Science, 2002. 296(5566): p. 280-284.
7. Wadley Research Group. *High Temperature Coatings*. Available from: http://www.virginia.edu/ms/research/wadley/high-temp.html.
8. Harris, K. and J.B. Wahl, *Improved Single Crystal Superalloys， CMSX-4 (SLS)[La+Y] and CMSX-486.* Superalloys, 2004.
9. Bose, S., *High Temperature Coatings*. 2007: Butterworth-Heinemann.
10. Harris, K., G.L. Erickson, and R.E. Schwer, *Directionally Solidified and Single-Crystal Superalloys*. Properties and Selection: Irons, Steels, and High-Performance Alloys (ASM International). Vol. Volume 1. 1990.
11. Gell, M., et al., *Advanced Superalloy Airfoil.* J. Met., 1987: p. 11-15.
12. Lapina, J., T. Pelachova, and O. Bajana, *The Effect of Microstructure on Mechanical Properties of Single Crystal CMSX-4 Superalloy.* METAL 2013. 5.
13. Shetty, M.N., *Dislocations and mechanical behaviour of materials*. 2013: PHI Learning.
14. Clarke, D.R. and S.R. Phillpot, *Thermal barrier coating materials.* Materialstoday, 2005. 8(6): p. 22-29.

15. Bose, S. and J. DeMasi-Marcin, *Thermal barrier coating experience in gas turbine engines at Pratt & Whitney.* Journal of Thermal Spray Technology, 1997. 6(1): p. 99-104.
16. Soares, C., *Gas Turbines: A Handbook of Air, Land and Sea Applications*. 2008: Butterworth-Heinemann.
17. Innovative Component Solutions Group. *Spare Parts of Gas & Steam Turbines and Compressors*. Available from: http://noavasys.com/en/products/item/64-gas-steam-turbines-spare-parts.
18. Chen, H.L., et al., *Ultrasonic Detection of Delamination and Material Characterization of Thermal Barrier Coatings.* Journal of Thermal Spray Technology, 2012. 21(6): p. 1184-1194.
19. Wright, P.K. and A.G. Evans, *Mechanisms governing the performance of thermal barrier coatings.* Current Opinion in Solid State & Materials Science, 1999. 4(3): p. 255-265.
20. Tolpygo, V.K., D.R. Clarke, and K.S. Murphy, *Oxidation-induced failure of EB-PVD thermal barrier coatings.* Surface & Coatings Technology, 2001. s 146–147(9): p. 124-131.
21. Reynolds, W.N., *Nondestructive evaluation of protective and thermal barrier coatings: a current survey.* Ndt International, 1987. 20(3): p. 153-156.
22. Zhang, B., *Nondestructive Evaluation of Thermal Barrier Coating Systems Using Ultrasonic Techniques.* Dissertations & Theses - Gradworks, 2010.
23. Ellingson, W.A., et al., *Optical NDE methods for ceramic thermal barrier coatings.* Materials evaluation, 2006. 64(1): p. 45-51.
24. Bose, S., *Chapter 8 - Nondestructive Inspection (NDI) of Coatings*. 2007: Elsevier Inc. 233-246.
25. Vaßen, R., et al., *Testing and evaluation of thermal-barrier coatings.* MRS bulletin, 2012. 37(10): p. 911-916.
26. Lescribaa, D. and A. Vincent, *Ultrasonic characterization of plasma-sprayed coatings.* Surface and Coatings Technology, 1996. 81(2–3): p. 297-306.
27. Ma, Z.Y., et al., *Ultrasonic characterization of thermally grown oxide in thermal barrier coating by reflection coefficient amplitude spectrum.* Ultrasonics, 2014: p. 1005–1009.

28. Mesrati, N., et al., *Characterization of thermal fatigue damage of thermal barrier produced by atmospheric plasma spraying.* Surface & Coatings Technology, 2004. 187(2): p. 185-193.
29. Zhao, Y., et al., *Investigation of interfacial properties of atmospheric plasma sprayed thermal barrier coatings with four-point bending and computed tomography technique.* Surface and Coatings Technology, 2012. 206(23): p. 4922-4929.
30. Jordan, D.W. and K.T. Faber, *X-ray residual stress analysis of a ceramic thermal barrier coating undergoing thermal cycling.* Thin Solid Films, 1993. 235(1-2): p. 137-141.
31. Siddiqui, S.F., et al., *Synchrotron X-ray measurement techniques for thermal barrier coated cylindrical samples under thermal gradients.* Review of Scientific Instruments, 2013. 84(8): p. 083904.
32. Asadizanjani, N., *3D Imaging and Investigation of Failure and Deformation in Thermal Barrier Coatings Using Computed X-ray Tomography.* 2014.
33. Mahmoud, M.M., et al., *40. Optimization and Development of X-ray Microscopy Technique for Investigation of Thermal Barrier Coating*. 2015: John Wiley & Sons, Inc.
34. Maurel, V., et al., *Three-dimensional investigation of thermal barrier coatings by synchrotron-radiation computed laminography.* Scripta Materialia, 2012. 66(7): p. 471-474.
35. Davies, S.J., et al., *Laser-generated ultrasound: Its properties, mechanisms and multifarious applications.* Journal of Physics D Applied Physics, 1993. 26(3): p. 329.
36. Ma, X., Y. Mizutani, and M. Takemoto, *Laser-induced surface acoustic waves for evaluation of elastic stiffness of plasma sprayed materials.* Journal of materials science, 2001. 36(23): p. 5633-5641.
37. Lima, R., et al., *Elastic modulus measurements via laser-ultrasonic and knoop indentation techniques in thermally sprayed coatings.* Journal of Thermal Spray Technology, 2005. 14(1): p. 52-60.
38. Krüger, S., et al., *Laser-Ultrasonic Evaluation of Thermal Spray Coatings.* 2008.

39. Rosa, G., et al., *Simultaneous laser generation and laser ultrasonic detection of the mechanical breakdown of a coating–substrate interface.* Ultrasonics, 2001. 39(5): p. 355-365.
40. Carlson, L., M. Ericsson, and L. Eva, *Laser-Ultrasonics (LUS) for examination of structure changes and defects in aluminium.* Stockholm: Corrosion and Metals Research Institute, 2005.
41. Zhao, Y., *Laser ultrasonic evaluation of bonding layer in thermal barrier coating.* Proceedings of SPIE - The International Society for Optical Engineering, 2015. 9438.
42. Schlichting, K.W., et al., *Application of Cr3+ Photoluminescence Piezo-Spectroscopy to Plasma-Sprayed Thermal Barrier Coatings for Residual Stress Measurement.* Materials Science & Engineering A, 2000. 291(1): p. 68-77.
43. Sohn, Y.H., et al., *Nondestructive evaluation of residual stress for thermal barrier coated turbine blades by Cr3+ photoluminescence piezospectroscopy.* Metallurgical & Materials Transactions A, 2000. 31(9): p. 2388-2391.
44. Gell, M., et al., *Photoluminescence Piezospectroscopy: A Multi-Purpose Quality Control and NDI Technique for Thermal Barrier Coatings.* International Journal of Applied Ceramic Technology, 2004. 1(4): p. 316–329.
45. Pilgrim, C.C., et al., *Photoluminescence for quantitative non-destructive evaluation of thermal barrier coating erosion.* Surface & Coatings Technology, 2012. 209(38): p. 44-51.
46. Ma, X.Q., Y. Mizutani, and M. Takemoto, *Laser-induced surface acoustic waves for evaluation of elastic stiffness of plasma sprayed materials.* Journal of Materials Science, 2001. 36(23): p. 5633-5641.
47. Shepard, S.M., et al. *Thermographic measurement of thermal barrier coating thickness*. in *Thermosense XXVII*. 2005.
48. Newaz, G. and X. Chen, *Progressive damage assessment in thermal barrier coatings using thermal wave imaging technique.* Surface and Coatings Technology, 2005. 190(1): p. 7-14.
49. Muralidhar, C., M.V. Reddy, and K. Kumaran. *Study and Performance Evaluation of Thermal Barrier Coatings (TBCs) using Infrared Thermography*. in *National Seminar on Nde*. 2006.
50. Eldridge, J.I., et al., *Health Monitoring of Thermal Barrier Coatings by Mid-Infrared Reflectance.* 2002. 24(3): p. 511-516.

51. Eldridge, J.I., et al., *Nondestructive Evaluation of Thermal Barrier Coatings by Mid-Infrared Reflectance Imaging.* Ceramic Engineering & Science Proceedings, 2005. 26(3): p. 121-128.
52. Eldridge, J.I., C.M. Spuckler, and R.E. Martin, *Monitoring Delamination Progression in Thermal Barrier Coatings by Mid-Infrared Reflectance Imaging.* International Journal of Applied Ceramic Technology, 2010. 3(2): p. 94-104.
53. Zhao, S.-b., et al., *Quality evaluation for air plasma spray thermal barrier coatings with pulsed thermography.* Progress in Natural Science: Materials International, 2011. 21(4): p. 301-306.
54. Bison, P., et al., *Ageing evaluation of thermal barrier coatings by thermal diffusivity*. Vol. 49. 2007. 286–291.
55. Macdonald, J.R. and W.B. Johnson, *Fundamentals of Impedance Spectroscopy*. 2005: John Wiley & Sons, Inc. 1-26.
56. Smialek, J.L. and N.G.R. Center, *Moisture-induced Alumina Scale Spallation: The Hydrogen Factor*. 2010: National Aeronautics and Space Administration, Glenn Research Center.
57. Ogawa, K., et al., *NDE of degradation of thermal barrier coating by means of impedance spectroscopy.* NDT & E International, 1999. 32(3): p. 177-185.
58. Wang, X., J. Mei, and P. Xiao, *Non-destructive evaluation of thermal barrier coatings using impedance spectroscopy.* Journal of the European Ceramic Society, 2001. 21(7): p. 855-859.
59. Song, S. and P. Xiao, *An impedance spectroscopy study of high-temperature oxidation of thermal barrier coatings.* Materials Science and Engineering: B, 2003. 97(1): p. 46-53.
60. Jayaraj, B., et al., *Electrochemical impedance spectroscopy of porous ZrO2–8wt.% Y2O3 and thermally grown oxide on nickel aluminide.* Materials Science and Engineering: A, 2004. 372(1): p. 278-286.
61. Jayaraj, B., et al., *Electrochemical impedance spectroscopy of thermal barrier coatings as a function of isothermal and cyclic thermal exposure.* Surface and Coatings Technology, 2004. 177: p. 140-151.
62. Zhang, C., et al., *Evaluation of thermal barrier coating exposed to different oxygen partial pressure environments by impedance spectroscopy.* Surface and Coatings Technology, 2006. 201(1–2): p. 446-451.

63. Deng, L., Y. Xiong, and P. Xiao, *Modelling and experimental study of impedance spectra of electron beam physical vapour deposition thermal barrier coatings.* Surface and Coatings Technology, 2007. 201(18): p. 7755-7763.

64. Ali, M.S., S. Song, and P. Xiao, *Evaluation of degradation of thermal barrier coatings using impedance spectroscopy.* Journal of the European Ceramic Society, 2002. 22(1): p. 101-107.

65. Patterson, T., et al., *Thermal cyclic lifetime and oxidation behavior of air plasma sprayed CoNiCrAlY bond coats for thermal barrier coatings.* Surface and Coatings Technology, 2008. 203(5): p. 437-441.

66. Hilpert, T. and E. Ivers-Tiffée, *Correlation of electrical and mechanical properties of zirconia based thermal barrier coatings.* Solid State Ionics, 2004. 175(1–4): p. 471-476.

67. Shinmi, A., X. Zhao, and P. Xiao, *Mechanical and electrical characterisation of a phase transformation in thermal barrier coatings.* Surface and Coatings Technology, 2010. 205(7): p. 2678-2686.

68. Anderson, P.S., X. Wang, and P. Xiao, *Impedance spectroscopy study of plasma sprayed and EB-PVD thermal barrier coatings.* Surface and Coatings Technology, 2004. 185(1): p. 106-119.

69. Tanno, M., K. Ogawa, and T. Shoji, *Influence of asymmetric electrode geometry on an impedance spectrum of a plasma-sprayed thermal barrier coating system.* Surface and Coatings Technology, 2010. 204(15): p. 2504-2509.

70. Hetmańczyk, M., L. Swadźba, and B. Mendala, *Advanced materials and protective coatings in aero-engines application.* Journal of Achievements in Materials and Manufacturing Engineering, 2007. 24(1): p. 372-381.

71. Chen, L.B., *Yttria-stabilized zirconia thermal barrier coatings 2014 a review.* Surface Review & Letters, 2006. 13(05): p. 535-544.

72. Miller, R.A., *Thermal Barrier Coatings for Aircraft Engines: History and Directions.* ASM International, 1997(42).

73. Stecura, S., *Effects of Compositional Changes on the Performance of a Thermal Barrier Coating System.* National Aeronautics and Space Administration, 1978(NASA TM-78976).

74. Goswami, B., A.K. Ray, and S. Sahay, *Thermal Barrier Coating System for Gas Turbine Application -A review*. High Temperature Materials and Processes, 2003. 23(2): p. 73-92.
75. Singh, J., et al., *An Overview: Electron Beam-Physical Vapor Deposition Technology Present and Future Applications.*
76. Leyens, C., U. Schulz, and M.B.M. Peters, *R&D Status and Needs for Improved EB-PVD Thermal Barrier Coating Performance.* Mrs Online Proceedings Library Archive, 2000. 645.
77. Hass, D.D., et al., *Multi-scale pore morphology in directed vapor deposited yttria-stabilized zirconia coatings.* Materials Science and Engineering: A, 2010. 527(23): p. 6270-6282.
78. Lee, K.N., *Protective coatings for gas turbines*. The Gas Turbine Handbook. 2005, NETL.
79. Xie, L., et al., *Formation of vertical cracks in solution-precursor plasma-sprayed thermal barrier coatings.* Surface and Coatings Technology, 2006. 201(3): p. 1058-1064.
80. Davis, J.R., *Handbook of Thermal Spray Technology*. 2004: ASM International.
81. Singh, J., et al., *An Overview: Electron Beam-Physical Vapor Deposition Technology-Present and Future Applications.*
82. Nash, P., M.F. Singleton, and J.L. Murray, *PhaseDiagrams of Binary Nickel Alloys.* aterials Park,, 1991: p. 3.
83. López, G.A., et al., *Kinetic behaviour of diffusion-soldered Ni/Al/Ni interconnections.* Materials Chemistry and Physics, 2003. 78(2): p. 459-463.
84. Brandl, W., et al., *The oxidation behaviour of sprayed MCrAlY coatings.* Surface and Coatings Technology, 1996. 86: p. 41-47.
85. Smeggil, J.G., *Some comments on the role of yttrium in protective oxide scale adherence.* Material Science and Engineering, 1987. 87: p. 261-265.
86. M., T.H., A.N. M., and B. A., *Role of Y during high temperature oxidation of an M-Cr-Al-Y coating on an Ni-base superalloy.* Surface & coatings technology, 1994. 68-69: p. 10-16.
87. Seraffon, M., et al., *The development of new bond coat compositions for thermal barrier coating systems operating under industrial gas turbine conditions.* Surface & Coatings Technology, 2011. 206(7): p. 1529-1537.

88. Zhang, J., *Preliminary Study On MCrAlX Thermal Spraying Material.* Mining & Metallurgy, 1998. 7(1).

89. Moskal, G., *Thermal barrier coatings: characteristics of microstructure and properties, generation and directions of development of bond.* Journal of Achievements in Materials and Manufacturing Engineering, 2009. 37(2): p. 323-331.

90. Lelait, L., S. Alperine, and R. Mevrel, *Alumina scale growth at zirconia-MCrAlY interface: a microstructural study.* Materials science 1992 (27): p. 5-12.

91. Doychak, J., J. Smialek, and T. Mitchell, *Transient oxidation of single-crystal β-NiAl.* Metallurgical Transactions, 1989. 20(3): p. 499-518.

92. Tolpygo, V.K. and D.R. Clarke, *Microstructural evidence for counter-diffusion of aluminum and oxygen during the growth of alumina scales.* Materials at High Temperatures, 2003. 20(3): p. 261-271.

93. Stott, F.H. and G.C. Wood, *Growth and adhesion of oxide scales on Al2O3-forming alloys and coatings.* Materials Science and Engineering, 1987. 87: p. 267-274.

94. Hou, P.Y., *Segregation Phenomena at Thermally Grown Al2O3/Alloy Interfaces.* Annual Review of Materials Research, 2008. 38: p. 275-298.

95. Kofstad, P., *High Temperature Corrosion. Elsevier Applied Science, London/New York 1988, 546 Seiten mit 222 Illustr. und 6 Tabellen, £ 68.00, ISBN 1-85166-154-9.* Crystal Research and Technology, 1989. 24(4): p. 378-378.

96. Clarke, D.R., *The lateral growth strain accompanying the formation of a thermally grown oxide.* Acta Materialia, 2003. 51(5): p. 1393-1407.

97. Evans, A.G., et al., *Mechanisms controlling the durability of thermal barrier coatings.* Progress in Materials Science, 2001. 46(5): p. 505-553.

98. Shillington, E.A.G. and D.R. Clarke, *Spalling failure of a thermal barrier coating associated with aluminum depletion in the bond-coat.* Acta Materialia, 1999. 47(4): p. 1297-1305.

99. Sohn, Y.H., R.R. Biederman, and R.D. Sisson, *Isothermal oxidation of physical vapor deposited partially stabilized zirconia thermal barrier coatings.* Journal of Materials Engineering and Performance, 1994. 3(1): p. 55-60.

100. Mumm, D.R. and A.G. Evans, *On the role of imperfections in the failure of a thermal barrier coating made by electron beam deposition.* Acta Materialia, 2000. 48(8): p. 1815-1827.

101. Tolpygo, V.K. and D.R. Clarke, *On the rumpling mechanism in nickel-aluminide coatings: Part I: an experimental assessment.* Acta Materialia, 2004. 52(17): p. 5115-5127.

102. Vaunois, J.-R., et al., *A new version of a rumpling predictive model in thermal barrier coatings.* European Journal of Mechanics - A/Solids, 2013. 42(Supplement C): p. 402-421.

103. Balint, D.S. and J.W. Hutchinson, *An analytical model of rumpling in thermal barrier coatings.* Journal of the Mechanics and Physics of Solids, 2005. 53(4): p. 949-973.

104. Chen, X., et al., *Foreign object damage in a thermal barrier system: mechanisms and simulations.* Materials Science and Engineering: A, 2003. 352(1): p. 221-231.

105. Hsieh, J. *Computed tomography: principles, design, artifacts, and recent advances*. 2009. SPIE.

106. Ketcham, R. *X-ray Computed Tomography (CT)*. May 29, 2012; Available from: http://serc.carleton.edu/research_education/geochemsheets/techniques/CT.html.

107. Kropas-Hughes, C.V. and S.T. Neel, *Basics of computed tomography.* Materials evaluation, 2000. 58(5): p. 630-633.

108. *X-ray Computed Tomography (CT)*. Available from: http://serc.carleton.edu/research_education/geochemsheets/techniques/CT.html.

109. Ketcham, R.A. and W.D. Carlson, *Acquisition, optimization and interpretation of X-ray computed tomographic imagery: applications to the geosciences.* Computers & Geosciences, 2001. 27(4): p. 381-400.

110. Kulkarni, A., et al., *Microstructural characterization of electron beam-physical vapor deposition thermal barrier coatings through high-resolution computed microtomography.* Metallurgical and Materials Transactions A, 2004. 35(7): p. 1945-1952.

111. Maurel, V., et al., *Three-Dimensional Damage Evolution Measurement in EB-PVD TBCs Using Synchrotron Laminography.* Oxidation of Metals, 2013: p. 1-11.
112. Kulkarni, A.A., et al., *Advanced microstructural characterization of plasma-sprayed zirconia coatings over extended length scales.* Journal of Thermal Spray Technology, 2005. 14(2): p. 239-250.
113. Helfen, L., et al., *Synchrotron-radiation computed laminography for high-resolution three-dimensional imaging of flat devices.* physica status solidi (a), 2007. 204(8): p. 2760-2765.
114. White, R., *Generation of elastic waves by transient surface heating.* Journal of Applied Physics, 1963. 34(12): p. 3559-3567.
115. Hutchins, D.A., *Ultrasonic Generation by Pulsed Lasers*, in *Physical Acoustics*, M. Warren P and T. R.N, Editors. 1988, Academic Press. p. 21-123.
116. Scruby, C.B. and L.E. Drain, *Laser Ultrasonics, Techniques and Applications*. 1990: CRC Press.
117. Krishnaswamy, S., *Photoacoustic Characterization of Materials*, in *Springer Handbook of Experimental Solid Mechanics*, W.N. Sharpe, Jr., Editor. 2008, Springer US. p. 769-800.
118. Royer, D., M.-H. Noroy, and M. Fink, *Optical generation and detection of elastic waves in solids.* Le Journal de Physique IV, 1994. 4(C7): p. C7-673-C7-684.
119. Davies, S., et al., *Laser-generated ultrasound: its properties, mechanisms and multifarious applications.* Journal of Physics D: Applied Physics, 1993. 26(3): p. 329.
120. Krishnaswamy, S., *Theory and applications of laser-ultrasonic techniques.* Ultrasonic nondestructive evaluation, 2003: p. 435-494.
121. S. Aithal, G. Rousset, and L. Bertrand, *Photoacoustic characterization of subsurface defects in plasma-sprayed coatings.* Thin Solid Films, 1984. 119: p. 153-158.
122. Barsoukov, E. and J.R. Macdonald, *Impedance Spectroscopy: Theory, Experiment, and Applications*. 2005: Wiley.
123. Lvovich, V.F., *Impedance Spectroscopy: Applications to Electrochemical and Dielectric Phenomena*. 2012: Wiley.

124. Orazem, M.E. and B. Tribollet, *Electrochemical Impedance Spectroscopy*. 2017: Wiley.
125. Macdonald, J.R., *Impedance Spectroscopy*. 1987, New York: Wiley.
126. Macdonald, J.R. and W.R. Kenan, *Impedance Spectroscopy: Emphasizing Solid Materials and Systems*. 1987: Wiley.
127. Amaral, S.T. and I.L. Muller, *Effect of Silicate on Passive Films Anodically Formed on Iron in Alkaline Solution as Studied by Electrochemical Impedance Spectroscopy.* CORROSION, 1999. 55(1): p. 17-23.
128. Fletcher, J.G., et al., *The AC-impedance response of the physical interface between yttria-stabilized zirconia and YBa2Cu3O7-X*. Journal of The Electrochemical Society, 1995. 142(8): p. 2650-2654.
129. Jacobsen, T., et al., *SOFC Cathode Mechanisms*. 1996, Risø National Laboratory. p. 29-40.
130. Zhang, D.-h., H.-b. Guo, and S.-k. Gong, *Impedance spectroscopy study of high-temperature oxidation of Gd2O3-Yb2O3 codoped zirconia thermal barrier coatings.* Transactions of Nonferrous Metals Society of China, 2011. 21(5): p. 1061-1067.
131. Liu, C., et al., *Evaluation of Thermal Barrier Coatings Exposed to Hot Corrosion Environment by Impedance Spectroscopy.* Chinese Journal of Aeronautics, 2011. 24(4): p. 514-519.
132. Fleig, J., *The grain boundary impedance of random microstructures: numerical simulations and implications for the analysis of experimental data.* Solid State Ionics, 2002. 150(1): p. 181-193.
133. Huang, H., et al., *Evaluation of microstructural evolution of thermal barrier coatings exposed to Na2SO4 using impedance spectroscopy.* Corrosion Science, 2011. 53(4): p. 1369-1374.
134. Gómez-García, J., et al., *Correlation of mechanical properties and electrochemical impedance spectroscopy analysis of thermal barrier coatings.* Surface and Coatings Technology, 2009. 204(6): p. 812-815.
135. Song, S.H., P. Xiao, and L.Q. Weng, *Evaluation of microstructural evolution in thermal barrier coatings during thermal cycling using impedance spectroscopy.* Journal of the European Ceramic Society, 2005. 25(7): p. 1167-1173.

136. Zhang, C., et al., *Evaluation of thermal barrier coating exposed to different oxygen partial pressure environments by impedance spectroscopy.* Surface and Coatings Technology, 2006. 201(1): p. 446-451.
137. Byeon, J.W., et al., *Non-destructive evaluation of degradation in multi-layered thermal barrier coatings by electrochemical impedance spectroscopy.* Materials Science and Engineering: A, 2005. 407(1–2): p. 213-225.
138. Wu, N.Q., et al., *Failure detection of thermal barrier coatings using impedance spectroscopy.* Thin Solid Films, 2004. 457(2): p. 301-306.
139. Näfe, N., *Solid State Ionics*. Vol. 13. 1984.
140. Ferber, M.K., et al., *Application of infrared imaging to the study of controlled failure of thermal barrier coatings.* Journal of Materials Science, 2000. 35(11): p. 2643-2651.
141. Franke, B. and B. Franke, *Nondestructive Evaluation of Thermal Barrier Coatings with Thermal Wave Imaging and Photostimulated Luminescence Spectroscopy.* 2005.
142. Franke, B., et al., *Monitoring damage evolution in thermal barrier coatings with thermal wave imaging.* Surface & Coatings Technology, 2005. 200(5): p. 1292-1297.
143. Lipkin, D.M. and D.R. Clarke, *Sample-probe interactions in spectroscopy: Sampling microscopic property gradients.* Journal of Applied Physics, 1995. 77(5): p. 1855-1863.
144. Christensen, R.J., et al., *Nondestructive evaluation of the oxidation stresses through thermal barrier coatings using Cr3+ piezospectroscopy.* Applied Physics Letters, 1996. 69(24): p. 3754-3756.
145. Clarke, D.R., R.J. Christensen, and V. Tolpygo, *The evolution of oxidation stresses in zirconia thermal barrier coated superalloy leading to spalling failure.* Surface & Coatings Technology, 1997. s 94–95(1-3): p. 89–93.
146. Lipkin, D.M., et al., *Stress development in alumina scales formed upon oxidation of (111) NiAl single crystals.* Corrosion Science, 1997. 39(2): p. 231-242.
147. Sergo, V. and D.R. Clarke, *Observation of Subcritical Spall Propagation of a Thermal Barrier Coating.* Journal of the American Ceramic Society, 1998. 81(12): p. 3237-3242.

148. Heeg, B. and D.R. Clarke, *Non-destructive thermal barrier coating (TBC) damage assessment using laser-induced luminescence and infrared radiometry.* Surface & Coatings Technology, 2005. 200(5–6): p. 1298-1302.
149. Gell, M., et al., *Bond strength, bond stress and spallation mechanisms of thermal barrier coatings.* Surface & Coatings Technology, 1999. s 120–121(99): p. 53-60.
150. Sohn, Y.H., et al., *Thermal cycling of EB-PVD/MCrAlY thermal barrier coatings: II. Evolution of photo-stimulated luminescence.* Surface & Coatings Technology, 2001. s 146–147(9): p. 102-109.
151. Xie, L., et al., *The effect of bond coat grit blasting on the durability and thermally grown oxide stress in an electron beam physical vapor deposited thermal barrier coating.* Surface & Coatings Technology, 2003. 176(1): p. 57-66.
152. Sridharan, S., et al., *Stress variation with thermal cycling in the thermally grown oxide of an EB-PVD thermal barrier coating.* Surface & Coatings Technology, 2004. 179(2): p. 286-296.
153. Tolpygo, V.K. and D.R. Clarke, *Microstructural study of the theta-alpha transformation in alumina scales formed on nickel-aluminides.* Materials at High Temperatures, 2000. 17(1): p. 59-70.
154. Salmanzadeh, M., M.J. Azizpour and H.M. Majd, *Evaluation of the Effect of Spray Distance on Fracture Toughness of Thermally Sprayed Coatings.* Journal of Applied Sciences, 2015. 15(4): p. 709-714.
155. Praxair Surface Technologies, I., *Model SG-100 Plasma Spray Gun Operator's Manual.* 2011: p. 26.
156. Bottiglieri, S., *The effect of microstructure in aluminum oxide ceramics on acoustic loss mechanisms.* 2012.
157. Querry, M.R., *Optical constants*, in *Contractor Report CRDC-CR-85034*. 1985.
158. Pedrotti, F.L., L.S. Pedrotti, and L.M. Pedrotti, *Introduction to optics*. 2007: Pearson.
159. Wood, D.L. and K. Nassau, *Refractive index of cubic zirconia stabilized with yttria.* APPLIED OPTICS, 1982. Vol. 21(16).
160. Heiroth, S., et al., *Optical and mechanical properties of amorphous and crystalline yttria-stabilized zirconia thin films prepared by pulsed laser deposition.* Acta Materialia, 2011. 59(6): p. 2330-2340.

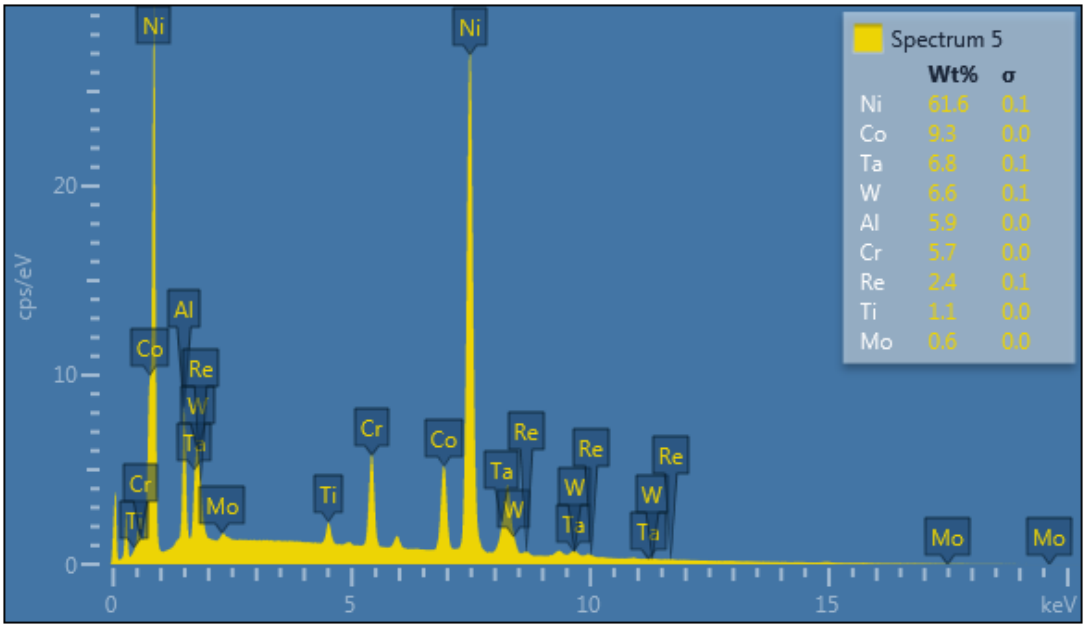
161. Weber, M.J., *Handbook of Optical Materials*. 2003: CRC PRESS.

162. Zhang, C., et al., *Ionic conductivity and its temperature dependence of atmospheric plasma-sprayed yttria stabilized zirconia electrolyte.* Materials Science & Engineering B, 2007. 137(1–3): p. 24-30.

163. Sokołowski, P., et al. *A comparison of microstructure and of thermal transport properties of yttria and ceria stabilized zirconia coatings deposited by suspension plasma spraying*. in *International Thermal Spray Conference*. 2014. Barcelona, Spain: DVS.

Appendix A

EDS elements analysis for composition of CMSX-4 nickel superalloy



Appendix B

List of thermally sprayed samples

Table B.1 List of thermal barrier coating samples

Sample ID	Substrate	Topcoat thickness (passes)	Tested at (number of cycles)	SEM Characterisation	NDT technique appiled
A	SX	14	0, 20, 40, 60	No	
B	SX	14	0, 20, 40, 60	No	
C	SX	14	0, 20, 40, 60	No	
D	SX	14	0	Yes	
E	SX	14	20	Yes	
F	SX	14	40	Yes	
G	SX	14	60	Yes	
H	SX	14	80	No	
I	SX	8	0, 20, 40	No	
J	SX	8	0, 20, 40, 60	No	
K	SX	8	0, 20, 40	No	
L	SX	8	0	Yes	
M	SX	8	0, 20	Yes	
N	SX	8	0, 20, 40	Yes	Laser photoacoustic spectroscopy
O	SX	8	0, 20, 40, 60	Yes	
P	SX	8	0, 20, 40, 60	No	
Q	SX	8	0, 20, 40, 60	No	
1	MG	14	0, 5, 10, 20, 40, 80	Yes	
2	MG	14	0, 5, 10, 20, 40, 80	Yes	
3	MG	14	0, 5, 10, 20, 40	Yes	
4	MG	14	0, 5, 10, 20, 40	Yes	
5	MG	14	0, 5, 10, 20	Yes	
6	MG	14	0, 5, 10, 20	Yes	
7	MG	14	0, 5, 10	Yes	
8	MG	14	0, 5, 10	Yes	
9	MG	14	0, 5	Yes	
10	MG	14	0, 5	Yes	
11	MG	14	0	Yes	
12	MG	14	0	Yes	

SX = Single crystal superalloy CMSX-4 MG = Nickel-based superalloy Mar-M-247 (Multigrain)

Table B.2 List of bond coat only samples

Sample ID	Substrate	Topcoat thickness (passes)	Tested at (number of cycles)	SEM Characterisation	NDT technique appiled
A	MG	-	0, 2, 5, 10, 20, 40, 80	No	Laser photoacoustic spectroscopy
B	MG	-	0	Yes	
C	MG	-	2	Yes	
D	MG	-	5	Yes	
E	MG	-	10	Yes	
F	MG	-	20	Yes	
G	MG	-	40	Yes	
H	MG	-	80	Yes	

MG = Nickel-based superalloy Mar-M-247 (Multigrain)

Table B.3 List of YSZ freestanding samples

Sample ID	Substrate	Topcoat thickness (passes)	Thickness (μm) Error: ±1 μm	Tested at (number of cycles)	NDT technique appiled
A	Mild steel, (Detached by placed in 5M hydrochloric acid at 80 °C for 48 hours	8	273	0	Laser photoacoustic spectroscopy (Measurement of laser attenuation in YSZ ceramic coating)
B		16	467	0	
C		32	875	0	
D		64	1722	0	
E		128	3375	0	
F		14	-	0	
G		14	-	0	
H		14	-	80	
I		14	-	80	

Appendix C

Calculation of surface temperature rise by single laser pulse

Assuming that a laser pulse uniformly radiates to an area A of the sample surface, and the energy of this single laser pulse is fully absorbed by the surface layer of sample throughout an effective depth of penetration δ, so that the energy of the laser pulse is transferred as heat that raises the surface temperature of the sample. As further assuming that the laser pulse is extremely short, so that the conductivity from the radiated area to the bulk of sample can be neglected. Therefore, the temperature rise in the surface layer is given by

$$\Delta T = \frac{E}{C\rho A\delta}$$

where E is the energy of a single laser pulse, 105 μJ. C is the specific heat capacity of YSZ layer, 438 J/kg·K [163]. ρ is the density of YSZ layer, 5.8 g/cm^3. The value of skin depth is estimated, which is greater than 126.4 μm, via the measurement of the attenuation of freestanding YSZ coating.

As a result, the temperature rise of sample surface ΔT is 0.0041 K.

Appendix D

MATLAB script for finding the centre of sample and Butterworth high-pass filter

```
square = Eng_501;

R = 440;

range = 10;

[true_centerX,true_centerY] = find_centre(square,R,range);


imageSizeX=501;

imageSizeY=501;

step_size = 32;  %um

true_radius = 6.944;  %mm

radius = true_radius/step_size*1e3;

[columnsInImage, rowsInImage] = meshgrid(1:imageSizeX, 1:imageSizeY);

circlePixels = (rowsInImage - true_centerY(1)).^2 + (columnsInImage - true_centerX(1)).^2 <= radius.^2;


cen_sig = abs(F20_pha_all.*circlePixels);

[b,a]= butter(2, 0.2, 'high');

for i=1:size(cen_sig,1)

   tmp=squeeze(cen_sig(i,:));

   %%% Digital filter Butterworth

   %plot magnitude spectrum of the signal

   tmp_mags = abs(fft(tmp));

%     figure(s+11);plot(tmp_mags);title('5th order Butterworth filter')

%     xlabel('DFT Bins')

%     ylabel('Magnitude')
```

```
%plot first half of DFT (normalised frequency)
   num_bins = length(tmp_mags);
%    plot([0:1/(num_bins/2 -1):1], tmp_mags(1:num_bins/2))
%    ylabel('Magnitude')
%    xlabel('Normalised frequency (\pi rads/sample)')
%plot the frequency response (normalised frequency)
   H = freqz(b,a,floor(num_bins/2));
%    hold on
%    plot([0:1/(num_bins/2 -1):1], abs(H),'r');


%filter the signal using the b and a coefficients obtained from the butter filter design function
   tmp_filtered = filter(b,a,tmp);
%    plot the filtered signal
%    figure(3);plot(t_cen, tmp_filtered,'r')
%    title('Filtered Signal - Using 5th Order Butterworth');
%    xlabel('Time/s');
%    ylabel('Amplitude');


   filtered_cen_sig(i,:)=tmp_filtered;
end


% Cut off phase shift
filtered_cen_sig_cut = filtered_cen_sig.*circlePixels;
```

Appendix E

EDS element mapping of un-melted NiCoCrAlY particle after thermal oxidation

